Spin waves in inhomogeneous magnetization distributions

Matías Pablo Grassi

UNIVERSITÉ DE STRASBOURG

ÉCOLE DOCTORALE DE PHYSIQUE ET CHIMIE-PHYSIQUE

Institut de Physique et Chimie des Matériaux de Strasbourg

THÈSE présentée par :

Matías Pablo GRASSI

soutenue le : **13 avril 2021**

pour obtenir le grade de : **Docteur de l'université de Strasbourg**

Discipline/ Spécialité : Physique/ Physique de la Matière Condensée

Ondes de spin dans des distributions d'aimantation inhomogènes

THÈSE dirigée par :

M. BAILLEUL Matthieu	Chargé de recherche CNRS, Institut de Physique et Chimie des Matériaux de Strasbourg

RAPPORTEURS :

M. CHUMAK Andrii	Professeur, Universität Wien
M. DE LOUBENS Grégoire	Chercheur CEA, Service de Physique de l'Etat Condensé

EXAMINATEURS :

Mme. TACCHI Silvia	Chercheuse CNR, Istituto Officina dei Materiali
M. HERTEL Riccardo	Directeur de recherche CNRS, Institut de Physique et Chimie des Matériaux de Strasbourg

Université de Strasbourg
Institut de Physique et Chimie des Matériaux de Strasbourg

Spin waves in inhomogeneous magnetization distributions

Matías Pablo Grassi

Contents

Abbreviation table

IP	In-plane (films)
OOP	Out-of-plane (films)
PMA	Perpendicular magnetic anisotropy (uniaxial)
VNA	Vector Network Analyzer
FMR	Ferromagntic resonance (spectroscopy)
MW	Microwave
CPW	Coplanar Waveguide
PSWS	Propagating-Spin-Wave Spectroscopy
BLS	Brillouin Light Scattering
MFM	Magnetic Force Microscopy
VSM	Vibrating Sample Magnetometry
DE	Damon-Eshbach (configuration)
BV	Backward-Volume (configuration)
FV	Foward-Volume (configuration)
PSSW	Perpendicular Standing Spin Wave
KS	Kalinikos-Slavin (approach)
SWIIM	Spin Wave fInite dIfference Modeling (finite-difference micromagnetic approach)
IPCMS	Institut de Physique et Chimie des Matériaux de Strasbourg
TUK	Technical University of Kaiserslautern
IJL	Institut Jean Lamour

Acknowledgments

As it is evident from the preface, this work was done in the context of several collaborations and with the support of a large team of researchers and technicians.

Of course, I'll start with the person that was fundamental for the development of this work, my advisor Matthieu Bailleul. In addition of giving me the opportunity of working at the IPCMS, you helped me in all the steps of the thesis while giving me my own space to work, and even if sometimes was difficult to follow all the ideas, I have learnt a lot with you. I really appreciate that you let me free to develop the ideas that come in my mind making your best to guide them in the good direction. In addition to this, you were always supportive in all the aspects of my PhD and in my personal life.

Also from the IPCMS, I have to mention the enormous help that I received from Yves and Daniel S. Yves not just developed the SWIIM algorithm and taught me how to use it, but you have never hesitated to give me your advice and I really appreciated your direct remarks. With Daniel, I have really enjoyed every time I arrived to your office to ask you a question and stay there discussing physics and trying to find the connections between the experiments and the simulations. Thanks to José S. for all the excellent discussions, your questions and remarks helped me a lot to understand many details. Damien Louis, thanks for introduce me to the laboratory and to teach me the lithography techniques.

All this work could not be possible without the help of the STnano crew, Sabine, Romain and Hicham. I really enjoyed working with you, and it was a pleasure to do it in such a good environment.

I would like to thank Salia C. for giving me the opportunity of working with the Kerr microscope and for teaching me how to use it.

I really appreciated the collaboration with the team of Kaiserslautern. In particular, I would like to thank Philipp P. (who was also invited jury in the defense of this work) for inviting me to take part of the BLS measurements, and to Moritz G., who introduced me to the BLS world and was my guide during my stay in Kaiserslautern. I would also like to thank Tobias and Moritz R. for their help with the measurements and Thomas B. for the discussions.

I also thank Michel H., Daniel L. (who was also invited jury in the defense of this

work) and Kosseila A., who invited me to work in the clean-room of the Institute Jean Lamour and whose knowledge on good-quality sample growing was fundamental for carry on the experiments.

From C2N, I would like to thank Thibaut D. and Jean-Paul A. for the interesting discussion at the SWANGATE meetings.

I would like to thank the jury members, who accepted to evaluate this work, and whose corrections and remarks improved the quality of this work.

I couldn't omit Véronique W. and Catherine B., the two secretaries that helped me through all the paper work and simplified my life considerably.

My passage through the IPCMS has been a lot better thanks to the priceless company of the collegues: Luis, Mauricio, Anna, Ben, Paula, Etienne, Swapneel, Raj, François, Kevin, Loïc, Alex, Ulrich, Kiril and Anatoli. And I would like to thank Julia, Inès, Sacha and Daniel N. for make my stay in Strasbourg more enjoyable.

Finally, I would like to also thank the all the people that made possible for me to arrive at the stage of doing the PhD, in particular to my high-school teacher Alejandra, who introduced me to the amazing world of Physics; to my professors at the Instituto Balseiro; and to my Master's advisors, Javier and Sebastian. I would also like to thank my family who supported me in all this adventure, and to Dani who give me unconditional support during the toughest part of this work.

Direction de la **recherche**
et de la **valorisation**
Collège **doctoral**
Université de Strasbourg

Déclaration sur l'honneur
Declaration of Honour

J'affirme être informé que le plagiat est une faute grave susceptible de mener à des sanctions administratives et disciplinaires pouvant aller jusqu'au renvoi de l'Université de Strasbourg et passible de poursuites devant les tribunaux de la République Française.

Je suis conscient(e) que l'absence de citation claire et transparente d'une source empruntée à un tiers (texte, idée, raisonnement ou autre création) est constitutive de plagiat.

Au vu de ce qui précède, **j'atteste sur l'honneur que le travail décrit dans mon manuscrit de thèse est un travail original et que je n'ai pas eu recours au plagiat ou à toute autre forme de fraude.**

I affirm that I am aware that plagiarism is a serious misconduct that may lead to administrative and disciplinary sanctions up to dismissal from the University of Strasbourg and liable to prosecution in the courts of the French Republic.

I am aware that the absence of a clear and transparent citation of a source borrowed from a third party (text, idea, reasoning or other creation) is constitutive of plagiarism.

In view of the foregoing, ***I hereby certify that the work described in my thesis manuscript is original work and that I have not resorted to plagiarism or any other form of fraud.***

Nom : GRASSI

Prénom : Matías Pablo

Ecole doctorale : 182

Laboratoire : IPCMS

Date : 30/04/2021

Introduction

Spin waves, the elementary low-energy excitation of magnetically ordered materials, and their associated quasi-particle, magnons, can propagate spin angular momentum and energy. In the so-called magnonic devices spin waves carry information coded into their phase or amplitude [1]. Such devices present several advantages, among which we can highlight the intrinsic versatility of magnetic materials that support the spin-waves, allowing for agile and reconfigurable architectures; the lack of Joule heating, reducing device energy consumption; the intrinsic non-linearity of magnetization dynamics and the micrometer-scale coherence length, making them suitable to perform wave computing [2]; and the ability to perform directly GHz and THz signal processing [3].

These properties make magnonic technology a suitable beyond CMOS alternative, as identified by the International Technology Roadmap for Semiconductors [4]. However, in order to build magnonic devices, spin-wave propagation has to be controlled efficiently. This task can be performed by magnonic crystals, periodic magnetic nanostructures which can be used to build passive and active magnonic circuit elements [5, 6]. However, these structures involve complex fabrication processes. An alternative is given by stable topological magnetic structures such as magnetic domain walls [7], vortices, and skyrmions [8]. These textures, which can be seen as a static counterpart of the dynamic spin-wave modes, influence directly spin-wave propagation. Moreover, the magnetic textures are more versatile than the magnonic crystals, as their structure can be easily modified, by a magnetic field, an electrical field/current, or even, in the ultimate scheme of reconfigurable magnonic devices by spin waves themselves, as in the case of domain walls [9]. These mutual interactions pave the way to the treatment of information in all-magnon approach, which totally avoids energy losses by Joule heating [10, 11].

In this context, we have studied the properties of spin waves interacting with nonuniform magnetic distributions. For that, we have studied two systems:

- Weak stripe domains, which are a magnetic texture that nucleates at low field in films with perpendicular magnetic anisotropy (PMA). In this system, the nonuniform distribution of the magnetization appears spontaneously at nucleation. Their periodic character identifies these structures as one-dimensional

magnonic crystals, while keeping the versatility of magnetic textures.

- A bilayer with contrast of saturation magnetization. Here, the inhomogeneity imposed at fabrication results in a specific nonreciprocal type of propagation which can be used for designing a magnonic diode.

Despite their differences, the two systems share several common characteristics:

- The specific broken-symmetries (periodic modulation and up-down broken symmetry) are fundamental to determine the spin-wave modes properties.
- The dipolar field, is a key ingredient that introduces complexity and makes these systems nontrivial.
- The two systems are studied in the so-called Damon-Eshbach (DE) configuration (applied field in the film plane, and spin-wave wave vector perpendicular to it). In this configuration, spin waves present a specific chiral character and a tendency toward flux closure which will be of major importance for the effects investigated.

These two systems were investigated in the framework of two projects, SWANGATE and MAGMATCH. Both projects included the participation of multiple researchers, and their collaboration was fundamental to the realization of this work.

SWANGATE

The ANR project "Spin-wave nanochannels for reprogrammable logic gates" (ANR-16-CE24-0027) involves three partners: Institut Jean Lamour (IJL), Centre de Nanosciences et de Nanotechnologies (C2N), and Institut de Physique et Chimie des Matériaux de Strasbourg (IPCMS). The Technical University of Kaiserslautern (TUK) was also involved as associated partner.

This project proposed to use domain walls —the interface between magnetic domains with different orientation of the magnetization— as reconfigurable spin-wave waveguides [7]. In this context, we have studied the spin-wave modes in magnetic stripe domains, which can be thought as an array of parallel domain walls.

Within this project, we have studied ferromagnetic thin films with PMA, which is a property required for the nucleation of stripe domains. In a first approach, the spin-wave propagation in multilayers of Co/Ni, a material with a strong PMA, has been studied in the saturated state by M. Sushruth, a postdoc in C2N [12]. Later, the project has focused on the spin-wave dynamics in films of CoFeB, as they present a lower damping, making them better candidates for the study of spin-wave propagation. The static properties of the stripe domains of CoFeB have been extensively studied by K. Ait Oukaci, during his PhD at IJL. High-resolution scanning transmission x-ray

microscopy (STXM) and magnetic force microscopy (MFM) provided information on their precise structure [13, 14]. Based on this knowledge, micromagnetic simulations were done to explore the related dynamics, finding that the spin-wave modes adapt to the symmetries imposed by the texture. All these studies served as background for the realization of this work, where we have focused on the experimental study of the dynamic properties and analytical understanding of the stripes.

The fabrication of all thin films, magnetometry and high-resolution magnetic imaging was done by K. Ait Oukaci, D. Lacour and M. Hehn, at IJL. BLS measurements were done in TUK by M. Geilen and P. Pirro, but the author of this work also traveled to Kaiserslautern to participate in the measurements. Mumax3 micromagnetic simulations were performed by D. Stoeffler at IPCMS. FMR and PSWS measurements and the analytical modeling were done at IPCMS.

MAGMATCH

The project "The spin-wave dioptre: towards magnon matching" was funded by the *Laboratoire d'excellence* "Nanostructures in interaction with their environment" (ANR-11-LABX-0058-NIE). Its primary aim was to understand how spin-wave can propagate in the presence of abrupt changes of the magnetic properties. More specifically, we focused our attention on ferromagnetic bilayers with thicknesses of several tens of nanometers where both the exchange and dipolar interaction play a fundamental role.

The samples used in this project were grown by D. Lacour and M. Hehn at IJL. D. Louis, initiated the fabrication of devices and the inductive measurements during his Post-Doc at IPCMS, but in the later steps he was substituted by the author of this work. BLS measurements were performed at TUK by M. Geilen and P. Pirro. D. Louis and the author of this work participated in the thermal and micro-focus BLS measurements, respectively. Mumax3 and SWIIM simulations were performed by D. Stoeffler and Y. Henry at IPCMS.

About this manuscript

This work was entirely written in LaTeX. Figures were mostly done using Inkscape, Origin and GNUplot. The analytical calculations were performed using Mathematica. Spin-wave simulations in the saturated state were performed using SWIIM [15].

The contents are organized in five chapters and a final general conclusion. The first two chapters are introductory and give the basics on statics and dynamics of magnetization. Chapter 3 presents the experimental techniques used in this work. The last two chapters show the results obtained on the ferromagnetic bilayers (Chapter 4) and on films presenting magnetic stripe domains (Chapter 5).

Chapter 1

Magnetization statics

This chapter introduces the physics of mesoscopic magnetic systems. The main interactions that affect the spatial distribution of the magnetization are reviewed. Then, a particular static texture is presented: the magnetic stripe domains.

1.1 Magnetic moments and magnetization

Different materials could present a variety of magnetic properties. This depends mostly on the interaction between the constituent magnetic moments $\boldsymbol{\mu}$, which can have two different origins: charge particles with an angular moment $\boldsymbol{L}$ —in particular atomic valence electrons—, and the electron intrinsic spin $\boldsymbol{S}$. In general, $\boldsymbol{\mu}$ depends on both contributions and can be expressed as

$$\boldsymbol{\mu} = \gamma \boldsymbol{J} \tag{1.1}$$

where $\boldsymbol{J} = \boldsymbol{L} + 2\boldsymbol{S}$ is the total angular moment, and γ is the gyromagnetic ratio which is a material property that depends on the proportion between $\boldsymbol{S}$ and $\boldsymbol{L}$ in the total angular moment. For most transition metals the main contribution is given by $\boldsymbol{S}$ and it is possible to take $\boldsymbol{L} = 0$[1]. For this case, $\gamma \approx 1.75\ 10^{11}$ rad/(T · s), or equivalently, $\frac{\gamma}{2\pi} \approx 28$ GHz/T.

Depending on the material structure, these magnetic moments could interact in different ways as it will be reviewed in Section 1.2. If they present little interaction between them, the material display a para- or diamagnetic behavior. On the contrary, if the exchange[2] is strong enough, long range order could develop. Depending on the nature of the exchange interaction, ferro, ferri or antiferromagnetic behaviors will be

[1] This phenomenon is known as the quenching of orbital angular momentum. It results from the effects of the strong electric fields from neighboring ions [16].

[2] Short range interaction appearing as a consequence of quantum mechanics. It will be reviewed in Section 1.2.2.

favored. This work will focus on different phenomena involving materials that present a ferromagnetic order, in which exchange promotes configurations with parallel magnetic moments. In such configurations, in absence of other interactions, all magnetic moments remain aligned in a certain direction.

For studying these materials at intermediate length- and time-scales, one uses a mesoscopic approach to study the dynamics of the magnetic moments. To do so, the material is divided in regions of volume V that are big enough to contain several magnetic moments but sufficiently small to ensure that they are parallel. Within this approach, the *mesoscopic* magnetization density $\boldsymbol{M}$ — or magnetization, for short— is defined as

$$\boldsymbol{M} = \sum_{V} \frac{\boldsymbol{\mu}(\boldsymbol{r'})}{V}, \tag{1.2}$$

where $\boldsymbol{r'} \in V$. $\boldsymbol{M}$ can be interpreted as a classical pseudovector, neglecting the quantum properties of $\boldsymbol{\mu}$. In the International System of Units (SI) $\boldsymbol{M}$ is expressed in A/m, while is expressed in emu/cm^3 in CGS. In our case, we will treat the magnetization density as a continuous parameter defining a smoothly varying magnetization field $\boldsymbol{M}(\boldsymbol{r})$, and we will think V as much smaller than all relevant dimensions in the considered problem.

The value of $|\boldsymbol{M}|$ is generally constant and can be considered a material property. We will use the standard notation and write $|\boldsymbol{M}| = M_S$, which is known as saturation magnetization. Nevertheless, the direction of $\boldsymbol{M}$ can change within the sample. The field which studies the behavior of the magnetization in the mesoscopic scale is called micromagnetism.

1.2 Magnetic interactions

The spatial distribution of the magnetization in a ferromagnetic sample will be given by the configuration which minimizes the total energy $\mathcal{E}_T$ of the studied system. In the next sections, the different interactions which contribute to $\mathcal{E}_T$ will be reviewed. For these interactions, an explicit expression for the energy density E will be found. The two quantities are related as $\mathcal{E} = \int_V E(\boldsymbol{r})\, d\boldsymbol{r}$. Near the energy minimum which defines the static configuration, a generalized force that drags $\boldsymbol{M}$ to the equilibrium can be defined. We will refer to this force as an effective magnetic field $\boldsymbol{H}^{\text{eff}}$, which can be calculated as[3]

$$\boldsymbol{H}^{\text{eff}} = -\frac{1}{\mu_0} \frac{\partial E_T}{\partial \boldsymbol{M}}, \tag{1.3}$$

This description is similar to the study of a particle in a potential. However,

[3]Calculate the partial derivative of the energy with respect to $\boldsymbol{M}$ is analogous to calculate the gradient in the real space as $\boldsymbol{\nabla} = \frac{\partial}{\partial \boldsymbol{R}}$, where $\boldsymbol{R}$ is the position vector.

the evolution of the magnetization towards the energy minimum is not direct. As a consequence of the constant module of $\boldsymbol{M}$, its trajectory must remain confined to a sphere, as shown in Fig. 1.1. Therefore, only the component of the effective field that is perpendicular to the magnetization, $\boldsymbol{H}_{\perp}^{\text{eff}}$, will have an effect on $\boldsymbol{M}$.

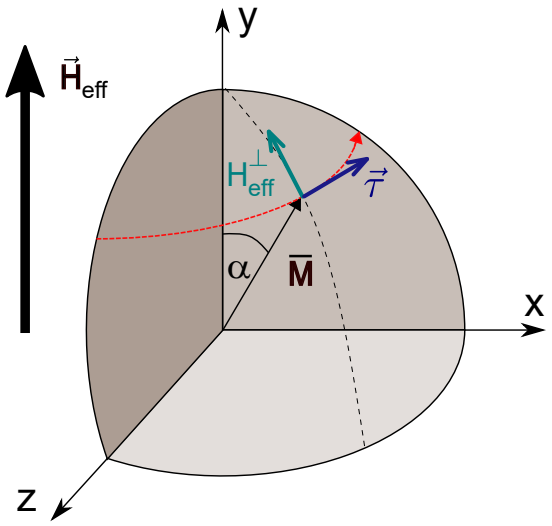

Figure 1.1: The magnetization vector $\boldsymbol{M}$ can move on the surface of the sphere $|\boldsymbol{M}| = M_S$. Because it must behave as an angular moment, the force $\boldsymbol{F}$ generates a torque τ that induces the precession of $\boldsymbol{M}$ around $\boldsymbol{H}^{\text{eff}}$.

Another constrain is that $\boldsymbol{M}$ is associated to the total angular moment $\boldsymbol{J}$ and their dynamics must coincide. Hence, the time evolution will be given by a torque $\boldsymbol{\tau} = \frac{\partial \boldsymbol{J}}{\partial t}$. An expression of this torque can be intuitively understood from the classical mechanics point of view. In this case, the force is calculated as the opposite of the gradient $\frac{\partial}{\partial \boldsymbol{r}}$ of the total energy of the system. Comparing with equation 1.3, the substitution $\boldsymbol{r} \to \boldsymbol{M}$ seems adequate to go from a mechanical system to the studied magnetic system, taking $\boldsymbol{M}$ as a generalized coordinate. From here, it is possible to propose the following torque expression

$$\boldsymbol{\tau} = \frac{\partial \boldsymbol{J}}{\partial t} = -\mu_0 \boldsymbol{M} \times \boldsymbol{H}^{\text{eff}}. \tag{1.4}$$

In general, the static magnetic configurations can be obtained by minimizing the total energy of the magnetic system, or equivalently, by finding the zero-torque configurations.

1.2.1 Zeeman interaction

Let us consider an external field $\boldsymbol{H}$ which is applied on a magnetization distribution. For a point with magnetization $\boldsymbol{M}$, the corresponding energy density can be expressed as [17]

$$E_Z = -\mu_0 \, \boldsymbol{M} \cdot \boldsymbol{H}, \tag{1.5}$$

where $\mu_0 = 4\pi\,10^{-7}$ kg m A^{-2} s^{-2} is the vacuum permeability. This contribution to the energy is called Zeeman interaction, after Pieter Zeeman who discovered the splitting of the spectral line of some elements when applying a magnetic field. This energy has one unique minimum, which leads to only one stable equilibrium point, where $\boldsymbol{M} \parallel \boldsymbol{H}$. From Eqs. 1.4 and 1.5 we observe that the effective field associated with the Zeeman interaction is H. This justifies the interpretation of the generalized force as an effective magnetic field.

Using the constant module of the magnetization $|\boldsymbol{M}| = M_S$ and writing the magnetic field as $\boldsymbol{H} = H\,\hat{y}$, the scalar product from definition 1.5 can be developed as

$$E_Z = \mu_0\,\boldsymbol{M}\cdot\boldsymbol{H} = \mu_0\,H\,M_y = \mu_0\,H\sqrt{M_S^2 - M_x^2 - M_z^2}. \tag{1.6}$$

This expression, which relates the Zeeman energy to of the transversal components of the magnetization, will be used in Section 1.3.

1.2.2 Exchange interaction

The ferromagnetic exchange is an interaction which favors single domain configurations, as it introduces a penalty for any deviation of the magnetization from a uniform distribution. It is a short range interaction and it has purely quantum origins, as it is a consequence of the permutation symmetry of fermionic —in our case, electronic— systems.

In a mesoscopic ferromagnetic system, the contribution of the exchange to the energy density can be written as[4]

$$E_{ex} = \frac{A_{\text{ex}}}{M_S^2}\sum_i \left(\frac{\partial \boldsymbol{M}}{\partial x_i}\right)^2 \tag{1.7}$$

where $x_i = x, y, z$, and A_{ex} is the exchange constant[5]. For most metallic ferromagnetic compounds, it takes values of the order of 10 pJ/m[19, 20]. The associated effective field can be calculated as

$$\boldsymbol{H}_{\text{eff}}^{ex} = -\frac{1}{\mu_0}\frac{\partial E_{ex}}{\partial \boldsymbol{M}} = \Lambda^2\nabla^2\boldsymbol{M} \tag{1.8}$$

where $\Lambda = \dfrac{1}{M_S}\sqrt{\dfrac{2\,A_{\text{ex}}}{\mu_0}}$ is the exchange length, typically of the order of some

[4]This formula is not only valid in the case of direct exchange but, with different coefficients, it also describes some indirect exchanges as super-exchange, double-exchange or RKKY.

[5]Some times this parameter is called *exchange stiffness constant*, in order to underline difference with the *exchange constant* J, from Heisenberg's model. These two parameters are related by $A_{\text{ex}} = \frac{nS^2}{a}J$, where n is the number of nearest neighbors, a is the lattice parameter, and S is the spin number [18].

nanometers [19], and ∇^2 is the vector Laplacian[6]. The exchange length can be interpreted as the typical maximum distance below which the exchange interaction between two magnetic moments is stronger that the dipolar interaction.

1.2.3 Dipolar interaction

Each magnetic moment can be thought as a source of dipolar field that interacts with the other magnetic moments. From the mesoscopic point of view, we can take all points of the sample with a given magnetization as a source of dipolar field.

This interaction depends strongly on the relative position between these magnetic moments and it will be determined by the geometry of the sample. From the micromagnetic point of view, it is the most difficult interaction to compute, as it is highly anisotropic and long ranged, implying integrals over the whole sample. Nevertheless, in some simple geometries, the resulting effective field $\boldsymbol{H}_d$ can be calculated analytically. We note that the effective field of the dipolar interaction is the dipolar field itself: $\boldsymbol{H}_{\boldsymbol{d}}^{\text{eff}} = \boldsymbol{H}_d$.

There are several ways of calculate $\boldsymbol{H}_d$. We will focus on one that is particularly intuitive as it is based on the concept of magnetic charge. From the constituent relations and Maxwell's equations the magnetic field satisfies

$$\boldsymbol{\nabla} \cdot \boldsymbol{B} = \mu_0 \boldsymbol{\nabla} \cdot (\boldsymbol{H}_d + \boldsymbol{M}) = 0. \tag{1.9}$$

As a useful notation, we will define

$$\boldsymbol{\nabla} \cdot \boldsymbol{H}_d = \rho_M, \tag{1.10}$$

where $\rho_M = -\boldsymbol{\nabla} \cdot \boldsymbol{M}$ is the magnetic-charge density, and is analogous to the conventional electric-change density. In the boundaries of the sample, where the magnetization vanish abruptly, this expression defines the surface magnetic charges $\sigma_M = \hat{n} \cdot \boldsymbol{M}$, where $\hat{n}$ is the outward versor normal to the surface.

In addition, in the magnetostatic regime and in absence of free currents, Ampère's law reduces to

$$\boldsymbol{\nabla} \times \boldsymbol{H}_d = 0, \tag{1.11}$$

which implies that $\boldsymbol{H}_d$ is a conservative field. Therefore, it follows the same laws than the static electric field, but instead of electric charges, the source of dipolar field is the magnetic charge distribution given by $\rho_M(\boldsymbol{r})$ and $\sigma_M(\boldsymbol{r})$.

For a point of the space where the dipolar field is $\boldsymbol{H}_d$, the dipolar energy density

[6] The vector Laplacian is defined as $\nabla^2 \boldsymbol{A} = (\boldsymbol{\nabla} \cdot \boldsymbol{\nabla} A_x, \boldsymbol{\nabla} \cdot \boldsymbol{\nabla} A_y, \boldsymbol{\nabla} \cdot \boldsymbol{\nabla} A_z)$, where $\boldsymbol{\nabla} \cdot \boldsymbol{\nabla}$ is the scalar Laplacian.

can be calculated in the two equivalent forms,

$$E_d = \frac{\mu_0}{2} \boldsymbol{H}_d^2 = \mu_0 \boldsymbol{H}_d \cdot \boldsymbol{M}, \tag{1.12}$$

and its minimization leads to magnetic-charge free magnetization distributions, where magnetic charges are avoided. These configurations are also known as stray-field free, as the field that a ferromagnetic sample irradiates is dipolar.

Due to the nonlocal nature of this interaction, the calculation of the total dipolar energy $\mathcal{E}_d$ involves two integrations. First from the distribution $\boldsymbol{M}(\boldsymbol{r})$, the magnetic charges are obtained, and the dipolar field can be calculated from Eq. 1.10 and the boundary conditions. Finally, the integration of 1.12 can be performed.

As an example, let us take an infinite single domain ferromagnetic medium, where $\boldsymbol{M}$ is constant in all the volume. In this case, $\boldsymbol{\nabla} \cdot \boldsymbol{M} = 0$, then, no magnetic charges are present and, as a consequence, the dipolar field is null. However, if the sample is not infinite, at the boundaries the magnetization will change abruptly, creating surface magnetic charges. Thus, for homogeneous magnetization samples, boundaries are the generators of magnetic charges and dipolar field. For this reason, the effects of the dipolar interaction on the magnetization are known as *shape anisotropy*.

In a single domain sample, volume charges are null and surface charges are the only source of dipolar field. From Eq. 1.10, the dipolar field inside $\boldsymbol{H}_d^i$ and outside $\boldsymbol{H}_d^o$ the sample satisfies

$$(\boldsymbol{H}_d^i - \boldsymbol{H}_d^o) \cdot \hat{n} = \sigma_M. \tag{1.13}$$

This condition, in addition to the other boundary conditions[7] defines the dipolar field in all the space. Moreover, σ_M is linear on $\boldsymbol{M}$, and $\boldsymbol{H}_d$ is linear on σ_M. This implies that, in the case of a uniform-magnetized sample, the dipolar field and the magnetization are proportional. Thus, it is possible to write[8]

$$\boldsymbol{H}_d(\boldsymbol{r}) = -\overline{\overline{N}}(\boldsymbol{r})\, \boldsymbol{M}, \tag{1.14}$$

where $\overline{\overline{N}}$ is the demagnetizing tensor [21]. For the most general case, the functional dependence of $\overline{\overline{N}}$ with the spatial coordinate $\boldsymbol{r}$ can be very complicated to calculate, as depicted in Figure 1.2. This is the reason why we will focus on certain geometries where its expression can be obtained analytically.

For the particular case of a uniformly magnetized ellipsoid, the dipolar field will be also constant in all the sample volume[22, 23], and $\overline{\overline{N}}$ can be calculated analytically.

[7] The component of $\boldsymbol{H}_d$ parallel to the surface must be continuous and in most systems $\boldsymbol{H}_d$ goes to zero at infinity.

[8] The case of nonuniform magnetization can be analytically solved in a few configurations. In the next Chapter, we will find an expression for the dipolar tensor in the case of thin films with sinusoidal distributions.

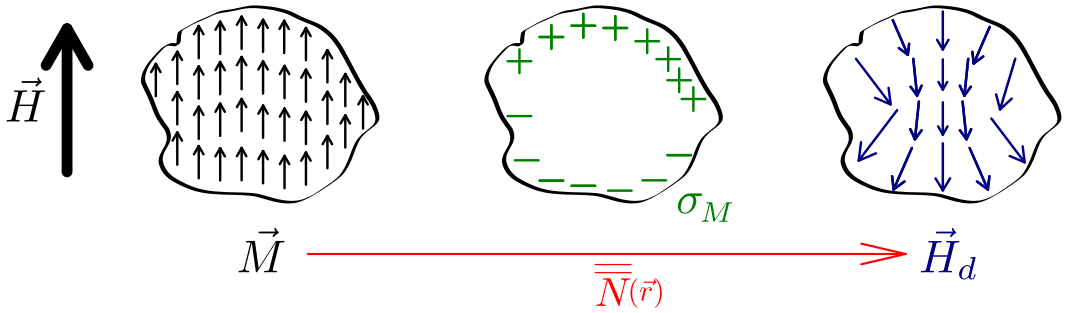

Figure 1.2: Schematic illustration of the dipolar field generated by a uniform magnetization $\boldsymbol{M}$ in a sample with an arbitrary shape. It is possible to see that $\overline{\overline{N}}$ strongly depends on the position.

Moreover, if the main axes of the ellipse are chosen as the xyz coordinates, the tensor is diagonal. For the case of a sphere, all directions are equivalent, leading to $N_{xx} = N_{yy} = N_{zz}$. All three components are also equal to 1/3 because $\overline{\overline{N}}$ has a unitary trace [21][23]. While ellipsoids are difficult to fabricate at the nanoscale[9], a thin film can be viewed as an asymptotic ellipsoid in which one of the axes is much smaller than the others.

Thin films are easy to grow, and they are highly symmetric implying that $\overline{\overline{N}}$ can be obtained from symmetry considerations. The in-plane (IP) directions are quite different from the out-of-plane (OOP) direction. If $\hat{z}$ is the OOP direction, M_x and M_y do not produce magnetic charges, thus $N_{xx} = N_{yy} = 0$ and the unitary trace imposes $N_{zz} = 1$. The last expression can be easily understood: the dipolar field in a uniformly magnetized thin film is equal to $-M_z$. Consequently, in the absence of other interactions, the dipolar interaction favors an IP equilibrium magnetization configuration. To overcome this *thin film shape anisotropy* and fully magnetize the film OOP, it is necessary to apply an OOP external field larger than the saturation magnetization M_S, which is able of compensating for the dipolar field, leading to $\boldsymbol{H}_{\text{eff},\,z} = \boldsymbol{H}_d + \boldsymbol{H} > 0$.

1.2.4 Uniaxial anisotropies

Due to the crystal structure, the magnetization could reduce the energy of the system when pointing in particular directions. This phenomenon originates from the spin-orbit interaction, that links the crystal anisotropy to the magnetization. As an example, the iron cubic structure generates a cubic magnetic anisotropy, implying that the magnetization will be energetically promoted to point in directions related to those of the crystal bonds. These directions are known as *easy axes*.

A particular case arises when there is only one easy axis, defining a *hard plane*. In

[9]Nevertheless, YIG spheres are widely used for technical purposes, as filters and resonators in radiofrequency devices.

this case the anisotropy is called uniaxial. At first order, the energy density can be written as

$$E_{K1} = K_1 \sin^2\theta = K_1 - K_1 \left(\frac{M_i}{M_S}\right)^2, \tag{1.15}$$

where K_1 is the first order uniaxial anisotropy constant, expressed in J/m^3, θ is the angle between the magnetization and the easy axis, and M_i is the component of the magnetization along this axis. The effective field that results is

$$H^a_{\text{eff}} = -\frac{1}{\mu_0}\frac{\partial E_a}{\partial \boldsymbol{M}} = \frac{2K_1 M_i}{\mu_0 M_S^2}\hat{e}_i. \tag{1.16}$$

In thin films, perpendicular magnetic anisotropy (PMA), i.e. uniaxial anisotropy along the film normal, is particularly relevant. When it is of easy-axis type ($K_1 > 0$), it has an effect opposite to that of the demagnetization field $-M_z$ (see Section 1.2.3), leading to an effective OOP demagnetization factor

$$N_{zz} = 1 - \frac{2K_1}{\mu_0 M_S^2} = 1 - Q. \tag{1.17}$$

Here, Q is the quality factor, which indicates how efficiently the PMA opposes to the thin film shape anisotropy. If $Q > 1$, in the single domain configuration, M_{eq} will point OOP at remanence ($H = 0$). However, if the magnetization is not constrained to be uniform in all the sample, it will break apart in the form of magnetic stripe domains, which will be described in details in the next sections. Another quantity widely used in the magnetic community is the effective saturation magnetization $M_{\text{eff}} = M_S - \dfrac{2\,K_1}{\mu_0\,M_S} = M_S\,(1 - Q)$.

The energy of the system can also contain anisotropy terms of higher order. In the case of an uniaxial anisotropy, the energy can be developed as

$$E_a = K_1 \sin^2\theta + K_2 \sin^4\theta + ..., \tag{1.18}$$

where K_n are the n-order uniaxial anisotropy constants.

1.2.5 Magnetic textures

The interplay between the different contributions to the total energy results in a large variety of static configurations. The spatially uniform magnetic distribution, which is also called saturated state, is favored by the exchange and Zeeman interactions. From the experimental point of view, such saturated configurations are easy to obtain, as a sufficiently strong applied magnetic field H ensures their realization.

The dipolar-field energy favors stay-field free configurations. In general, at low applied fields, specially if dealing with confined structures, the magnetization is no longer

saturated. One possibility is that the sample divides itself in uniformly magnetized regions called magnetic domains. Also, depending on the symmetries of the interactions involved, more complex structures can be nucleated. These non-saturated states are grouped together under the name of *magnetic textures*. Some of these structures are particularly interesting as they are robust and can be manipulated. We can mention, among others, the magnetic domain walls, vortices, Skyrmions and spiral helical structures [8, 24]. Due to the complex profile of these textures, in order to execute a complete analysis, micromagnetic simulations should be performed.

In the following section a particular magnetic texture will be introduced: the magnetic stripe domains[10]. Their static properties will be reviewed, serving as background to study the dynamic approach to the stripe domain nucleation and the stripe dynamics, that will be discussed in Chapter 5.

1.3 Stripe domain structure

Modulated phases, in which the order parameter is not constant but oscillates in the space, are ubiquitous in physics [25]. They appear in several systems, including ferroelectric materials [26], superconductors [27], organic macro-molecules [28] and confined ferrofluids [29], among others. These phases show up as a response to competing interactions favoring spatial inhomogeneities in an otherwise uniform ground state.

In this work, we are interested in a particular modulation of the magnetization which appears in thin films with PMA (perpendicular magnetic anisotropy) described by the parameter Q (Eq. 1.17). In absence of anisotropies, the static configuration that is energetically favored is totally in-plane (IP), because the out-of-plane (OOP) component of the magnetization generates surface magnetic charges leading to an increase of the dipolar energy.

However, if the sample presents a PMA, a competition between it and the dipolar-induced shape anisotropy appears. Both contributions can be satisfied if the OOP-component alternates between positive and negative values on a short length-scale. However, this configuration has a high cost in exchange energy. The so-called magnetic stripe domains constitute a compromise between these three interactions. In this magnetic texture both IP and OOP transversal components of the magnetization are periodically modulated along one direction, as shown in Fig. 1.3.

The spatial distribution of the magnetization within stripe domains depends on the magnetic parameters of the sample —K_1, A_{ex}, M_S, and t— and the applied field H. The latter is usually oriented in the film plane, its direction setting that of the stripes. One can distinguish two types of stripe domains. On one hand, *weak stripes* are textures

[10] In this context, magnetic stripes should not be mistaken with *magnetic strips*. The later are also known as buses, which consist in a long narrow piece of magnetic material.

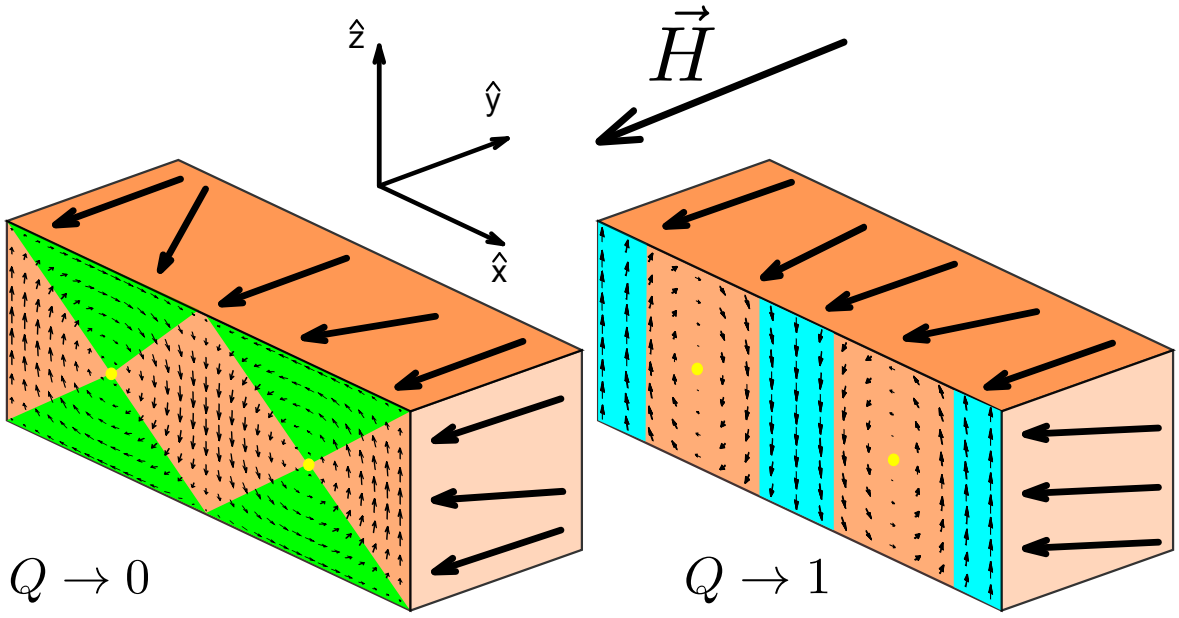

Figure 1.3: Magnetization distribution for thin film with weak stripes ($Q \to 0$) and strong stripes ($Q \to 1$) at nucleation. The green area in the weak stripe configuration show the Néel caps, while the blue water regions in the strong stripes indicate the OOP magnetic domains. The yellow points indicate the stripe core position. The distribution of the weak stripes was obtained by the dynamic approach for CoFeB 180nm, while for the strong stripes it was extracted form Ref. [24].

in which the magnetic flux is nearly closed [24] (Fig. 1.3(a)). It is an almost stray-free configuration with very small dipolar energy. On the other hand, in *strong stripes* the magnetic flux is not closed, and the dipolar interaction contributes significantly to the texture energy (Fig. 1.3(b)). While the weak-stripe configuration is favored as $Q \to 0$, when increasing Q, the system softly transitions to a strong-stripe configuration, as the OOP component of the magnetization M_z increases creating magnetic charges. These zones where the magnetization points almost uniformly OOP can be recognized as up and down magnetic domains (see Fig. 1.3(b)), and the interface region as a domain wall. As Q increases, these domains are better defined, however, the magnetization at the center of the domain wall is always saturated in the direction of the applied magnetic field. These particular points, which are common to both weak and strong stripes, are denominated *cores* of the stripes. As the film is translation invariant, the position of the cores in the direction perpendicular to $\boldsymbol{H}$ is determined at the stripe nucleation by a spontaneous symmetry breaking. For the case of weak stripes, the zones where $\boldsymbol{M}$ points IP to close the magentic flux are well defined and they are called *Néel caps*.

Historically, magnetic stripe domains were first proposed theoretically by Muller in 1961 [30]. He studied the magnetization distribution in a thin slab with a normal easy-axis and an IP external magnetic field by solving the zero-torque equation, $\boldsymbol{M} \times \boldsymbol{H} = 0$. For thinner films, similar results were obtained by Brown [31] who performed energy-

variational calculations. Experimentally, the stripes were evidenced indirectly by their effect of *rotatable anisotropy* [32–34], as once nucleated, the stripes generate an effective anisotropy with an easy axis oriented in the direction on which they are aligned. Later, the stripe domains were directly observed by Spain [35] (in $Ni_{80.5}Fe_{17.5}Co_2$) and Saito et al. [36] (in Permalloy) using Bitter decoration. Both experiments revealed that stripes could develop only if the thickness was larger than a critical thickness t_c. This behavior was explained by Murayama [37], who extended Brown's variational method to find the dependence of t_c and the corresponding stripe period λ as function of Q. He obtained analytical results in the case where $Q \to 0$. Up to our knowledge, there is no analytical solution to fully describe the magnetization distribution for arbitrary magnetic parameters. In this case, it is necessary to perform numerical calculations.

1.3.1 Energy minimization

In this section we will focus on the study of weak stripes, i.e. $Q \to 0$. For that, we will first calculate analytically the total energy of such magnetic texture to find the parameters that minimize it. We will consider three interactions: dipolar, exchange and PMA.

By definition, if $Q \to 0$, the PMA energy density ($\sim K_1$) is much smaller than the typical dipolar energy in thin films ($\sim \mu_0 M_S^2/2$). As for the exchange interaction, it is proportional to the square of the modulation wave vector, and each oscillating component of the magnetization contributes to the energy. Therefore, this contribution can not be minimized in an oscillatory texture. Consequently, the dipole interaction would become the most relevant contribution to the energy that can be minimized by correctly choosing the stripe shape.

Hence, as suggested in Ref. [24], we can propose a surface-charge-free ansatz. Developing the texture as a perturbation from the uniform configuration $\boldsymbol{M} = -M_S\hat{y}$, the transversal components are written as[11]

$$\begin{aligned} m_x &= A\,\sin(k\,x\ \ +\phi)\,\sin\left(\kappa\,z\right), \\ m_z &= B\,\cos(k\,x+\phi)\,\cos\left(\kappa\,z\right), \end{aligned} \tag{1.19}$$

where $k = \frac{2\pi}{\lambda}$ and κ, are the IP and OOP wave vectors, respectively, and $m_i = M_i/M_S$ are the normalized components of the magnetization[12]. The OOP coordinate is z, while the non-homogeneous IP coordinate is x (see Fig. 1.4). For a given sample with a defined thickness, we will consider $\kappa(t)$ as a constant. The phase ϕ is an extra degree of freedom. It will be omitted ($\phi = 0$) in this part of the discussion as it does

[11] In this definition A should not be confused with the exchange constant A_{ex}.

[12] The magnetization components of the stripes are static. However, we will refer to them in lowercase when normalized.

not contribute to the stripe energy.

To ensure surface charges are zero ($m_z(z = \pm t/) = 0$), we assume that $\kappa = \pi/t$. For the distribution to be stray-field free, it must also be free of volume magnetic charges, and it must satisfy

$$\rho_M = \frac{\partial m_x}{\partial x} + \frac{\partial m_z}{\partial z} = 0. \tag{1.20}$$

Substituting in this expression, the proposed ansatz yields to

$$\begin{aligned} &(A\,k - B\,\kappa)\,\cos(k\,x)\sin(\kappa\,z) = 0 \\ &B = A\,\frac{k}{\kappa} \end{aligned} \tag{1.21}$$

Thus, the following profile is obtained

$$\begin{aligned} &\boxed{m_x = A\,\sin(k\,x + \phi)\sin(\kappa\,z)} \\ &\boxed{m_z = A\,\frac{k}{\kappa}\,\cos(k\,x + \phi)\cos(\kappa\,z)}. \end{aligned} \tag{1.22}$$

One period of the obtained magnetization profile is shown in Figure 1.4.

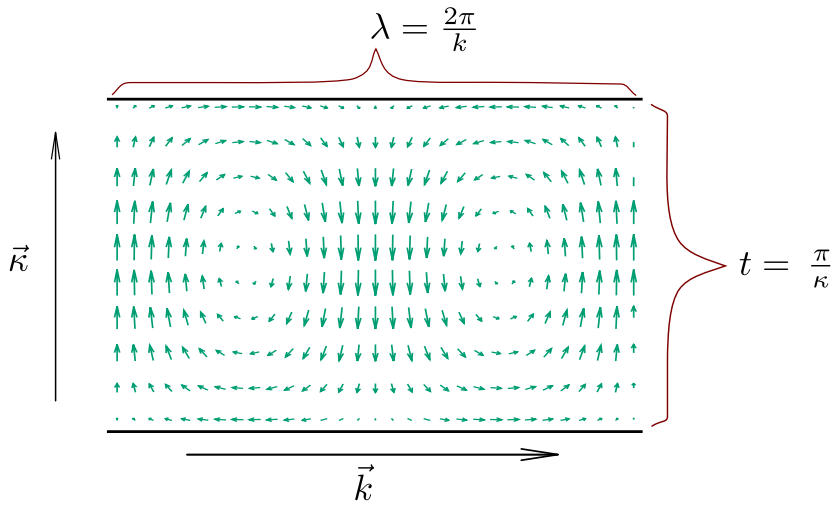

Figure 1.4: Distribution of the traversal components of the magnetization of the proposed magnetic-charge-free ansatz. Note that the magnetic flux is totally closed.

To simplify the energy calculations, the one-period-average energy density will be calculated. This average will be indicated by the symbol $\langle\ \rangle$. As dipolar energy is required to be zero, the total energy for the calculated configuration present three terms

$$\langle E_T \rangle = \langle E_{K1} + E_{ex} + E_Z \rangle\,; \tag{1.23}$$

which correspond to the PMA, the exchange and the Zeeman interactions, given by Equations 1.15, 1.7 and 1.6, respectively. Developing each term and defining $h =$

H/M_S, it reads[13]

$$\frac{2}{\mu_0 M_S^2}\langle E_T\rangle = -Q\left\langle m_z^2\right\rangle + \Lambda^2\left\langle(\vec{\nabla}\vec{m})^2\right\rangle - 2\,h\left\langle\sqrt{1-m_x^2-m_z^2}\right\rangle. \tag{1.24}$$

Following Landau theory of second-order phase transitions [38], this expression can be expressed as Taylor series around $A = 0$ as

$$\frac{2}{\mu_0 M_S^2}\langle E_T\rangle = 2\,h + a(h,k)A^2 + b(h,k)A^4 + \mathcal{O}(A^6). \tag{1.25}$$

The explicit calculation of the coefficients a and b is detailed in Appendix A.0.1. Let us now consider the coefficient describing the quadratic part of this energy, is given by

$$a(h,k) = -Q\left(\frac{k}{2\,\kappa}\right)^2 + \frac{\Lambda^2}{4}\left[2\,k^2+\kappa^2+\left(\frac{k^2}{\kappa}\right)^2\right] + h\,\frac{1}{4}\left[1+\left(\frac{k}{\kappa}\right)^2\right]. \tag{1.26}$$

From here, we clearly note that if $Q = 0$, the energy always increases with the squared amplitude A^2 of the excitation, meaning that stripe domains cost more energy than the uniform state. On the contrary, for $Q > 0$, there may be situations for which stripes domain cost less energy than the uniform state. Therefore, there must exist a point where the cost difference is null. This point defines the stripe nucleation, to be identified to a second-order phase transition. This is equivalent to impose

$$\frac{\partial^2\langle E_T\rangle}{\partial A^2} = a(h,k) = 0. \tag{1.27}$$

This equation determines a quadratic equation for k^2 as function of κ^2 and h:

$$k^4\left[\frac{-\Lambda^2}{2\,\kappa^2}\right] + k^2\left[\frac{Q'}{2\,\kappa^2}-\frac{\Lambda^2}{2}\right] - \left[\frac{\Lambda^2\,\kappa^2}{8}+\frac{h}{4}\right] = 0, \tag{1.28}$$

where $Q' = Q - h$. Solving the quadratic equation on k^2, we obtain

$$k^2 = \frac{\left(\frac{Q'}{2\,\kappa^2}-\frac{\Lambda^2}{2}\right) \pm \sqrt{\left(\frac{Q'}{2\,\kappa^2}-\frac{\Lambda^2}{2}\right)^2 - \frac{\Lambda^4}{4} - \frac{\Lambda^2\,h}{2\,\kappa^2}}}{\frac{\Lambda^2}{\kappa^2}}. \tag{1.29}$$

We note that the reduced magnetic field h enters in the square root (in the last term and in Q') with a negative coefficient. The biggest its value, the smaller the argument of the square root. Thus, the largest value of h that ensures $k^2 \in \mathbb{R}$ is given when the square root vanishes. We define h_c and k_c as the critical field and critical wave vector that fulfill those conditions, and $Q'_c = Q - h_c$. Therefore, the null square-root

[13] $(\vec{\nabla}\vec{m})^2$ expresses a short notation for the operation shown in Eq. 1.7.

condition can be written as

$$\begin{aligned}\left(\frac{Q_c'}{2\,\kappa^2}-\frac{\Lambda^2}{2}\right)^2&=\frac{\Lambda^4}{4}+\frac{\Lambda^2\,h}{2\,\kappa^2},\\ \frac{Q_c'^2}{2\,\kappa^2}-Q_c'\,\Lambda^2&=\Lambda^2\,h_c,\\ \frac{Q_c'^2}{2\,\kappa^2}-Q\,\Lambda^2&=0.\end{aligned}\tag{1.30}$$

From here, the critical field h_c for a given thin-film thickness t can be written as

$$\boxed{h_c=Q-\frac{2\pi\Lambda\sqrt{Q}}{t}}.\tag{1.31}$$

The minimum thickness necessary to develop stripes in a sample with a certain PMA is given when $h_c = 0$. In this case, we obtain $t_{\min} = 2\pi\dfrac{\Lambda}{\sqrt{Q}} = 2\pi\Delta$, where $\Delta = \sqrt{A/K_1}$ is nominal domain-wall width [39], and the factor 2π accounts for the sinusoidal shape of the oscillation. Thus, even with $Q > 0$, if the thickness of the sample is not sufficiently big in relation with the exchange length, stripes will not develop. This stripe-forbidden area is shown in Figure 1.5(a). The two samples that will be described in Chapter 5 are in the region where they are supposed to present stripes domains.

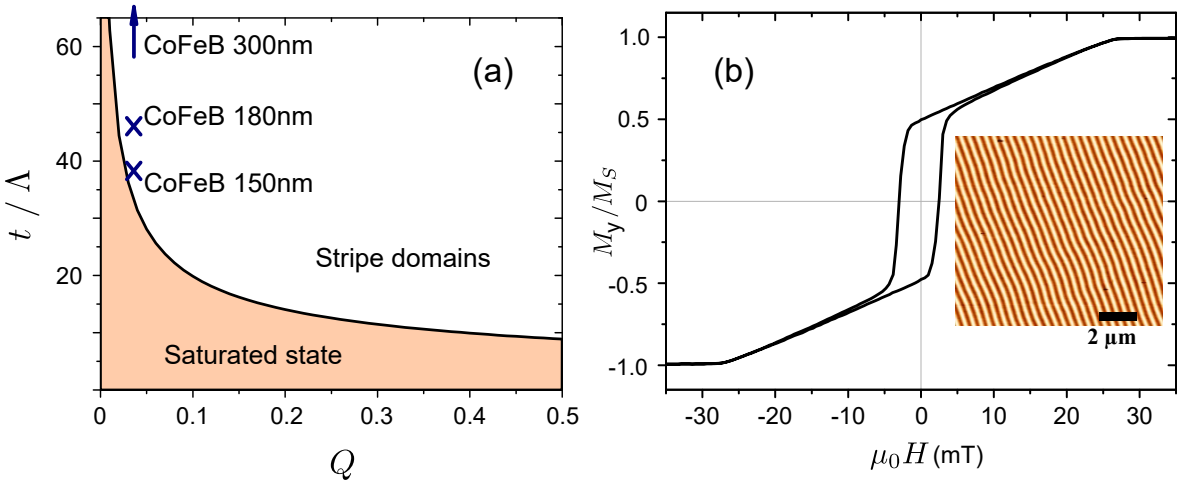

Figure 1.5: (a) Phase diagram indicating which parameters allow stripe nucleation at $h_c \geq 0$. The line indicates t/Λ for $h_c = 0$. The two crosses show the parameters of two samples studied in this work. (b) Hysteresis loop of a sample (CoFeB 300nm) presenting weak stripes and measured by VSM. The inset shows an MFM image of the stripe domains on the same sample at remanence. The hysteresis loop and the image were measured at IJL [40].

Substituting Expression 1.31 in Equation 1.29, we obtain

$$k_c^2=\frac{\kappa^2}{2}\frac{Q+h_c}{Q-h_c},\qquad\text{and}\qquad\boxed{\lambda_c=2\,t\sqrt{\frac{Q-h_c}{Q+h_c}}=2\,t\sqrt{\frac{\pi\Lambda\sqrt{Q}}{Qt-\pi\Lambda\sqrt{Q}}}}.\tag{1.32}$$

The same results are found in Refs. [24] and [41], which use the same ansatz, but do not report the explicit calculation.

We note that the derivative of the IP component of the ansatz (Eq. 1.22, first line) is not zero at the film surfaces, as required by the Rado-Weertman boundary conditions, which will be explained in detail in Section 2.3.2. The corrections required to cancel out these derivatives are given by hyperbolic cosine contributions [24], which remain small as $Q < 0.1$, and can be safely ignored when dealing with the total energy.

To conclude this section, for illustration purposes, a typical hysteresis loop is shown in Fig. 1.5(b). In this example, if $\mu_0 H > \mu_0 H_c = 27$ mT, the magnetization is saturated in the y direction, because the uniform magnetization distribution has less energy than the stripe configuration. At the critical field, the stripes nucleate, and when decreasing the field from this point the stripe amplitude A increases, reducing the value of M_y.

1.3.2 Zero-torque approach

The minimization of the energy allows to find the parameters of a certain ansatz. As we have seen, at $Q \to 0$, the magnetic profile takes a particular simple expression (see Eq. 1.22). Nevertheless, when increasing Q, dipolar energy can not be ignored and more complex profiles have to be proposed. For that we must specify the torque that each interaction produces on the magnetization and propose an ansatz likely to fulfill the zero total torque condition. We will follow a procedure similar to that of Refs. [24, 42, 43], which were inspired by Muller's work.

Stripes are static structures, therefore the magnetization profile must satisfy $\frac{\partial \boldsymbol{M}}{\partial t} = 0$. From linearized LL equation, this condition reduces to[14]

$$\begin{aligned} &\boldsymbol{m} \times \boldsymbol{H}_{\text{eq}} + \boldsymbol{M}_{\text{eq}} \times \boldsymbol{h}_{\text{eff}} = \\ &= \boldsymbol{m} \times H\,\hat{y} + M_{\text{S}}\,\hat{y} \times \left[\Lambda^2 \nabla^2 \boldsymbol{m} + Q\, m_z \hat{z} - \boldsymbol{\nabla}\psi\right] \end{aligned} \tag{1.33}$$

where the axis are orientated as Fig. 1.3 shows and, as we are departing from an IP uniform magnetization, $\boldsymbol{H}$ is the IP external applied field. Only terms linear on m_i were kept, and the magnetization profile along $\hat{y}$ is considered to be constant, leading to $\partial/\partial y = 0$. With these considerations, the restoring field in each component can be calculated as

$$\begin{aligned} &\text{torque in } \hat{x} \to \ (h - Q)\, m_z - \Lambda^2\, \nabla^2\, m_z + \frac{\partial \psi}{\partial z} = 0, \\ &\text{torque in } \hat{z} \to \ h\, m_x - \Lambda^2\, \nabla^2\, m_x + \frac{\partial \psi}{\partial x} = 0, \end{aligned} \tag{1.34}$$

where $h = \frac{H}{M_S}$. In addition, the magnetic potentials inside, and outside (ϕ and $\tilde{\psi}$,

[14] As in the previous section, lowercase variables do not depend on time, but they remain smaller than their capital-letter counterparts. Also, $\boldsymbol{h}_{\text{eff}}$ is still produced by $\boldsymbol{m}$, the deviations from the saturated state.

respectively) the film relate to the magnetization as

$$\begin{aligned} \nabla^2\psi &= \rho_M = \frac{\partial m_x}{\partial x} + \frac{\partial m_z}{\partial z}, \\ \nabla^2\tilde{\psi} &= 0. \end{aligned} \tag{1.35}$$

For this case, magnetostatic and exchange boundary conditions 1.13 and 2.32 at the surfaces ($z = \pm\, t/2$) are written as

$$\psi = \tilde{\psi}, \qquad \frac{\partial\tilde{\psi}}{\partial z} - \frac{\partial\psi}{\partial z} = -m_z, \qquad \frac{\partial m_z}{\partial z} = \frac{\partial m_x}{\partial z} = 0. \tag{1.36}$$

All quantities must remain finite at $x, z \to \infty$ and the magnetic potential $\tilde{\psi}$ must go to zero at $z \to \infty$. As we are searching solutions with a periodic-IP behavior, we propose the to build the solution as a linear combination of the following functions

$$\begin{aligned} (m_x, m_z, \psi) &= (B, C, U)e^{i(kx+\kappa z)}\Big|_{\text{inside}} \\ \tilde{\psi} &= \tilde{U}e^{i(\tilde{k}x+\tilde{\kappa}z)}\Big|_{\text{outside}}, \end{aligned} \tag{1.37}$$

where k is IP and κ the effective OOP wave vector which can take real or imaginary values. We must note that the final dependence on the OOP coordinate will be given by a combination of exponentials, leading to cosines and hyperbolic cosine functions. Substituting the last expression in equations 1.35 and 1.36 leads to a linear equation system, where non-trivial solutions are given by a vanishing determinant. This function combination generates a functional space much larger than the one used in the approximation $Q \to 0$. Therefore it can adapt properly to satisfy the increasing dipolar field that appears when increasing Q. Once the new ansatz is obtained the procedure is similar to the one already explained: the critical parameters are found by minimizing the energy.

The results are shown in Fig. 1.6. Knowing the thickness of the sample, the exchange constant A_{ex}, the PMA K_1, and the saturation magnetization M_S, the reduced critical field $\mathfrak{h}_c = h_c/Q$ can be found. As Q increases also does the dipolar field enabling the creation of magnetic charges σ_M in order to compensate the anisotropy torque. When Q approaches the unity, the anisotropy field compensates the dipolar field issued form the surface charges. From this limit the stripe nucleation is always possible.

We observe that this approach agrees with the stray-free ansatz simplification for $Q \to 0$ (compare Eq. 1.32 and the $Q = 0$ limit in Fig. 1.6(b) for $h_c = 0$).

1.3.3 Magnetic stripe measurements

From the experimental point of view, stripes can be measured by several techniques. Magnetometry experiments could reveal their presence. By observing the hysteresis

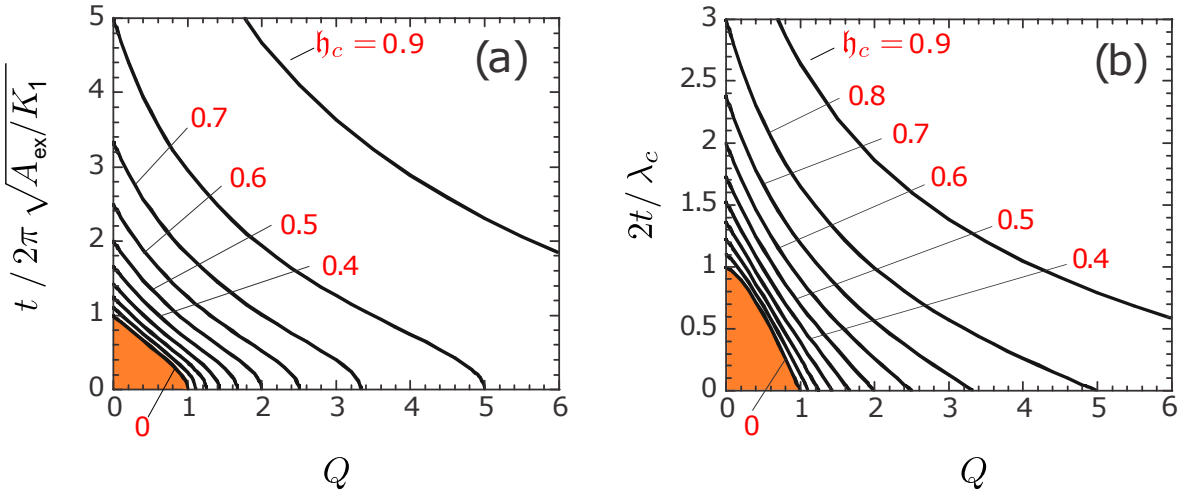

Figure 1.6: Stripe nucleation. (a) Reduced critical thickness as function of the quality factor Q and the reduced nucleation field $\mathfrak{h}_c = h/Q$. (b) Ratio between the thickness and the stripe period at nucleation λ_c. The orange area marks out the region where stripe nucleation is impossible. Adapted form Asti et al. [43].

loop, some of their properties, as the nucleation field, can be revealed. In particular the linear and reversible —closed loop— decrease of the longitudinal IP magnetization is a characteristic signature from stripes, as shown in Fig. 1.5(b).

The magnetic force microscopy (MFM) is a useful tool to directly visualize their static configuration. It can resolve details of the order of 10 nm, making it suitable to study stripe systems, which have typical lengths of the order of the thin film thickness. This technique is sensitive to the stray field produced by the stripes. Therefore, our stray-free ansatz for $Q \to 0$ should not be visible using this technique. However, the mentioned hyperbolic corrections to this ansatz lead to the creation of surface charges, ensuring a minimum stray field. To access the stripe static internal structure, both transmission x-ray microscopy (TXM) and scanning-TXM (STXM) are suitable techniques, as the x-rays can penetrate some depth of the material. A detailed study using this technique can be found in Ref. [13].

Chapter 2

Magnetization dynamics

This chapter introduces the dynamics of the magnetization $\boldsymbol{M}$ in the presence of the interactions reviewed in the former chapter. In particular, the physics of spin waves, the central topic of this thesis, are reviewed. Special attention will be paid to spin-wave propagation in thin films with a spatially-uniform distribution of the equilibrium magnetization.

2.1 Larmor precession

In the previous chapter we have seen that the effective magnetic field acts on the magnetization as a torque affects an angular moment. This torque can be obtained from Equation 1.4. Multiplying this expression by the gyromagnetic radio γ from Eq. 1.1, the well-know lossless form of the Landau-Lifshitz (LL) equation [44, 45] is obtained[1]:

$$\frac{\partial \boldsymbol{M}}{\partial t} = -\mu_0 \gamma \, \boldsymbol{M} \times \boldsymbol{H}^{\text{eff}}. \tag{2.1}$$

This is a first order differential equation, from which the temporal evolution of $\boldsymbol{M}$ can be calculated. We can notice that it does conserve $|\boldsymbol{M}|$ during its temporal evolution, as required.

The simplest magnetic system whose temporal evolution can be studied is a single magnetization $\boldsymbol{M}$ in a static and spatially uniform magnetic field $\boldsymbol{H}$. Here, the only contribution to effective magnetic field is given by the Zeeman interaction, and $\boldsymbol{H}^{\text{eff}} = \boldsymbol{H}$. In order to solve the LL equation, the magnetization can be separated in its static and dynamical components as

$$\boldsymbol{M}(t) = \boldsymbol{M}_{\text{eq}} + \boldsymbol{m}(t), \tag{2.2}$$

[1] This equation can be also derived from the quantum properties of $\boldsymbol{\mu}$ as explained in Refs. [46] and [47].

where $\boldsymbol{M}_{\text{eq}}$, is the equilibrium magnetization. Knowing that $\frac{\partial \boldsymbol{M}_{\text{eq}}}{\partial t} = 0$ and $\boldsymbol{M}_{\text{eq}} \times \boldsymbol{H} = 0$, it is possible to substitute $\boldsymbol{M}(t)$ by $\boldsymbol{m}(t)$, and equation 2.1 can be written as

$$\frac{\partial \boldsymbol{m}}{\partial t} = -\mu_0 \gamma \, \boldsymbol{m} \times \boldsymbol{H}. \tag{2.3}$$

Given the form of the equation, the exponential solution $\boldsymbol{m} = \boldsymbol{m}_0 e^{i\omega t}$ can be proposed. Replacing this proposal in equation 2.3, we obtain $\omega = \omega_H = \gamma \, \mu_0 H$ which is called the Larmor frequency. Therefore, the magnetization $\boldsymbol{M}$ will precess with this frequency around the direction defined by the applied field.

2.2 Ferromagnetic resonance

The interactions described in Chapter 1 modify the magnetization dynamics with respect to those obtained in the previous section, where the only interaction considered was the Zeeman one. Therefore, $\boldsymbol{M}$ will no longer precess at the Larmor frequency ω_H. We will first describe the uniform precession in highly symmetric confined structures: ellipsoids, including the particular case of a thin film. In this case, the dipolar field plays a predominant role. The study and understanding of uniform precession is quite relevant, specially when the excitation field is constant within the magnetic sample volume —or equivalently, when it has zero linear momentum[2]. Historically, the uniform modes are called *Ferromagnetic Resonance modes* (FMR) or *Kittel modes*.

In order to be able of analytically solving the complexities introduced by the new interactions, the static (uppercase) and dynamic (lowercase)[3] parts of both the magnetization and the effective field are explicitly separated as

$$\begin{aligned} \boldsymbol{H}^{\text{eff}}(t) &= \boldsymbol{H}^{\text{eff}}_{\text{eq}} + \boldsymbol{h}^{\text{eff}}(t), \\ \boldsymbol{M}(t) &= \boldsymbol{M}_{\text{eq}} + \boldsymbol{m}(t). \end{aligned} \tag{2.4}$$

Both $\boldsymbol{H}^{\text{eff}}_{\text{eq}}$ and $\boldsymbol{h}^{\text{eff}}(t)$ include all magnetic interactions that are being considered to solve the problem. With this notation, the LL equation is written

$$\frac{\partial \boldsymbol{m}(t)}{\partial t} = -\mu_0 \gamma \, \left[\boldsymbol{m}(t) \times \boldsymbol{H}^{\text{eff}}_{\text{eq}} + \boldsymbol{M}_{\text{eq}} \times \boldsymbol{h}^{\text{eff}}(t) + \boldsymbol{m}(t) \times \boldsymbol{h}^{\text{eff}}(t) \right]. \tag{2.5}$$

If $|\boldsymbol{m}(t)|$ is much smaller than M_s and $\boldsymbol{H}^{\text{eff}}_{\text{eq}} \parallel \boldsymbol{M}_{\text{eq}} \parallel \hat{y}$, at first order, $\boldsymbol{M}_{\text{eq}} \approx M_S \hat{y}$. Additionally, if both $\boldsymbol{m}$ and $\boldsymbol{h}^{\text{eff}}$ are small respect their static components, the last term of equation 2.5 can be neglected at first order. As result, the linearized LL equation is

[2] This is also the case of polar-incidence Brillouin Light Scattering (BLS), which will be introduced in Chapter 3.

[3] In this chapter, the lowercase notation does not indicate normalization.

obtained:

$$\frac{\partial \boldsymbol{m}(t)}{\partial t} = -\mu_0 \gamma \left[\boldsymbol{m}(t) \times H_{\text{eq}}^{\text{eff}}\, \hat{y} + M_S\, \hat{y} \times \boldsymbol{h}^{\text{eff}}(t) \right]. \tag{2.6}$$

This expression describes a precession of $\boldsymbol{m}$ in the plane xz. As in the case of the Larmor precession, we are searching for time-periodic solutions. Consequently, the dynamic magnetization can be expressed as $\boldsymbol{m}(t) = \boldsymbol{m}_0\, e^{i\omega t}$, where $\boldsymbol{m}_0$ and ω are unknowns.

2.2.1 Ellipsoids and thin films

With these simplifications, let us analyze the dynamics of a uniform ellipsoid with a diagonal demagnetization tensor. Taking as referential system the main axes, the dipolar field can be calculated as

$$\begin{pmatrix} h_x^d \\ H_y^d \\ h_z^d \end{pmatrix} = - \begin{pmatrix} N_{xx} & 0 & 0 \\ 0 & N_{yy} & 0 \\ 0 & 0 & N_{zz} \end{pmatrix} \begin{pmatrix} m_x \\ M_S \\ m_z \end{pmatrix}. \tag{2.7}$$

In addition to the dipolar field, the effective field also includes the external magnetic field $\boldsymbol{H} = H\, \hat{y}$. Therefore, the static effective field can be written as $H_y^{\text{eff}} = H + H_y^d = H - N_{yy}\, M_S$. As the mode is uniform, the exchange field is null. On the other hand, the dynamic effective field will be given by the dipolar field:

$$\begin{aligned} h_x^{\text{eff}} &= -N_{xx} m_x, \\ h_z^{\text{eff}} &= -N_{zz} m_z. \end{aligned} \tag{2.8}$$

Replacing both static and dynamic components of the effective field in Equation 2.6, we obtain

$$i\omega \begin{pmatrix} m_x^0 \\ m_z^0 \end{pmatrix} = \gamma \mu_0 \begin{pmatrix} 0 & 1 \\ -1 & 0 \end{pmatrix} \left[\begin{pmatrix} m_x^0 \\ m_z^0 \end{pmatrix} (H - N_{yy}\, M_S) + M_S \begin{pmatrix} N_{xx}\, m_x^0 \\ N_{zz}\, m_z^0 \end{pmatrix} \right], \tag{2.9}$$

where the operator $\times \hat{y}$ was substituted by a rotation matrix multiplicated at left. From here, a 2×2 equation system is obtained,

$$\begin{pmatrix} i\omega & \omega_x \\ -\omega_z & i\omega \end{pmatrix} \begin{pmatrix} m_x^0 \\ m_z^0 \end{pmatrix} = 0. \tag{2.10}$$

Here, the off-diagonal terms are $\omega_{x,z} = \gamma \mu_0 \left[H + (N_{xx,zz} - N_{yy}) M_S \right]$. This system

has a non-trivial solution if and only if

$$\det\left[\begin{pmatrix} i\omega & \omega_x \\ -\omega_z & i\omega \end{pmatrix}\right] = 0. \tag{2.11}$$

Solving this equation, we find that the system will resonate if $|\omega| = \sqrt{\omega_x \omega_z}$. This expression is known as the Kittel formula. By calculating the eigenvectors, the ratio between the dynamic components can be expressed as

$$\frac{m_z^0}{m_x^0} = -i\sqrt{\frac{\omega_x}{\omega_z}}. \tag{2.12}$$

The ratio is imaginary, signaling that both components are $\pi/2$ out of phase.

Lets us take a look on some relevant examples. In a sphere, $N_{nn} = 1/3$ leading to a resonance frequency equal to ω_H, the Larmor frequency.

Another interesting case is the case of an IP magnetized thin film. Here, the two in-plane components of tensor N_{xx} and N_{yy} are null, while the OOP component is $N_{zz} = 1$, as explained in Section 1.2.3. The resonance frequency will be given by

$$\omega_{\text{res}}^{\parallel} = \gamma\mu_0\sqrt{H(H + M_S)}. \tag{2.13}$$

The thin film is anisotropic, thus the IP and OOP components are expected to behave differently. Therefore, the precession becomes elliptic depending on the applied field as $\frac{m_z^0}{m_x^0} = \frac{m_{\text{OOP}}}{m_{\text{IP}}} \propto \sqrt{\frac{H}{M_S + H}}$. When $H \to 0$, the precession is polarized linearly in the plane of the sample. As the applied magnetic field H increases, the precession becomes more circular and the shape anisotropy becomes less important.

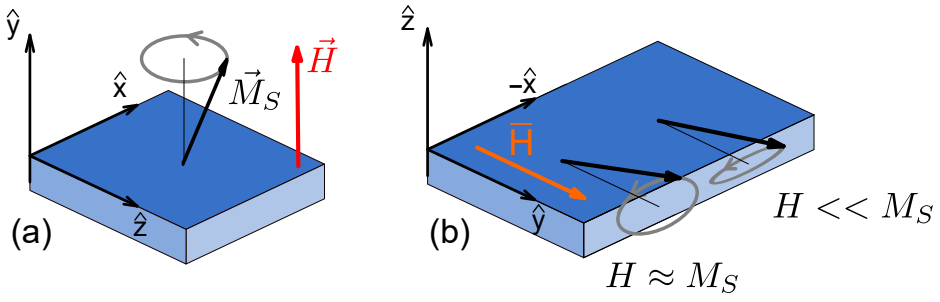

Figure 2.1: Uniform modes in a thin film.(a) Both magnetization $\boldsymbol{M}$ and applied field $\boldsymbol{H}$ are out-of-plane. (b) In-plane $\boldsymbol{M}$ and $\boldsymbol{H}$, at low applied field the precession is linear with $m_z^0 \to 0$ as $H_y \to 0$. Note that the frame of reference rotates between the IP and OOP configurations, keeping $\boldsymbol{H} = H\,\hat{y}$.

In a normally magnetized thin film, $N_x = N_z = 0$, and $N_y = 1$, leading to the

following resonance frequency

$$\omega_{\text{res}}^{\perp} = \gamma\mu_0(H - M_S). \tag{2.14}$$

In this configuration, the two in-plane coordinates x and z (Fig. 2.1(a)) are symmetric. Consequently, the precession remains circular as in an isotropic medium.

If the thin film presents a OOP uniaxial anisotropy, Equations 2.13 and 2.14 are still valid if the saturation magnetization M_S is substituted with $M_{\text{eff}} = M_S\,(1 - Q)$.

2.3 Spin waves

Until now, we have restricted the study of magnetization dynamics to the case of uniform precession. Nevertheless, as the magnetization can depend on the position, a ferromagnetic sample also holds non-uniform modes, called *spin waves*. For a uniform (translation invariant) equilibrium configuration, the dynamic components of the magnetization oscillate in space, in addition to their oscillatory dependence on time. Therefore, the dynamic magnetization can be expressed as $\boldsymbol{m} = \boldsymbol{m}_0\, e^{i(\boldsymbol{k}\cdot\boldsymbol{r}-\omega t)}$, where $\boldsymbol{k}$ is the wave vector of the spin wave and $\boldsymbol{m}_0$ is its complex amplitude vector.

The FMR, can be considered as a particular case of a spin wave with $\boldsymbol{k} = 0$. For the case of thin films, we will call FMR-modes all modes with null IP wave vector, even if these modes are not uniform across the film thickness. In the next sections we will focus on the calculation of the functional relation between ω and $\boldsymbol{k}$, that is, the dispersion relation.

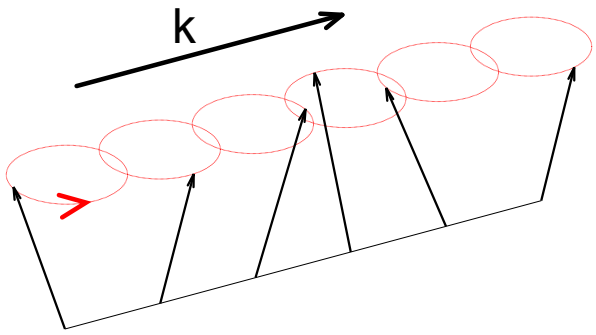

Figure 2.2: Magnetization dynamics of a spin wave. When $\boldsymbol{k} \neq 0$ the magnetization distribution at a given time is not uniform, but it precesses as one moves along the direction of the wave vector.

2.3.1 Magnetostatic waves

For the moment, only the dipolar interaction will be considered, as it is the driving phenomenon for most effects described in this work. Dipolar effects are long-ranged, meaning that the magnetization of all the sample will contribute to the dipolar field at

the point $\boldsymbol{r}$. In the case of a non-uniform magnetization distributions, equation 1.14 and can be written as a non-local (integral) equation,

$$\boldsymbol{H}_d(\boldsymbol{r}) = \int_V \overline{\overline{G}}(\boldsymbol{r}, \boldsymbol{r'})\ \boldsymbol{M}(\boldsymbol{r'})\ d^3\boldsymbol{r'}, \tag{2.15}$$

where $\overline{\overline{G}}(\boldsymbol{r}, \boldsymbol{r'})$ is the tensorial magnetostatic Green's function [48]. To calculate this kernel, we will work in the magnetostatic limit[4]. As $\boldsymbol{H_d}(\boldsymbol{r})$ is a conservative field (see Eq. 1.11), it can be calculated from a scalar potential as

$$\boldsymbol{H_d}(\boldsymbol{r}) = -\boldsymbol{\nabla}\psi(\boldsymbol{r}). \tag{2.16}$$

Looking at the expression of equation 1.10, in analogy with the electric potential, ψ must fulfill the magnetostatic Poisson equation,

$$\nabla^2\psi(\boldsymbol{r}) = \rho_M. \tag{2.17}$$

Its solution (see [17] p. 196) is given by

$$\psi(\boldsymbol{r}) = \frac{-1}{4\pi}\int_V \frac{\boldsymbol{\nabla'}\cdot\boldsymbol{M}(\boldsymbol{r'})}{|\boldsymbol{r}-\boldsymbol{r'}|}d\boldsymbol{r'} + \text{surface charge distribution}. \tag{2.18}$$

Integration by parts yields

$$\psi(\boldsymbol{r}) = \frac{1}{4\pi}\int_V \boldsymbol{M}(\boldsymbol{r'})\cdot\boldsymbol{\nabla'}\left(\frac{1}{|\boldsymbol{r}-\boldsymbol{r'}|}\right)d\boldsymbol{r'}. \tag{2.19}$$

Replacing this expression in 2.16,

$$\boldsymbol{H_d}(\boldsymbol{r}) = \frac{-1}{4\pi}\int_V \boldsymbol{M}(\boldsymbol{r'})\cdot\left[\boldsymbol{\nabla}\ \boldsymbol{\nabla'}\left(\frac{1}{|\boldsymbol{r}-\boldsymbol{r'}|}\right)\right]d\boldsymbol{r'}. \tag{2.20}$$

Finally, by comparing the obtained expression with 2.15, it is possible to express $\overline{\overline{G}}$ in Cartesian coordinates as

$$\overline{\overline{G}}_{ij}(\boldsymbol{r}, \boldsymbol{r'}) = \frac{-1}{4\pi}\frac{\partial^2}{\partial x_i \partial x'_j}\frac{1}{|\boldsymbol{r}-\boldsymbol{r'}|}. \tag{2.21}$$

This expression is totally general and can be applied in non-homogeneous magnetic configurations, for both the static and dynamic components of the magnetization. As a Dirac delta distribution, this expression has not well-defined physical meaning until it is integrated. That means that when considering different samples geometries, partial integrations will lead to simplified versions of this function. Some examples can be

[4]The limits where this approximation remains valid are studied in Ref. [49] p.26.

seen in Refs. [50] (thin film stripes), [51] (dot arrays), [52] (parallel stripes), [53, 54] (rectangular elements) and [55] (thin films).

In the linear regime, the dynamic magnetization can be decomposed as $\boldsymbol{m}(\boldsymbol{r},t) = \sum_n a_n \boldsymbol{m}_n(\boldsymbol{r}) e^{i\omega_n t}$, with ω_n being the frequency of the n mode with spatial profile $\boldsymbol{m}_n(\boldsymbol{r})$ and amplitude a_n. Limiting ourselves to a uniform magnetized sample, for example, in the $\hat{y}$ direction, the LL equation 2.6 reads

$$i\frac{\omega_n}{\omega_M}\boldsymbol{m}_n(\boldsymbol{r}) = \boldsymbol{m}_n(\boldsymbol{r}) \times \left[\overline{\overline{N}} + \frac{\omega_H}{\omega_M}\right]\hat{y} + \hat{y} \times \int_V \overline{\overline{G}}(\boldsymbol{r},\boldsymbol{r'})\ \boldsymbol{m}_n(\boldsymbol{r'})\ d^3\boldsymbol{r'}. \tag{2.22}$$

where $\omega_M = \gamma\mu_0 M_S$. Excepted the one of the dynamic dipolar interaction, all the operators are local, thus their eigenfunctions $\boldsymbol{m}_n(\boldsymbol{r})$ are trivial (no conditions are imposed on the dependence on $\boldsymbol{r}$). As a consequence, this eigenvalue problem reduces to that of only one non-trivial operator, which is

$$\lambda_n \boldsymbol{m}_n(\boldsymbol{r}) = \int_V \overline{\overline{G}}(\boldsymbol{r},\boldsymbol{r'})\ \boldsymbol{m}_n(\boldsymbol{r'})\ d^3\boldsymbol{r'}. \tag{2.23}$$

The frequencies ω_n will be simple functions of the eingenvalue λ_n. Unfortunately, this integral is generally not analytical[48]. However, when considering particular problems, boundary conditions can simplify this expression. Also, by taking account the symmetries of the system, partial integration can be performed over the expression of $\overline{\overline{G}}$, yielding to closed expressions.

As a particular case of interest in this thesis, the thin film Green's function will be obtained. Later, it will be used in the calculation of $\omega_n(k)$ in the most relevant configurations. The studied system is sketched in Fig. 2.4. In the following, we shall determine the spatial Fourier transform of the Green's function, named $\overline{\overline{G}}_{\boldsymbol{k}}$. In a thin film, the parallel surfaces break the spatial isotropy, as only the OOP $\boldsymbol{m}$ component creates surface magnetic charges. Therefore, we will separate the IP wave vector, defined as $\boldsymbol{k} = k_x\hat{x} + k_y\hat{y}$ and the IP position $\boldsymbol{\rho} = x\hat{x} + y\hat{y}$ from their OOP counterparts.

In order to calculate the Fourier transform of expression 2.21, let us use the following identity[17],

$$\frac{1}{|\boldsymbol{r}-\boldsymbol{r'}|} = \frac{1}{2\pi}\int_S \frac{e^{-|k(z-z')|}}{|k|} e^{i\boldsymbol{k}\cdot(\boldsymbol{\rho}-\boldsymbol{\rho'})}\ d^2k, \tag{2.24}$$

that represents the decomposition of $1/r$ in the IP reciprocal space. In this expression, the integrand can be interpreted as the decay along $\hat{z}$ of the magnetostatic potential generated by a magnetic surface charge density localized at $z = z'$, and oscillating with a wave vector $\boldsymbol{k}$ [56].

Then, by applying the derivatives, we are able of finding the components of $\overline{\overline{G}}_{\boldsymbol{i},\boldsymbol{j}}$.

Separating $\hat{z}$ from the other coordinates $\alpha, \beta = x, y$, we obtain

$$G_{\alpha\beta}(\boldsymbol{r}, \boldsymbol{r'}) = \frac{-1}{8\pi^2} \int \frac{k_\alpha k_\beta \; e^{-|k(z-z')|}}{|k|} e^{i\boldsymbol{k}\cdot(\boldsymbol{\rho}-\boldsymbol{\rho'})} \; d^2k;$$

$$G_{\alpha z}(\boldsymbol{r}, \boldsymbol{r'}) = \frac{-i \; \mathrm{sign}(z-z')}{8\pi^2} \int k_\alpha \; e^{-|k(z-z')|} e^{i\boldsymbol{k}\cdot(\boldsymbol{\rho}-\boldsymbol{\rho'})} \; d^2k \qquad \alpha \neq z; \tag{2.25}$$

$$G_{zz}(\boldsymbol{r}, \boldsymbol{r'}) = \frac{1}{8\pi^2} \int \left[|k| \; e^{-|k(z-z')|} - 2\delta(\boldsymbol{r} - \boldsymbol{r'}) \right] \; e^{i\boldsymbol{k}\cdot(\boldsymbol{\rho}-\boldsymbol{\rho'})} \; d^2k.$$

As the $\hat{x}, \hat{y}$ plane is isotropic, we can choose to set the wave vector along the $\hat{x}$ direction. In that case, $\boldsymbol{k} = k_x\hat{x}$ and $G_{\alpha y}(\boldsymbol{r}, \boldsymbol{r'}) = 0$. From the usual definition of the 2D Fourier transform $f_{\boldsymbol{k}} = (2\pi)^{-2} \int_S f_{\boldsymbol{\rho}} \, e^{i\boldsymbol{k}\cdot\boldsymbol{\rho}} \, d^2k$, and expressions 2.25, the Green's tensor in the reciprocal space can be written as (see Ref. [48] p.2421 for details)

$$\overline{\overline{G}}_k(z-z') = \begin{pmatrix} -G_P(z-z') & 0 & iG_Q(z-z') \\ 0 & 0 & 0 \\ iG_Q(z-z') & 0 & G_P(z-z') - \delta(z-z') \end{pmatrix}, \tag{2.26}$$

with $G_P(z-z') = \frac{|k|}{2} \; e^{-|k(z-z')|}$ and $G_Q(z-z') = \mathrm{sign}(z-z') \; G_P(z-z')$. This tensor describes the dipolar field created by an IP sheet of oscillating magnetization. Their components are depicted schematically in 2.3. The imaginary unit here expresses a $\pi/2$ dephasing between one component of the magnetization and other component of the dipolar field that it creates. This dephasing can be easily understood when representing the spatial distribution of the dipole field, as shown in Figure 2.3.

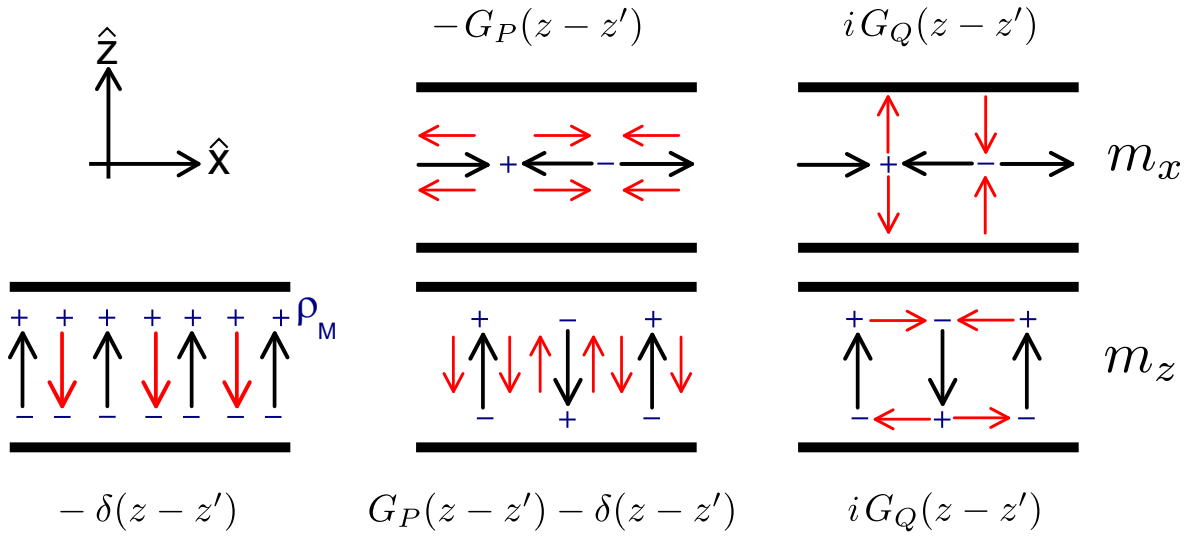

Figure 2.3: Magnetostatic Green's function representation in a thin film. The magnetization is depicted in black, the dipolar field is represented by the red arrows and the volume charges are shown in blue. The thin film surfaces are shown as a reference, but they are not included in the model before integration of $\overline{\overline{G}}_k(z-z')$.

Knowing the explicit form of the Green's function allows to solve the eigenvalue

problem from Equation 2.23 in the case of a thin film of thickness t. There are three high-symmetry magnetic configurations, depicted in Fig. 2.4.

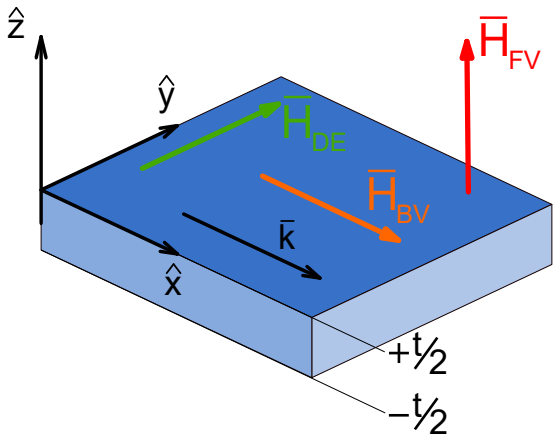

Figure 2.4: Schematic representation of the three high-symmetry configurations of spin-wave propagation in a thin film. The wave vector is depicted parallel to the $\hat{x}$ axis, while the three possible orientations of the magnetic field are indicated in different colors: green (Damon-Eshbach), orange (Backward-Volume) and red (Forward-Volume).

First, we will consider the case where the magnetization is in-plane and $\boldsymbol{k} \parallel \boldsymbol{M}^{\text{eq}}$. This spin wave is called **Magnetostatic Backward-Volume Wave (BV)**. The backward behavior —the wave has a negative group velocity, $v_g = \frac{\partial \omega}{\partial k} < 0$— can be understood by studying two extreme cases: $k = 0$ and $k \to \infty$. If $\boldsymbol{k} = 0$ (Fig. 2.5(a)) all $\boldsymbol{m}$ in the volume are aligned and $N_{zz}\,(k = 0) = 1$ as shown to deduce expression 2.13. A totally different situation is found when $k \to \infty$. In this extreme case we will consider that neighbor dynamic moments $\boldsymbol{m}$ are antiparallel, as shown in Fig. 2.5 (b). Here, the dipolar field generated m_z is canceled by the $\boldsymbol{h}_d$ generated by the neighbor $\boldsymbol{m}$, resulting in an effective demagnetization factor $N_{zz}\,(k \to \infty) = 0$, leading to a lower resonance frequency $\omega(k \to \infty) = \omega_H < \sqrt{\omega_H(\omega_M + \omega_H)}$. Being the normal components of $\boldsymbol{m}$ the only source of charges, the transition between these two configurations must be continuous and it is possible to grasp the origin of the backward character of the BV spin waves.

Analytically, Equation 2.23 can be solved as the BV configuration symmetries simplify its expression. First, the precession is in the plane $\{yz\}$, so $m_x = 0$. Also, the IP magnetization do not generate magnetic charges, as $G_{\alpha y}(z, z') = 0$. As an approximation, it is possible to consider a constant depth profile for the dynamic magnetization: $m_z(z) = \frac{1}{\sqrt{t}}$ (where $\sqrt{t}$ serves for amplitude normalization). By applying $\int_{-t/2}^{t/2} m_z(z)\, dz$ on equation 2.23, we obtain the eigenvalue for the first thickness mode as[5]

$$\lambda_1^{\text{BV}} = \frac{1}{t}\int_{-t/2}^{t/2}\int_{-t/2}^{t/2} \left[G_P(z - z') - \delta(z - z')\right]\, dz\, dz' = \frac{1 - e^{-|k|t}}{|k|t}. \tag{2.27}$$

[5]Calculation of this kind of integrals can be found in the Appendix of Ref. [57].

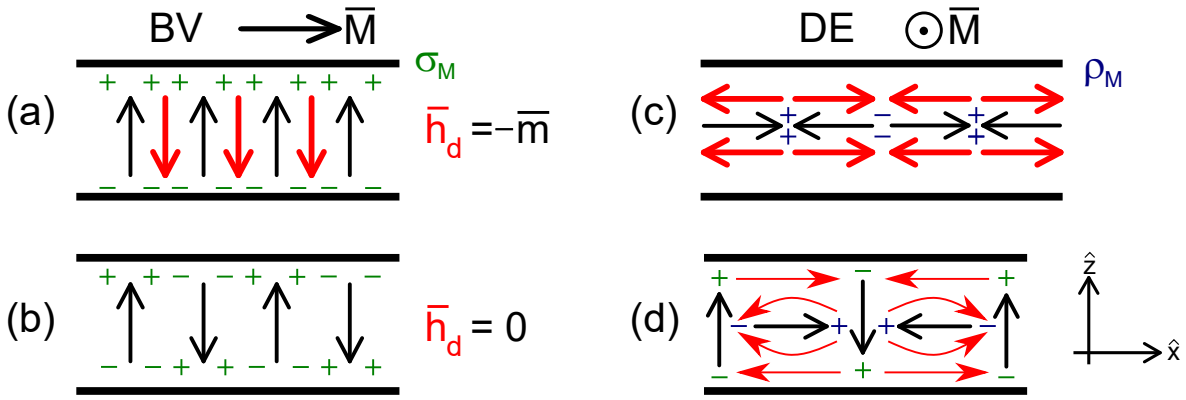

Figure 2.5: Demagnetization field (red arrows) in a thin film. In the Backward-Volume configuration, when of $k = 0$ (a) the dipolar field is equal to the OOP component of the dynamic magnetization. In the case of $k \to \infty$ (b), no net magnetic surface charge σ_M are created, and in consequence, the shape anisotropy "disappears" leading to a smaller resonance frequency. In the Damon-Eshbach configuration, the situation is quite different, the in-plane $\boldsymbol{m}$ component creates volume magnetic charges ρ_M (c) and an in-plane dipolar field exists even for $k \to \infty$. Also in this configuration, when taking account both components, we notice an asymmetry in the resultant $\boldsymbol{h_d}$,as seen in (d).

This term can be considered as an effective k-dependent demagnetization factor that reduces the effect of the surface magnetic charges when k increases. By replacing it in the LL equation, we obtain the BV relation dispersion that reads

$$\omega_{\mathrm{BV}}^2 = \omega_H \left[\omega_H + \omega_M \left(\frac{1 - e^{-|k|t}}{|k|t} \right) \right]. \tag{2.28}$$

As an extension of what happened in the $k = 0$ case, the ellipticity also depends on the wave vector. As k increases, the precession becomes more circular. In the limit case of $k \to \infty$, the Larmor frequency is recovered.

Another relevant case is when the magnetization is normal to the thin film surface. Spin waves excited in this configuration are called **Magnetostatic Foward Volume Wave (FV)**. Here, the dynamic components of $\boldsymbol{m}$ produce volume charges instead of producing surface charges. As m_z is null, equation 2.23 reduces also to a single-component equation. Using the same approximation as above, one gets

$$\lambda_1^{\mathrm{FV}} = \frac{1}{t} \int_{-t/2}^{t/2} \int_{-t/2}^{t/2} G_p(z - z')\, dz\, dz' = 1 - \frac{1 - e^{-|k|t}}{|k|t}, \tag{2.29}$$

leading to the following dispersion relation

$$\omega_{\mathrm{FV}}^2 = \omega_H \left[\omega_H + \omega_M \left(1 - \frac{1 - e^{-|k|t}}{|k|t} \right) \right]. \tag{2.30}$$

The third relevant case is the so-called **Magnetostatic Surface Wave** or **Damon-Eshbach Wave (DE)**, which corresponds to the green-color magnetic field shown in

Figure 2.4. The first name came from the fact that spin waves with opposite $\boldsymbol{k}$ are localized at the two different surfaces of the thin film[6]. The second name —that is the one that will be used across this work— is given after J. R. Eshbach and R. W. Damon, who described this configuration first [58]. As the static magnetization is in-plane, it can seem tempting to think about it as similar to the BV spin waves. However, there is a fundamental difference: the in-plane magnetization m_x, (see Fig. 2.5(c)) produces volume magnetic charges. As a consequence, the backward signature presented by the BV waves is lost. Another difference is that this configuration breaks an extra symmetry by localizing the modes with opposite k in different surfaces. An intuitive picture of how this happens is shown in Figure 2.5(d). At $k \neq 0$ both surface and volume magnetic charges are created by OOP and IP components of $\boldsymbol{m}$, respectively. While in the bottom half the dipolar field that they create add up, in the top half they cancel each other. The result of this is that the profile of the dynamic magnetization, in order to adjust itself to this asymmetry, becomes asymmetric with a typical shape of evanescent decay from one of the surface.

Another interesting consequence arises when considering the OOP uniaxial anisotropy in the DE configuration. This interaction has the opposite effect than the dipole-induced shape anisotropy. Therefore, it does increase the ratio m_z/m_y, decreasing the effect of the volume magnetic charges produced by m_y. As a consequence, if the PMA is sufficiently large, we expect to recover the backward behavior from the BV configuration. This fact will prove quite relevant when studying the magnetic stripe nucleation in Chapter 5.

To finish this section, it is important to point that the case of an arbitrary non-uniform static magnetization distribution is much more complicated to solve, as volume magnetic charges ρ_M have to be calculated, along with σ_M. Usually, micromagnetic simulations are required to study the dynamics of this kind of systems.

2.3.2 Dipole-exchange waves

The magnetostatic regime described in the previous section remains a good approximation in the limit of millimeter-scale samples and millimeter-long wave vectors. However, it does not take in account the exchange interaction, that is always present in the ferromagnetic materials. This interaction dominates over the dipolar field for scales under Λ. Nevertheless, exchange can also play an important role in the spin-wave dynamics at scale lengths of the order of several tens of Λ [57, 59, 60], i.e. up to the micrometer scale.

In particular, in thin films, exchange plays an important role as it increases the res-

[6] As it will be seen in Chapter 4, this localization is modified when the exchange interaction is taken into account.

onance frequency of the different thickness modes at null in-plane wave vector ($\boldsymbol{k} = 0$), which we call perpendicular standing spin-wave modes (PSSW). To fulfill the LL equation the thickness dependence[7] $\boldsymbol{m}(z)$ has to be an eigenfunction of the exchange operator, leading to sinusoidal profiles characterized by a transversal wave vector κ, as show in Figure 2.6.

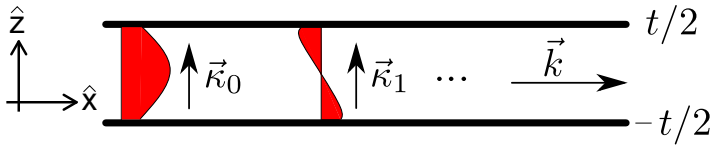

Figure 2.6: Dipole-exchange spin wave in a thin film. The thickness profiles are sinusoidal, and the boundary conditions are influenced by the surface anisotropy, determining the pinning of the modes and defining the transversal wave vectors $\boldsymbol{\kappa_n}$ of the different PSSWs. The IP wave vector $\boldsymbol{k}$ is also depicted.

These profiles have to satisfy the boundary conditions imposed by the surfaces, where the magnetization may sense a different environment due to extra magnetic interactions. The typical example is an uniaxial surface magnetic anisotropy with an axis oriented along the surface normal. Its magnitude K_s is expressed in J/m^2. As the exchange interaction introduces a second-order differential operator, extra boundary conditions are needed. This problem is solved in Ref. [61], which finds the following boundary conditions

$$\frac{2A}{M_S}\left(\boldsymbol{M} \times \frac{\partial \boldsymbol{M}}{\partial z}\right) + \boldsymbol{T} = 0 \tag{2.31}$$

where $\boldsymbol{T}$ represents all the surface torque densities other than the exchange, in particular the surface anisotropy. If $\boldsymbol{T} = 0$, both components of $\boldsymbol{M}$ have zero derivative at the surface of the thin film and the mode is totally unpinned. In the case of a nonzero surface magnetic anisotropy, the boundary conditions simplify to

$$\begin{aligned} \frac{\partial M_\alpha}{\partial z} &= 0, \\ A\,\frac{\partial M_z}{\partial z} - K_s\, M_z &= 0, \end{aligned} \tag{2.32}$$

where M_α is any component of the magnetization (dynamic or static) that is not normal to the thin-film surface.

The different eigenfunctions of the exchange operator that satisfy the boundary conditions can be enumerated using the index n. For $k = 0$, if the applied magnetic field is perpendicular to the film surface ($H \parallel \hat{z}$), the relation between κ_n and K_s is

[7] Even if these modes are not uniform across the thickness we will refer at them as a FMR modes, because they can be measured by FMR spectroscopy.

given by [62]

$$\tan(\kappa_n\, t) = \frac{2\, A\, K_s\, \kappa_n}{(A\, \kappa_n)^2 - K_s^2}, \tag{2.33}$$

where $n \in [0, 1, ...]$ is the mode number, and t is the thickness of the film. From this expression it is possible to calculate the set of OOP wave vectors κ_n that describes the profile of the n-PSSW-mode. When $\boldsymbol{M}$ is OOP, the two IP components of $\boldsymbol{m}$ are symmetric and the exchange contribution to the dynamic effective field corresponding to each of these modes can be easily calculated as $\boldsymbol{H}_n^{ex} = \Lambda^2 \kappa_n^2 M_s \hat{z}$. Thus, at a certain resonance frequency, at $k = 0$, the PSSW modes will appear with a field shift of $\boldsymbol{H}_n^{ex}$.

In addition to introduce a shift between the FMR modes, the exchange also modifies the dispersion relation. For $k \neq 0$ the LL equation can be solved by using the dipole-exchange theory [57, 63] developed by Kalinikos and Slavin (KS). From it, it is possible to calculate the dispersion relation $\omega_n(\boldsymbol{k})$ of spin waves in a thin film taking account the effects of the exchange interaction.

To resolve the LL equation, Kalinikos and Slavin propose to express the dynamic magnetization as $\boldsymbol{m}(\boldsymbol{r}) = M_S\, \boldsymbol{\eta}(z)\, e^{i(\omega t - k_x x)}$, and develop the thickness profile $\boldsymbol{\eta}(z)$ in a complete basis of functions $\{\boldsymbol{S}(z)\}$, that are eigenfunctions of the exchange operator and satisfy the boundary conditions. Then, it is possible to solve the matrix eigenvalue problem obtained when truncating the development a certain order.

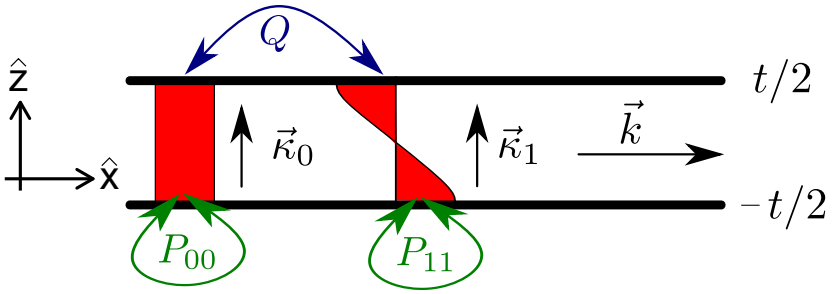

Figure 2.7: Fully unpinned modes with zero surface anisotropy. The self- and mutual-dipolar interaction are depicted by the arrows.

As an example, we will obtain the Damon-Eshbach dispersion relation in the totally unpinned condition ($K_s = 0$). In a first approximation we will consider the first two basis functions, the fully homogeneous ($n = 0$) and fully antisymmetric ($n = 1$) modes, as shown in Figure 2.7. This defines a four element basis $\{S_0\hat{x},\ S_0\hat{z},\ S_1\hat{x},\ S_1\hat{z}\}$, with $S_0(z) = \frac{1}{\sqrt{t}}$ and $S_1(z) = \sqrt{\frac{2}{t}}\, \sin(\frac{\pi z}{t})$. In this basis, $\boldsymbol{\eta}(z)$ can be decomposed in a four element vector: $\boldsymbol{\eta} = (\eta_{0,x}, \eta_{0,z}, \eta_{1,x}, \eta_{1,z})^T$.

Replacing in the LL equation, we obtain

$$i\omega\boldsymbol{\eta}(z) = \gamma\mu_0\, [-H_{\text{eq}}\, \boldsymbol{\eta}(z) + \boldsymbol{h}_{\text{eff}}(z)] \times \hat{y}, \tag{2.34}$$

where the effective field has the contributions of the exchange and dipolar field, and

it is written as

$$\boldsymbol{h}_{\text{eff}}(z) = \Lambda^2 \boldsymbol{\nabla}^2 \boldsymbol{m}(z) + \boldsymbol{h}_{dip}(\boldsymbol{m}, z). \tag{2.35}$$

Expressing the dynamic dipolar field in the Green's function formalism and defining $H_{\text{eq}}/M_S = h$, we find

$$\begin{aligned} i\omega\boldsymbol{\eta} =& \omega_M[-h\,\boldsymbol{\eta}(z) + \Lambda^2\left(\frac{\partial^2}{\partial z^2} - k^2\right)\boldsymbol{\eta}(z) + \\ &+ \int_{-t/2}^{t/2} \overline{\overline{G}}(\boldsymbol{z}, \boldsymbol{z'})\boldsymbol{\eta}(z)\, dz'] \times \hat{y} \end{aligned} \tag{2.36}$$

which is an eigenvalue equation. Applying the operator, $\int_{-t/2}^{t/2} S_n dz$ in both terms we obtain a 4×4 equation system than can be expressed in a matricial form as $i\Omega\boldsymbol{\eta} = \overline{\overline{C}}\boldsymbol{\eta} \times \hat{y}$, where $\Omega = \omega/\omega_M$ and

$$\bar{C} = \begin{pmatrix} \Omega_{x0} & 0 & 0 & -i2Q \\ 0 & \Omega_{y0} & -i2Q & 0 \\ 0 & i2Q & \Omega_{x1} & 0 \\ i2Q & 0 & 0 & \Omega_{y1} \end{pmatrix}. \tag{2.37}$$

The matrix elements are

$$\begin{aligned} \Omega_{0,x} &= P_{00} + h + \Lambda^2 k^2, \\ \Omega_{0,z} &= 1 - P_{00} + h + \Lambda^2 k^2, \\ \Omega_{1,x} &= P_{11} + h + \Lambda^2 k^2 + \frac{\Lambda^2 \pi^2}{l^2}, \\ \Omega_{1,z} &= 1 - P_{11} + h + \Lambda^2 k^2 + \frac{\Lambda^2 \pi^2}{l^2}, \end{aligned} \tag{2.38}$$

where $1-P_{00}$, P_{00}, $1-P_{11}$, and P_{11} are k-dependent self-demagnetizing factors for the $S_0\hat{\mathbf{x}}$, $S_0\hat{\mathbf{z}}$, $S_1\hat{\mathbf{x}}$, and $S_1\hat{\mathbf{z}}$ basis components, respectively. They can be found by integration of the Green's function

$$\begin{aligned} P_{00} &= \frac{1}{t}\int_{-t/2}^{t/2}\int_{-t/2}^{t/2} G_P(z - z')\, dz\, dz' = 1 - \frac{1 - e^{-|k|t}}{|k|t}, \\ P_{11} &= \frac{2}{t}\int_{-t/2}^{t/2}\int_{-t/2}^{t/2} G_P(z - z')\cos(\frac{z\pi}{t})\cos(\frac{z'\pi}{t})\, dz\, dz' = \\ &= \frac{(kt)^2}{\pi^2 + (kt)^2}\left[1 - \frac{2(kt)^2}{\pi^2 + (kt)^2}\frac{1 + e^{-|k|t}}{|k|t}\right], \end{aligned} \tag{2.39}$$

The coupling between the uniform ($\boldsymbol{\eta} = (\eta_{0,x}, \eta_{0,z}, 0, 0)^T$) and antisymmetric ($\boldsymbol{\eta} = (0, 0, \eta_{1,x}, \eta_{1,z})^T$) precession modes is described through the off-diagonal terms $i2Q$,

which involve the mutual demagnetizing factor

$$Q = \frac{\sqrt{2}}{t}\int_{-t/2}^{t/2}\int_{-t/2}^{t/2} G_Q(z-z')\cos(\frac{z\pi}{t})\,dz\,dz' = \frac{\sqrt{2}kt}{\pi^2+(kt)^2}(1+e^{-|k|t}). \tag{2.40}$$

The cross product $\times\hat{y}$ can be interpreted as a $\pi/2$ rotation operator around the $\hat{y}$ axis, and corresponds to the cross interaction between the components of the magnetization that allows its precession. It is possible to express it as $\times\hat{y}^R = \begin{pmatrix} 0 & 1 \\ -1 & 0 \end{pmatrix}$ in the real space basis $R = \{\hat{x},\, \hat{z}\}$. In the 4×4 space where $\overline{\overline{C}}$ belongs, it is expressed as

$$(\times\hat{y}) = \begin{pmatrix} 0 & 1 & 0 & 0 \\ -1 & 0 & 0 & 0 \\ 0 & 0 & 0 & 1 \\ 0 & 0 & -1 & 0 \end{pmatrix}, \tag{2.41}$$

Doing the multiplication, we get

$$\overline{\overline{C'}} = \overline{\overline{C}} \times \hat{y} = \begin{pmatrix} 0 & \Omega_{z0} & -i2Q & 0 \\ -\Omega_{x0} & 0 & 0 & i2Q \\ -i2Q & 0 & 0 & \Omega_{x1} \\ 0 & i2Q & -\Omega_{x1} & 0 \end{pmatrix} \tag{2.42}$$

Solving for $\det\left(\overline{\overline{C'}} - i\Omega\mathbb{I}\right) = 0$, where $\mathbb{I}$ is the identity matrix, yields the eigenfrequencies of the first two hybrid DE modes in a single layer.

If we consider $Q = 0$, the two modes ($n = 0$ and $n = 1$) would be independent. In that case we obtain the following two eigenfrequencies

$$\omega_{nn} = \omega_M \Omega_{nn} = \omega_M \sqrt{\Omega_{n,x}\,\Omega_{n,z}}. \tag{2.43}$$

However, if we take the whole expression, including the corresponding $Q \neq 0$, we obtain

$$\Omega_{0,1}^2 = \frac{\Omega_{00}^2 + \Omega_{11}^2}{2} - Q^2 \mp \frac{1}{2}\sqrt{\left(\Omega_{11}^2 - \Omega_{00}^2\right)^2 + 4Q^2\left[(P_{00}-P_{11})^2 - \frac{\Lambda^4\pi^4}{t^4}\right]}. \tag{2.44}$$

The sign of Q depends on the sign of k. Nevertheless, it appears always squared in the expression of $\Omega_{0,1}$, leading to reciprocal dispersions ($f(\boldsymbol{k}) = f(-\boldsymbol{k})$).

As an example, the dispersion relation of a thin film of Permalloy with $t = 50$ nm was calculated using the KS approach and the results are shown in Fig. 2.8. It is clear that the interaction mostly affects the points of the dispersion relation where the different modes cross. While at $k = 0$ the modes are purely symmetric and anti-

symmetric, near the crossing we observe that both DE0 and DE1 have symmetric and antisymmetric components. We also note that, as the applied magnetic field is small compared with M_S, DE0 is almost linearly polarized at $k = 0$.

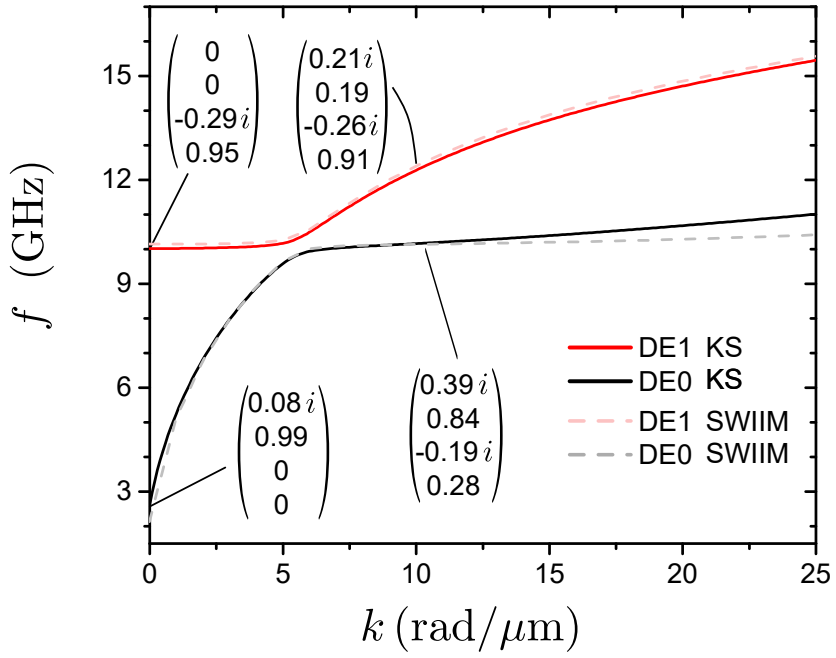

Figure 2.8: Dispersion relation calculated with the dipole-exchange method and SWIIM of the first two spin-waves modes in the DE configuration. The values of $\boldsymbol{\eta}$ for $k = 0$ and $k = 10$ rad/μm are shown. The thin film thickness is $t = 50$nm. Permalloy's magnetic parameters were used: $M_S = 800$ kA/m , $A = 10$ pJ/m [64], and $\mu_0 H_{\text{eq}} = 5$ mT.

SWIIM

The KS approach depends strongly on the basis proposed. The more elements this basis has, more exact the results will be. When working with a small basis, it has to be carefully chosen to take into account the physical symmetries of the system. On the contrary, a more generic basis could be used. Following this idea, a numerical treatment was proposed by Y. Henry et al. [15]: an in-house developed finite difference method, which performs a plane spin-wave normal-mode analysis and which we will denominate *SWIIM* — **S**pin **W**ave f**I**nite d**I**fference **M**odeling. In this approach, the proposed basis is the set of N adjacent rectangular gate-functions that covers the thickness of the sample. This is equivalent to divide the thin film in N parallel slices of equal thickness. From this procedure a $2N \times 2N$ matrix is obtained. When numerically solving this system, the eigenvalues provide the mode frequencies. The $2N$-element eigenvector gives the thickness profile of the two components of the dynamic magnetization.

SWIIM will be used several times in this work along with analytical calculations, as it provides a more precise description of the dynamic magnetization profile. In particular, this numerical method proves quite useful to calculate the dispersion relation

in samples with inhomogenous distributions of the magnetic parameters. For the case of homogeneous M_S, the results are similar to the ones obtained with the KS approach, as shown in Fig. 2.8.

2.4 External excitation

Spin-wave modes can be excited by introducing an oscillating external field $\boldsymbol{h}(t, \boldsymbol{r}) = \boldsymbol{h}_0(\boldsymbol{r})\, e^{i\omega t}$ with the correct spatial modulation. This field will contribute to $\boldsymbol{h}^{\text{eff}}(t)$, producing a coupling with the mode $\boldsymbol{m}(\boldsymbol{r})$ proportional to $\boldsymbol{h}_0(\boldsymbol{r}) \cdot \boldsymbol{m}(\boldsymbol{r})$.

In the case of the FMR modes, if only the Zeeman interaction is considered — condition equivalent to the Larmor precession—, Equation 2.6 becomes

$$\begin{aligned} i\omega m_x &= \omega_M h_z - \omega_H m_z; \\ i\omega m_z &= -\omega_M h_x + \omega_H m_x, \end{aligned} \tag{2.45}$$

where $\omega_H = \gamma\mu_0 H$ is the Larmor frequency, and $\omega_M = \gamma\mu_0 M_S$. From these relations, the magnetization dependence on the variable magnetic field can be written as $\boldsymbol{m} = \overline{\overline{\chi}}\boldsymbol{h}$, where

$$\overline{\overline{\chi}} = \begin{pmatrix} \chi & i\kappa \\ -i\kappa & \chi \end{pmatrix} \tag{2.46}$$

is the Polder susceptibility tensor. Its components are $\kappa = \frac{\omega\,\omega_M}{\omega_H^2 - \omega^2}$ and, $\chi = \frac{\omega_H\,\omega_M}{\omega_H^2 - \omega^2}$ and they diverge when $\omega = \omega_H$. The divergence of the system response can be understood as a resonance, where even a vanishing excitation field $\boldsymbol{h}$ is able of drive a precession of finite amplitude.

2.5 Damping

Until now, we have studied the dissipationless dynamics of the magnetization given by the Landau-Lifshitz equation. However, dynamic magnetization modes have a finite lifetime as their energy leaks to the environment and the system tends to return to the equilibrium configuration when the excitation ceases. Several dissipative interactions can be identified, such as magnon-magnon scattering, where energy flows from one spin-wave mode to another; magnon-phonon interaction; and relaxation via impurities [65, 66].

Even if they are mediated at the quantum level, these processes lead to a global dissipation which can be integrated in a mesoscopic description. The simplest form can be derived from an analogy with viscous friction: the dissipative term will be proportional to the precession velocity, and it can be added as an effective force to $\boldsymbol{H}_{\text{eff}}$

as

$$\frac{\partial \boldsymbol{M}}{\partial t} = -\boldsymbol{M} \times \left[\gamma\, \mu_0\, \boldsymbol{H}_{\text{eff}} + \frac{\alpha}{M_S} \frac{\partial \boldsymbol{M}}{\partial t} \right], \tag{2.47}$$

where α is the dimensionless Gilbert damping parameter, which sums up all dissipation terms. This equation is known as the Landau-Lifshitz-Gilbert (LLG) equation after T. Gilbert, who redefined the damping term[8] in his thesis in 1956 [67]. This equation implies that in absence of excitation, the magnetization will spiral towards the equilibrium position defined by $\boldsymbol{H}_{\text{eff}}$, as shown in Fig. 2.9.

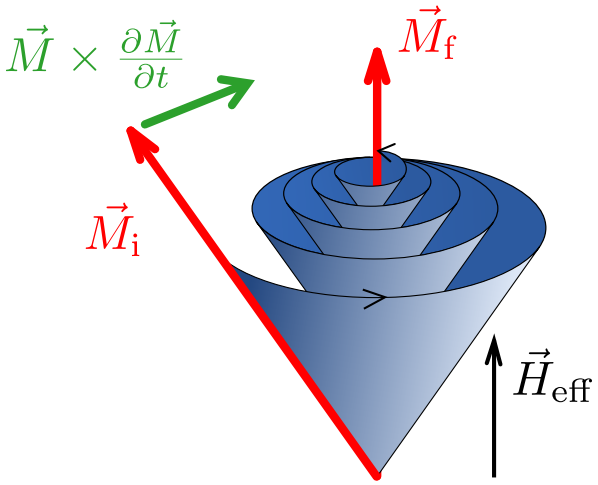

Figure 2.9: Magnetization trajectory on the $|\boldsymbol{M}| = M_{\text{S}}$ sphere in absence of external excitation. From its initial position M_i, it spirals to the equilibrium configuration $\boldsymbol{M} \parallel \boldsymbol{H}_{\text{eff}}$. The green arrow indicates the direction of the torque induced by the damping term.

Performing linearization and taking temporal Fourier transform, this equation reads

$$\begin{aligned} i\omega \boldsymbol{m} &= -\left(\boldsymbol{M}_{\text{eq}} + \boldsymbol{m}\right) \times \left[\gamma\, \mu_0 \, \left(\boldsymbol{H}_{\text{eq}}^{\text{eff}} + \boldsymbol{h}^{\text{eff}} \right) + \frac{\alpha}{M_S} i\omega \boldsymbol{m} \right] \\ &= -\left[\gamma\, \mu_0 \boldsymbol{M}_{\text{eq}} \times \boldsymbol{h}^{\text{eff}} + \boldsymbol{m} \times \left(\gamma \mu_0 \boldsymbol{H}_{\text{eq}}^{\text{eff}} + i\alpha\omega \frac{\boldsymbol{M}_{\text{eq}}}{M_{\text{S}}} \right) \right]. \end{aligned} \tag{2.48}$$

Thus, the damping parameter enters as an imaginary static magnetic field, and it can be included in all the obtained expressions by replacing $\omega_H \rightarrow \omega_H + i\alpha\omega$. For example, neglecting α^2 terms, the damping modifies the diagonal term in the Polder tensor described in Section 2.4 as

$$\chi = \frac{\omega_M(\omega_H + i\alpha\omega)}{\omega_H^2 - \omega^2 + i\ 2\alpha\omega\omega_H}. \tag{2.49}$$

Nearby the resonance, when $\omega \approx \omega_H$ this equation defines a complex Lorentzian

[8] Originally, Landau and Lifshitz have defined the damping term as $\frac{\lambda}{\gamma\, M_{\text{S}}^2} \boldsymbol{M} \times \boldsymbol{H}_{\text{eff}}$, which leads to identical dynamics if the gyromagnetic constant is adjusted between the two expressions.

function, whose imaginary part can be approximated as

$$\mathrm{Im}(\chi) \approx -\frac{\omega_M \, \Delta\omega}{(\omega_H - \omega)^2 + \Delta\omega^2}, \tag{2.50}$$

with $\Delta\omega \approx \alpha\omega_H$[9]. Both components of χ are shown in Fig. 2.10. The half-width at half-maximum on the imaginary part is given by $\Delta\omega$, which may be interpreted as the reciprocal of the lifetime, $\tau = \Delta\omega^{-1}$. This can be understood by analyzing the time response of the $m_i(t)$, with $i = x, y$ when applying an impulse of magnetic field $h_i(t) = h_0 \, \delta(t)$,

$$m_i(t) \propto \int_{-\infty}^{\infty} \frac{e^{i\omega t}}{[\omega - (\omega_H - i\,\alpha\,\omega_H)][\omega - (-\omega_H - i\,\alpha\,\omega_H)]} d\omega, \tag{2.51}$$

where the Dirac's delta has been developed in the frequency space, and the denominator of expression 2.49 is expressed as two complex poles. Applying the residue theorem, we obtain $m_i(t) \propto e^{\pm i\omega_H |t|} e^{-\alpha\omega_H |t|}$ —for details, see Ref. [68] Appendix B or [16] p. 51. The first term gives the oscillatory dependence, while the second shows the exponential decay with the expected τ.

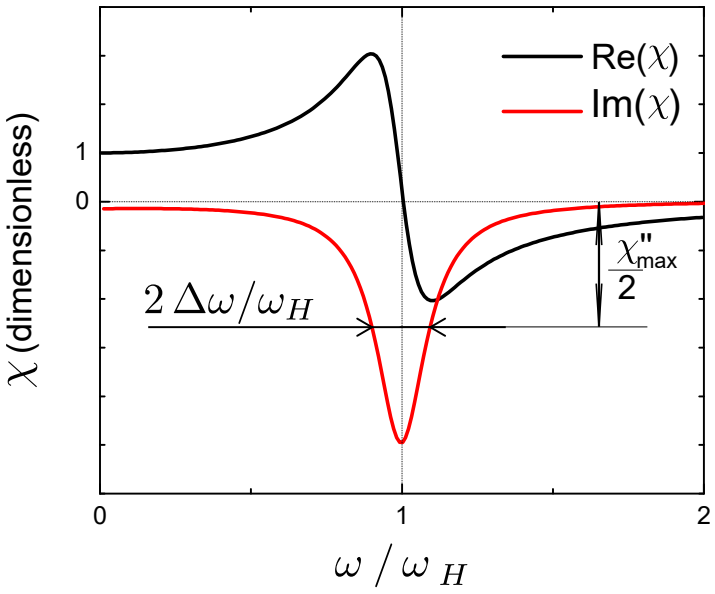

Figure 2.10: Susceptibility Lorentzian dependence on the excitation frequency with $\omega_M = \omega_H$, $\alpha = 0.1$ and a consequent $\Delta\omega/\omega_H = 0.1$.

As the resonance frequency goes to zero, the damping term becomes less important. Nevertheless, the experimental line-width often does not extrapolates to zero. The extra contribution is called inhomogeneous-width ΔH_0, and it is an extrinsic contribution due to the distribution of effective magnetic field in the sample, caused mostly by its imperfections.

[9]For $k \neq 0$, the derivation of these expressions follows the same logic. As an example, Appendix A of Ref. [12] makes the explicit calculation for the FV configuration.

From the concept of τ, it is possible to define a spin-wave attenuation length as $L_{\mathrm{att}} = v_g \tau$, with v_g the group velocity of the studied spin waves. L_{att} describes the distance from a time-steady source at which the amplitude of the spin waves has decreased by a factor e^{-1}.

Chapter 3

Experimental methods

In this chapter we review the main experimental techniques used in this work. Special attention is paid to the two inductive techniques, as they constitute the core of the work done at IPCMS. The magneto-optic techniques are also reviewed. While Brillouin Light Scattering measurements where done at TUK by M. Geilen and P. Pirro, Kerr microscopy measurements were performed at IPCMS with the supervision of S. Cherifi.

The lithography techniques described were used to fabricate devices for Propagating-Spin-Wave Spectroscopy and micro-focus Brillouin Light Scattering experiments.

3.1 Ferromagnetic Resonance

The susceptibility calculated in Section 2.4 characterizes the coupling between an external oscillating field $\boldsymbol{h}$ and the magnetization precession represented by $\boldsymbol{m}$. Because the gyromagnetic ratio is of the order of tens of GHz/T, and typical effective fields are of the order of magnitude of some fraction of Tesla, microwave (MW) electromagnetic waves with frequencies between 100 MHz and 100 GHz are generally chosen to directly excite spin waves. This technique shares several characteristics with Nuclear Magnetic Resonance (NMR) and Electron Paramagnetic Resonance (EPR). Nevertheless, important differences are found. First, due to the strong dipolar interaction, FMR signal depends strongly on the shape of the sample. Secondly, FMR transverse susceptibilities are much larger, as magnetization is larger than in a paramagnet or a system of nuclei [69].

The spin wave-electromagnetic wave coupling can be measured by placing the ferromagnetic sample in a microwave cavity and sensing the change in reflected power when applying an external magnetic field $\boldsymbol{H}$, which can be tuned such that the resonance frequency match the natural frequency of the cavity. The absorbed MW power is given by

$$P_{\text{abs}} \propto \chi_{ii}\, h_i^2, \tag{3.1}$$

where χ_{ii} is the susceptibility of the material in the direction of the MW pumping field h_i. At first order, this direction has to be transversal to the equilibrium magnetization $\boldsymbol{M}$ to obtain a non-zero value of χ_{ii}. The utilization of cavity presents the advantage that its quality factor can greatly increase the signal measured. However, it forces one to work at a specific frequency and do magnetic field scans. Therefore, this is not a good technique to measure magnetic textures, whose structure depends on the applied field.

To overcome this problem, we have used a broadband FMR set-up, where the sample is coupled to a non-resonant coplanar waveguide (CPW), providing a large frequency range to work [70–72]. Fig. 3.1 shows a schematic view of the used CPW. The MW signal is conducted by the central conductor (S), while the two lateral and bottom planes serve as grounds (G). To ensure that the three ground planes are at the same potential, they are connected by via fences. The ferromagnetic sample is positioned on the top of this configuration, at a position where the CPW presents a constriction of its width (W) and thickness (T-R). The film is in contact with the grounds, but a gap separates it from the signal line.

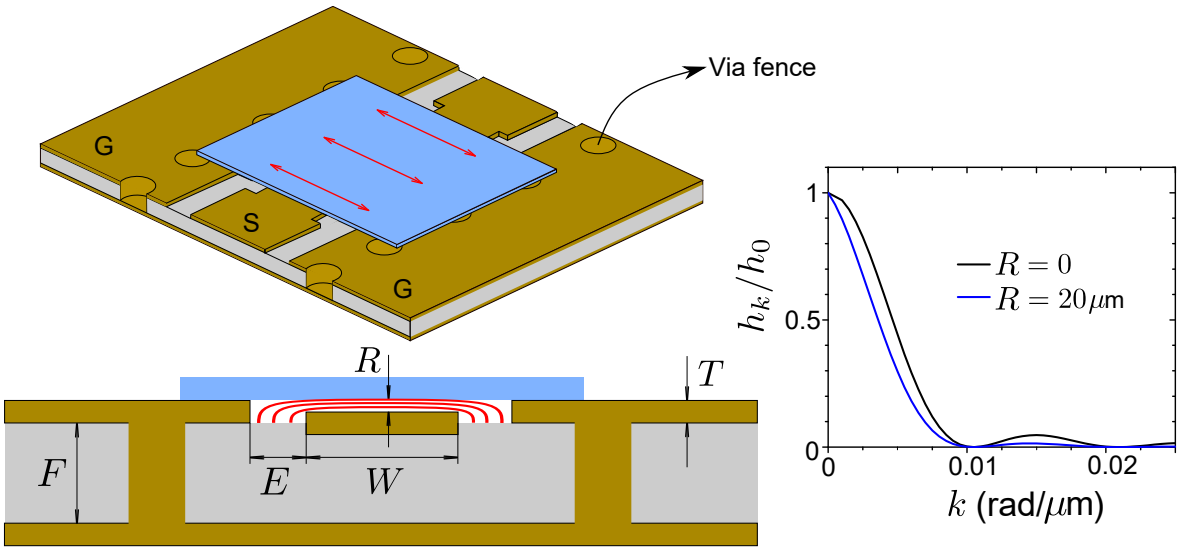

Figure 3.1: Schematic view of the coplanar waveguide (brown) coupled to the ferromagnetic sample (blue) by the electromagnetic field. The approximate distribution of excitation magnetic field h is depicted by the red lines. The dimensions are: $W = 200$ μm, $E = 110$ μm, $F = 120$ μm and $T = 50$ μm. The bottom ground plane is connected to the top ground planes by via fences. The Fourier transform of h is shown for the two possible distances R between the central conductor and the sample. It is normalized by $h_0 = h(k = 0)$.

As the studied samples are metallic, the oscillating electromagnetic field induces Eddy currents that produce a shielding effect, which concentrates the electromagnetic field in the gap between the sample and the central line [73], as shown in Fig. 3.1. Due

to this shielding the electromagnetic field distribution is not longer the one of a CPW, and the inductance per length unit increases. This produces an impedance mismatch which implies unwanted reflections, hindering the signal from the sample. To prevent this effect, the impedance of the waveguide under the sample is artificially increased by the width constriction of the central line. Another consequence of the shielding is that the magnetic field decreases rapidly inside the sample[1]. Therefore, $\boldsymbol{h}$ distribution is not homogeneous and it can couple to modes with nonzero OOP wave vector ($\kappa \neq 0$).

The coupling between the magnetization precession modes and $\boldsymbol{h}$ is given by $\overline{\overline{\chi}}$. This coupling changes the complex self-inductance ΔL of the waveguide, which can be measured by a Vector Network Analyzer (VNA). To obtain a quantitative approximation of the magnetic susceptibility, a proper de-embedding technique has to be used. In our case, we have used a 2-port VNA, which allows to measure the four complex S-parameters, which are given by the following expression

$$V_i = \Sigma_j S_{ij} V_j \tag{3.2}$$

where V_j is the applied voltage at port $j = 1, 2$ and V_i is the measured voltage at port $i = 1, 2$. The VNA have access to the phase and the magnitude of the voltages, thus, the elements S_ij are represented in the complex plane.

In order to eliminate unwanted reflections from the wires and connectors, a full two-port calibration was performed, using a Thru-Reflect-Line calibration kit fabricated with the same printed circuit board geometry as the CPWs serving for FMR measurements. From the S-matrix, it is possible to calculate the complex propagation index $n_{\text{eff}}\,(S_{ij})$ of the loaded CPW, as shown in Ref. [74]. We can approximate the effective relative permeability of the waveguide loaded by the ferromagentic film $\tilde{\mu}_r$ as

$$\tilde{\mu}_r = \frac{n_{\text{eff}}^2}{\tilde{\epsilon_r}}, \tag{3.3}$$

where $\tilde{\epsilon_r}$ is the effective relative permittivity of the loaded waveguide, assumed constant[2]. Finally, we extract the effective susceptibility as

$$\tilde{\chi} = \tilde{\mu}_r - \tilde{\mu}_r^{\text{ref}}, \tag{3.4}$$

where $\tilde{\mu}_r$ is the measured effective permeability and $\tilde{\mu}_r^{\text{ref}}$ is a reference permeability measured far from the ferromagnetic resonance condition. The effective susceptibility $\tilde{\chi}$ is proportional to the film susceptibility tensor χ, however, the calculation of the proportionality factor is quite complex, as it requires to simulate the exact distribution

[1] In a scale much smaller than the typical skin depth [73].

[2] The used samples are conductors, and as the imaginary part of the permittivity in low-loss dielectrics is small it can be neglected. It is the real part which is found to remain constant, as shown in Ref. [71].

of the electromagnetic field in the configuration formed by the CPW and the sample.

The FMR addresses primarily the spin-wave mode with $k = 0$, also known as FMR-mode. Nevertheless, due to the finite dimension of the waveguide, non-zero wave-vector spin waves could also be excited. The maximum wave-vector $k_{\max}$ is imposed by the width of the central track of the coplanar waveguide used. This determines a $k_{\max} \approx \pi/300\,\mu\text{m} = 0.01\,\text{rad}/\mu\text{m}$.

In this work, two FMR configurations have been implemented. In the standard transverse pumping configuration, the excitation field is perpendicular to the applied DC field, $\boldsymbol{h} \perp \boldsymbol{H}$. We will also use the so-called longitudinal pumping configuration, in which $\boldsymbol{h} \parallel \boldsymbol{H}$.

3.2 Propagating-Spin-Wave Spectroscopy

Using lithography techniques, it is possible to fabricate waveguides that are much smaller than the ones used in FMR set-ups, reaching the hundreds-of-nanometers scale. Therefore, single waveguide measurements can access different parts of the dispersion relation, being limited by the lithography resolution. Nevertheless, no information about the actual propagation of spin waves could be extracted from this method. To obtain such information it is necessary to perform an experiment of excitation and detection using two spatially separated microwave transducers: one to generate the oscillating magnetic field and another one to probe inductively the electromagnetic field created by the propagating spin wave. This technique is called *Propagating-Spin-Wave Spectroscopy* (PSWS).

3.2.1 Preliminary works on this technique

The coupling of the electromagnetic waves with the spin waves would be efficient only if they have similar spatial distributions. In the microwave range, electromagnetic waves have a wavelength larger than 1 mm, so if the antennas generate plane waves, this will be the smaller spin wave length that could be detected or measured. To couple to smaller wavelength spin waves, it is necessary to modulate the spatial distribution of the electromagnetic field by fabricating antennas with a proper size.

This technique has been used to excite and detect propagating spin waves for the first time in 1967 by Olson et al. [75]. The experiment has been performed in Yttrium Iron Garnet (YIG) rods, connecting each end to different resonant cavities. When injecting an MW signal in one cavity, a local magnetic field is generated, which couples to the surface and volume spin wave modes. These spin waves propagate along the rod and induce an MW voltage in the other cavity. The same concept was used by Brundle and Freedman to excite DE modes in millimeter-scale YIG thin films [76].

But in their case, instead of using two cavities, they extended the center wires of two coaxial cables along the two sides of the film. By measuring the coupling between the wires they were able of observing the propagation of the DE spin-waves. In this case they do not use two closed cavities, and the magnetic field is not applied locally. As a consequence, the transmitted microwave signal contains two contributions. On the one hand, as the dynamic applied magnetic field decays slowly, it excites spin waves in the whole extension of the film, even nearby the second wire. At resonance, when the permeability of the ferromagnetic medium diverges, the second wire will pick up a signal to be associated to "non-propagating spin waves". On the other hand, spin waves excited nearby one of the wire will propagate until the other extreme of the slab and produce a signal which corresponds to the true "propagating spin waves".

The main difference between these two signals is their propagation velocity, the non-propagating spin-wave signal at the speed of light, while the second one many proceeds more slowly. This implies that the two contributions have a different time delay. By using an excitation pulse shorter than the propagation time[3] Brundle and Freedman could separate these two contributions, confirming the presence of true propagating spin waves. Even in some devices used if this work, it is necessary to separate the two contributions [12].

In the following years, more experiments were performed in YIG samples. This material has many advantages, as having a low damping (FMR linewidth generally smaller than $5\,10^{-2}$ mT [77]), and being an electrical insulator (reducing capacity losses). Nevertheless, ferromagnetic materials that are conductors present several characteristics that are interesting to study. In particular, ferromagnetic metals can reach a much higher saturation magnetization than YIG [4]. Moreover, conducting films can be easily deposited with nanometer-scale thickness, giving experimental access to the sub-micrometer scale dipole-exchange regime. In the metallic film case antennas have to be separated by a insulating layer and the lithography process has to be improved to reduce the capacity loses. The first experiment on such films was performed by Bailleul et al. in 2001 [78]. While the mentioned work used micrometer-scale antennas, improvements on e-beam lithography allowed to miniaturize the fabricated antennas to the nano-scale [79, 80]. At this scale, it is possible to explore a larger range of the dispersion relation. This is fundamental to explore phenomena that scales with the spin-wave wave vector k, as current-induced spin-wave Doppler shift [81], frequency nonreciprocity due to asymmetric surface anisotropy [82] or Dzyaloshinkii-Moriya constant determination [83]. Now, we will describe experimental method used in the

[3] By this year they had access to the theoretical work of Damon and Eshbach [58], allowing them to make the delay predictions.

[4] As an example, the saturation magnetization of cobalt is one order of magnitude bigger than YIG (1400 kA/m vs 140 kA/m).

present work. The basic set-up is shown in Fig. 3.2. In this case, two shorted CPW are used as antennas, but the versatility of lithography process allows to change the geometry depending on studied system.

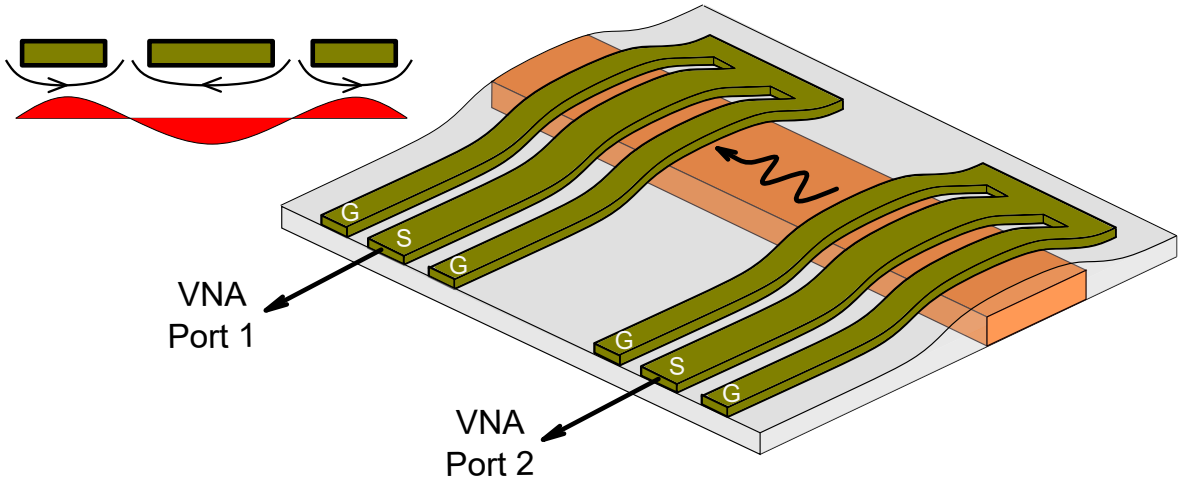

Figure 3.2: Schematic view of the basic PSWS set-up. Two antennas with the typical size of the wavelength of the spin wave to be measured are fabricated on a ferromagnetic strip which serves as bus. The MW magnetic field distribution under one CPW antenna is shown in the top-left corner.

From the MW device characterization, a typical PSWS experiment has some common points with the VNA-FMR. As in the FMR experiments, a VNA is connected to the antennas to serve both as a generator and detector for determining the complex scattering parameters S_{ij} of the antenna pair. Upon injection of an MW-current with a certain frequency f in the emitting antenna (index j), this couples inductively to the magnetization of the waveguides and spin waves are excited. If those waves travel far enough and reach the receiving antenna (index i) before being fully damped, a microwave magnetic flux with frequency f is picked up[5]. The ratio of the measured flux to the injected current defines the mutual inductance L_{ij} of interest, which is extracted from S_{ij}. In practice, in order to extract spin-wave related signals more accurately, relative measurements are systematically taken: a background signal acquired at much larger applied magnetic field so that no spin wave resonance occurs, is subtracted from the raw data.

3.2.2 Device fabrication

The main function of a PSWS device is to connect the VNA signal ports with the typically much smaller antennas. This implies a transition between two different scales: the millimeter-scale pico-probe connected with the VNA; and the nanometer-scale antennas. To work at the correct resolution for each scale, both laser and electronic

[5]This technique is therefore sensitive to linear processes in which the magnon has the same frequency as the excitation field.

lithography were used. An image of a typical device is shown in Fig. 3.3.

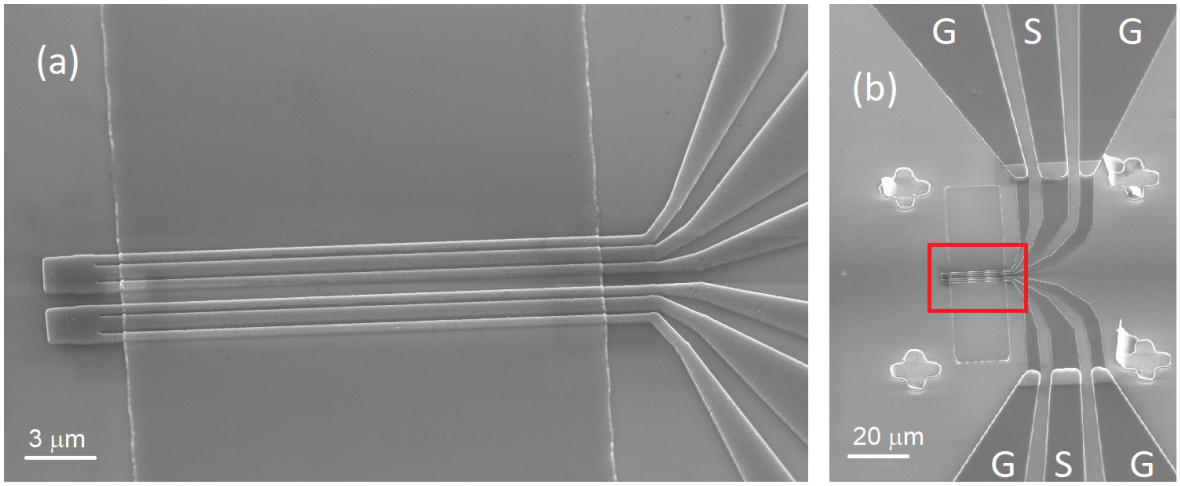

Figure 3.3: Electronic image of the one PSWS device. (a) Zoom on the two shorted CPW antennas. The vertical track at the center is the ferromagnetic bus line. (b) Transition with the micrometer-sized CPW pads to connect the pico-probes. The crosses are used for the alignment of the antennas and the bus line.

Film fabrication

All ferromagnetic films used in this work were fabricated at IJL. They were deposited by DC magnetron sputtering on silicon substrates. To limit possible capacitive losses it is recommendable to use high-resistivity intrinsic silicon, but in some cases doped silicon was also used. To ensure a good adhesion of the deposited metal on the substrate, an extra layer of a few nanometers could be deposited in between. For example, 3nm of tantalum were used as interface between Si and CoFeB. Also, a protective layer could be deposited on the top of the stack to avoid oxidation and general degradation. For CoFeB and Permalloy, this layer was made of platinum and gold, respectively. The composition of each used stack will be detailed in the corresponding chapters.

Bus etching

In order to minimize the capacitance between the ferromagnetic metallic layer and the antenna pads, all nonessential parts of the metallic layer were removed, leaving only a strip (also called bus) where spin waves will propagate. Because this strip has a typical size of several micrometers, it is possible to use optical lithography to pattern it. This process is done in two steps: firstly an auxiliary hard mask with the desired shape is deposited; secondly the sample is etched, leaving only the ferromagnetic material protected by the hard mask. The first step is schematically shown in Fig. 3.4.

The first step is achieved using a resist bilayer made of AZ1505 (top layer) and LOR3A (bottom layer). The first one is a photosensitive resist that when exposed by

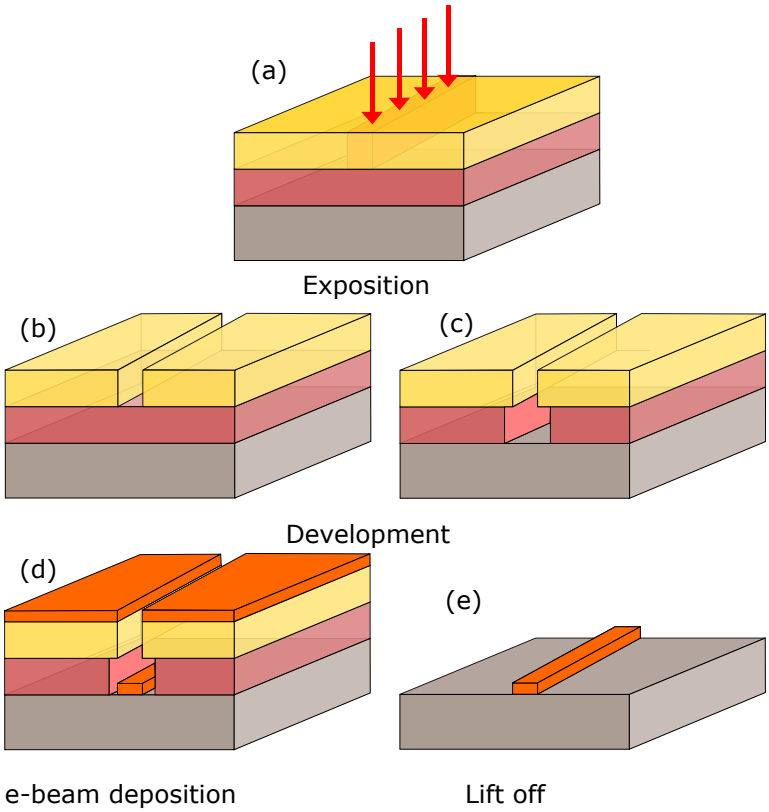

Figure 3.4: Patterning of the hard mask. (a) The resist bilayer spread on the ferromagnetic film is exposed with a laser to pattern the desired structure. The developer removes the exposed part of the top layer (b) and dissolves also part of the bottom layer (c), producing the "overhang" profile. (d) A hard-to-etch material is evaporated on the top of all the structure. (e) After lift-off, the resist is removed, leaving the hard mask pattern.

the μPG100 laser lithography system can be removed by an AZ-726-MIF solvent in the development step. The second layer is not photosensitive and will be dissolved by the solvent only in the areas where the AZ1505 has been removed. Because the bottom layer dissolves relatively fast, an overhang profile is ensured (Fig. 3.4(c)).

Once the development was completed, a hard-to-etch material, in our case titanium, is deposited in a Plassys 550S e-beam. By leaving the sample one hour in a Remover PG bath at 60 degrees, the resist bilayer is removed. The advantage of the overhang resist profile is that it avoids the continuity between the evaporated material in the developed areas and the one on top of the resist, which facilitates the "lift-off" process. The remaining titanium will serve as hard mask to protect the ferromagnetic material under it. The next step, the etching, is also performed in the Plassys 550S loadlock, using an argon ion beam gun. The etching time and the deposited titanium thickness are calculated after doing calibration tests.

Insulating spacer deposition

Once etching process is finished, a protective silicon oxide (SiO_2) layer is deposited by magnetron sputtering. Its thickness depends on the thickness of the ferromagnetic

material, because it is intended to smooth out the height step between the substrate, where the pads are going to be deposited, and the top surface of the strips, where the antennas will be deposited. This layer has also an electric isolation function separating the antennas from the conducting film. Here, the thickness also plays a relevant role defining the capacitance between the antennas and the ferromagnetic material.

Pad lithography

The pads will serve as interface between the micro-probes and the ebeam-fabricated antennas. They are patterned using the same resist bilayer and exposing process as described in Fig. 3.4. But in this case, 50nm of gold are deposited on 10nm of titanium. The gold is resistant to mechanic pressure, preventing scratches when connecting the pico-probe, and the titanium guarantees a good adhesion with the SiO_2 layer underneath.

Antenna lithography

Antenna typical size is of order of hundred nanometers. Thus, optical lithography is no longer suitable to fabricate them and another technique is required. The electron-beam (or e-beam) lithography equipment available at IPCMS enables to fabricate structures as small as 50 nm in good conditions. In this case an electron sensitive positive tone resist bilayer All Resist PMMA 600K/ PMMA 950K was used. This bilayer has the same function as the one used for optical lithography, which is to produce an overhang profile facilitating lift-off. The two resists were deposited by spin coating at 4000 rpm and each of them was baked for 90 s at 180°C. The bilayer exposition was performed using a Zeiss Supra 40 Scanning Electron Microscope equipped with a Raith Elphy Plus pattern generator. An acceleration voltage of 20 keV and a beam current of the order of 300 pA were used. The electron dose (in the range of 200 to 350 $\mu C/cm^2$) was determined by preliminary tests before each lithography. After exposure, the sample is developed for 30 s in All Resist 600.56 developer followed immediately by its immersion in All Resist 600.60 Stopper for another 30 s. Before evaporation the sample is cleaned by an Oxygen Plasma for 45 s with an applied power of 30 W. This step removes possible contamination or even remains of resist in the exposed area. Later, the Plassys 550S e-beam evaporator is used to deposit 10 nm of titanium and 90 nm of aluminum. Titanium is chosen to act as barrier between gold and aluminum, two materials that, when put in contact, diffuse in each other reducing the conductivity. Aluminum is chosen because it presents a low resistivity for nanometer-scale films.

3.2.3 Device characterization

The fabricated device can be modeled as a resistance and an inductance in series. The capacitive losses are represented by a capacitor connected in parallel to the ground. To estimate the value of these components the device is connected and characterized by a previously calibrated two-port VNA (Agilent PNA E8364B). This calibration is performed with a SOLT[6] calibration kit CS-5 from GGB industries in the desired frequency range. The maximum frequency span of this VNA is from 10MHz to 50GHz.

The device characterization is done by measuring the S-parameters defined in Section 3.1 as a function of the frequency. In general, the elements S_{ij} with $i = j$ are called “reflection parameters” and if $i \neq j$ they are called "transmission parameters".

From the S-parameters, it is possible to calculate the impedance matrix Z_{ij} that relates the current I with the voltage V as

$$Z_{ij} = \left.\frac{V_i}{I_j}\right|_{I_i=0}, \tag{3.5}$$

it can be calculated from the S-parameters as

$$\begin{aligned} Z_{ii} &= Z_0 \frac{(1+S_{ii})(1-S_{jj}) + S_{12}S_{21}}{(1+S_{ii})(1-S_{jj}) - S_{12}S_{21}}, \\ Z_{ij} &= Z_0 \frac{2S_{ij}}{(1+S_{ii})(1-S_{jj}) - S_{ij}S_{ji}}, \quad \text{if } i \neq j \end{aligned} \tag{3.6}$$

where $Z_0 = 50\Omega$ is the VNA characteristic impedance.

During a PSWS experiement, all S-parameters are measured twice as a function of the frequency. One time at the desired measurement magnetic field H_m and a second time at a reference magnetic field H^{ref}. This last field has to be chosen in a way that no resonance occurs in the measured frequency range. From this data, the differential inductance matrix can be calculated as

$$\Delta L_{ij}(\omega) = \frac{1}{i\omega}[Z_{ij}(\omega, H_m) - Z_{ij}(\omega, H_r)]. \tag{3.7}$$

Following this method, all electric resonances that were not eliminated in the calibration are erased in $\Delta L_{ij}(\omega)$; leaving only the resonances of magnetic origin.

3.3 Kerr Microscopy

Magneto-optic interactions, i.e. interactions between magnetic materials and light, are known since 1845. In that year, M. Faraday observed that, in some transparent materials, the birefringence could be changed by an external magnetic field [84]. Today,

[6] Shortening of the four calibration standards used: Short, Open, 50Ω Load and a Through.

two main magneto-optic effects can be noted: the Kerr [85] and Faraday effects. They affect the polarization upon interaction with magnetized materials of the reflected and transmitted light, respectively.

These effects originate from the non-diagonals terms of the permittivity tensor of the material. It can be understood as the effect of a Lorentz force which modifies the dynamic response of electric charges in the oscillating electric field of the light. As a consequence, if the incident light is linearly polarized in a given direction, after reflection this polarization rotates in an angle proportional to the sample magnetization [86, 87]. This rotation can be detected using a second polarizer (usually called analyzer) and a camera (normally a charge-coupled device). A schematic view of the used set-up is presented in Fig. 3.5(a). This configuration allows to measure the spatial distribution of the static magnetization at the micrometer-scale.

In this work we have studied IP magnetized samples. To measure this component of the magnetization, the light path is chosen to arrive to the sample in angle with its normal, defining an optical plane. In the so-called longitudinal Kerr configuration, one probes the IP magnetization component directed along the optical plane. This criterion is used to define the sensitivity axis. Figures 3.5(b) and (c) show the effect of rotating this axis by 90 degrees. If the intensity of the obtained images is integrated, the averaged magnetization of the surface of the observed region can be obtained as a function of the applied field. With this, the surface magnetization hysteresis loop can be obtained.

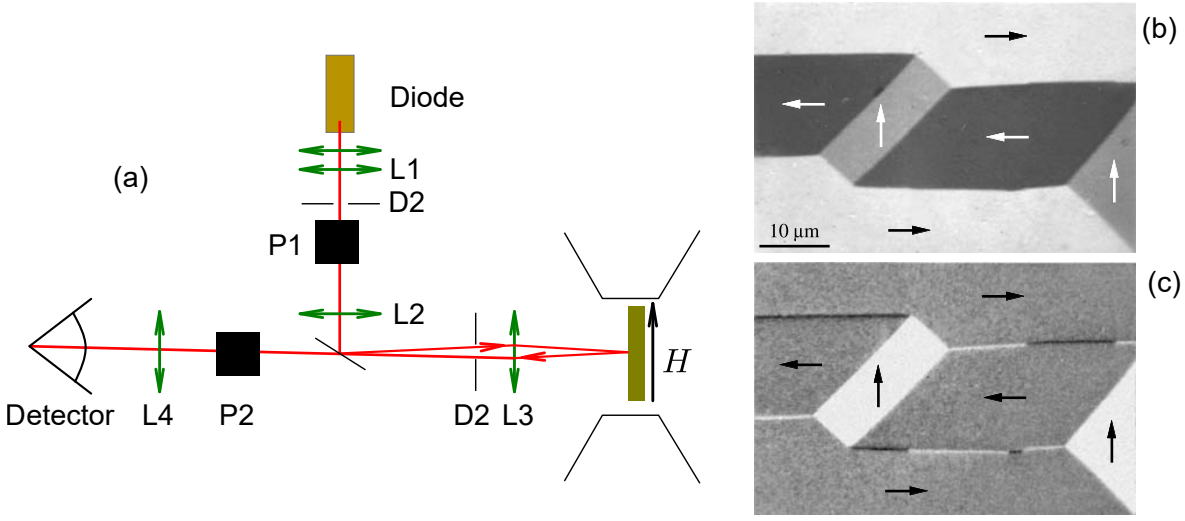

Figure 3.5: (a) Schematic set-up of the used Kerr microscope. The optical path is depicted in red. The light is emitted by the diode and passes a linear polarizer P1, then it is reflected by the sample to pass through the analyzer P2 and be measured by the detector. The lens system (L1 to L4) form an optical microscope. An IP magnetic field can be applied at the position of the sample. (b) and (c) show an example of a typical Kerr microscopy image of magnetic domains (adapted from [24]). In (b) the sensitivity axis is horizontal, while in (c) it is vertical.

3.4 Brillouin Light Scattering

As does Kerr microscopy, this technique relies on the dependence of the non-diagonal terms of the permittivity on the local magnetization [88]. In the case of spin-waves, the dynamic components of the magnetization produce a periodic modulation of the permittivity of the medium [89]. These fluctuations induce an inelastic scattering of light, leading to an effective coupling between light and spin waves.

At the quantum level, this implies a magnon-photon interaction. In general, interactions between photons and pseudoparticles in matter in the frequency range of 1-100 GHz enter in the category of *Brillouin scattering*[7]. This gives the name to the experimental technique able of measuring the frequency shift of the photons at those energies: Brillouin Light Scattering (BLS) or Brillouin spectroscopy. The microscopic details of the photon-magnon coupling are governed by the spin-orbit and the exchange interaction[89]. As a consequence, the BLS contrast depends strongly on the exact nature of the sample. In the case of metals, the optical skin-depth is of the order of several tens of nanometers giving to the film coating a relevant role, as it can substantially modify both the intensity of optical scattering and the spin-orbit effects at the surface.

As a consequence of this interaction, photons could couple to the magnonic system. Inasmuch as the system is time- and space-translation invariant, the linear moment and energy are conserved in the scattering process. The frequency f_s and wavevector k_s of the light inelastically scattered from spin waves with f and k are given by

$$\begin{aligned} f_s &= f_i \pm f \\ k_s &= k_i \pm k \end{aligned} \tag{3.8}$$

where f_i and k_i correspond to the frequency and wave vector of the incident photons. The $\pm$ signs represent the two possible processes: the creation of a magnon and decrease of photon frequency (Stokes); and the absorption of a magnon and increase of the photon frequency (anti-Stokes). The intensity of the two processes depends on the availability of a preexisting magnon, prior to the arrival of the photon. As magnons are bosons, they follow the Bose-Einstein distribution, and their density is given by the product of it with the density of states given by the spin wave dispersion relation.

Incoherent magnons are induced by thermal fluctuations. On the contrary, coherent magnons can be also excited by others sources as antennas. This difference in the source of magnons defines two variant of the technique: *thermal BLS* [90] and *coherent BLS*

[7] This phenomenon is similar to Raman scattering (and its associated spectroscopy), although the frequencies involved are much greater (>THz). Originally, the difference of between the two processes was their target, while Raman scattering designates the interaction with optical phonons (and vibrational modes of molecules), Brillouin scattering designates the one with acoustic phonons.

[91, 92]. The last method is particularly useful to measure non-linear phenomena, as the frequency of the backscattered photons could be different from the excitation frequency in presence of non-linearities

Another difference in the technique is the focusing of the light on the sample. If the light is collimated towards the sample (quasi-parallel beam with an angle of incidence θ) and if the light is collected in the backscattering geometry ($\theta_s = \theta_i$), then the transferred wave-vector is

$$k = \frac{4\pi}{\lambda}\sin(\theta), \tag{3.9}$$

where λ is the wavelength of the incident photons. This variant of the technique is called *k-resolved BLS*. On the other hand, in the *micro-focus BLS* the light beam is focused on a point on the sample. In this case, one obtains a spatial resolution of the order of the wavelength of light, but a broad range of wave vector is probed. These two variants are illustrated in Fig. 3.6.

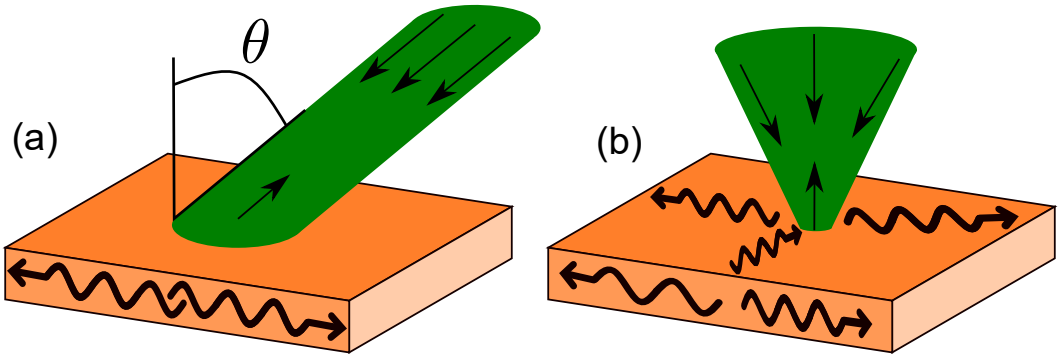

Figure 3.6: BLS scattering configurations. (a) In the k-resolved BLS a parallel light beam arrives at the sample with an incidence angle θ, and the scattered light is collected in the same direction. (b) In micro-focus BLS, the light is focused covering a range of angles of incidence and, therefore, a range of wave vectors.

In all mentioned cases, to measure the frequency shift, a Fabry-Pérot interferometer is used. Several technical difficulties have to be overcome in order to detect the small amount of back scattered photons. In particular, the laser amplitude has to be controlled by a loop system in order to obtain consistent data during the scans and the room temperature should be constant.

Chapter 4

Spin-wave propagation in a ferromagnetic bilayer

In ferromagnetic materials, broken symmetries affect the excitation and propagation of spin waves, leading to a number of intriguing phenomena. In this chapter, we study how spin-wave propagation is affected by a symmetry breaking in the transverse plane, namely an up-down asymmetry across a thin film. We will see that this asymmetry leads to a nonreciprocal hybridization of the fully symmetric and anti-symmetric thickness modes.

More specifically, we study the propagation of spin-waves in a bilayer with a saturation magnetization contrast in the Damon-Eshbach (DE) configuration. We find, by means of simulations and experiments (Propagating Spin Wave Spectroscopy and Brillouin Light Scattering), that this system holds a strong nonreciprocity which can be used for the realization of a spin-wave diode. While the experimental data is identical to Ref. [93], a more pedagogical interpretation of the origin of the nonreciprocity is given below.

4.1 Motivation

This chapter presents both fundamental and technological motivations. On the one hand, a bilayer can be seen as a perturbation of a well-known system —the ferromagnetic thin film— in which a controlled symmetry breaking can be introduced. This allows to study new spin-wave physics, departing from a well-establish background. On the other hand, spin-waves could serve as data carriers in magnonic circuits as future wave-based computing architectures [8]. In this context, the development of a diode-like device capable of transmitting spin-waves in only one direction, thus allowing controlled signal routing, is an essential step. Indeed, the isolator, or wave diode, is an essential building block in wave-computing architectures, which is necessary to

mitigate unwanted reflections and prevent signal backflow [94].

Designs of magnonic diodes [95] and unidirectional spin-wave emitters [96] relying on the chiral Dzyaloshinskii-Moriya interaction for producing nonreciprocity have been proposed theoretically but have not been realized yet. Recently, another type of unidirectional spin-wave emitter has been demonstrated experimentally [97], the working principle of which is based on the nonreciprocal magneto-dipolar coupling between a nanoscale grating made of hard ferromagnetic nanowires and a magnetically softer ultrathin film. In this scheme, the emitter (the grating) plays an essential role in producing nonreciprocity. In contrast, the system studied in this chapter, presents a sizeable frequency non-reciprocity in the absence of any patterning.

4.2 Nonreciprocity on bilayers

Reciprocity is the property of a physical system to behave equally in one direction (say left to right) than in the opposite (say right to left), and nonreciprocity is the lack of it. In electromagnetism, dealing with a reciprocal system means to obtain the same signal if the emitter and the receptor are swapped [98]. Equivalently, if working with sinusoidal signals, changing the sign of the wave vector $\boldsymbol{k}$ leaves the equations of a reciprocal system invariant. As Maxwell's equations in vacuum are reciprocal, obtaining nonreciprocity requires the use of a material with specific properties. In magnetic systems, the time-reversal (T) symmetry is broken as the precession of the magnetic moments around the effective field has a unique direction defined by the cross product of the LL equation. As a consequence, counterpropagating spin waves are chiral, that is the spatial distribution of $\boldsymbol{m}(\boldsymbol{k})$ is the mirror image of $\boldsymbol{m}(-\boldsymbol{k})$, as shown in Fig. 4.1. Nevertheless, if no other symmetry-braking takes place, this chirality is not translated in a difference of behavior for counterpropagating spin-waves. This is explained by the fact that in highly-symmetric systems, the dynamic effective magnetic field created by $\boldsymbol{m}$ also changes its handedness, resulting in equal excitation frequencies for both propagation directions.

We can distinguish two kinds of nonreciprocity: amplitude and frequency nonreciprocity. The first is trivially obtained in DE configurations, because, as explained in Section 2.3.1, modes with opposite sign of $\boldsymbol{k}$ are localized in different surfaces of the thin film. This leads to an amplitude nonreciprocity when the excitation is stronger in one of the thin film surfaces. Also in this configuration, the spin-waves chirality changes with the sign of $\boldsymbol{k}$. Thus, if the excitation field —the one produced by an antenna, for example— has an intrinsic chirality, it will couple better with the spin waves with a given sing of $\boldsymbol{k}$, generating an amplitude nonreciprocity.

On the other hand, frequency nonreciprocity implies $\omega(\boldsymbol{k}) \neq \omega(-\boldsymbol{k})$, and is not always obtained in the DE configuration. An extra symmetry has to be broken. For

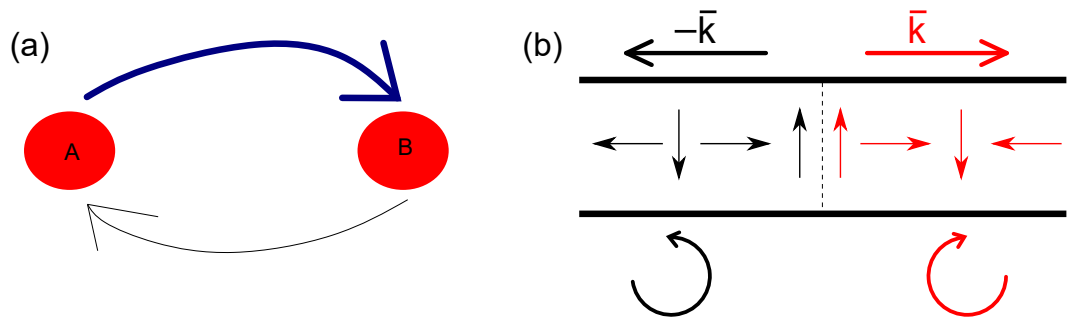

Figure 4.1: Nonreciprocity. (a) Schematic definition of nonreciprocity, if the emitter is placed in A and the receptor in B, the pick up signal will be different if they are exchanged. (b) The dynamic components of the magnetization of counterpropagating spin waves have different handedness.

example, at the millimeter-scale, using films in which top-bottom symmetry is broken either by adding a nonmagnetic conductor to one side of the film [99], or by using a magnetic bilayer stack [100], one can even reach an extreme situation in which, at some frequencies, propagation is possible only in one direction. In the above situations, the effect can be described simply in terms of localized magnetostatic DE spin waves traveling through different materials. When scaling-down the film thickness to the nanometer scale, however, this description becomes incorrect as exchange interaction starts to play a crucial role and spin-wave modes lose their surface character. An adapted strategy to achieve spin-wave unidirectionality then needs to be devised.

In this context, frequency nonreciprocity could be introduced by an interaction which does not change its handedness when inverting the propagation direction of spin-waves. If so, such interaction would couple strongly to the spin-waves presenting the same handedness. As we will show in this section, this is the case of the dipolar interaction in the DE configuration in a nanometer-scale thin film composed by two different materials with a contrast of saturation magnetization[1]. In our description, this effect shows up as a nonreciprocal hybridization between the first low frequency exchange modes. In the case of fully unpinned boundary conditions, these two modes correspond to a symmetric ($\kappa = 0$) and an asymmetric ($\kappa = \frac{\pi}{t}$) modes across the thickness.

To understand which role the hybridization plays to produce frequency nonreciprocity, we will first study the interaction between the first modes in a single layer. In the Kalinikos-Slavin approach, this interaction is given by Q (see Eq. 2.40), and can be conceptually understood from Fig. 4.2(a). The OOP components of the asymmetric mode generate magnetic charges that produce an IP dipolar field that couples to the symmetric mode[2].

[1] Layers with constrast of any magnetic parameter, as exchange or PMA, would be also suitable to obtain nonreciprocity.

[2] A similar coupling exists between the IP components of the asymmetric mode and the OOP dynamic magnetization of the symmetric mode (not shown).

The case of a bilayer with saturation magnetization contrast is quite different. As shown in Fig. 4.2(b), the dynamic magnetization in the top layer is larger than in the bottom layer[3]. Consequently, the magnetic charge distribution is asymmetric in the thickness, inducing an additional OOP magnetic field. Thus, the OOP magnetization creates both IP and OOP dipolar fields, which has the same handedness[4] for both propagation directions. This will translate in a nonreciprocal coupling, leading to a nonreciprocal hybridization.

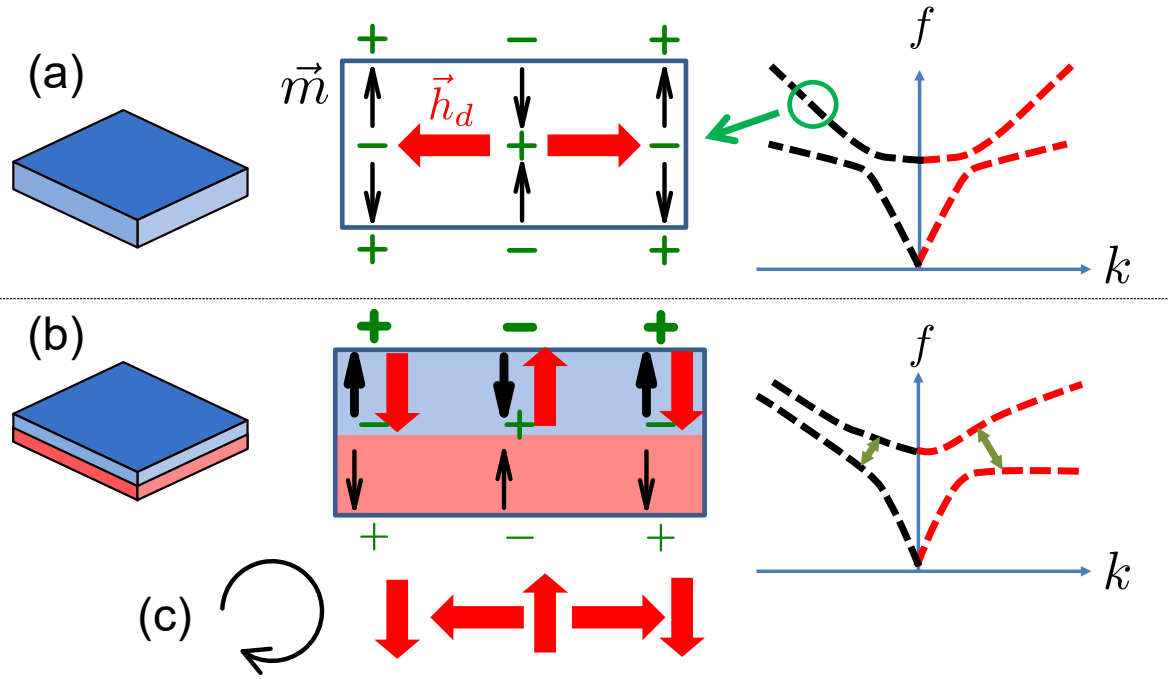

Figure 4.2: Hybridization of the symmetric and asymmetric modes in the DE configuration. We represent there the symmetric part of the dipole field generated by the antisymmetric OOP $\boldsymbol{m}$ component. In the case of a single layer (a), the hybridization is governed by two mutually orthogonal components of the dynamic magnetization: an antisymmetric OOP component $m_{z,1}$ generates an IP dipolar field which couples to a symmetric IP component $m_{x,0}$. Therefore, this interaction does not favor a particular handedness. On the contrary, in the bilayer (b), an extra component of $\boldsymbol{h}_d$ is introduced by the asymmetric distribution of the magnetic charges. The new dipolar field is totally out-of-plane. Thus, the combination of the single-layer and bilayer components of $\boldsymbol{h}_d$, shown by the red arrows (c), has a handedness that depends solely on the magnetic contrast of the bilayer, leading to a nonreciprocal hybridization. The self-demagnetization terms of each component have be omitted for the sake of visualization.

We must note that when working with samples relatively thin, because the exchange plays an important role, the typical spin-wave surface-localization of the DE spin-waves [58] does not apply. Therefore, the spin-wave nonreciprocity should not be interpreted as counterpropagating waves traveling through different media. Indeed, even if the source of the nonreciprocity is the dipolar interaction, the exchange interaction controls the position of the avoided crossing in the dispersion relation. If the

[3]This is true if the precession angle is the same in both bilayers. In the dipole-exchange approach this is assured by choosing $\boldsymbol{m}(\boldsymbol{r}) = M_S(z)\,\boldsymbol{\eta}(\boldsymbol{z})\,e^{i(\omega t - k_x x)}$ and imposing the symmetric and asymmetric profile to $\boldsymbol{\eta}(\boldsymbol{z})$.

[4]The handedness sign depends on which layer, top or bottom, has the largest M_S.

exchange is small (or the thickness large), the crossing happens at low k, and the handedness is weakly defined, as the IP component of $\boldsymbol{h}_d$ becomes fainter. In this case, the nonreciprocity would be too weak to be measured. On the other hand, if we consider the limit of high exchange constant (or very thin films), the crossing takes place at large k, being out-of-scope of the measurements techniques and having no practical use.

4.3 Theoretical model

We now describe the bilayer magnetization dynamics using the Kalinikos-Slavin approach [57], already introduced in Chapter 2. To simplify the calculations, we will consider two layers with equal thickness $t/2$, as shown in Fig. 4.3. If each layer has a saturation magnetization $M_{S,1}$ and $M_{S,2}$, the magnetization as a function of the OOP coordinate z can be expressed as[5]

$$M_S(z) = \langle M_S \rangle \left[1 + \beta \, \mathrm{sg}(z)\right], \tag{4.1}$$

where $\langle M_S \rangle = (M_{S,1} + M_{S,2})/2$ is the average magnetization, $\beta = \frac{M_{S,1} - M_{S,2}}{M_{S,1} + M_{S,2}}$ is the magnetization contrast and $\mathrm{sg}(z)$ is the sign function. We will also assume that the ratio of the exchange constant to the saturation magnetization has a constant value, i.e. $A_1/M_{S,1} = A_2/M_{S,2} = \langle A \rangle / \langle M_S \rangle$. The dynamic magnetization can be expressed as $\boldsymbol{m}(x,z,t) = M_S(z)\, \boldsymbol{\eta}(z)\, e^{i(\omega t - kz)}$. With these simplifications, the linearized LL equation can be written as

$$\begin{aligned} i\omega \boldsymbol{\eta}(z) = &- \gamma \mu_0 H_0 \, \boldsymbol{\eta}(z) \times \hat{\mathbf{y}} + \gamma \frac{2\langle A \rangle}{\langle M_S \rangle} \left(\frac{\partial^2}{\partial z^2} - k^2 \right) \boldsymbol{\eta}(z) \times \hat{\mathbf{y}} \\ &+ \gamma \mu_0 \langle M_S \rangle \int_{-t/2}^{t/2} \bar{\bar{G}}_k(z - z') [1 + \beta \, \mathrm{sg}(z')] (\boldsymbol{\eta}(z') \times \hat{\mathbf{y}}) \, dz', \end{aligned} \tag{4.2}$$

where γ is the gyromagnetic ratio, μ_0 is the permeability of vacuum, $\hat{\mathbf{y}}$ is a unit vector along the applied magnetic field $\mathbf{H}_0$, and $\bar{\bar{G}}_k$ is the magnetostatic Green's function Eq. 2.26. We note that the bilayer asymmetry only affects the dynamic dipolar field, as $\frac{\partial^2}{\partial z^2} \mathrm{sg}(z) = 0$. We propose to use the same vector basis as the one used for a single layer, which consists of the x and z components of the first two unpinned exchange modes with homogeneous ($n = 0$) and fully antisymmetric ($n = 1$).

When $\beta \neq 0$, the dynamic matrix $\bar{\bar{C}}'$ of Eq. 2.42 acquires new elements with different symmetries, namely the diagonal elements in the $\bar{\bar{C}}'_{nn}$ blocks and the off-diagonal

[5] Note that the coordinates axis are rotated with respect to those of [93], in order to maintain a consistent convention between the different chapters of the manuscript.

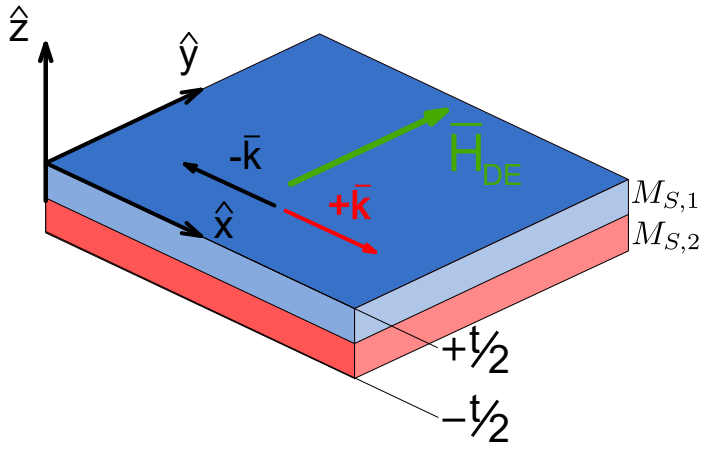

Figure 4.3: Schematic representation of the bilayer system considered in the analytical model.

elements in the $\bar{\bar{C}}'_{n\neq m}$'s are no longer zero and the dynamic matrix becomes[6]

$$\bar{\bar{C}}'(\beta) = \bar{\bar{C}}'(0) + \begin{pmatrix} -iP'_{00} & 0 & 0 & Q' \\ 0 & iP'_{00} & Q'-I' & 0 \\ 0 & Q' & -iP'_{11} & 0 \\ Q'-I' & 0 & 0 & iP'_{11} \end{pmatrix}, \tag{4.3}$$

where $\bar{\bar{C}}'(0)$ is given by Eq. 2.42 and

$$\begin{aligned} P'_{00} &= \frac{1}{kl}\left[\sinh(|k|l) - 2\sinh\left(\frac{|k|l}{2}\right)\right]\beta, \\ P'_{11} &= \frac{2kl}{(\pi^2+k^2l^2)^2}\left(\pi - |k|l\, e^{-|k|l/2}\right)^2\beta \\ I' &= \frac{2\sqrt{2}}{\pi}\,\beta, \\ Q' &= \frac{2\sqrt{2}}{\pi^2+k^2l^2}\left[\pi\left(1-e^{-|k|l/2}\right) + k^2l^2\left(\frac{1}{\pi} - \frac{1-e^{-|k|l}}{2|k|l}\right)\right]\beta. \end{aligned} \tag{4.4}$$

Not surprisingly, all newly non-zero matrix elements are proportional to the contrast in saturation magnetization β. The coefficients Q' and I' account for the additional mutual-demagnetizing effects produced in the presence of magnetic asymmetry. They describe how hybridization between the symmetric and fully antisymmetric modes is affected in a bilayer. The coefficient I', in particular, corresponds to the term $\delta(z-z')$ in the Green's tensor, and is the one responsible for the extra OOP dipolar field explained in the previous section (compare Figs. 2.3 and 4.2(b)).

The coefficients P'_{nn}, on the other hand, describe the additional self-demagnetizing

[6] For details on the matrix element calculation, see Appendix A in Ref. [93].

effects produced by the magnetic asymmetry on uncoupled modes $\bar{\eta}_n$ $(n = 0, 1)$. As revealed by the imaginary character of the corresponding matrix elements in the $\bar{\bar{C}}'_{nn}$ blocks, these take the form of transverse dipole fields, which oscillate with a phase difference of $\pi/2$ with respect to the dynamic magnetization components creating them. In the sample studied in the next sections, these terms contribute little to the nonreciprocity.

From the dynamic matrix it is possible to calculate analytically the dispersion relation. As done in the case of a single layer, the value of frequencies can be obtained from $\det[\bar{\bar{C}}'(\beta) - i\Omega\bar{\bar{1}}] = 0$. The Figure 4.4 shows the dispersions calculated for a single layer and a bilayer. The magnetic parameters of the latter were chosen to obtain a zero group velocity for positive k while keeping a finite value for negative k in a certain frequency range. In both cases we observe two different modes, that we will call DE-mode 0 and DE-mode 1 [7].

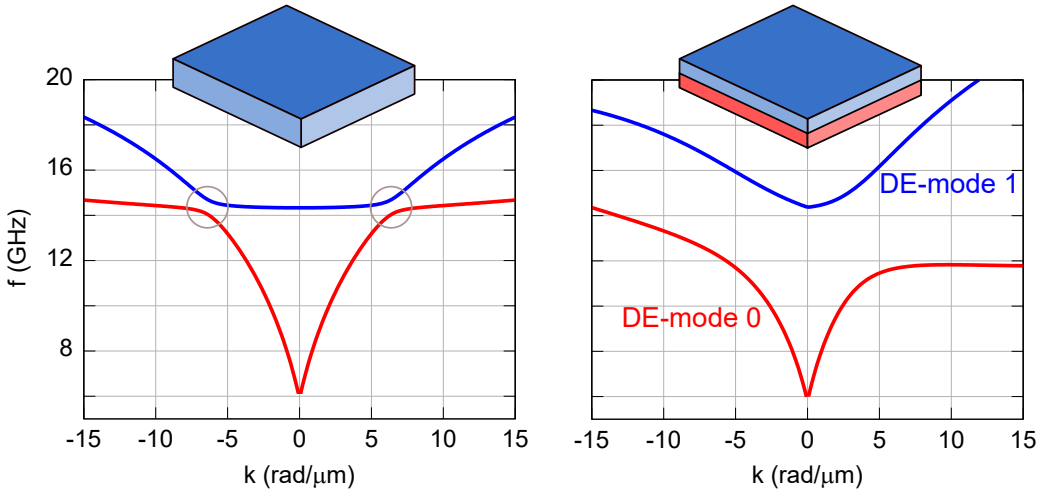

Figure 4.4: Implementation of the Kalinikos-Slavin theoretical model for a single layer (left) and a bilayer (right) with $\beta = 0.2$. The gray circles indicate the reciprocal anticrossing. Calculations were performed using the following parameters: $t = 46$nm, $\langle A \rangle = 15$pJ/m and $\mu_0 \langle M_S \rangle = 1.32$T.

It is also possible to obtain an approximated expression for the frequency nonreciprocity. Keeping only terms up to first order in β, yields the following dispersion relation for the two lowest DE modes in a bilayer[8]

$$\begin{aligned} &(\Omega_0^2 - \Omega^2)(\Omega_1^2 - \Omega^2) \\ -2Q\Omega\,&[(Q' - I')(\Omega_{1,x} - \Omega_{0,x}) + Q'(\Omega_{1,z} - \Omega_{0,z})] = 0. \end{aligned} \tag{4.5}$$

Treating further QQ' and QI' as small parameters, in a perturbative manner, the

[7] In some published works, including Ref. [93], these modes are called MSSW-mode 0 and MSSW-mode 1, respectively.

[8] P'_{nn} coefficients only appear in this relation at second order in β.

eigenfrequencies of these modes can be obtained as

$$\Omega_{0,1}(\beta) = \Omega_{0,1}(0) \pm \Delta\Omega(\beta). \tag{4.6}$$

Here, $\Omega_0(0)$ and $\Omega_1(0)$ are the reduced oscillation frequencies corresponding to the single layer obtained in the introduction(Eq. 2.44). By substituting the last expression in 4.5, a closed expression is obtained

$$\Delta\Omega(\beta) = \frac{Q}{\Omega_1^2(0) - \Omega_0^2(0)} \left[(I' - Q')(\Omega_{1,z} - \Omega_{0,z}) - Q'(\Omega_{1,x} - \Omega_{0,x})\right].$$

The expression of $\Delta\Omega$ involves two products of dipolar matrix elements, QQ' and QI'. In both of them, one term (Q' or I') is even in k and the other (Q) is odd. Then $\Delta\Omega$ is odd in k and, since $\Omega_0(0)$ and $\Omega_1(0)$ are fully reciprocal, $|2\Delta\Omega|$ is a measure of the frequency nonreciprocities for the two hybrid DE modes. These elements, QQ' and QI', verify the conceptual explanation given in the previous section: I' and Q' produce a dipolar field which has the same component (x or z) that $\boldsymbol{m}$ but different symmetry (symmetric or antisymmetric), while Q mixes both components and symmetries. The combination of these dipolar fields has a given handedness, as shown in Fig. 4.2(c).

4.4 Experimental results

Until now we have explained how the nonreciprocity appears in a bilayer with M_S contrast. The next section has two goals. Firstly, we experimentally verify the proposed model. Secondly, we proceed to implement this nonreciprocity to create a material which acts as a spin-wave diode.

4.4.1 Sample fabrication

The bilayer films used in the present work have been fabricated in the Institute Jean Lamour, Nancy, by M. Hehn. They were deposited on natively oxidized intrinsic (100)Si substrates by DC magnetron sputtering from material targets with nominal compositions $Co_{40}Fe_{40}B_{20}$ and $Ni_{80}Fe_{20}$. Deposition of the magnetic stack was preceded by that of a 3 nm thick Ta seed layer, for ensuring low layer roughness, and followed by that of a 3 nm thick Au overlayer, for protecting the magnetic alloys against oxidation. Using SWIIM simulations, we have selected the thicknesses of each layer to maximize the diode behavior shown in Fig. 4.4.

The devices used in PSWS and μ-BLS where fabricated in by the author of this thesis following the procedures explained in Section 3.2.2.

The magnetic parameters of each layer —saturation magnetization M_S and exchange constant A— were measured by Damien Louis during his PostDoc at IPCMS, by means of AGFM and FMR on single layers of $Co_{40}Fe_{40}B_{20}$ and $Ni_{80}Fe_{20}$.

4.4.2 Nonreciprocal dispersion relations

The dispersion relations of thermally excited spin-waves in the $Co_{40}Fe_{40}B_{20}$(20nm)/ $Ni_{80}Fe_{20}$(26nm) bilayer system have been determined using wave-vector resolved BLS experiments carried out on a plain film. These measurements were performed in the Technical University of Kaiserslautern by M. Geilen and D. Louis. To evidence the nonreciprocal character of these dispersions, both Stokes and anti-Stokes peaks have been recorded for the two possible polarities of the applied magnetic field, in the DE configuration. Figure 4.5 shows a BLS spectra obtained when measuring the frequency shift of the backscattered photons. From here, it is possible to extract four magnon frequencies: the two modes with positive k (red) and the two modes with negative k (black).

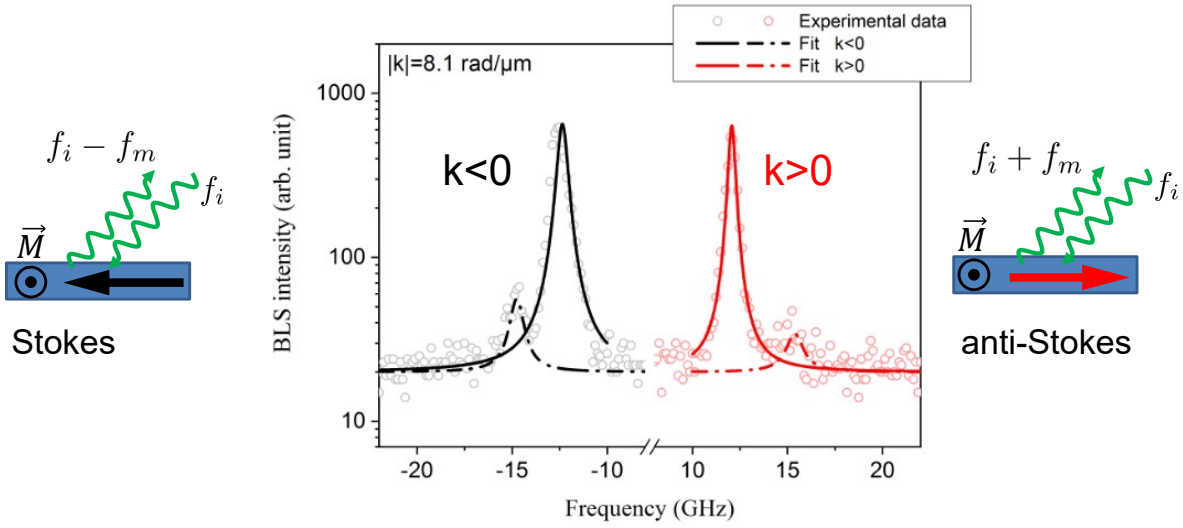

Figure 4.5: Typical BLS spectra measured for a given photon-incidence angle. While the Stokes process create magnons with the same propagation direction than the incident photon, the anti-Stokes does it in the opposite direction. For both positive and negative k two peaks are observed. They correspond to the DE-mode 1 and 0.

In order to obtain the full dispersion relation, a scan in angle was performed. Figure 4.6(a-c) shows BLS spectra obtained with $\mu_0 H_0 = +30$ mT, at different values of the in-plane wave vector k. Again, the four different peaks, two Stokes and two anti-Stokes, can be identified, which are related to the first (red) and second (blue) DE branches. These peaks have been fitted to Lorentzian lines in order to extract their central frequencies and thereby reconstruct the $f(k)$ curves. The obtained dispersion relations were compared with theoretical results calculated with SWIIM. This method

of calculation is more precise than the theoretical model proposed in the previous section, as it does not assume a particular thickness profile. We see that these numerical results are in very good agreement with the measurements (Fig. 4.6(d)). As required to fulfill our ambition to build a magnonic diode, a well-defined frequency plateau is present at about 12.5 GHz in the dispersion of DE-mode 0, which corresponds to the anti-Stokes peak with k-independent position in Fig. 4.6(a-c). This constitutes a clear experimental evidence for the occurrence of nonreciprocal zero-velocity group spin-waves in our system.

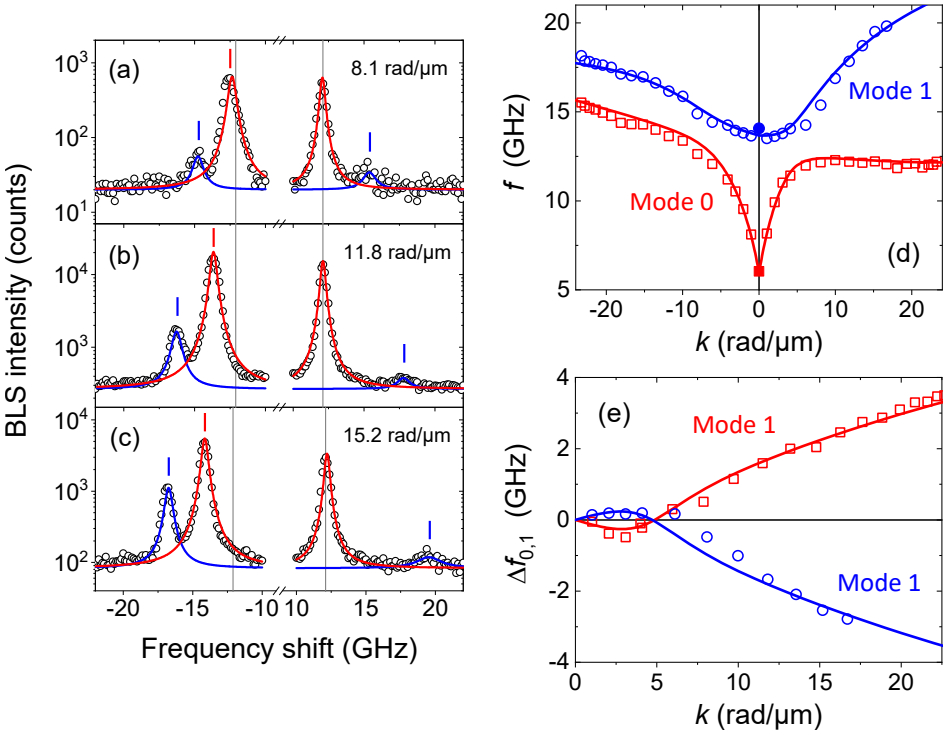

Figure 4.6: (a-c) BLS spectra recorded in the DE configuration ($\mu_0 H_0 = +30$ mT) on a $Co_{40}Fe_{40}B_{20}$(20nm)/$Ni_{80}Fe_{20}$(26nm) bilayer film (symbols), for three different values of the in-plane wave vector: (a) $|k|=8.1$ rad/μm, (b) $|k|=11.8$ rad/μm, and (c) $|k|=15.2$ rad/μm. Lines are Lorentzian fits. (d) Dispersion relations of the two lowest DE modes deduced from BLS data (open symbols) and comparison with predictions from SWIIM numerical simulations (lines). Solid symbols correspond to data from a complementary ferromagnetic resonance experiment. (e) Frequency nonreciprocities $\Delta f_n(k) = f_n(-|k|) - f_n(+|k|)$ of DE modes 0 and 1. As in (d), symbols and lines correspond to experimental and numerical data, respectively.

From Fig. 4.6(a-c) we note that the anti-Stokes peak with the highest frequency has a small amplitude, whatever k. The peak even becomes undetectable for wave-vector values exceeding 17 rad/μm, hence the lack of some (blue) data points in Fig. 4.6(d,e). This is attributed to the fact that, as verified in numerical simulations (see Section 4.5), DE-mode 1 has very small amplitude in the upmost part of the bilayer film, whose magneto-optic contribution dominates the BLS signal. In Fig. 4.6(e) we also note that the frequency nonreciprocities of the two DE modes, $\Delta f_n(k) = f_n(-|k|) - f_n(+|k|)$ ($n = 0, 1$) show very specific behaviors. First, $\Delta f_0(k)$ and $\Delta f_1(k)$ are almost equal in

absolute value and opposite in sign, which comes naturally in our analytical theory of the nonreciprocal hybridization. Second, these quantities do not vary monotonously as a function of k. Instead, they exhibit a local extreme followed by a change of sign at about 5 rad/μm. This behavior reveals the transition between a regime dominated by exchange across the film thickness, in the $k \to 0$ limit, to a regime where in-plane dipole fields gain importance, at larger k. Here, we must insist that both the dipolar field and the hybridization between the symmetric and asymmetric mode are necessary to obtain the nonreciprocity. However, as in the case of the reciprocal hybridization in the single layer (see last term of Eq. 2.44), contains both an exchange part ($\Lambda^2\pi^2/t^2$) and a dipole part ($P_{00} - P_{11}$), the former being the dominant one at low k.

4.4.3 Magnonic diode behavior

Propagating spin-wave spectroscopy

In order to clearly demonstrate the diode-like behavior of the studied bilayer system, propagating spin-wave spectroscopy (PSWS) experiments have been performed. The used devices are shown in Figure 4.7(a). Each one of them contains a pair of 50μm-long, 10μm-wide bilayer waveguides and two pairs of single-wire antennas connected in parallel. This device layout, in which spin-waves are traveling simultaneously along two magnetic buses, ensures a good symmetry match with the Ground-Signal-Ground (GSG) microwave probes used for connection to the VNA. Importantly, the 200nm wide single-wire antennas used here can couple inductively to spin-waves with a broad range of wave vectors, $0 \leq |k| \lesssim 12$ rad/μm, as shown in the spatial Fourier transform of the excitation field in Fig. 4.7(b). The distance between the emitting and receiving antennas ($D = 2$ μm or 5 μm) is adapted to the typical attenuation length expected for surface spin-waves with such k values in a $Co_{40}Fe_{40}B_{20}$(20nm)/$Ni_{80}Fe_{20}$(26nm) bilayer.

Figure 4.8(a) shows the real part of the spin-wave-induced change in mutual inductance ΔL_{12} and ΔL_{21} as a function of frequency for a device with a relatively large distance between the emitting and receiving antennas [$D = 5\,\mu$m, see Fig. 4.7(a)], submitted to a transverse in-plane magnetic field $\mu_0 H_0 = +30$ mT. The two data sets presented correspond to opposite directions of spin-wave propagation. Comparing them, one immediately sees that the spin-wave signal at 12.5 GHz $\leq f \leq$ 14.5 GHz is vanishingly small for $k > 0$ (red symbols), meaning that no spin wave travel from the left antennas to the right antennas, whereas it is comparatively large for $k < 0$ (black symbols) as spin-waves do propagate effectively from the right antennas to the left ones. This nonreciprocal behavior is of course related to the presence of a plateau in the positive-k part of the dispersion relation of DE-mode 0 [Fig. 4.6(d)], which has two main consequences. First, rightward propagating spin-waves with $f \sim 12.5$ GHz and $0 \leq k \leq k_{\max}$ are excited by the left antennas but, due to their very low group velocity,

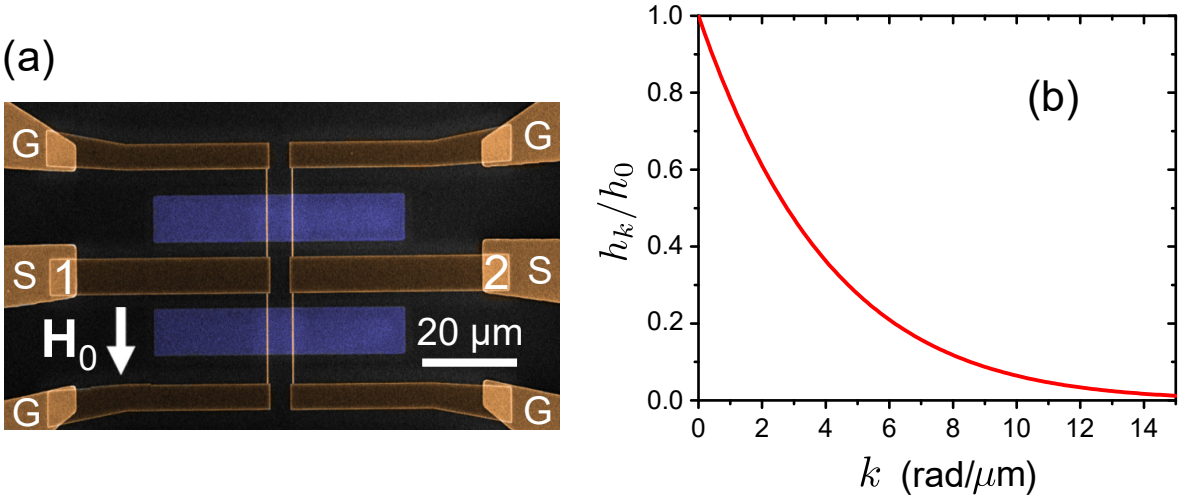

Figure 4.7: Propagating spin-wave spectroscopy. (a) False color scanning electron micrograph of a PSWS device with a distance $D = 5$ μm between the emitting and receiving antennas. (b) Normalized Fourier transform of the IP magnetic field produced by a current uniformly distributed over a $W = 200$ nm width at a distance $S = 120$ nm. These dimensions correspond to the width of the antenna and the SiO_2 thickness of the device depicted in panel (a).

they die out under the effect of magnetic damping before reaching the receiving antennas. Second, due to the large extension of the plateau, the group velocity of DE-mode 0 becomes sizable again only for k values, which lie far beyond the k range accessible with the used antennas, meaning that rightward propagating DE 0 spin-waves with frequency well above 12.5 GHz are simply not produced. For $f \geq 14.5$ GHz, DE-mode 1 eventually gets excited so that a clear spin-wave signal is transmitted again for both directions of propagation. An effective forbidden gap with a width of about 2 GHz is thus formed for rightward propagating spin-waves (shaded zone in Fig. 4.8(a)). In view of the possible application of this phenomenon, it is worth mentioning that the gap can naturally be shifted up and down in frequency by adjusting the amplitude of the applied magnetic field. A tunability of the order of 50 MHz/mT could be measured experimentally over the 10-50 mT range, as shown in Figure 4.8(b).

Because the wave vector k is constrained to change according to the dispersion relation $k(f)$, the phase delay kD acquired by spin-waves after propagation over the distance D varies continuously as the frequency f is swept. This variation in phase delay translates into pronounced oscillations of the recorded spin-wave signal as the ones appearing in Fig. 4.8(a). As we shall describe below, this provides us with a way to extract the wave vector value corresponding to each driving frequency f. For that, one needs to record both the real and imaginary parts of the spin-wave induced change in mutual inductance over a large range of frequencies [Fig. 4.9(a,c)] encompassing the ferromagnetic resonance frequency (FMR), $f_{\mathrm{FMR}} = f_0(k = 0)$, which corresponds to the onset of the oscillations[9]. From such data, the spin-wave wave vector can be

[9]The short-period small-amplitude oscillations of the mutual inductance observed at frequencies between 6 and 7 GHz are related to reflections of the spin waves at the extremities of the magnetic

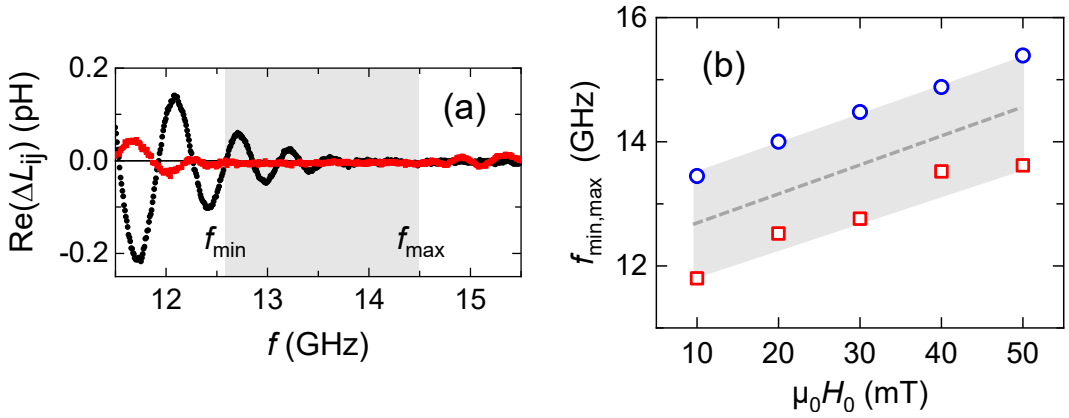

Figure 4.8: (a) Real part of the spin-wave induced change in mutual inductance ΔL_{ij} as a function of the excitation frequency f ($\mu_0 H_0 = +30$ mT), for spin-waves propagating from antennas 1 to antennas 2 ($k>0$, red squares) and vice versa ($k<0$, black circles), in the device shown in 4.7(a). Upper limit ($f_{\max}$, blue circles) and lower limit ($f_{\min}$, red squares) of the frequency gap for rightward propagating spin-waves as a function of the applied magnetic field, as deduced from PSWS data such as shown in panel (a).

determined as

$$k(f) = \pm \frac{\phi_{ij}(f) - \phi_0}{D}. \tag{4.7}$$

In this expression, the $\pm$ sign accounts for the change of sign of k upon reversing the direction of spin-wave propagation [+ corresponding to spin-waves travelling from the left antennas ($j = 1$) to the right ones ($i = 2$)], $\phi_0 = \frac{\pi}{2}$ is the reference phase at f_{FMR}, where ΔL_{ij} is purely imaginary (pure absorption), and, more important, $\phi_{ij}(f) = \arg[\Delta L_{ij}(f)] + 2n\pi$ (with n integer) is the spin-wave phase, which must be unwrapped in a continuous manner, starting from f_{FMR}.

The open symbols in Fig. 4.9(b) show the dispersion relation of DE mode 0 reconstructed by applying the above method (Eq. 4.7) to ΔL_{ij} data recorded between 5.8 and 14.5 GHz. As expected, for $k>0$, the dispersion can only be followed up to approximately +7 rad/μm, which corresponds to the lower edge of the frequency plateau. In contrast, for $k<0$, it can be followed down to -12 rad/μm, thus confirming the ability of our PSWS device to probe the expected wave-vector range $[-k_{\max}, +k_{\max}]$. As a support to our conclusions, Figure 4.9(b) also displays in the background the "weighted" dispersion relation computed for a CoFeB(20nm)/Py(26nm) bilayer with the mumax3 software using space and time Fourier transforms of in-plane magnetization traces obtained under square pulse excitation of 10 ps duration. The simulations have been performed by D. Stoeffler. They use elementary cell sizes $h_x = 0.5$ nm, $h_y = 10$ nm, $h_z = 4$ nm and periodic boundary conditions in both longitudinal (z) and transverse (y) in-plane directions, include a realistic spatial distribution for the excitation field produced by the antenna and account for magnetic losses through Gilbert damping

waveguides.

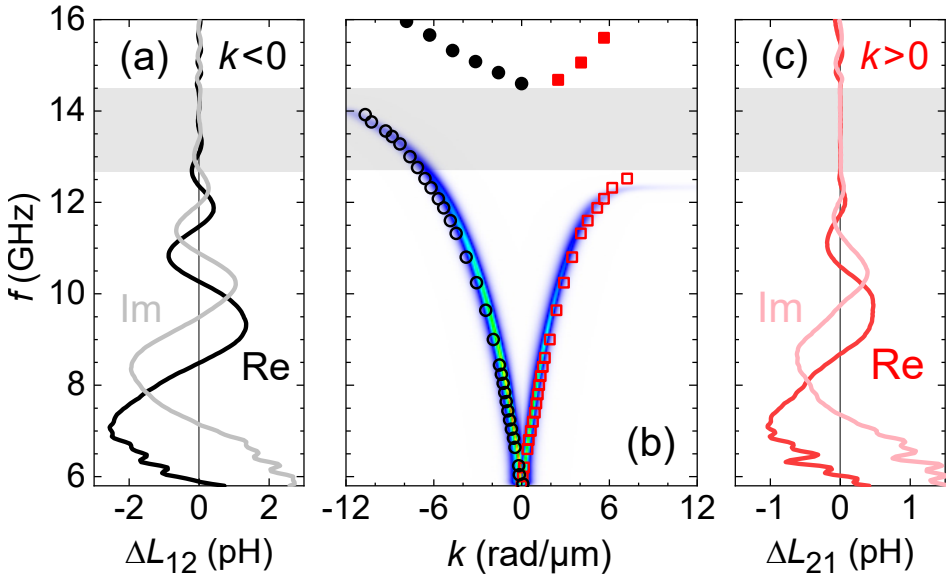

Figure 4.9: Spin-wave propagation in a device with $D = 2$ μm. (a,c) Real and imaginary parts of ΔL_{ij} as a function of frequency for $k < 0$ (a) and $k > 0$ (c). (b) Dispersion relations of the lowest (open symbols) and second lowest (solid symbols) DE branches deduced from the experimental spin-wave signals shown in (a) and (c), and spin-wave spectral weight (color map) as obtained from mumax3 micromagnetic simulations. See text for details.

factors of 0.008 and 0.012 for CoFeB and Py, respectively. A very good agreement between the two kinds of data may be observed, particularly regarding the asymmetric way in which the amplitude of the transmitted spin-wave vanishes upon increasing f. Figure 4.10(b) shows a cross-sectional map of the dynamic magnetization as simulated under continuous-wave excitation at $f = 13$ GHz, which illustrates how this nonreciprocity translates in real space: Once the excitation frequency enters the gap, the dynamic magnetization profile becomes essentially evanescent on the right side of the source as the far-field coupling of the antenna to the magnetic precession vanishes. The same figure, in the panel (a), also shows the the nonreciprocal hybridization outside the gap. The propagation to the left is mostly symmetric, while to the right we can clearly observe the antisymmetric component.

Micro-focus Brillouin Light scattering

To visualize directly the spatial decay of spin-waves, we have performed micro-focus BLS imaging [101] (credit M. Geilen TUK) on a similar device as used for PSWS [Fig. 4.7(a)]. In those experiments, the spin-wave intensity has been mapped next to an antenna while microwave power (-5 dBm) was continuously injected into it. In the DE configuration, switching the direction of the equilibrium magnetization is equivalent to reversing the wave vector $\mathbf{k}$ [102, 103]. Then, instead of looking on both sides of the source for imaging counterpropagating waves, we have concentrated ourselves on one side and recorded spin-wave intensity maps for the two polarities of the transver-

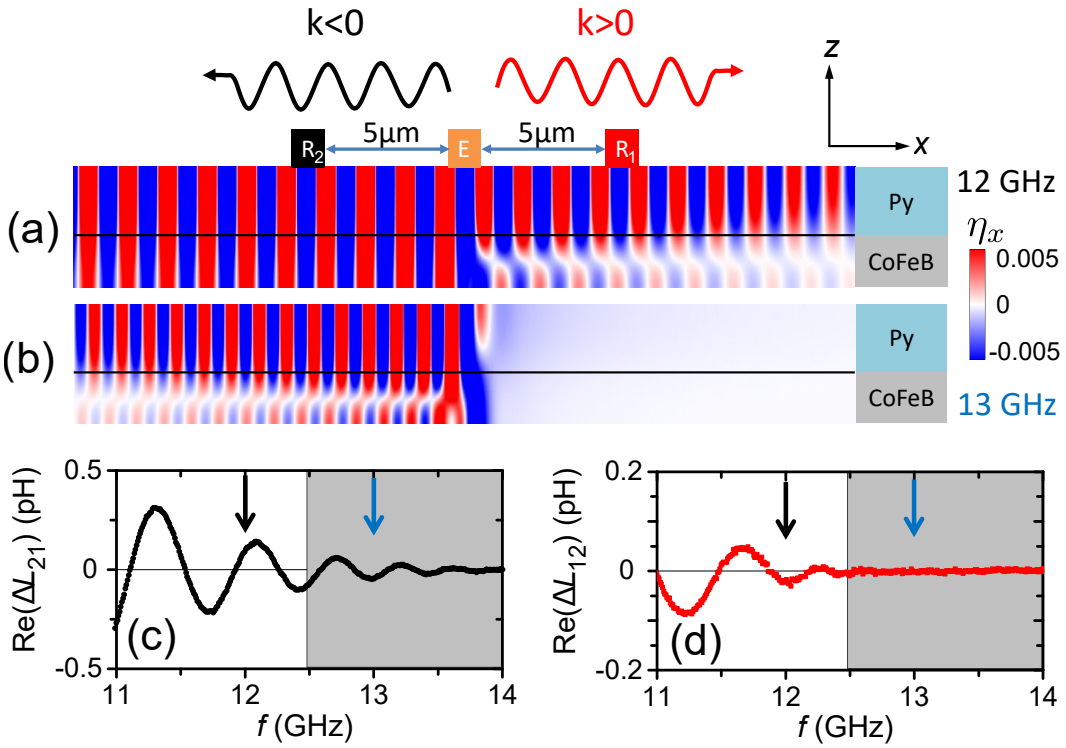

Figure 4.10: MuMax simulations of the spin-wave propagation. Simulated cross-sectional map of the in-plane component of the normalized dynamic magnetization, $\eta_x = m_x/M_S$, for an excitation frequency of 12 GHz (a) and 13GHz (b). Both emitter (E) and receptor (R_1 and R_2) antennas are shown. The AC current assumed in the emitter antenna is 3 mA, which yields an in-plane magnetic field of about 3 mT at the top surface of the bilayer, right beneath the source. The two receptors show where the pick-up of the signal was performed when using the device displayed in Fig. 4.7(a). The experimental data form the spin-wave propagation signal measured by R_1(c) and R_2(d) is shown. The arrows indicate the frequencies at which the simulations were performed.

sally applied magnetic field. Accordingly, the data obtained for $H_0 < 0$ are mirrored horizontally in Fig. 4.11(a,c). The benefit of this experimental strategy is that it allows us probing counterpropagating spin-waves in the very same optical conditions, thus avoiding artifacts related, for instance, to differences in the surface state of the waveguide.

To support these observations, mumax3 simulations have also been performed for a finite, 50 μm-long, 10 μm-wide bilayer strip. The expected BLS signal has been calculated by assuming that it is mostly related to the out-of-plane component of the dynamic magnetization (m_z) at the top surface of the magnetic medium. As in the experiments, spin-waves were excited by an alternating magnetic field with frequency f produced by a 100 nm thick, 200 nm wide antenna, located 120 nm above the spin-wave conduit. For each magnetic cell (with size $h_z = 4$ nm, $h_y = 40$ nm, $h_x = 8$ nm [10]), the time dependence of m_z was recorded over a full period $1/f$, in the steady excitation regime,

[10]Here, the cell size in the transverse (y) direction is larger than the exchange length. However, tests performed using cells 10 times smaller allowed us to check that this does not affect the obtained static configuration.

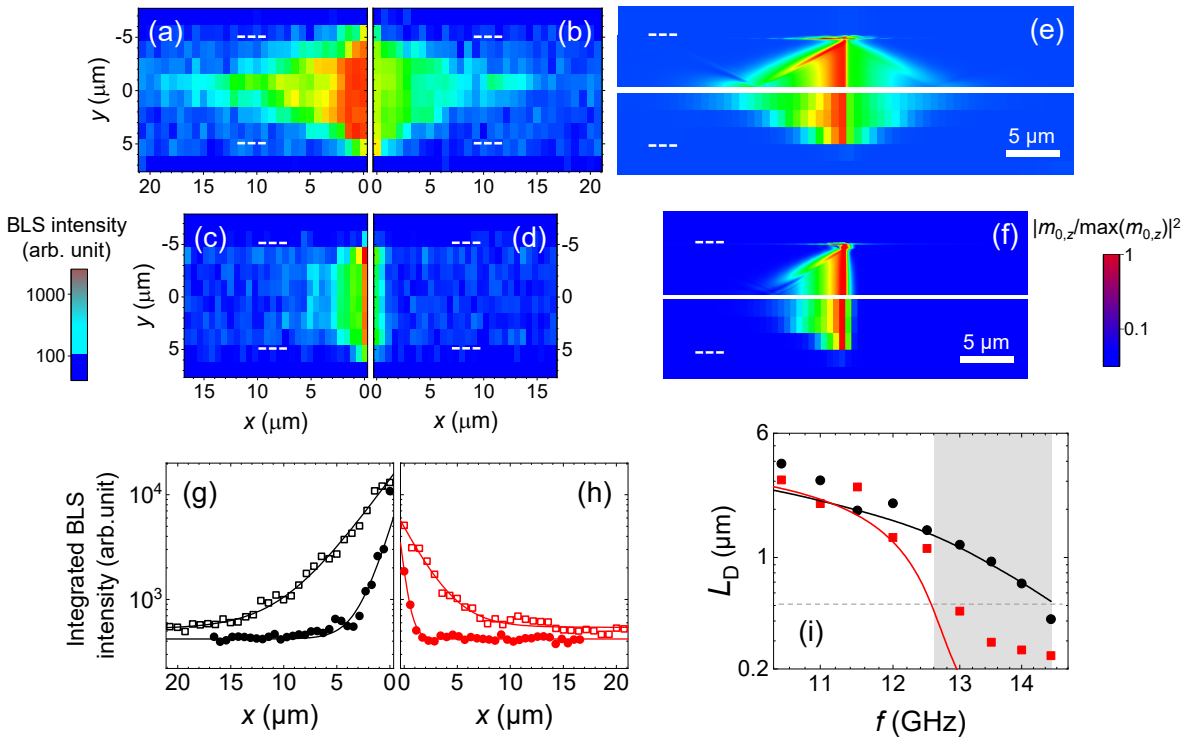

Figure 4.11: (a-d) Experimental BLS intensity maps for excitation frequencies of 11 GHz (a,b) and 13 GHz (c,d) and applied magnetic fields $\mu_0 H_0 = -30$ mT (a,c) and $\mu_0 H_0 = +30$ mT (b,d) (logarithmic scale). The dashed lines indicate the position of the waveguide edges. (e,f) Computed BLS intensity maps for $f = 11$ GHz (e) and $f = 13$ GHz (f), $\mu_0 H_0 = +30$ mT. The current assumed in the antenna is 0.1 mA (linear regime). In each panel, the upper part shows raw data whereas the lower part shows pixelated data obtained by averaging raw data over $1.6\,\mu\text{m} \times 0.8\,\mu\text{m}$ rectangular areas. See text for further details. (g,h) y-profiles of the BLS intensity integrated over the width of the waveguide as deduced from the maps shown in panels (a-d). Open and solid symbols correspond to $f = 11$ GHz and $f = 13$ GHz, respectively. The lines are fits of the experimental data to the expression $I(x) = I_0 \exp(-x/L_D) + I_{\text{Noise}}$. (i) Variation of the decay length of the spin-wave intensity, L_D, with the excitation frequency f for spin-waves propagating to the right ($H_0 > 0$, red) and to the left ($H_0 < 0$, black). The symbols and the solid lines are data derived from experiments and simulations, respectively. The horizontal dashed line indicates the smallest spin-wave wavelength compatible with the chosen antenna design.

and analyzed to extract its maximum value $m_{0,z}$. Finally, normalized intensity maps were constructed, which show $|m_{0,z}/\max(m_{0,z})|^2$, either with the full resolution of the simulations [top panels in Fig. 4.11(e,f)] or with a degraded resolution mimicking that of micro-focussed BLS images [bottom panels in Fig. 4.11(e,f)]. Overall, a good agreement is obtained between experimental and computed images, assuming damping values of 0.008 and 0.012 for CoFeB and Py, respectively. Quite naturally, upon pixelation, sharp features, like those related to localized edge modes, tend to be washed out. Yet, we note that for $f = 11$ GHz, a long oblique contrast arising from the interference between the fundamental and higher-order width modes of the waveguide remain discernible [Fig. 4.11(a,e)].

Expectedly, for frequencies in the range 6-12 GHz (i.e. below the frequency plateau), significant spin-wave intensity is systematically detected up to distances of several mi-

crometers from the antenna [Fig. 4.11(a,b,e)]. We note that although plateau-related spin-wave filtering is not yet active, a difference in intensity may be observed between the two directions of propagation. This is nothing but the usual amplitude nonreciprocity described in Section 4.2. When the frequency reaches 13 GHz (above the frequency plateau), on the other hand, the spin-wave intensity remains relatively large for one direction of propagation [Fig. 4.11(c,f)] but drops abruptly for the opposite one [Fig. 4.11(d,f)]. Based on the discussion above, we naturally attribute this fast drop in intensity to the phenomenon of spin-wave slow-down associated with the presence of a plateau in the positive-k part of the dispersion relation of DE mode 0.

This phenomenon is best illustrated by extracting the spin-wave decay length L_{D} from the BLS data. For this, one may average the spin-wave intensity over the width of the waveguide (i.e. along y) to mitigate finite-width effects, plot the integrated intensity as a function of the space coordinate along the direction of propagation, x, and fit this dependence to an exponential decay of the form $I(x) = I_0 \exp(-x/L_{\mathrm{D}}) + I_{\mathrm{Noise}}$ [see Fig. 4.11(g,h)]. Figure 4.11(i) shows the variation of L_{D} with f obtained treating both experimental and numerical data in this manner. A clear difference in behavior may be observed depending on the sign of k. For spin-waves travelling to the left ($k<0$, black circles and line), L_{D} decreases steadily with increasing f. For spin-waves travelling to the right ($k>0$, red squares and line), in contrast, this steady decay is interrupted by a sudden drop in L_{D} as f reaches the frequency of the plateau, f_p. Beyond f_p, L_{D} becomes smaller than the minimum spin-wave wavelength $2\pi/k_{\mathrm{max}} \simeq 0.5$ μm attainable with our single-wire antenna. This reveals the evanescent character of the magnetization dynamics induced when the frequency falls into the effective gap, also evidenced in the micromagnetic simulation of Fig. 4.9(b).

4.5 Spin-wave modal profiles

For completion, we present examples of spin-waves eigenmodes [Fig. 4.12] obtained as solutions to the CoFeB(20nm)/Py(26nm) bilayer problem, using the SWIIM numerical method [15]. The magnetic parameters are the same as those used to calculate the dispersion relation of Fig.4.6(d) and the modal profiles discussed here are those for $|k| = 20$ rad/μm. We start by considering only $|\boldsymbol{\eta}|$, that is, the amplitude of the oscillating magnetization normalized to M_{S} [Fig. 4.12(a,b)]. Two important conclusions can be drawn from these data.

i) First, the mode with the lowest frequency, DE0, has maximum amplitude at the top surface for both directions of propagation [see red lines in panels (a) and (b)]. This is different from the behavior of DE modes in thicker films ($l > 100$nm), where leftward and rightward travelling spin-waves are confined near opposite surfaces [104]. This clearly shows that one cannot relate directly the frequency nonreciprocity that

we observe to a preferential localization of counterpropagating spin-waves in the two different materials which constitute the bilayer.

ii) Second, for $k > 0$, the second lowest frequency mode, DE1, always has a small amplitude near the top surface of the film. This amplitude reaches virtually zero for $k \sim +20$ rad/μm [see blue line in Fig. 4.12(a)]. This explains why the anti-Stokes peak corresponding to DE1 is globally much weaker than its Stokes counterpart [Fig.4.6(a-c)] and why, as mentioned in Sec. 4.4.1, it hardly becomes discernible for k in the range $17 - 25$ rad/μm.

If instead of looking at mode amplitudes, we now consider the in-plane (η_x) and out-of plane (η_z) components of the variable magnetization separately, as is done in [Fig. 4.12(c)] for mode DE0 with $k < 0$, the hybrid character of this mode appears very clearly: the modal profile contains both a uniform (non-zero-average, S_0-like) contribution and an antisymmetric (cosine, S_1-like) contribution. Noticeably, the relative weights of these contributions are not the same for the two components, which translates into nodes located at different depths for η_x and η_z. This justifies the need for using a set of four vectors (as opposed to a set of only two vectors) as a basis for the dynamic matrix model developed in Sec. 4.3.

4.6 Chapter conclusion

A new concept of spin-wave diode is proposed, which makes use of the particular dynamic dipolar interactions in the DE configuration. The device is made from a thin film consisting of two exchange-coupled layers with different saturation magnetization values. Our theoretical analysis reveals that, in such a film, chiral dipolar couplings develop, which results in nonreciprocal hybridization. Using this phenomenon, we engineer carefully the dispersion of surface waves to reduce the group velocity of waves traveling in a particular direction to a very low value (slow waves) while maintaining a large value for those propagating the other way.

These results are experimentally verified by combining PSWS with thermal-k-resolved-BLS and micro-focus BLS. The three techniques verify that the spin-wave modes excited by a source of finite size take the form of propagating waves in the forward direction of the diode and reduce to evanescent waves in the reverse one. In addition, we have validated the phase unwrapping method to obtain the spin-wave dispersion relation from the PSWS experiments. This technique has been used in the millimeter-scale [105], but up to our knowledge, this work represents its first implementation at the nanometer-scale.

This spin-wave diode is quite versatile as its operational frequency window can be adjusted by tuning the amplitude of the applied magnetic field. Moreover, the forward and reverse directions can be interchanged by switching the polarity of the field. In

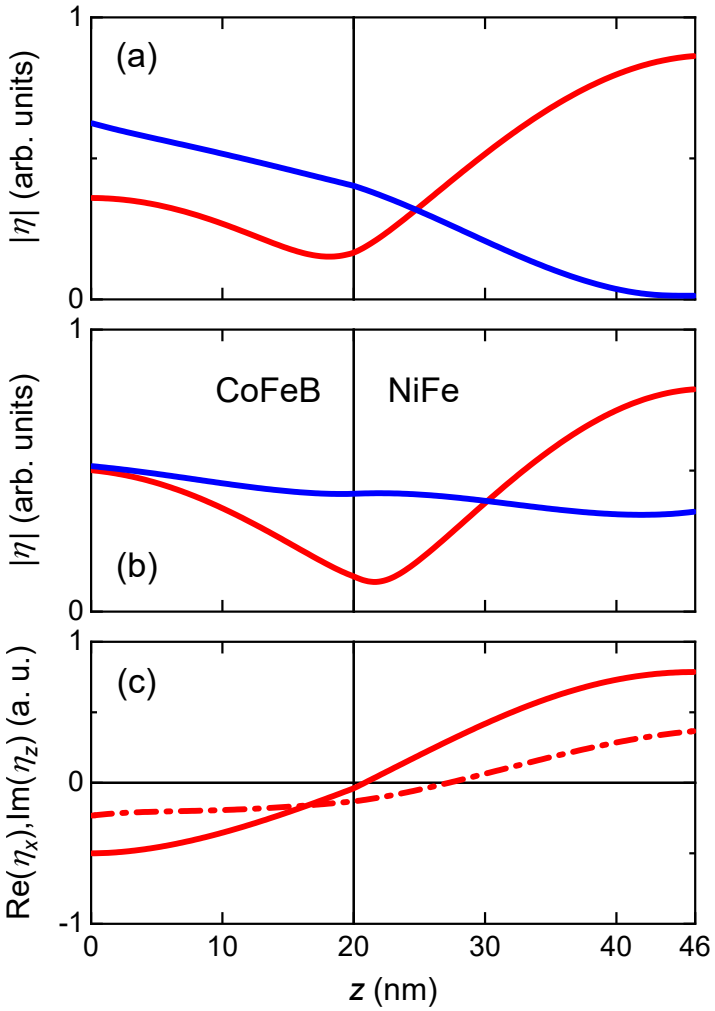

Figure 4.12: Depth profiles of modes DE0 and DE1 in the CoFeB(20nm)/Py(26nm) bilayer stack as computed using the SWIIM numerical method ($\mu_0 H_0 = +30$ mT). (a,b) Amplitude of the dynamic magnetization normalized to M_S versus vertical coordinate z, for $k = +20$ rad/μm (a) and $k = -20$ rad/μm (b). Red (resp. blue) lines correspond to DE0 (resp. DE1). (c) In-plane (solid line) and out-of-plane (dash-dotted line) components of the reduced dynamic magnetization in mode DE0 as a function of the vertical coordinate z, for $k = -20$ rad/μm.

addition, engineering of unidirectionally slow spin waves could also prove useful in more general situations where long interaction times are needed within a limited space, for instance, for promoting nonreciprocal nonlinear coupling in the channel of a magnonic transistor [11].

Chapter 5

Statics and dynamics of magnetic stripe domains

The present chapter presents a study of the dynamics of the stripe domains that were introduced in Section 1.3. We show how their spin-wave spectrum can be interpreted as an extension of the Damon-Eshbach (DE) spectrum of the saturated state, but adapted to the symmetry breaking occurring at nucleation. In order to compare these theories with experimental data, we have studied these modes in CoFeB ferromagnetic films, which present weak stripe domains at low magnetic field.

First, we will present a characterization of the CoFeB samples, allowing one to determine the values of the relevant magnetic parameters. Later, the static properties of the stripes —amplitude and period— will be theoretically described by including fourth-order terms in the energy-calculations for the stray-free ansatz, described by Expression 1.22. By doing so, we arrive at an elementary description of the stripes in terms of a complex order parameter and an energy potential having the shape of a "Mexican hat" (Ginzburg-Landau-type theory). This description of the statics allows one to predict the apparition of two different dynamic modes: a zero-frequency Goldstone-mode which corresponds to the rigid translation of the stripe system; and an amplitude precession mode, which can be identified as a Higgs-mode.

We also show how the Kalinikos-Slavin method can be adapted to describe the evolution of the fundamental spin-wave mode upon approaching stripe nucleation, and the emergence of the Higgs mode. Finally, by means of BLS and FMR measurements, we observe the softening of the DE mode, and we measure the frequency of the Higgs mode.

5.1 Sample fabrication and characterization

A suitable material for studying the dynamics of stripes domains should have a sufficiently strong PMA while presenting a low damping α, as a big damping would prevent the detection of low-frequency dynamics. Unfortunately, such magnetic material is not easy to obtain; normally, a strong PMA requires an important interaction of the magnetization with the molecular or atomic orbitals of the material, and this is usually accompanied by a large damping. Therefore, we have chosen to work with samples presenting a weak PMA ($Q \to 0$). As a consequence, in order to allow the stripe nucleation, the thickness of the sample must be quite large. With these restrictions, we have chosen to work with $Co_{40}Fe_{40}B_{20}$. Despite its amorphous structure, it presents an uniaxial-OOP anisotropy, probably from magnetostrictive origin [40, 106, 107].

5.1.1 VSM and MFM

The $Co_{40}Fe_{40}B_{20}$ sample was grown by M. Hehn at IJL using magnetron sputtering. Intrinsic silicon substrates were used, together with a buffer layer of Ta of 3 nm and a capping layer of Pt of 5 nm. The static magnetic properties of these films were characterized in detail in the framework of the PhD work of K. Ait-Oukaci (dir. D. Lacour and M. Hehn) using magnetometry (mostly VSM) and magnetic imaging (MFM and STXM) [14, 40]. To summarize the findings of this work, a sizable PMA can be inferred from the presence of stripes, which were observed for thicknesses over 126 nm by MFM, as shown in Fig. 5.1(b). Vibrating sample magnetometry (VSM) measurements display the typical signature of stripe-domains (see Fig. 5.1(a)): M_y decreases linearly and reversibly under the stripe nucleation field H_c [108, 109]. A magnetization reversal of the cores can be observed at a lower field (the coercive is $\mu_0 H_{\text{coe}} = 2.8$ mT in the example shown). It is possible to observe that this reversal implies an abrupt change in M_y, as expected from a first-order phase transition. Finally, the saturation magnetization, $M_S = 1331$ kA/m ($\mu_0 M_S = 1.67$ T), was determined as an average of several VSM, PPMS-VSM and SQUIID-VSM measurements.

Some measurements were performed within a period of few weeks from the film deposition (including the VSM and MFM measurements described above and the transverse FMR measurements described below). Nevertheless, other measurements were done in the last months of this PhD work, which is at least one year later (including the MOKE, BLS and longitudinal FMR measurements described below). From these measurements, it has been observed that the nucleation field decreases from $\mu_0 H_c = 17.5$ mT to 12 mT. This behavior was observed in several samples of CoFeB 180nm which were stored at room temperature but in different rooms. Given the high mobility of boron it is possible that it has migrated, rearranging the amorphous struc-

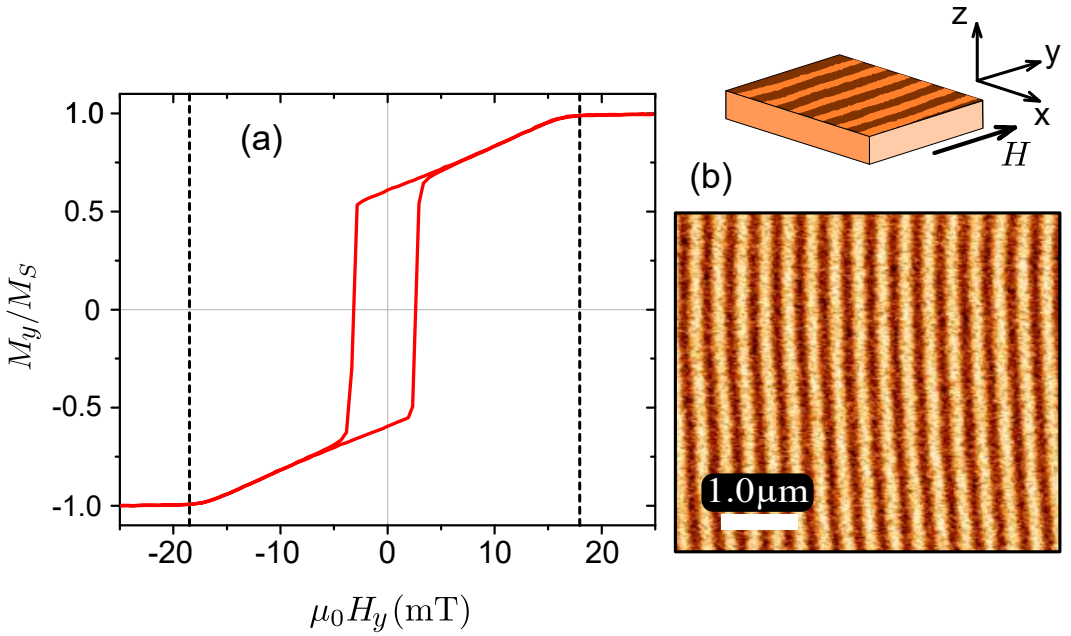

Figure 5.1: (a) VSM measurements showing the hysteresis cycle of a $Co_{40}Fe_{40}B_{20}$ film of a thickness of 180 nm. The nucleation field is indicated by the dashed lines at $\mu_0 H_c = \pm 17.5$ mT. (b) MFM image taken at remanence on the same sample [40].

ture, and in consequence, changing the value of K_1 and Q. Figure 5.2(a) shows the change of the VSM hysteresis cycle for two samples. While one was measured immediately before its deposition (new), the other was measured two years later (old). In the following, we shall therefore use reduced values of PMA for measurements carried out long after film deposition

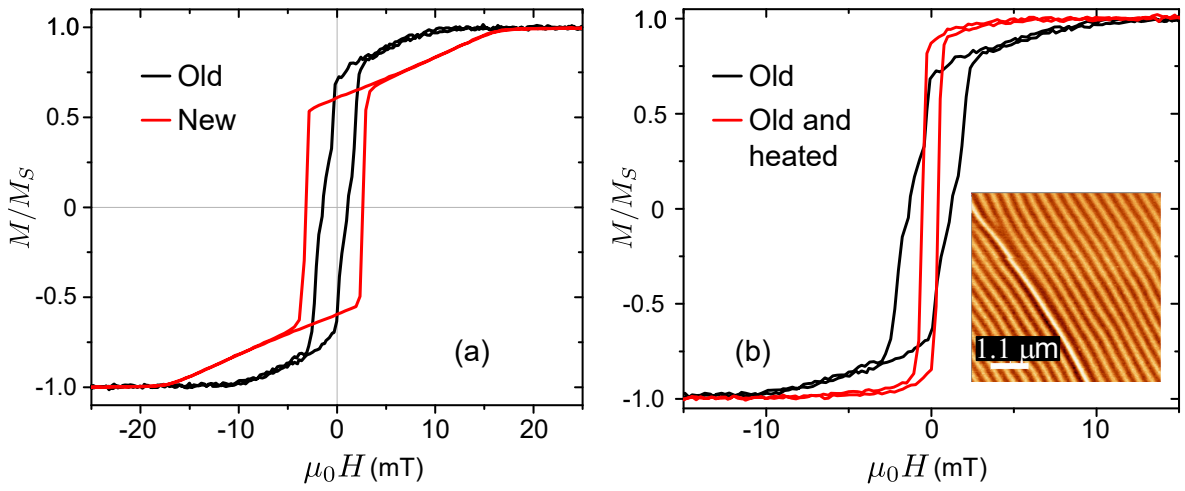

Figure 5.2: VSM measurements on aged and annealed CoFeB films. (a) Both CoFeB-180nm samples had the same properties at after the deposition. While the *new* sample was measured shortly after deposition, the hysteresis loop of the *old* sample was measured two years after deposition. Coercive fields are 2.85 mT (new) and 1.4 mT (old). (b) The hysteresis cycle also changes if the sample is heated at 180°. The inset shows that, after the thermal process the stripe domains are still found at remanence, although with a reduced contrast. The brighter domain could show a wall separating landau IP domains. This image was taken at IPCMS with the help of H. Majjad.

VSM measurements have also evidenced a change of the magnetic properties of $Co_{40}Fe_{40}B_{20}$ with the temperature. In particular, a baking at 180°C for 90s repeated two times produces a decrease of the nucleation field H_c, as shown in Fig 5.2(b). However, the stripe structure at remanence observed by MFM implies that K_1 is big enough to keep $H_c > 0$. A similar behavior which was already identified in CoFeB [110] and in another amorphous compound, $Co_{89-x}Fe_xZr_{11}$ [109]. We believe this is the main reason why we could not observe any clear signature of stripe domains in PSWS and microfocus-BLS measurements, because of the relatively large temperature applied during the lithography process required for producing devices adapted to these measurement techniques.

5.1.2 Kerr microscopy

Kerr microscopy measurements were performed on $Co_{40}Fe_{40}B_{20}$ films with $t = 150$ nm and $t = 180$ nm. These measurements were performed with the set-up mounted by S. Cherifi and counting with her help. For both thicknesses, it was observed that the core reversal process is dominated by the motion of domain walls, which separate zones where the magnetization of the cores has opposite directions. If the IP anisotropy is null, the domain wall must be aligned with the core magnetization and the external applied field. However, as Fig. 5.3(c) shows, this is not the general case, as for some IP angles the observed domain wall was not aligned with the applied field $\boldsymbol{H}$.

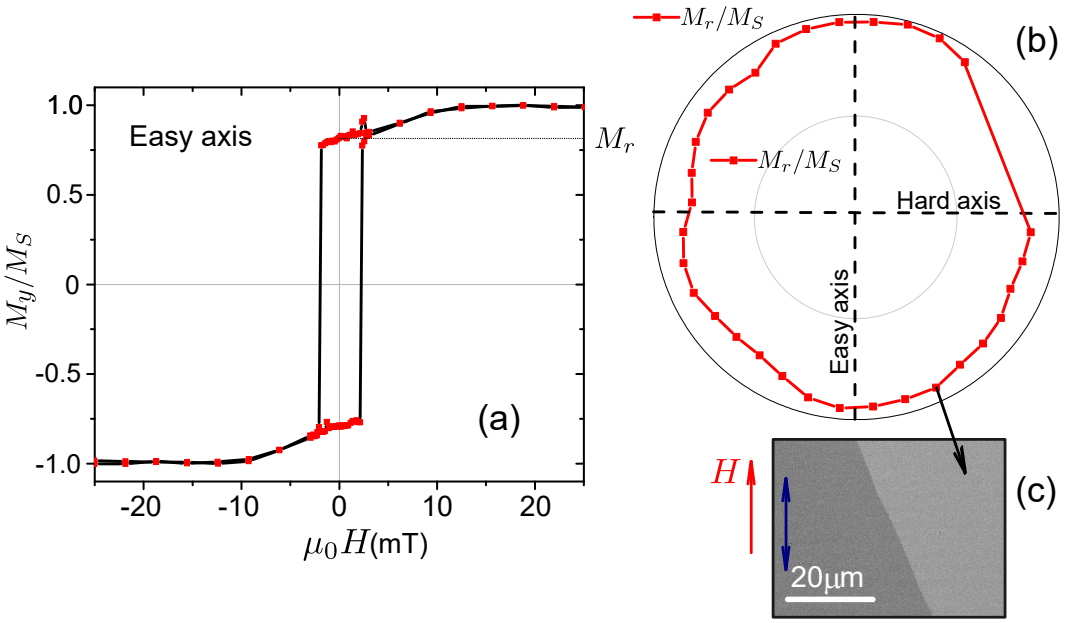

Figure 5.3: (a) Longitudinal-Kerr integrated-intensity as function of the IP applied magnetic field. (b) The variation of M_r/M_S with the applied field angle is shown in the polar plot. (c) Kerr-microscope image obtained at the coercive field for an IP intermediate angle. All the measurements were performed in a full-plane sample —without any lithography or etching.

In order to determine the IP anisotropy, the hysteresis cycle of M_y at the surface was

measured by integrating the intensity of the recorded images for different applied fields. The results obtained for the sample with $t = 180$ nm are shown in Fig. 5.3. We have observed that there was some dependence of the hysteresis loop as function of the IP angle of the applied field. This is summarized in the polar plot of Figure 5.3(b), where the angular dependence of the normalized remanence magnetization M_r is shown. From the variation of M_r with the angle, we conclude that some IP anisotropy is present. The hysteresis loop corresponding to the easiest IP direction is shown in Fig. 5.3(a). In it, it is possible to identify the nucleation field at $\mu_0 H = 12.5(1)$ mT, and the reversible linear decrease of M_{sur} as function of H at low field.

The Kerr measurements done for CoFeB 150nm show a larger IP anisotropy, which affects significantly the magnetic state at remanence. These measurements are shown in Appendix B. From these measurements, we have chosen to focus our studies on the sample with $t = 180$ nm as the IP anisotropy affects less the stripe properties. Also, it presents a larger saturation field, assuring a broader range of magnetic field where the stripe behavior can be studied. When possible, measurements have been done with the external field applied parallel to the IP easy axis, in order to avoid extra complications.

5.1.3 Transverse FMR

In order to obtain the magnetic parameters of $Co_{40}Fe_{40}B_{20}$ 180nm (in particular the gyromagnetic ratio and the exchange constant), we have performed FMR measurements using our broadband set-up (see Section 3.1) in the standard mode; which is under a magnetic field strong enough to saturate the sample, and in the transverse pumping geometry (excitation field $\boldsymbol{h}$ perpendicular to the applied field $\boldsymbol{H}$).

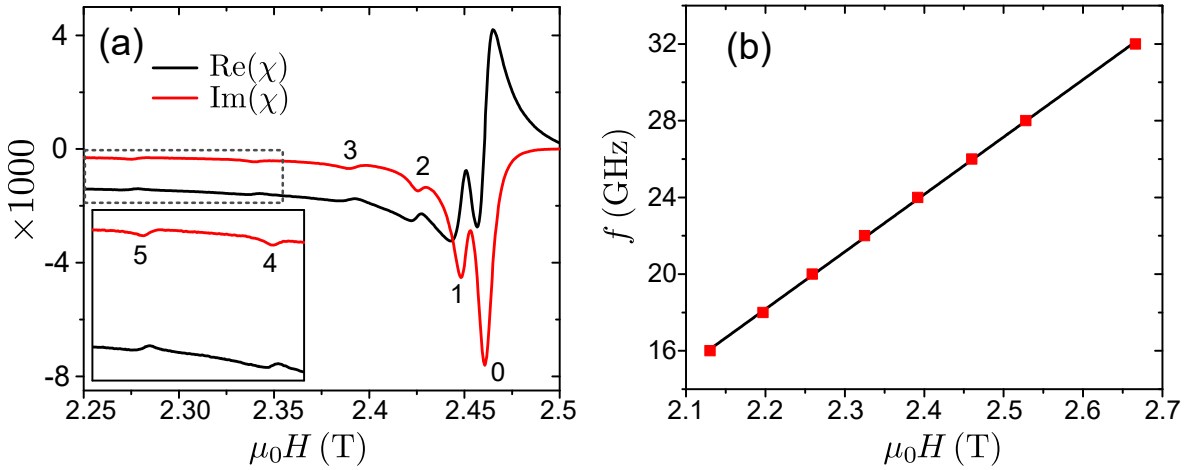

Figure 5.4: OOP-FMR-spectroscopy measurements. (a) Imaginary and real parts of the effective susceptibility at f =26 GHz as function of the OOP applied field H. The numbers correspond to the perpendicular wave vector κ_n. The inset shows the detail of the smaller peaks at low field. (b) Position of the minimum of the imaginary part extracted from field-scans for different frequencies. This minimum corresponds to $\kappa_n = \kappa_0$, the biggest amplitude peak in panel (a).

In the OOP configuration, in which $\boldsymbol{H}$ is along the film normal, magnetization is saturated if $\mu_0 H_S^{\perp} \geq 2$ T. In this magnetic field range, the FMR-resonance frequency is given by Eq. 2.14. At a given frequency, several additional peaks of resonances are found, as shown in Fig. 5.4(a). They correspond to the perpendicular standing spin-wave modes with different κ_n, determined from Eq. 2.33. For the higher frequencies as many as six peaks could be identified, allowing a precise determination of the surface anisotropy K_s and the exchange constant A_{ex}, as explained in Appendix C. The fit shown in Fig. 5.4(b) and Eq. 2.14 allows to determine the PMA K_1, and the gyromagnetic ratio γ. Therefore, the values of the measured parameters are:

- $\mu_0 M_{\text{eff}} = 1.59(2)\,\text{T} \rightarrow K_1 = 50(15)\text{kJ/m}^3 \rightarrow Q = 0.04(2)$
- $A_{\text{ex}} = 16.6(1)\,\text{pJ/m}$.
- $K_s = 0.18(3)\,\text{mJ/m}^2$
- $\dfrac{\gamma}{2\pi} = 29.9(2)\text{GHz}$

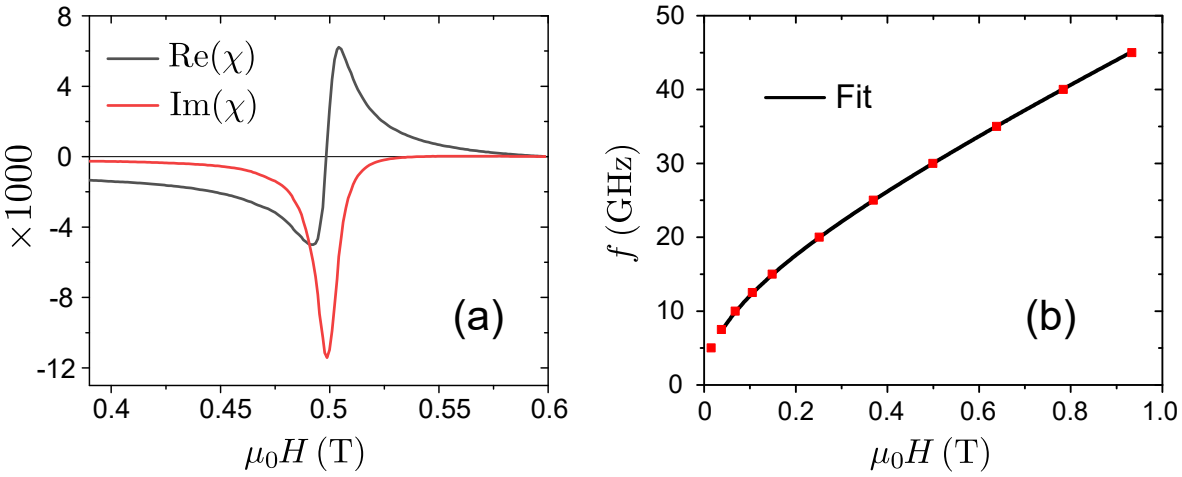

Figure 5.5: IP FMR spectroscopy measurements. (b) Example of a field scan for an excitation frequency $f = 30$ GHz. (c) Position of the minimum of the imaginary part extracted from field-scans as a function of the frequency. The fit was performed with the points corresponding to the saturated state using Eq. 2.13.

The error in Q is quite large, but it remains consistent with $Q = 0.036$, the expected value from the nucleation field $\mu_0 H_c = 17.5$ mT (see Fig. 5.1) and Eq. 1.31. This anisotropy value also determines that the minimum thickness which allows stripe nucleation is $t_{\text{min}} = 127$ nm, which agrees with the MFM measurements. The fit of the IP line-width as a function of H gives $\alpha = 5\,10^{-3}$ and $\Delta H_0 = 1.6(4)$ mT[1]

The results for the IP configuration ($\boldsymbol{m}$ oriented in the film plane) are shown in Fig. 5.5.

[1]Note that in our broadband measurement mode, this inhomogeneous broadening is primarily due to the finite width of the coplanar waveguide used.

From the IP-FMR fit a different gyromagnetic constant is obtained. In this case $\gamma/2\pi = 28.9(2)$ GHz/T. This difference could be explained from an anisotropic gyromagnetic factor. For the fits and calculations of this work, we will take $\gamma/2\pi = 29.0$ GHz/T, as it is consistent with BLS measurements that will be shown in the next sections.

5.2 Stripe amplitude

In Section 1.3.1 a certain ansatz of stripe domains was proposed, and its energy cost was determined. For $Q \to 0$, the stray-free ansatz proves to be a realistic approximation, allowing the calculation of the nucleation field H_c. At the critical condition, when $H = H_c$, the second derivative of the energy is zero. If the applied magnetic field continues to decrease, this derivative becomes negative, implying an amplitude divergence. However, the stripe amplitude A remains finite if higher-order terms in the energy are included in the calculation.

Using the same notation as in Section 1.3, the total stripe energy density, including the fourth-order terms, can be written as

$$\frac{2}{\mu_0 M_S^2}\langle E_T\rangle = 2\,h + a(h,\,k)A^2 + b(h,\,k)A^4 + \mathcal{O}(A^6). \tag{5.1}$$

The coefficient $a(h,\,k)$ vanishes at the reduced nucleation field h_c and becomes negative at smaller fields. On the other hand, the coefficient $b(h,\,k)$ remains positive for all fields. It includes the fourth-order terms from the exchange and Zeeman interactions. These terms are a consequence of the fixed norm of the magnetization $|\boldsymbol{M}| = M_S$. This constrain imposes a relation between the three components of $\boldsymbol{M}$, and determines the value of M_y, which, at fourth-order can be expressed as

$$M_y = M_s\sqrt{1 - m_x^2 - m_z^2} \approx M_S\left(1 - \frac{1}{2}\left(m_x^2 + m_z^2\right) - \frac{1}{8}\left(m_x^4 + 2\,m_x^2 m_z^2 + m_z^4\right)\right). \tag{5.2}$$

From here we can define the normalized longitudinal deviation from saturation as $m_y = M_y/M_S - 1$. Thus, the fourth-order energy terms are calculated as[2]

$$b(h,\,k^2)A^4 = \Lambda^2\left\langle(\vec{\nabla}m_y)^2\right\rangle + 2\,\frac{h}{8}\left\langle m_x^4 + 2\,m_x^2\,m_z^2 + m_z^4\right\rangle \tag{5.3}$$

This expression can be modified to include a nonzero second-order anisotropy. In our case, the fits done on the FMR data from CoFeB are compatible with $K_2 = 0$, and micromagnetic analysis on the hysteresis loop also suggest this parameter is null [13]. Therefore, these terms are not explicitly written, but they can be found in Appendix A.

[2] $(\vec{\nabla}m_y)^2$ expresses a short notation for the operation shown in Eq. 1.7.

The explicit calculation of the average values is also developed in Appendix A. Following these calculations, a and b parameters of Eq. 5.1 read

$$a(h,k) = -Q\left(\frac{k}{2\,\kappa}\right)^2 + \frac{\Lambda^2}{4}\left[2\,k^2 + \kappa^2 + \left(\frac{k^2}{\kappa}\right)^2\right] + h\,\frac{1}{4}\left[1 + \left(\frac{k}{\kappa}\right)^2\right]; \tag{5.4}$$

$$b(h,k) = \frac{\Lambda^2}{64}\left(k^2 + \frac{k^4}{\kappa^2} + 3\,\frac{k^6}{\kappa^4} + 3\,\kappa^2\right) + \frac{h}{256}\left[9\left(1 + \frac{k^4}{\kappa^4}\right) + \frac{2\,k^2}{\kappa^2}\right]. \tag{5.5}$$

These calculations define an energy landscape that depends on several parameters. As h and κ are imposed, minimization of the energy gives the equilibrium values of A and k, that will be named A_e and k_e. For fields higher than H_c, the minimum is trivially located at $A = 0$. When decreasing the value of the applied magnetic field, A_e becomes finite. Differentiating Eq. 5.1 with respect to A, one obtains $2\,aA + 4\,bA^3 = 0$, which results in

$$A_e(h,\,k_e) = \sqrt{\frac{-a(h,\,k_e)}{2\,b(h,\,k_e)}}. \tag{5.6}$$

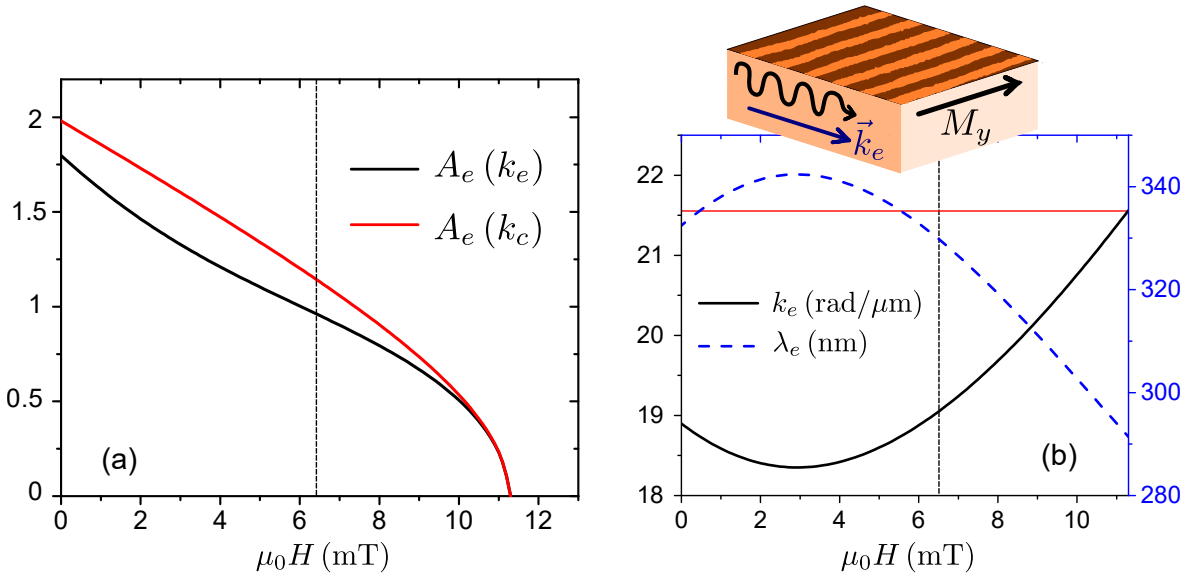

Figure 5.6: (a) Equilibrium stripe amplitude A_e as function of the applied field H. (b) Equilibrium wave vector and wavelength of the stripes versus the applied field. The red line shows the value of k_c. The vertical black line in (a) and (b) shown the minimum applied field at which the ansatz is valid. On the top, the direction of $\boldsymbol{k}_e$ with respect to an MFM image is shown. The parameters used are: $M_S = 1331$ kA/m ($\mu_0\,M_S = 1.67$ T), $\Lambda = 3.85$ nm ($A = 16.5$ pJ/m), $t = 180$ nm and $Q = 0.03$ ($K_1 = 33.4$ kJ/m^3).

The equilibrium amplitude A_e depends on k_e. Therefore, we must first find the equilibrium value of k for each magnetic field. In the general case, k_e can be found from[3]

$$\left.\frac{\partial\,\langle E_T\rangle}{\partial k}\right|_{k_e} = 0. \tag{5.7}$$

[3]This derivative can also be performed as function of k^2, simplifying the calculations.

The two former equations have a mutual dependence, i.e. $A_e(k_e)$ and $k_e(A_e)$, leading to an equation system that is not solvable analytically. Nevertheless, this system can be solved easily with numerical methods. The obtained results are shown in Fig. 5.6.

Exactly at nucleation, the value k_e coincides with k_c, as expected. However, when decreasing the magnetic field, $k_e \neq k_c$. Thus, the period of the stripe system is not fixed but varies slightly with H. Near the nucleation, the same tendency was observed in MFM measurements done by K. Ait-Oukaci [40][4]. The value obtained for A_e is shown in Fig. 5.6(a). This figure also shows the value for A_e under the approximation $k_e = k_c$. We notice that near the nucleation field, the exact and approximated solution do not differ significantly.

Finally, we can calculate $\langle E_T \rangle (h)$ as a function of A. For that, the calculated $k_e(h)$ is substituted in Eq. 5.1. The results are shown in Fig. 5.7. We can observe that energy adopts the shape of the well-known Ginzburg–Landau-theory potential. As expected, under the nucleation field H_c, the energy minimum is localized at $A_e \neq 0$.

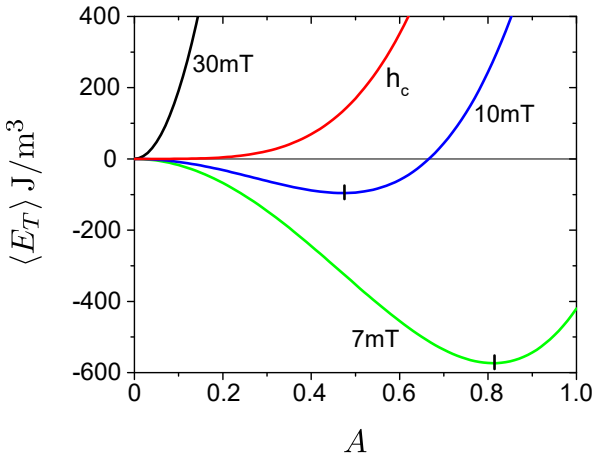

Figure 5.7: One-period averaged energy as a function of A for different values of $\mu_0 H$ at $k = k_e$. At $\mu_0 H_c = 11.8$ mT the second derivative vanishes. At lower fields, the minimum is found at $A_e \neq 0$, as indicated by the black dash. Same magnetic parameters as in Fig. 5.6.

Substituting k_e and A_e in the stray-free ansatz (expressions 1.22) gives the magnetization profile as a function of the applied magnetic field. A clear limitation to our approach appears when any component of the magnetization exceeds M_S. In our case, $m_z > m_x$, and this limit is expressed as

$$m_z = A_e(h)\frac{2\,k_e(h)}{\kappa} < 1. \tag{5.8}$$

For the parameters of CoFeB 180nm, the field range where this approach is valid is $\mu_0 H > 6.5$mT. To explore lower fields, an extension of the theory would be needed,

[4]We must note that fourth-order terms play a crucial role to perform this calculation under nucleation. If they are omitted, $k_e = k_c$ is a monotonically increasing function of h.

for example, by introducing a suitable Lagrange multiplier, but this is left for future work.

5.3 Stripe-dynamics theory

From the description of the statics, it is clear that the wave vector related with the critical behavior is k_c. In order to understand the dynamics of the system before and after the nucleation, we will study the dispersion relation of spin waves in CoFeB 180nm, focusing our attention on the range around k_c.

5.3.1 Dynamic approach to the nucleation

As mentioned in Section 2.3.1, the PMA in the DE configuration reduces the resonance frequency of the uniform magnetic modes when k is increased. As a consequence, the group velocity becomes negative like in the BV case. Nevertheless, an important difference can be noticed between these two configurations: in the BV configuration the dynamic magnetic flux can never be closed and the dipolar field always produces some torque, leading to a non-null frequency. On the contrary, in the DE configuration with PMA, the dynamic magnetic flux can be closed, even in the limit of $Q \to 0$. In this case, in the magnetostatic approximation, the frequency could be zero for a certain wave vector k.

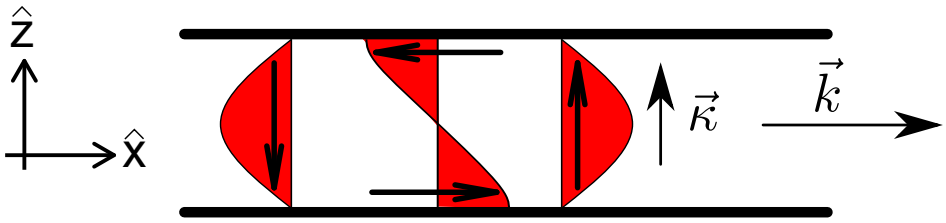

Figure 5.8: Distribution of the dynamic magnetization corresponding to the eigenvalue $\boldsymbol{\eta} = (1, 0, 0, i)^T$ in the sine-cosine basis.

To include the exchange in this magnetostatic picture, the dispersion relation at $H > H_c$ in the DE configuration should be calculated using the Kalinikos-Slavin (KS) approach already used in this manuscript. Nevertheless, the thickness profile basis used there (uniform and antisymetric modes) is not suitable to characterize the stripes. We expect that at k_c the mode profile coincides with the static ansatz proposed in the energy-minimization approach. Consequently, we have used the "sine-cosine" basis:

$$\{S(z)\hat{x},\, S(z)\hat{z},\, C(z)\hat{x},\, C(z)\hat{z}\}, \tag{5.9}$$

with $S(z) = \sqrt{\frac{2}{t}}\sin(\kappa\, z)$ and $C(z) = \sqrt{\frac{2}{t}}\cos(\kappa\, z)$. We can observe that the first and last elements of the basis can combine in a closed-flux configuration, as shown

in Fig. 5.8. As a notation, we will name the combination of these two elements A-component because it coincides with the static ansatz, whose amplitude is given by the parameter A. The other two elements ($S(z)\hat{x}$ and $C(z)\hat{z}$) can not close the magnetic flux and are forced to create magnetic charges. We will name their combination T-component (from transversal)[5]. We must note that, individually, these two components cannot form precession modes —in contrast with the uniform and antisymmetric components of Section 2.3.1, (S_{0x}, S_{0z}) and (S_{1x}, S_{1z}), respectively— as they combine functions with a different symmetry.

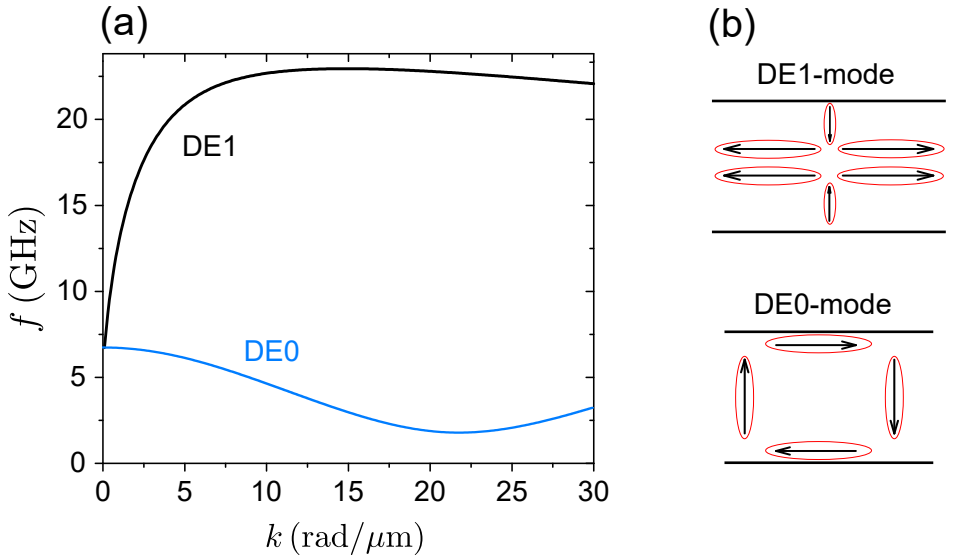

Figure 5.9: (a) CoFeB 180nm spin-wave dispersion relation in the Damon-Eshbach configuration calculated with the KS approach at $\mu_0 H = 15$ mT $> \mu_0 H_c$. (b) The precession ellipses of the dynamic magnetization of the two modes are shown. The arrows show the dynamic magnetization distribution at a given time. While DE0 closes the magnetic flux at $k = k_c$, DE1 produces surface magnetic charges and oscillates with a higher frequency.

This change of basis affects the expression of the dynamic matrix found in the introduction, but the procedures to perform the calculations reviewed in the Section 2.3.2 remain valid. Details on this calculation can be found in Appendix D.

By solving analytically the corresponding eigenvalue problem, the dispersion relation of the two modes is calculated, as shown in Fig. 5.9(a). An analysis of the resulting eigenvectors shows that the DE0-mode is mainly composed of A-components, and in the DE1-mode, the T-components are predominant. However, to build a true precession mode, both DE0- and DE1-modes present also small T- and A-components, respectively. From the energy minimization calculations, we already know that the dipolar energy, if not brought to zero by suitable flux closure, is by far the largest among the different contributions. As the T-components are associated with nonzero charges, these components increase significantly the frequency of the modes.

If the applied magnetic field is reduced, the DE0-mode at k_c becomes softer. At

[5]The naming of these components will become clearer in next section.

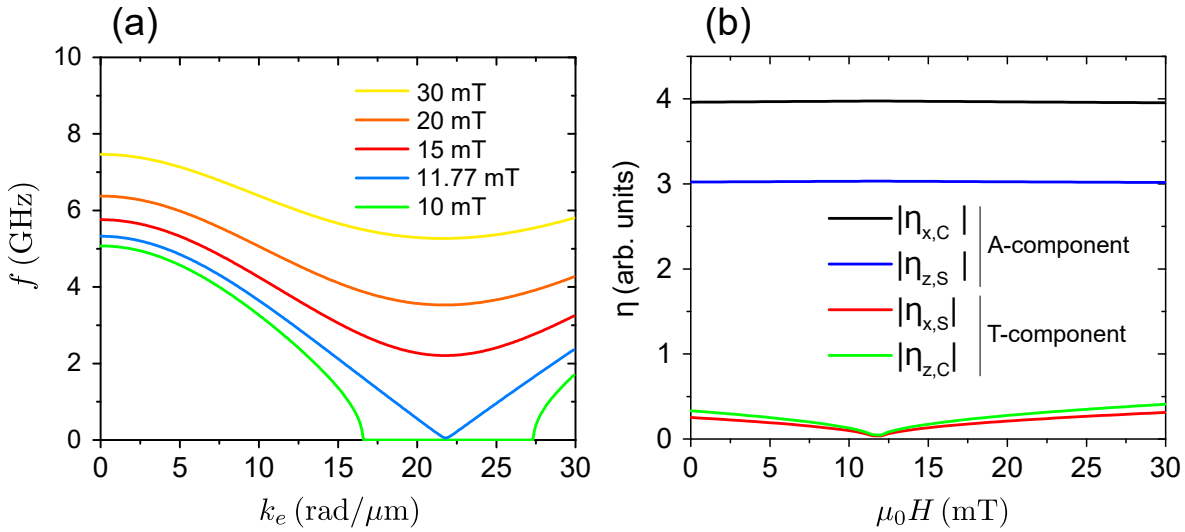

Figure 5.10: (a) DE0-mode dispersion for different applied magnetic fields. When decreasing the field, the mode becomes soft for $k = k_c \approx 22$ rad/μm. At $\mu_0 H_c = 11.77$ mT, $f(k_c) = 0$ and stripes nucleate. (b) Components of the eigenvector obtained in the KS approach for the DE0 at $k = k_e(h)$.

the nucleation field H_c its frequency vanishes, giving rise to the stripe nucleation. These results are shown in Fig. 5.10(a). From an intuitive point of view, we can think the stripes as "frozen" spin-waves with a wave vector defined by the minimum of the dispersion. From Fig. 5.10(b), we see that the T-components of the DE0 mode vanish at nucleation. Therefore, near nucleation, we expect the dynamic mode to be linearly polarized, becoming a pure amplitude mode to be identified to the static ansatz used in the energy approach.

This way of calculating the nucleation of stripes is a natural extension of solving the LL equation with the zero-torque condition. The softening of spin-waves was also invoked to explain domain nucleation in ferromagnetic Co-bars, where the size effects substitute the PMA [111], and in transversely magnetized strips [112]. Quite generally, domain structure nucleation is usually accompanied by the occurrence of soft spin-wave modes at the critical point [113]. In this work, we will proceed one step further and consider the dynamics of the stripes, once they are nucleated. For this purpose, we will combine our understanding of the statics of stripe domains and that of the dynamics of saturated PMA films. In particular, we shall use the following "side-product" of our Kalinikos-Slavin calculation.

If $H < H_c$, the DE0 modes with a wave vector near k_c present a calculated frequency which is totally imaginary, as shown in Fig. 5.11. This can be interpreted as the amplitude-divergence obtained when only the first order terms of the total energy are considered: in the absence of higher-order terms (not considered in the linearized dipole-exchange spin-wave theory), the dynamic magnetization would grow exponentially. The exponential growth rate is to be identified with the imaginary part of the

angular frequency. In the next pages we will give a precise interpretation to the maximum of this imaginary frequency, but before that, let us come back to our energy approach.

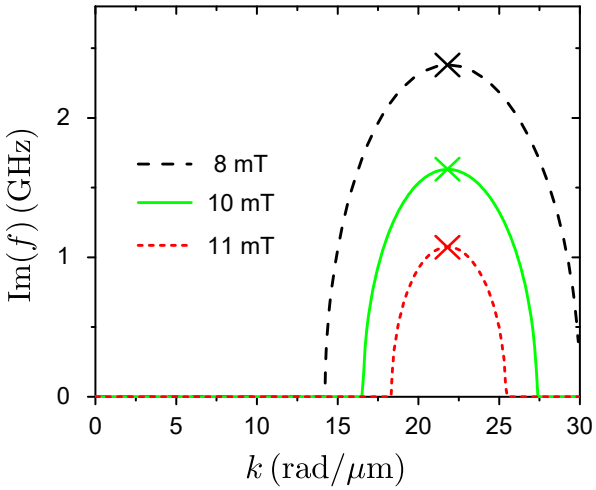

Figure 5.11: Imaginary part of the frequency for magnetic field values under H_c. The wave vector of the maximum of these imaginary parts coincides with that of the minimum of the real parts of the frequencies above saturation, which is $k = 22$ rad/μm (see Fig. 5.9).

5.3.2 Stripe modes

Magnetic stripe nucleation is a second-order phase transition, which is accompanied by a spontaneous symmetry-breaking when the stripe phase ϕ takes a defined value ϕ_e[6]. Above nucleation, this phase is not defined. The global phase of the stripe system can be physically represented as a position: a change of ϕ_e rigidly moves the stripes in the direction of their wave vector.

The stripe texture is completely defined by the combination of this static phase and the amplitude A. In other words, it is described by a complex scalar order-parameter $\psi = A\,e^{i\phi}$ which defines a U(1) symmetry-group. In this parameter space, the energy density defines a "Mexican hat" potential, as shown by Fig. 5.12. This energy does not depend on the phase, thus phase-oscillations are Goldstone modes[7]. On the other hand, amplitude oscillations define a so-called Higgs mode. Both Goldstone and Higgs modes appear in all systems that present a broken U(1) symmetry. They were firstly described in the context of particle physics [115, 116], but they are also relevant in

[6]For the definition of this phase, see Expression 1.22.

[7]In general, for each broken continuous symmetry a gapless (Goldstone) mode develops. For example, the solid crystal violates translational and rotational invariance, and possesses phonons; liquid helium violates (in a certain sense only) gauge invariance, and possesses a longitudinal phonon; ferro-magnetism violates spin rotation symmetry, and possesses spin waves; superconductivity violates gauge invariance, and would have a zero-mass collective mode in the absence of long-range Coulomb forces [114].

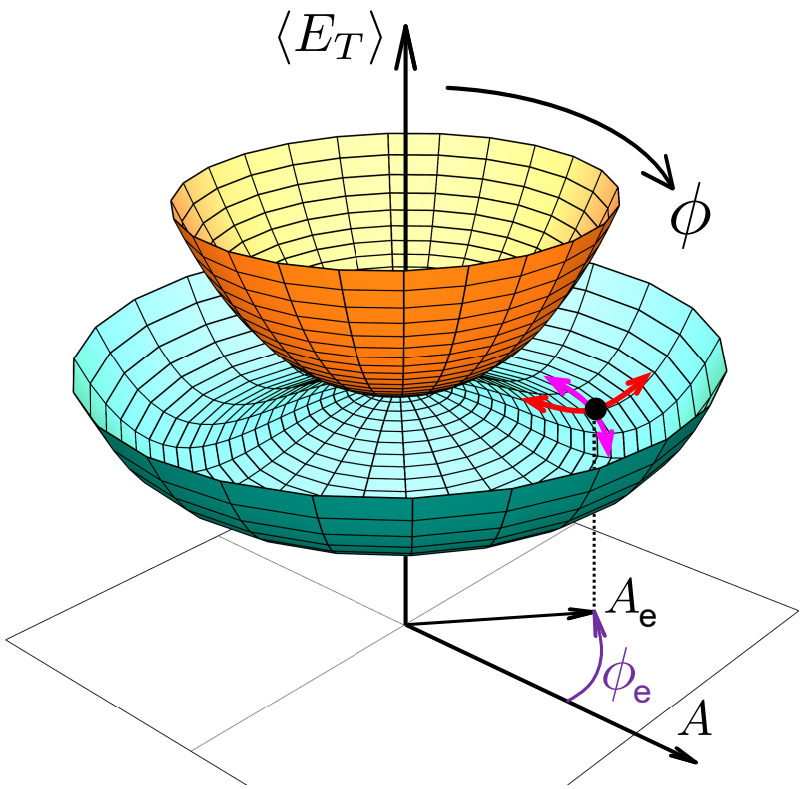

Figure 5.12: Total energy surfaces of the system at $H > H_c$ (yellow) and at $H < H_c$ (blue) in the space defined by the amplitude parameter A and the global phase ϕ. The system position is represented by the black dot, located in the minimum $A = A_e$ at an arbitrary phase ϕ_e. The Goldstone and Higgs modes of the stripe systems are indicated by the magenta and red arrows, respectively.

condensed-matter studies [117]. They can be found in superconductors [118], Bose-Einstein condensates [119], phonons in structural-phase transitions [120] and magnetic systems [121, 122], among others.

In order to visualize the Golstone and Higgs modes, we can introduce the amplitude and phase perturbations, ΔA and $\Delta\phi$, in the static ansatz $\boldsymbol{m}$ defined in Expression 1.22. The normalized dynamic magnetization of the Higgs and Goldstone modes is obtained from the difference $\Delta\boldsymbol{m}^H = \boldsymbol{m}(A_e) - \boldsymbol{m}(A_e + \Delta A)$ and $\Delta\boldsymbol{m}^G = \boldsymbol{m}(\phi_e) - \boldsymbol{m}(\phi_e + \Delta\phi)$, respectively. For small perturbations, these expressions coincide with the derivatives with respect to A and ϕ. Therefore, the components of the dynamic magnetization of the Higgs mode are

$$\begin{aligned} \Delta m_x^H &= \Delta A \sin(k_e\, x) \sin(\kappa\, z)\,, \\ \Delta m_z^H &= \Delta A \frac{k_e}{\kappa} \cos(k_e\, x) \cos(\kappa\, z)\,, \end{aligned} \tag{5.10}$$

while for the Goldstone mode they read

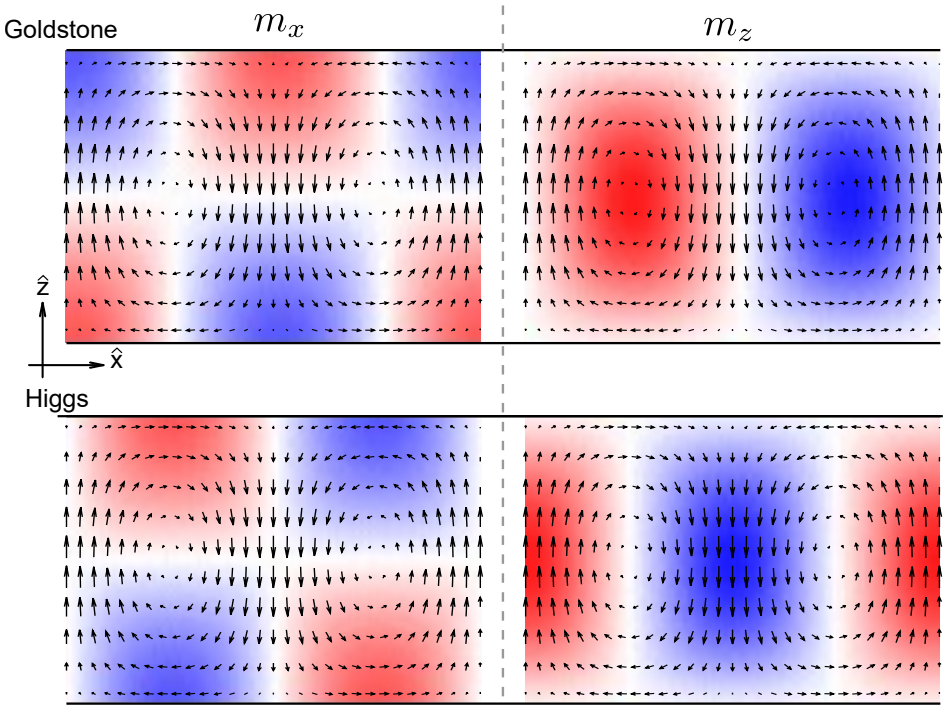

Figure 5.13: The color scale (red positive, blue negative, white zero) show the value of the dynamic components of the magnetization corresponding to the Goldstone and Higgs modes at $k = k_c$. The black arrows depict the static stripe magnetization distribution. For both modes, the components are shown at the moment of the precession when they have maximal amplitude. Thus, the T-components of the Higgs mode are not shown.

$$\begin{aligned} \Delta m_x^G &= \Delta\phi\, A_e\, \cos(k_e\, x) \sin\left(\kappa\, z\right), \\ \Delta m_z^G &= -\Delta\phi\, A_e\, \frac{k_e}{\kappa}\, \sin(k_e\, x) \cos\left(\kappa\, z\right). \end{aligned} \tag{5.11}$$

Figure 5.13 shows, in color, the calculated dynamic components of the two modes. While the Higgs mode is in phase with the background stripe structure shown by the arrows, the Golstone mode presents a $\pi/2$ phase shift in the x direction. Consequently, Δm_z^G is maximum at the stripe cores, while the maximum of Δm_x^G is localized in between the Néel caps.

Higgs mode frequency

The mode described in Eq. 5.10 is linearly polarized, and therefore, its frequency should be zero. However, we know that the Higgs-mode frequency is not zero, as it is related to the radial second derivative of the energy in the minimum (see Figs. 5.7 and 5.12). This apparent paradox can be solved by introducing another degree of freedom allowing the magnetization to precess. For this purpose, we define a local system of coordinates (see Fig. 5.14). We set A as the local amplitude coordinate (in red), which is parallel to the direction defined by the static magnetization of stripes (in black), and T as the

local transverse coordinate (in blue). These two coordinates are the extension of the A- and T-components of 5.9 once the symmetry-breaking defines the static phase ϕ_e.

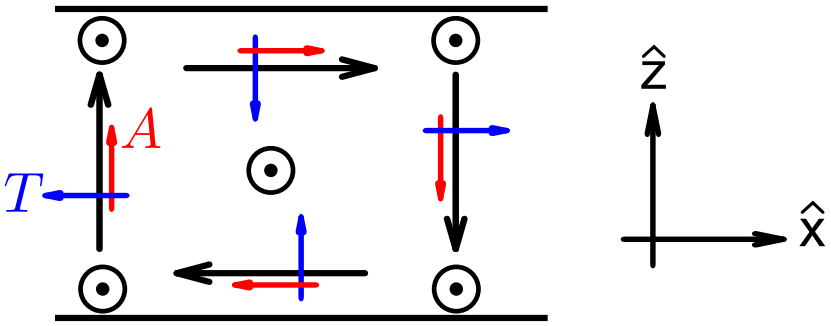

Figure 5.14: Local frame of reference defined by the stripes. In each point of the stripe profile an orthogonal set of coordinates is defined. A-direction is parallel to the magnetization direction in the xz plane, while T-direction is perpendicular to it.

In the $A-T$ space, in the same way the frequencies are calculated in the saturated state, the frequency of the Higgs mode is given by a Kittel formula which reads $\omega_{\text{Higgs}} \propto \sqrt{K_A^H\, K_T^H}$. Here, $K_A^H = \frac{\partial^2 \langle E_T \rangle}{\partial A^2}$ is the stiffness related to a motion of the magnetization distribution in the A-direction and K_T^H is the same in the T-direction.

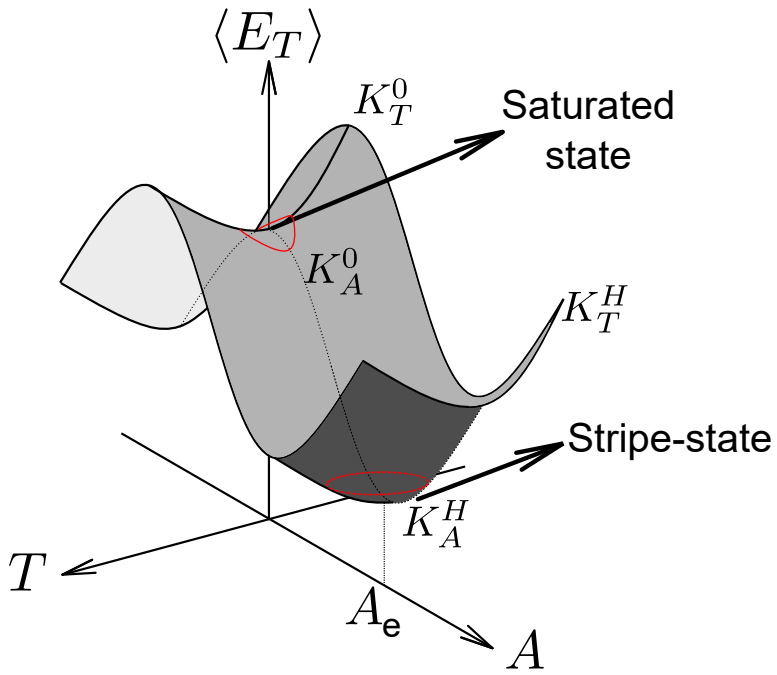

Figure 5.15: Schematic potential in the $A-T$ space. The KS approach is able of calculating the "oscillation" frequency around $A = T = 0$ (saturated state). When the stripes are nucleated, the saturated state becomes unstable and the minimum is displaced to A_e. The precession associated to the Higgs mode is depicted by the red oval. The Hessian at this point defines the Higgs frequency. For visualization reasons, A and T coordinates are not at scale, as the T-curvature must be much larger.

A schematic view of the energy potential in the $A-T$ space is presented in Fig. 5.15. At $H < H_c$, two regions can be identified: the saturated state at $A = T = 0$, which is unstable below the nucleation field; and the stable stripe-state in the energy minimum

at $A = A_e$, $T = 0$. The calculations done in the KS approach are performed in the saturated state, and the calculated imaginary frequency can also be related to a Kittel formula, $\omega_{\mathrm{DE0}}(k_c) \propto \sqrt{K_A^0\, K_T^0}$, where the index 0 designates the point $A = T = 0$. We will proceed to demonstrate that the stiffnesses in the (unstable) saturated state ($K_{A,T}^0$) and in the (stable) stripe state ($K_{A,T}^H$) are related. As explained in Section 5.3.1, excursions of the magnetization distribution along the T-direction induce significant magnetostatic charges which translate into a high-demagnetizing energy cost, much larger than the other contributions to the energy. As a consequence, the stiffness along the T-direction is much larger that the one along the A-direction and it does not depend on the exact state around which the excursions occur. In other terms, $K_T^H \approx K_T^0 >> K_A^{H,0}$.

As far as the K_A are concerned, we can derive them directly from the Landau-type expansion of the energy Eq. 5.1, inserting the value of the stripe amplitude of Eq. 5.6. Doing so, they read

$$\begin{aligned} K_A^0 &= \left.\frac{\partial^2 \langle E_T \rangle}{\partial A^2}\right|_0 = 2\,a, \\ K_A^H &= \left.\frac{\partial^2 \langle E_T \rangle}{\partial A^2}\right|_{\sqrt{\frac{-a}{2b}}} = 2\,a + 12\,b\left(\sqrt{\frac{-a}{2\,b}}\right)^2 = -4\,a. \end{aligned} \tag{5.12}$$

From here, we obtain $K_A^H = -2\,K_A^0$. In conclusion, the Higgs-mode frequency can be calculated from the KS approach as

$$\omega_{\mathrm{Higgs}} = i\,\sqrt{2}\,\omega_{DE0}(k_c). \tag{5.13}$$

This relation is valid in the same range where the energy approach holds. It is limited by the saturation of the OOP magnetization component. For the case of CoFeB 180nm, this limit imposes 6.5mT $< \mu_0 H < \mu_0 H_c$.

5.3.3 Mode splitting and phase

The KS approach can also help to understand the splitting of one single mode around k_c for $H > H_c$ into two separate modes for $H < H_c$: Higgs and Goldstone modes.

In general, at saturation ($H > H_c$), the dynamic magnetization can be written in the sine-cosine basis as

$$\boldsymbol{m} \propto \left(\eta_{x,S}\,S(z)\hat{x} + \eta_{z,S}\,S(z)\hat{z} + \eta_{x,C}\,C(z)\hat{x} + \eta_{z,C}\,C(z)\hat{z}\right)\; e^{i(kx-\omega t+\phi)}, \tag{5.14}$$

with ϕ a global phase determined by the initial conditions of the system. However, in absence of external excitation, ϕ is not determined. We can represent the four-

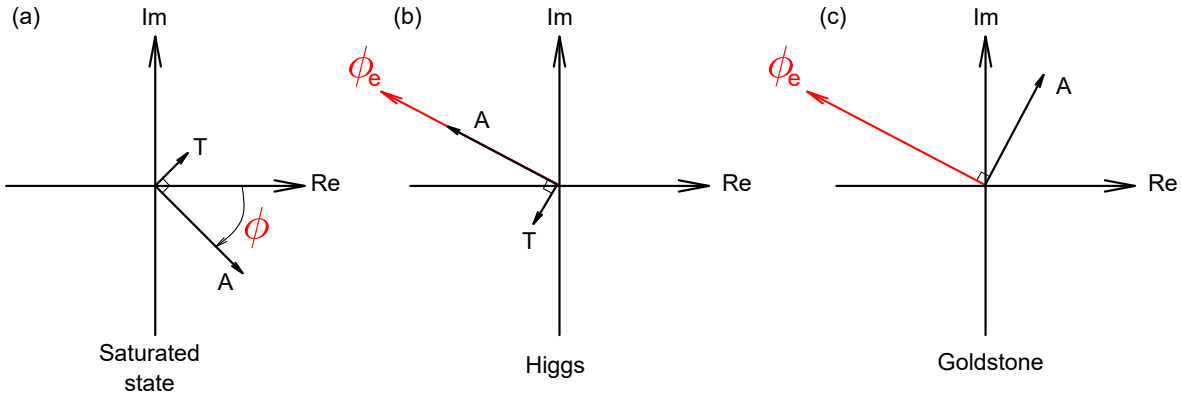

Figure 5.16: Representation of the eigenvectors of the DE0 modes with at $k = k_c$ in the KS approach. (a) At saturation A- and T-components vectors are dephased by $\pi/2$, but the global phase ϕ is not defined. At nucleation, the spontaneous symmetry-break defines a global phase ϕ_e. Two combinations are possible, (b) the A-components are in phase with ϕ leading to a Higgs mode, and (c) the A-components are at $\pi/2$ from ϕ_e in the Goldstone mode. As the Goldstone frequency is zero, the magnetization displacements follows the A-direction and the T-components magnitude vanish.

element vector $\boldsymbol{\eta}$ in a two-dimensional space by defining the A-component $\eta_{x,C} + \eta_{z,S}$ and the T-component $\eta_{z,C} + \eta_{x,C}$. As $\eta_{x,S}$, $\eta_{x,C}$ are in quadrature with respect to $\eta_{z,S}$, $\eta_{z,C}$, the vector can be represented in a complex plane, as shown in Fig 5.16(a).

At nucleation, the spontaneous symmetry-breaking fixes the global phase of the DE0-mode in a particular value ϕ_e, as shown in Figs. 5.16(b,c). Therefore, two possible configurations of high-symmetry arise. If A-components are aligned with ϕ_e, we obtain a Higgs mode[8]. On the other hand, if the A-components have a relative phase of $\pi/2$ with respect to ϕ_e, then the Goldstone mode is obtained. Therefore, it is the spontaneous symmetry-break which introduces a global phase creating two modes that emerge from a single one with an arbitrary global phase at saturation.

5.4 Stripe-dynamics measurements

In the last section we have developed several hypotheses regarding the magnetic stripe domains:

- Stripe nucleation is given by the softening of a spin-wave mode in the DE configuration.
- At nucleation this soft mode splits in two: a Goldstone/phase- and a Higgs/amplitude-mode.
- Higgs-mode frequency can be calculated within the KS approach.

[8]The Higgs mode has small but non-zero T components, which can be viewed as inertial terms arising from its non-zero freqeuncy.

To verify these hypothesis, we have performed BLS and FMR measurements on the aged-CoFeB 180nm sample.

5.4.1 k-resolved BLS

Thermal-k-resolved-BLS, does not require any thermal treatment that would damage temperature sensitive properties of the CoFeB 180nm film. Therefore, it is an ideal tool to measure the spin-wave dispersion of this film. The experiments presented in this section were performed at TUK by M. Geilen and P. Pirro.

We must notice that CoFeB behaves as a metal, and it has two important consequences. First, a high thermal-conductivity is expected, which, in addition to the large thickness of the sample, should dissipate the heat from the laser, preventing a local temperature increase and the consequent anisotropy variations. Secondly, skin depth in metallic samples is restrained to tens of nanometers. Therefore, photons interact mainly with the superficial components of the magnetization, which are mostly IP.

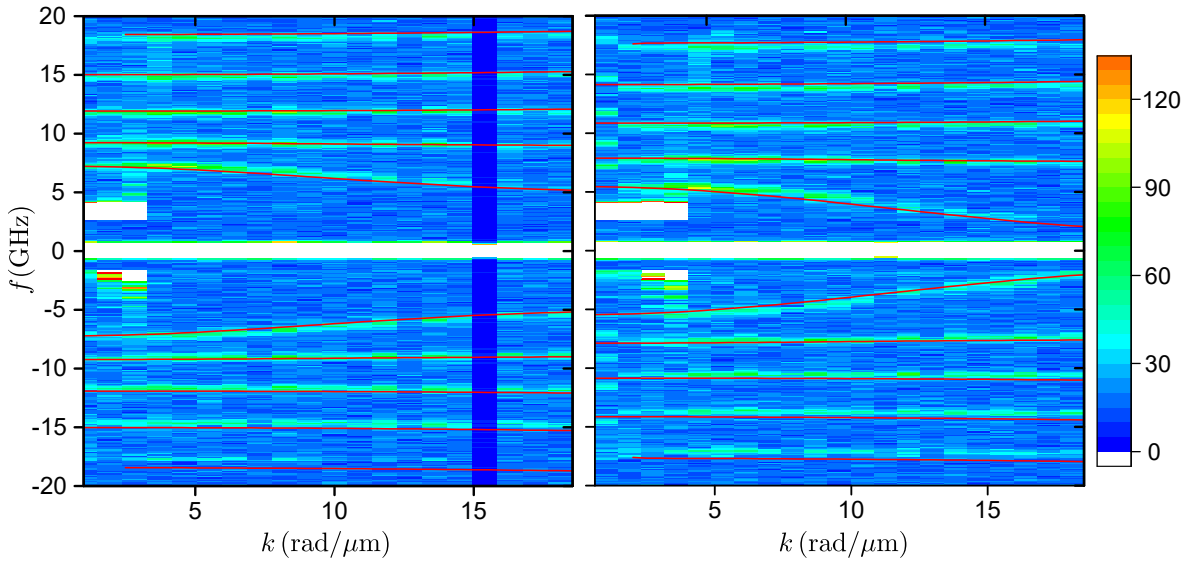

Figure 5.17: k-resolved-BLS spectra obtained at 30 mT (left) and 14 mT (right). The color scale indicates the number of BLS counts. The red lines show the dispersion relation of modes DE0, DE1, DE2, DE3, DE4 and DE5 calculated with SWIIM. CoFeB magnetic parameters were used to perform the simulation, using $K_1 = 32.7$ kJ/m^3.

To investigate the spin-wave dispersion in the saturated state, constant-field BLS measurements were performed while varying the laser incidence angle, and therefore the excited spin-wave wave vector. A laser with a wavelength $\lambda = 532$ nm (green) and a power of 200 mW was used. Figure 5.17 shows the results at $\mu_0 H = 30$ mT and 14 mT. At these fields the magnetization is saturated and several perpendicular standing spin-wave modes can be distinguished. The lowest frequency branch of the dispersion corresponds to DE0. It presents the negative slope expected from a sample with PMA. The minima at $k = 22$ rad/μm is out of scope, but we can extrapolate easily

that it comes closer to $f = 0$ as H approaches the nucleation field. In order to simulate these results, SWIIM simulations were performed using the CoFeB parameters. The large basis that is used in this simulation allows to obtain all the high-frequency modes. The simulation results show a good agreement with the experimental data.

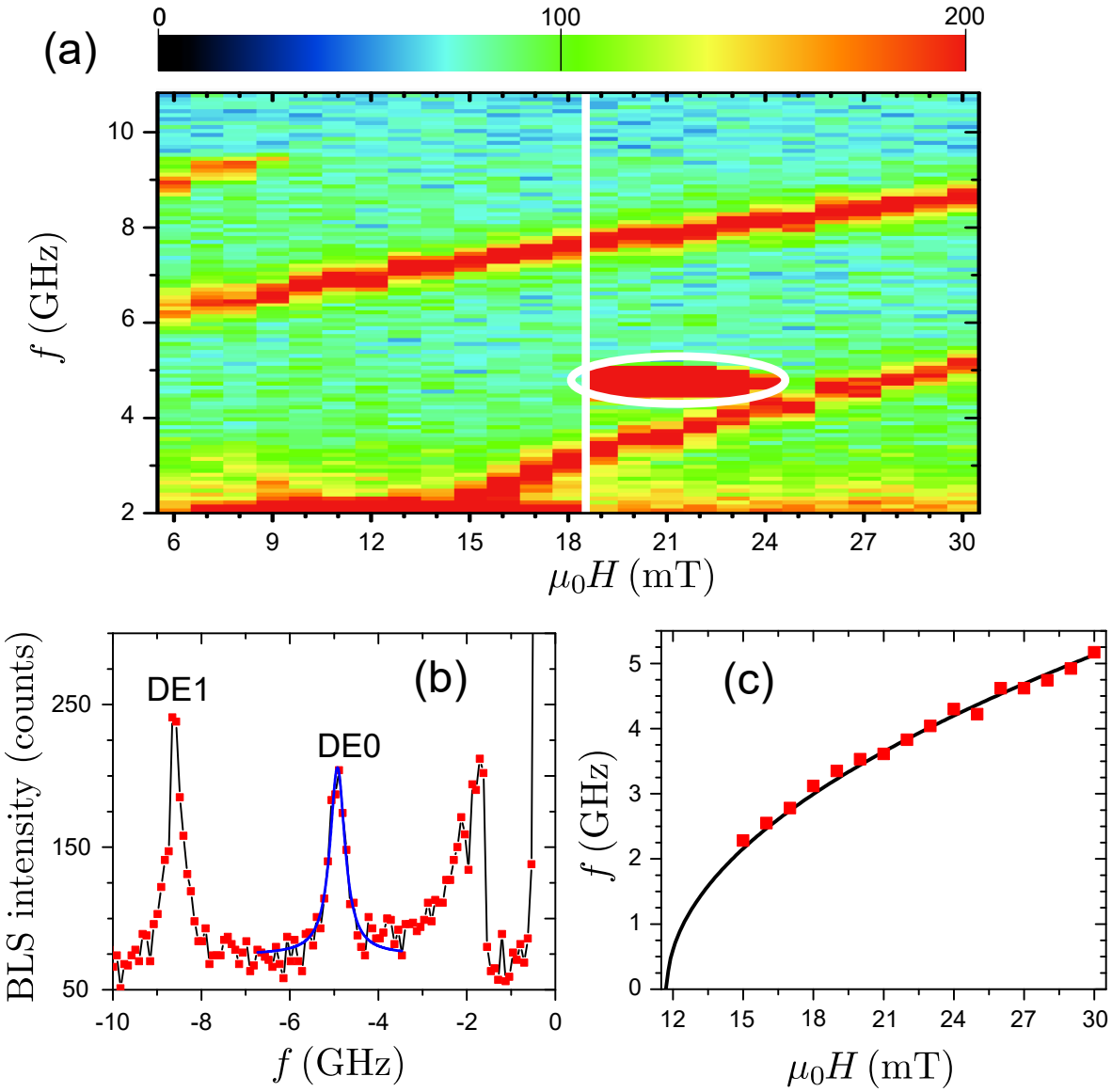

Figure 5.18: Stokes BLS-spectra corresponding to $k = 21$ rad/μm. (a) Experimental BLS-intensity raw data. The peak indicated by the white oval is an artifact due to the laser modes. The vertical white line indicates the measurement halt performed to correct this laser mode. The frequency sign has been changed to help data interpretation. (b) Example of the BLS intensity spectra measured at 29mT. The two main peaks corresponding to the two lower-frequency modes at saturation are indicated. The DE0-peak is fitted by a Lorenz function to determine its frequency. The peaks at 2 GHz and 0 GHz are produced by the elastic scattering of the photons on the sample and its filtering. (c) Symbols correspond to the frequency of the soft mode extracted from Lorentzian fits of the BLS data shown in panel (a). The line shows the frequency calculated by the KS approach. The extrapolated nucleation field is $\mu_0 H_c = 11.8$ mT. Fit parameters: $k = 21$ rad/μm, $K_1 = 33.4$ kJ/m^3, $M_S = 1.67$ T, $\Lambda = 3.85$ nm.

To verify that the DE0-mode softening is the precursor of the stripe domain nucleation, BLS measurements at $k \approx k_c$ were performed using a laser with wavelength

$\lambda = 451$ nm (blue). Figure 5.18 summarizes these results. Panel (a) shows the raw data obtained by measuring the frequency shift of the back-scattered photons with an incidence angle of 50 degrees. This corresponds to a wave vector $k = 21$ rad/μm. The softening of the mode is clearly visible. The frequency of the DE0-mode peak for different applied magnetic-fields was extracted and compared with SWIIM simulations at the same wave vector. The agreement is good, and the extrapolation shows that the frequency of the mode vanishes at H_c, as expected.

To study the dispersion relation of the stripe domain modes, k-resolved measurements were performed at $\mu_0 H = 7$ mT$< \mu_0 H_c \approx 12$ mT. The experimental method is identical to the one used to measure the data of Fig. 5.17. The results are presented in Fig. 5.19(a). The Stokes and anti-Stokes signals show a low frequency branch that can be associated to the Goldstone mode (frequency extrapolating to zero at k_c). The anti-Stokes spectrum shows an additional branch with higher frequency that can be related to the Higgs mode (frequency not extrapolating to zero at k_c). These two branches represent the same Goldstone and Higgs modes that we have studied in the previous sections.

The weak amplitude of the signal could be explained by the laser-spot diameter, which is of the order of 50 μm. Indeed, if the stripes are not perfectly aligned in this range, decoherence effects could appear and reduce the measured signal. The signal-to-noise rate could be improved by using a non-aged CoFeB sample, which should present better defined stripes.

To better understand these results, mumax3 simulations have been performed by D. Stoeffler at IPCMS to generate the spin wave dispersions in the stripe phase. The magnetic parameters of CoFeB 180nm were used (see Section 5.1.3), including an anisotropy $K_1 = 32.7$ kJ/m^3. This simulation used elementary cell sizes $h_x = 2.86$ nm, $h_y = 100$ nm, $h_z = 3$ nm and periodic boundary conditions. The number of cells in the $\hat{x}$ direction was chosen to fit exactly one stripe domain period. After relaxation to the equilibrium state, a very local and very short impulse excitation was applied and the x- and t-Fourier transform of the excited OOP magnetization component $m_z(x, z, t)$ was calculated. The results are shown in Fig. 5.19(c) and compared to the experimental data. It is possible to observe the same two branches. The Goldstone-branch has zero frequency at $k = k_c$, as expected. As for the Higgs-branch, it has a nonzero frequency for all the simulated wave vectors. At $k = k_c$, we can calculate analytically its frequency using Eq. 5.13. The obtained value, $f_{\text{Higgs}}(7\text{ mT}) = 3.5$ GHz, is indicated by a black cross in Fig. 5.19(c).

From these the BLS data, a coherent picture arises. When approaching the nucleation field H_c from saturation, the DE0 mode gets soft at k_c. Once the stripes are nucleated, the mode DE0 splits is two, giving rise to the Higgs- and Goldstone-branches.

A similar experiment had been previously performed by Banerjee et al. [123, 124]

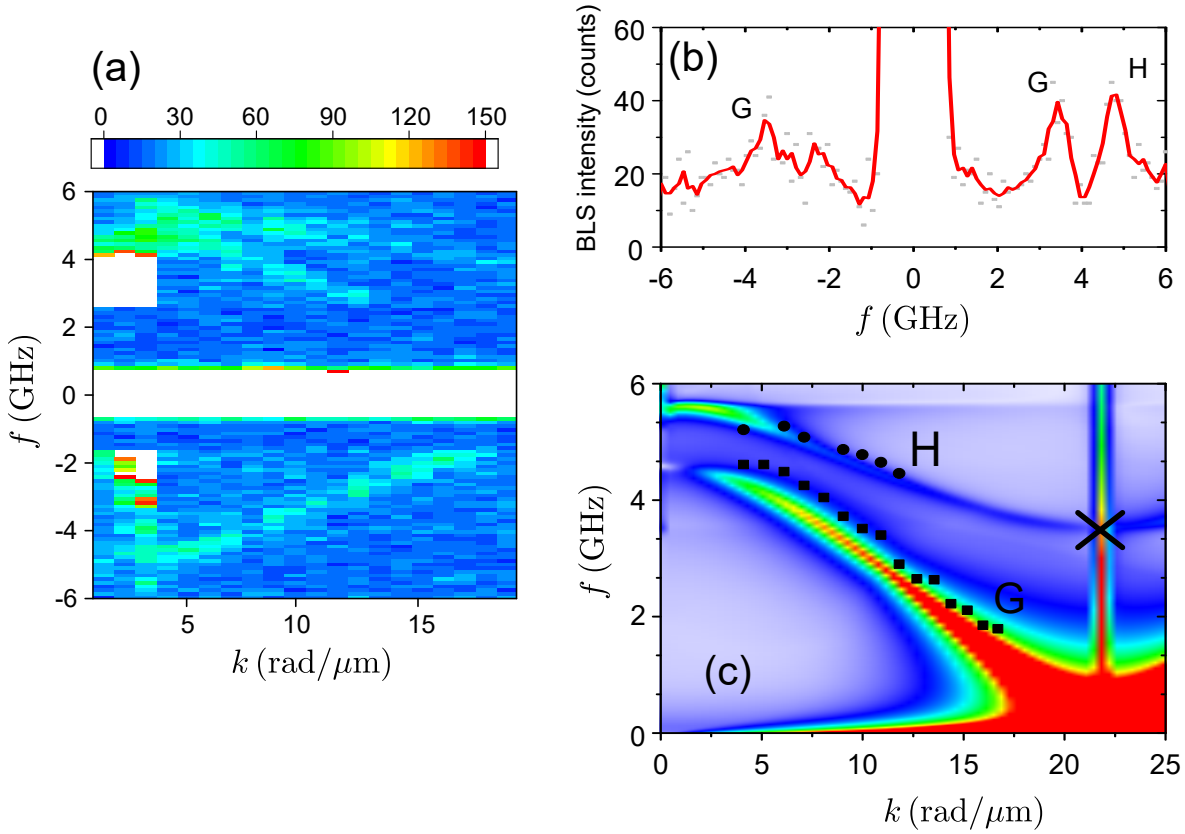

Figure 5.19: (a) k-resolved-BLS spectra obtained at 7 mT after saturate the sample at 30 mT. The color scale indicates the number of BLS counts. (b) The BLS intensity corresponding to $k = 9$ rad/μm. Goldstone and Higgs modes are labeled with G and H letters, respectively. The raw data (gray points) were smoothed by performing a 3-point average. (c) Simulated susceptibility at 7 mT. The black points correspond to the experimental data from (a). The black cross shows the Higgs mode at k_c, the signal measured by longitudinal FMR.

on Co/Pd thin film multilayers with $Q = 0.3$. They have identified theoretically the Goldstone mode related to the rigid oscillation of the stripes[9]. Nevertheless, they have worked with a much thinner film ($t = 42.5$ nm), which presents smaller-period stripes. In consequence, the softening lies far away from the BLS wave-vector range and could not be measured. Within our knowledge, our experiments are the first to show the existence of Goldstone and Higgs modes in magnetic stripes systems.

5.4.2 Longitudinal FMR

BLS measurements were not able of resolving the Higgs mode at $k = k_c$ (see Fig. 5.19(a) and Fig. 5.18(a) at $H < H_c$). However, this mode presents an interesting property: the distribution of m_y (the dynamic magnetization component in the direction of H) has a non-vanishing integral in one stripe period, as shown in Fig. 5.20. Therefore, this mode could be excited when performing FMR experiments in the (non-conventional)

[9]Goldstone modes representing rigid motion of an otherwise static structure have been founded in several magnetic systems, as skirmions or single domain walls [125]. However, none of these works have identified the corresponding Higgs mode.

longitudinal pumping configuration. In contrast, the m_y component of the Goldstone mode presents a vanishing integral over one period, thus it is invisible to FMR.

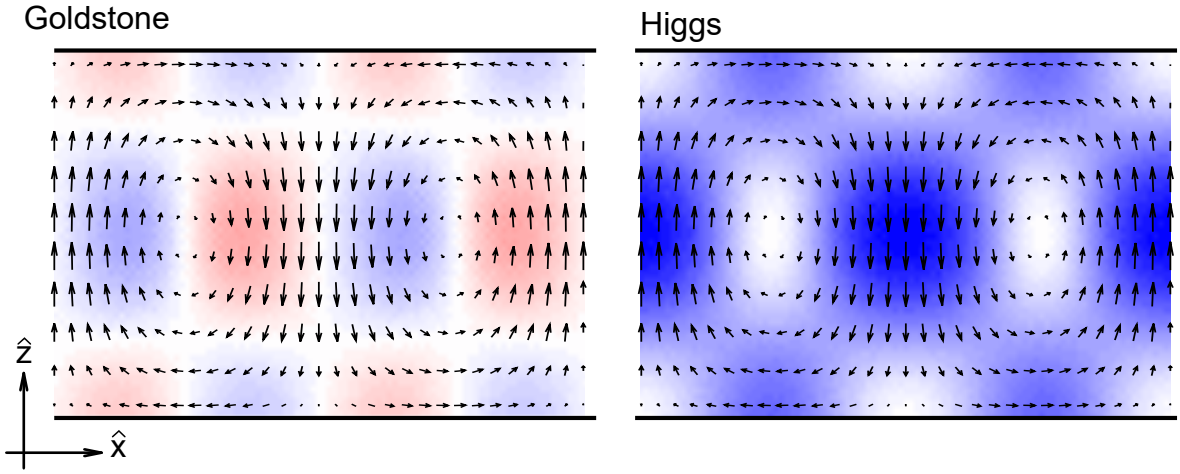

Figure 5.20: Distribution of the y component of the dynamic magnetization of the Higgs- and Goldstone modes. Calculation done using Eqs. 5.10 and 5.11, and $m_y = \sqrt{1 - m_x^2 - m_z^2}$.

In the saturated state, the longitudinal terms of the susceptibility are zero at first order. That means that an external excitation field $\boldsymbol{h}$ applied in the same direction that $\boldsymbol{M}$ does not induce any magnetization dynamics in the linear regime[10]. Therefore, we expect no longitudinal-FMR signal at $H > H_c$.

Figure 5.21 shows the microwave effective susceptibility measured in this configuration as function of the frequency and the magnetic field. As expected, a strong signal appears below the nucleation point. In order to verify that it corresponds to the Higgs mode, we have also plotted the expected frequency given by relation 5.13. The analytical model agrees with the measured points in the expected field range. For doing the KS calculations we have used the constant value $k_c = 22$ rad/μm. As we are working on the maximum of the imaginary frequency (see Fig. 5.11), the small changes on the equilibrium wave vector $k_e(H)$ predicted in the energy approach do not significantly modify the frequency.

Longitudinal pumping FMR measurements have been reported for stripe domains systems in Refs. [128–134]. However, the interpretation given is completely different from ours. In particular, in the work by Camara et al. [128], several avoided crossings are observed, yielding a much more complex classification and preventing the identification of the Higgs mode as a single mode. Vukadinovic et al. and Ebels et al. [130, 131, 133] identified the Higgs mode as a single entity, but without unveiling its signature as an amplitude mode. Similar results were also found in FMR experiments on strong stripes [135, 136]. In this case, domains and domain walls are well-defined. Therefore, the $k = 0$ point on the Goldstone branch is identified as a wall mode and the Higgs mode with $k = k_c$ is recognized as a domain mode.

[10] However, non-linear effects are expected in some conditions [126, 127].

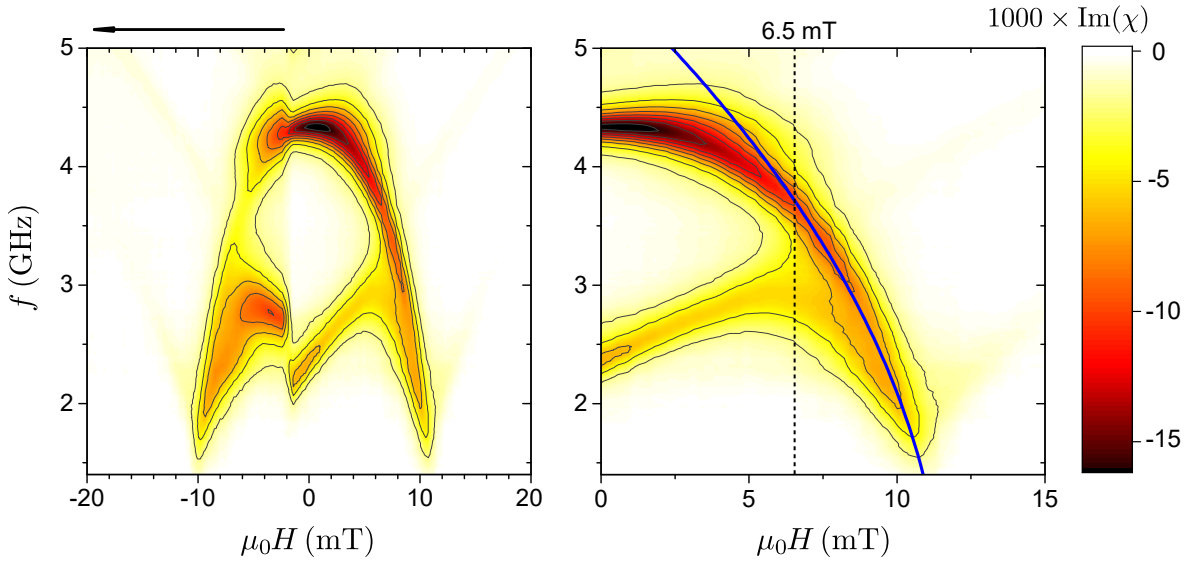

Figure 5.21: Longitudinal FMR performed on CoFeB 180nm. (Left) Full susceptibility map in the field-frequency space. The field scan was done in the direction indicated by the arrow. (Right) Zoom of the region of interest where the Higgs mode can be fitted by $i\sqrt{2}\omega_{\mathrm{DE0}}(k_c)$. The dashed line indicates the lower field limit where this method is valid.

In addition to the Higgs mode, other interesting features are present in the FMR measurement and highlighted in Fig 5.22. As shown in Fig. 3.1, the dynamic applied field $\boldsymbol{h}$ presents an unavoidable OOP component due to the finite size of the central strip of the coplanar waveguide. This small component couples to the transverse component of the susceptibility and excites the modes with $k = 0$ in the saturated states. In particular, the DE0-mode, that is slightly visible at saturation (I in Fig. 5.22(a)), becomes much stronger once the stripes are nucleated (III in Fig. 5.22(a)). To verify the origin of I and III , we also examine the transverse IP FMR measurement shown in Fig. 5.22(d). There, we observe the DE0-mode at $k = 0$, and we recognize features I and III.

Another relevant point on these data is the gap measured at negative fields on the Higgs mode (II in Fig. 5.22(a)) but not in the positive field. Mumax simulations (not shown) show that the stripes can present a small misalignment with respect to the applied field after magnetization reversal (at $\mu_0 H = -1.4$ mT in Fig. 5.22(a)). This angle difference between positive and negative fields can explain the asymmetry of the feature II.

To better understand the origin of this gap, mumax3 simulations of the longitudinal dynamic response of oblique stripes were performed by D. Stoeffler at IPCMS. In these simulations the static stripes were forced to define an angle of 10° with the applied field. With this constrain the static magnetization distribution of the stripes was simulated. Then, for a given applied field, a step excitation field of $\mu_0 h = 0.1$ mT was applied in the longitudinal direction ($\hat{y}$). By performing a temporal Fourier transform, the longitudinal susceptibility as function of the frequency was obtained. This procedure

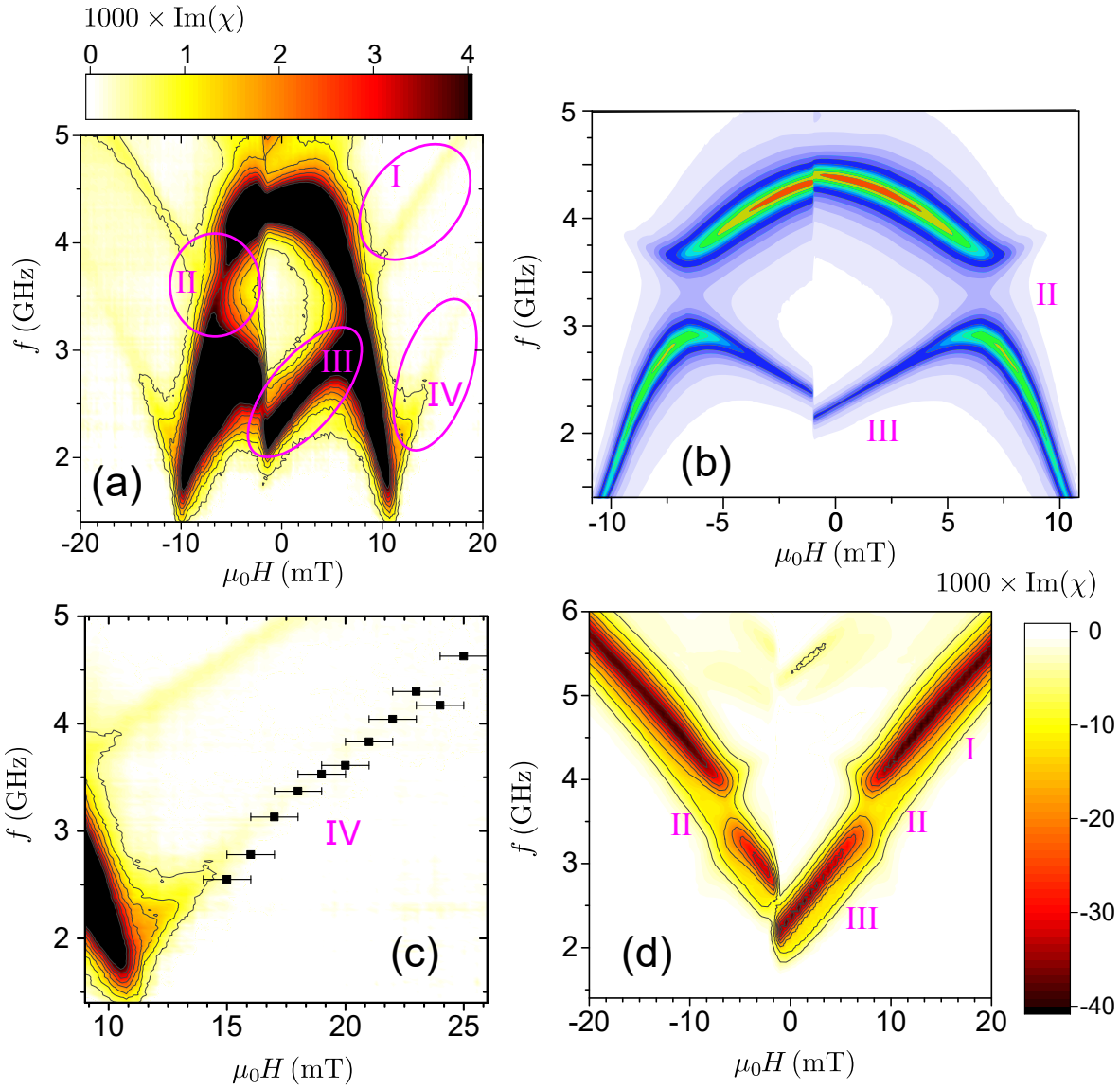

Figure 5.22: (a) Extra features in the longitudinal FMR data: (I) DE0 at $k = 0$ at $H > H_c$ (II) Obliques stripes hybridized with the Higgs mode with DE0 at $k = 0$. (III) DE0 at $k = 0$ at $H < H_c$. (IV) Linear excitation of DE0 at k_c. (b) Mumax3 simulation of the longitudinal susceptibility at $k = 0$ with stripes in an angle respect to the applied field. (c) Comparison with the BLS data from Fig. 5.18. (d) Transverse FMR in the IP configuration.

was repeated for a range of magnetic field. The results of these simulations are shown in Fig. 5.22(b). We can observe that the gap II is present, confirming that this is a consequence of the angle between the stripes and $\boldsymbol{H}$ [11]. Therefore, we can interpret this gap as an anticrossing between the DE0 at $k = 0$ and the Higgs mode. We can observe that the same gap is present in Fig. 5.22(d), which confirms the participation of the DE0 mode at $k = 0$.

Finally, we observe a mode of low frequency in the saturated state (IV in Fig. 5.22(a)). The fact that it seems to get soft at nucleation suggest that it is the mode DE0 at $k = k_c$. As it is a mode of low frequency, it could be excited by a non-linear process.

[11] In the same simulation is done with stripes aligned with $\boldsymbol{H}$, no gap is found.

Nevertheless, it does not appear at the double or 3/2 of the soft mode frequency, as usually observed in parametric pumping experiments [126, 127], but exactly at the same frequency. This appears clearly in Fig. 5.22(c) where the position of the DE0-mode at $k = 21$ rad/μm extracted from the BLS data is plotted onto the longitudinal susceptibility map. This suggests that feature IV corresponds to a linear-regime excitation of the DE0-mode at $k = k_c$. However, in a uniform magnetization distribution nothing couples the uniform excitation field $\boldsymbol{h}$ with a high-wave-vector spin-wave. However, as the minimum at k_c exhibits a strong transverse-susceptibility[12], a small inhomogeneity of a magnetic parameter could be enough to lead to a considerable microwave absorption. For example, if the value of K_1 is not homogeneous in the sample, as usually assumed, but it fluctuates around a mean value $\langle K_1 \rangle$ it could present a non-zero Fourier-component at k_c. These fluctuations would act as a transducer to couple the uniform $\boldsymbol{h}$ to high k spin-waves.

5.5 Chapter conclusions

The static properties of CoFeB 180nm, were calculated analytically by taking in account the fourth-order terms in the total energy. This sample proves to be a good system to study the dynamics of stripe domains in the limit of $Q \to 0$.

We demonstrate, both theoretically and experimentally, that the minimum of the DE0-mode is the precursor of the stripe nucleation. We showed that the spontaneous symmetry-breaking splits this soft mode in two different modes that can be identified as a Goldstone and a Higgs mode. These results were verified by FMR and BLS measurements. This work simplifies the analysis of the complex spin-wave modes present in stripe domains, and paves the way to their utilization in reprogrammable magnonic crystals [3, 137, 138].

Goldstone and Higgs modes were measured previously in other condensed-matter systems which present phase transitions. Nevertheless, stripe domains present the advantage that their order parameter can be easily understood as it has a simple, visible, physical interpretation: the amplitude and the phase of the stripes. Therefore, this system could be used as a platform to study the symmetry-breaking physics.

The theory presented in this chapter is quite generic and should be valid to predict the dynamic properties of the magnetization of weak stripes in other system.

[12] Mumax simulations show that the susceptibility at k_c near the nucleation field is hundredfold larger than the one at $k = 0$.

Chapter 6

General conclusions

The goal of this work was to study how inhomogenous magnetization distributions in thin films affect the spin-wave modes. For that, we have studied two systems: a stripe domains magnetic texture where the nonuniform distribution of the magnetization appears spontaneously; and a bilayer, where the contrast of saturation magnetization is imposed by fabrication.

Both systems were studied in the DE configuration, which presents the particularity that the anisotropic precession ($\boldsymbol{m}$) takes place in the plane delimited by the direction of propagation (k) and that of confinement (film normal), leading to complex dynamic magnetization profiles. Moreover, the dipolar interaction plays a fundamental role in the physics of both structures. In the bilayer, it is responsible for the nonreciprocal hybridization of the low frequency modes. In the weak stripes, the dipolar energy minimization imposes a closed-flux structure which determines, in ultimate instance, the static magnetization profile and the related dynamics.

In both cases, symmetry breaking plays a fundamental role. On the one hand, for the case of a bilayer, the up-down broken symmetry translates into a left-right nonreciprocity due to the dipolar interaction, which mixes the IP and OOP coordinates. On the other hand, stripe nucleation imposes a spontaneous symmetry breaking, which can be described by a scalar complex order parameter, related to a U(1) symmetry. The identification of this symmetry allows one to distinguish phase oscillations, to be identified with a Golstone mode (translation invariance), and amplitude oscillations, which correspond to a Higgs mode.

The two reported studies contribute to the long-term scientific aim of a better control of spin-wave propagation. The bilayer was engineered to perform as a magnonic diode, which could be used as a basic block in all-magnonic circuits to avoid unwanted reflections. As for the stripe domains, their configuration depends on field history and can be modified by electric currents [139]. This permits their implementation as reprogrammable magnonic crystals [8]. Besides, this work represents a step forward in

the study of the spin-wave modes in magnetic textures. By revisiting the static stripe domain texture as a particular case of a spin-wave mode, the complexity of the problem is reduced. In other words, we proved that the dynamic approach to the nucleation of textures is a useful tool to understand the dynamics of the texture once nucleated.

Perspectives

The present study tackles several questions. However, as usually happens, it also opens the door to many questions which remain unsolved. Here, we propose some experiments related with the results obtained.

In CoFeB 180nm thin films, the soft mode at k_c seems to couple linearly with a homogeneous excitation field at saturation (see Fig. 5.22(c)). The mechanism of this process is not clear, but its study may reveal interesting physics, as high wave-vector spin-waves are excited without any intrinsic modulation. Also, due to the low frequency of this mode, it could be a good candidate to perform nonlinear experiments. The threshold to excite this mode with a parametric excitation depends on the frequency gap [126], which can be make as small as desired when approaching the nucleation field.

The bilayer studied in Chapter 4 constitutes also an interesting platform to study nonlinear physics. In particular, in reciprocal systems, parametric excitation creates two counterpropagating magnons with same $|\boldsymbol{k}|$. The bilayer nonreciprocity should alter this scheme, introducing new physics.

In the stripe system, no spin-wave propagation experiments could be done. This was due to the dependence of the studied material on annealing, which hinders the lithography process. However, by adapting the fabrication processes to avoid the high-temperature treatment, it would be possible to perform inductive experiments with sub-micrometer-sized antennas. Three PSWS experiments are proposed:

- In the DE configuration, at $H > H_c$, hundred-nanometer-scale antennas could be fabricated in order to excite the soft mode at k_c. This mode could present interesting features due to its large lifetime and susceptibility.

- Also in the DE configuration, at $H < H_c$, an experiment similar to longitudinal FMR could be performed with micron-sized antennas. These antennas could couple to the Higgs mode at $\sim k_c$. This would be a simple way of measuring the propagation of nanometer-scale spin-waves with relatively large antennas.

- In the BV configuration, at $H < H_c$, spin waves could be excited at nonzero but relatively low wave vector. This low-frequency mode corresponds to the Goldstone mode with a certain modulation along the stripes direction.

Chapter 7

Résumé en français

Les ondes de spin, les excitations fondamentales des matériaux qui présentent un ordre magnétique et leur pseudo-particule associée, les magnons, peuvent propager du moment angulaire et de l'énergie. Donc, dans les dispositifs magnoniques, les ondes de spin transportent des informations codifiées dans leur phase ou amplitude [1]. Ces dispositifs présentent plusieurs avantages, entre lesquelles nous pouvons souligner la versatilité intrinsèque des matériaux magnétiques qui servent de substrat aux ondes de spin, permettant ainsi la conception des architectures reconfigurables ; l'absence de dissipation de Joule, qui réduit le gaspillage énergétique ; les non-linéarités intrinsèques de la dynamique de l'aimantation et une longueur de cohérence à l'échelle micrométrique, les rendant adéquats pour la computation en parallèle (*wave-computing*) [2] ; et finalement, la possibilité de traiter les signaux dans la gamme de GHz et THz [3].

Ces propriétés font de la technologie magnonique une alternative bien adaptée pour remplacer l'actuel CMOS, comme il a été identifié par l'International Technology Roadmap for Semiconductors [4]. Or, pour la conception des dispositifs magnoniques, la propagation des ondes de spin doit être contrôlée efficacement. Cette tâche peut être réalisée par des cristaux magnoniques, nanostructures magnétiques qui peuvent être utilisées pour construire les éléments passifs et actifs dans les circuits magnoniques [5, 6]. Pourtant, ces structures ont besoin d'un processus de fabrication complexe. Une alternative est donnée par les structures topologiques, comme les parois de domaines magnétiques, les tourbillons (*vortex*) et les skirmions [8]. Ces textures, qui peuvent être comprises comme la partie statique des modes dynamiques —les ondes de spin—, influencent directement la propagation des ondes de spin. En outre, les textures magnétiques sont plus polyvalentes que les cristaux magnoniques, car leur structure peut être facilement modifiée par un champ magnétique, un champ/courant électrique ou même, dans le schéma ultime des dispositifs magnoniques reconfigurables, par les ondes de spin elles-mêmes, comme dans le cas des parois de domaine. [9]. Ces interactions mutuelles ouvrent la voie au traitement des informations dans le schéma

purement magnonique, qui évite les pertes par dissipation Joule [10, 11].

Dans ce contexte, nous avons étudié les propriétés des ondes de spin qui interagissent avec des distributions non-uniformes. Dans ce but, nous avons étudié deux systèmes :

- Domaines à rubans, une texture qui nuclée à bas champ dans les films avec une anisotropie perpendiculaire (PMA, de l'anglais *Perpendicular Magnetic Anisotropy*). Dans ce système la distribution non-homogène apparait spontanément à la nucléation. Grâce à leur périodicité, ils sont identifiés comme des cristaux magnonique unidimensionnels, mais ils conservent la versatilité des textures magnétiques.
- Une bicouche avec un contraste d'aimantation de saturation. Ici, l'inhomogénéité imposée lors de la fabrication entraîne un type de propagation non-réciproque, qui peut être utilisée pour concevoir une diode magnonique.

Malgré leurs différences, les deux systèmes partagent plusieurs caractéristiques :

- Les brisures de symétrie (modulation périodique et brisure du symétrie haut/bas) jouent un rôle fondamentale pour déterminer les propriétés des ondes de spin.
- Le champ dipolaire, est un ingrédient clé qui introduit de la complexité et rend ces systèmes non-triviales.
- Les deux systèmes sont étudiés dans la configuration appelée Damon-Eshbach (champ magnétique appliqué dans le plan de l'échantillon et perpendiculaire à la direction de propagation des ondes de spin). Dans cette configuration, les ondes de spin présentent une chiralité donnée et une tendance à la fermeture du flux magnétique qui seront de vital importance pour les effets étudiés.

Ces deux systèmes ont été étudiés dans le cadre de deux projets, SWANGATE et MAGMATCH. Tous les deux ont inclut la participation de plusieurs chercheurs et leur collaboration a été fondamentale pour la réalisation de ce travail.

Propagation des ondes de spin dans une bicouche

Dans la plupart des systèmes de la physique des ondes, les relations de dispersion sont réciproques, c.-à-d., $f(k) = f(-k)$. Les systèmes magnétiques, qui ont la particularité de briser la symétrie d'inversion du temps, peuvent présenter, à l'inverse, des fortes non-réciprocités [103]. C'est le cas en particulier pour des ondes de spin dans un film ferromagnétique asymétrique dans la configuration Damon-Eshbach. Dans le cadre du projet MAGMATCH, nous avons étudié cette non-réciprocité [93]. Elle peut être mise à profit dans le cas d'une bicouche ferromagnétique qui présente un contraste d'aimantation de saturation pour construire une diode magnonique, c.-à-d., un matériau qui permet la propagation des ondes de spin dans une seule direction.

Notre objectif était de concevoir une diode magnonique à onde lente où les ondes ne peuvent se propager que dans une seule direction, car dans la direction opposée la vitesse de groupe est beaucoup plus lente. Dans ce but, à l'aide des simulations SWIIM, nous avons choisi les paramètres magnétiques de la bicouche de façon que, pour une certaine gamme de fréquences, la vitesse de groupe soit nulle dans une direction.

La Figure 7.1 montre la relation de dispersion obtenue à partir de simulations SWIIM. On n'observe le plateau (vitesse de groupe nulle) que pour les ondes avec k positif.

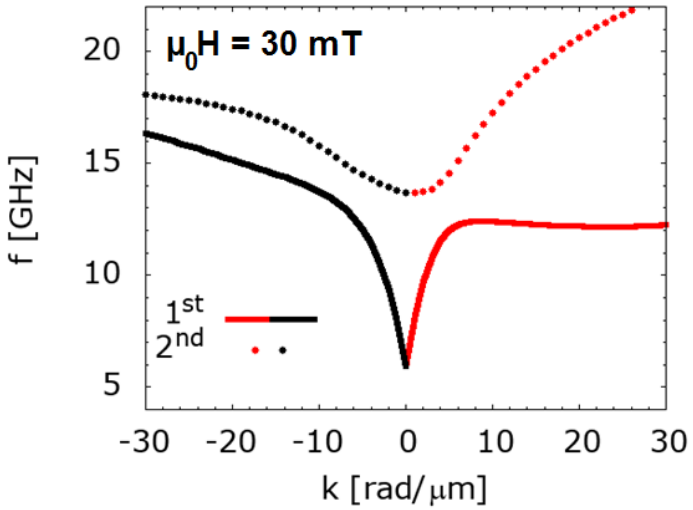

Figure 7.1: Relation de dispersion simulée par SWIIM. Les lignes continues (pointillés) montrent le premier (deuxième) mode des ondes de spin dans une bicouche CoFeB(20nm)/Py(26nm). On observe, à cause de l'hybridation non-réciproque, que les modes qui correspondent à un vecteur d'onde k positif présentent une vitesse de groupe nulle.

Nous avons aussi développé un modèle analytique simplifié qui nous a permis de comprendre que l'interaction entre le mode homogène au fil de l'épaisseur (mode acoustique) et le mode asymétrique (mode optique) dans une bicouche dépend de la chiralité des modes, qui dépend aussi de que l'on obtient une non-réciprocité si forte.

Pour vérifier expérimentalement le comportement de diode magnonique, plusieurs dispositifs constitués de deux antennes de 200 nm de largeur et séparées par une distance variable D ont été fabriquées par lithographie optique et électronique sur une bicouche CoFeB(20nm)/Py(26nm). Nous les avons utilisé pour réaliser des expériences de spectroscopie d'ondes de spin propagatives. Le changement de l'inductance mutuelle associé à la propagation des ondes de spin entre les deux antennes a été mesuré en fonction de la fréquence pour les deux sens de propagation (Fig. 7.2(a)). La relation de dispersion a ensuite été extraite de ces données et comparée au résultat d'une simulation micromagnétique (Fig. 7.2(b)) et à des mesures de diffusion Brillouin (ne sont pas montrées). On reconnaît un plateau (vitesse de groupe nulle) uniquement pour des ondes se propageant vers la droite. Ainsi, au-dessus de cette fréquence, la propa-

gation s'effectue uniquement vers la gauche, confirmant le comportement de diode de ce système, qui pourrait être utilisé pour réaliser une des briques de base des circuits magnoniques.

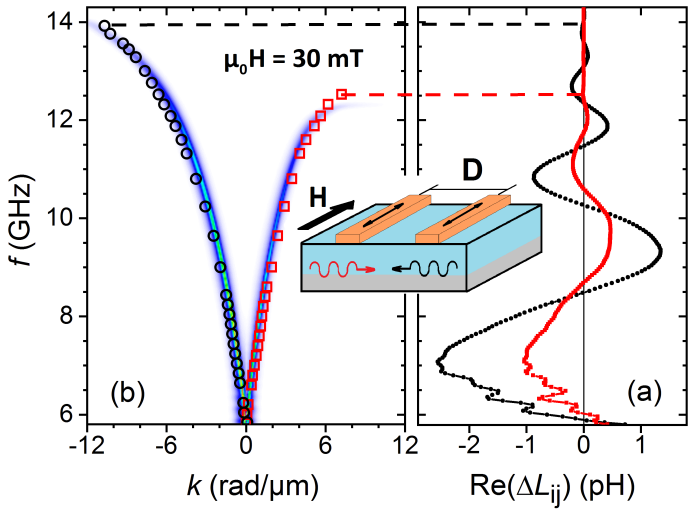

Figure 7.2: Au milieu, schéma du dispositif utilisé pour les mesures inductives. (a) Signal de propagation d'ondes de spin mesuré sous un champ magnétique μ_0H = 30 mT. À partir de f = 13 GHz aucun signal n'est détecté pour une propagation vers la droite (carrés rouges). (b) Relation de dispersion extraite de la phase du signal de propagation (symboles). La carte colorée montre le résultat d'une simulation micromagnétique mumax3.

Statique et dynamique des domaines en rubans

Dans le cadre du projet SWANGATE, en collaboration avec l'Institut Jean Lamour, à Nancy et l'Université Paris-Sud/Institut d'Electronique Fondamentale nous avons commencé à étudier l'utilisation des parois de domaine magnétique comme guide d'onde magnonique. Afin de mieux comprendre la propagation des ondes de spin dans les parois de domaines, nous nous sommes intéressés aux domaines magnétiques en rubans, qui présentent une grande quantité de parois alignées parallèlement, permettant *a priori* la transmission d'un signal plus fort qu'une seule paroi isolée. Un matériau adéquat pour réaliser nos mesures de propagation des ondes de spin dans les rubans doit présenter une PMA suffisamment importante pour développer des rubans magnétiques en même temps qu'il présente un amortissement faible. Par contre, un tel milieu magnétique n'est pas facile à obtenir : pour avoir une PMA forte il faut une interaction importante des ondes de spin avec le moment orbital du matériau ; cela est normalement accompagné d'un amortissement grand. Donc, nous avons choisi de travailler avec des matériaux qui ont une PMA faible. Or, pour avoir des rubans magnétiques, ce type de matériaux doivent être suffisamment épais pour éviter que les charges magnétiques de surface créés par les rubans ne les déstabilisent complètement. Ainsi, avec ces restrictions, nous avons étudié des échantillons de $Co_{40}Fe_{40}B_{20}$ fabriqués

à Nancy. Même si le CoFeB est un matériau ferromagnétique amorphe, il présente une PMA faible, d'origine magnetostrictive [40]. Les films que nous utilisons présentent des rubans magnétiques lorsque leur épaisseur dépasse la centaine de nanomètres. En particulier, nous avons choisi de travailler avec une épaisseur de 180nm car ces échantillons présentent des rubans magnétiques bien alignés avec le champ magnétique externe $\vec{H}$, comme montrent les Figs. 7.3(a) et 7.3(b). Puisque leur anisotropie est relativement faible par rapport à l'interaction dipolaire (facteur de qualité $Q = 0.034$), il est possible de l'introduire comme une perturbation à l'état fondamental d'une couche mince où les moments magnétiques sont saturés dans le plan. Dans cette situation, on trouve que les composantes perpendiculaires au champ magnétique définissent une configuration de fermeture de flux magnétique, comme est montré dans la Fig. 7.3(c), pendant que la composante principale de l'aimantation reste dans la direction définie par de $\vec{M}$ à la saturation. Ce genre de rubans sont appelés faibles (*weak stripes*), en contraste avec les rubans forts (*strong stripes*) dans lesquels l'aimantation pointe largement hors du plan dans les domaines qui sont séparés par de parois.

Approche dynamique de la nucléation des rubans magnétiques

La dynamique de l'aimantation est donnée par l'équation de Landau-Lifshitz (LL) [45],

$$\frac{\partial \vec{M}(t)}{\partial t} = -\mu_0 \gamma \, \vec{M}(t) \times \vec{H}_{eff}, \tag{7.1}$$

où $\vec{H}_{eff}$ est le champ magnétique effectif qui prend en compte tous les interactions qui contribuent à l'énergie des moments magnétiques, μ_0 est la perméabilité du vide et γ est le rapport gyromagnétique du matériau, qui ne ne joue ici que le rôle d'une constante. Donc, pour les cas des structures magnétiques statiques (comme les rubans), $\frac{\partial \vec{M}(t)}{\partial t} = 0$. Mais, contrairement à la plupart des autres textures magnétiques, les rubans ont une forme sinusoïdale dans la direction perpendiculaire à la composante principale de $\vec{M}$ (voir Fig. 7.3(c)). Étant donné que les ondes de spin ont également une dépendance spatiale sinusoïdale, et qu'elles satisfont l'équation de LL ; il est possible de se représenter les rubans comme des ondes de spin de fréquence zéro à un vecteur d'onde $\vec{k}$ différent de zéro. L'idée de penser aux rubans magnétiques comme une solution de l'équation de LL est largement connue dans la communauté scientifique [24]. Néanmoins, il n'y a pas d'étude sur l'approche dynamique, c.-à-d., sur le comportement de ce mode à fréquence non-nulle dans l'état saturé. Les seules études que lui ressemblent[111, 113] concernent des systèmes nanostructurés et non des couches minces infinies.

Dans ce contexte, nous avons réalisé des simulations en utilisant le code SWIIM [15], développé à l'IPCMS. Il permet de trouver les modes normaux de l'aimantation

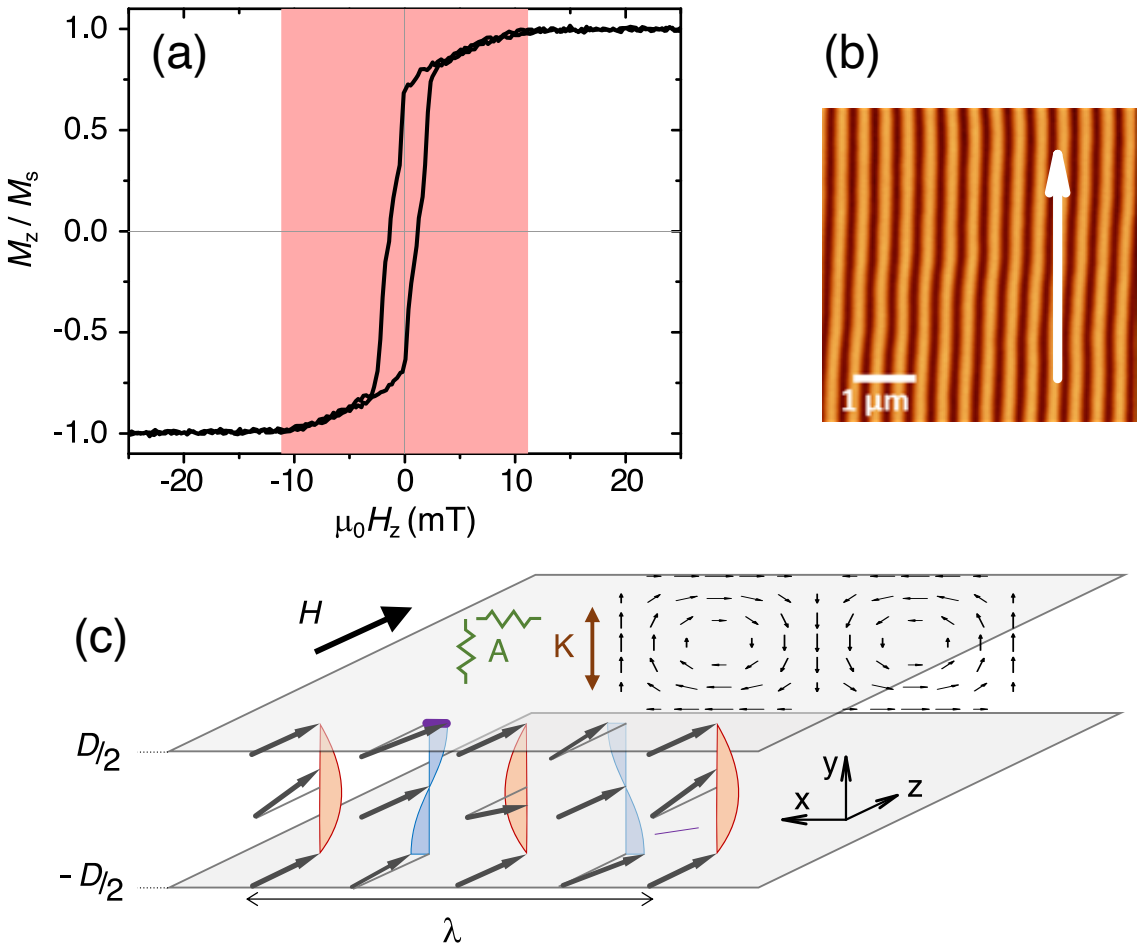

Figure 7.3: Statique des rubans magnétiques dans l'échantillon $Co_{40}Fe_{40}B_{20}$ 180nm. (a) Cycle d'hystérésis de l'aimantation dans le plan du film mesuré par magnétométrie à échantillon vibrant (*VSM*). (b) Image du microscope de force magnétique (MFM) prise en rémanance après avoir apliqué un champ magnétique dans la direction indiquée par la flèche blanche. (c) Schéma 3D de l'aimantation normalisée $\boldsymbol{M}(x, y, z)/M_S$ des rubans magnétiques une fois nucléés. À l'arrière-plan, les composantes du plan xy sont montrées.

des couches minces en résolvant l'équation de Landau-Lifshitz linéarisée en utilisant de la méthode de la matrice dynamique. Car les rubans sont toujours nucléés dans la direction du champ magnétique $\vec{H}$, le vecteur d'onde correspondant est orienté perpendiculairement à $\vec{H}$ (voir Figs. 7.3(b) et 7.3(c)). Donc, nous avons étudié la relation de dispersion des couches minces dans la configuration appelé « Damon-Eshbach », c'est-à-dire, $\vec{k} \perp \vec{H}$ et $\vec{H}$ dans le plan de l'échantillon. Ces simulations ont été réalisées dans l'état saturé, en absence de rubans.

Les résultats sont montrés dans la Fig. 7.4(a), où la branche de la relation de dispersion de plus basse fréquence a été tracée pour différents champs magnétiques. On voit que, effectivement, un mode devient mou[1] à $\vec{k} \neq 0$. En outre, nous avons trouvé que pour les systèmes avec une anisotropie faible, c'est l'hybridation entre les deux premiers modes dans l'épaisseur qui est à l'origine du mode mou. Le champ

[1]Par analogie avec un ressort, quand sa raideur devient faible, sa fréquence d'oscillation devient nulle.

vectoriel de $\vec{m}$ que l'on obtient est montré dans la Fig. 7.4(b), où la structure de fermeture de flux typique des rubans faibles est obtenue. Finalement, nous avons constaté que le vecteur d'onde $\vec{k}$ de ce minimum correspond à la période λ des rubans, soit $\lambda = \frac{2\pi}{k}$. En conséquence, d'après de ces simulations nous pouvons conclure que le mode de fréquence zéro dans la configuration Damon-Eshbach est responsable de la nucléation des rubans magnétiques[2].

Nous avons aussi développé une approche analytique simplifiée pour pouvoir calculer ces relations de dispersion. Pour ce faire, nous avons utilisé l'approche de la matrice dynamique avec une base inspirée des résultats de SWIIM : la composante hors du plan totalement ancrée tandis que la composante dans le plan peut osciller librement sur les surfaces du film. Avec ces combinaisons, nous avons pu obtenir un mode mou au champ de nucléation. Aussi, nous avons inclus dans ce modèle les effets de deuxième ordre introduits par le module constante de l'aimantation. Cela nous a permis de développer un modèle pour calculer l'amplitude des rubans magnétiques une fois nucléés.

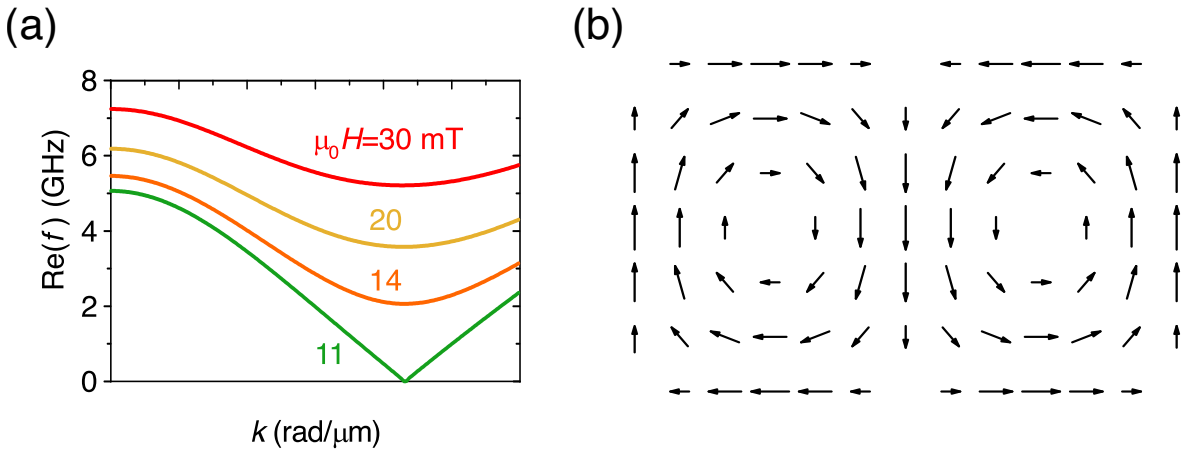

Figure 7.4: Simulations SWIIM sur les modes normales des ondes de spin du $Co_{40}Fe_{40}B_{20}$(180nm). (a) Branche de basse fréquences de la relation de dispersion à différents champs magnétiques appliqués. À 11 mT la branche présente un mode de fréquence zéro. (b) Champ vectoriel correspondant à l'aimantation dynamique du mode mou. Le flux magnétique est totalement fermé, donc il n'y a pas de charges magnétiques de volume.

Du point de vue expérimental, ces simulations ont été mises à l'épreuve par des mesures de diffusion de Brillouin résolues en vecteur d'onde (*k-resolved BLS*) réalisées avec nos collègues de l'équipe du Pr. Hillebrands, Université de Kaiserslautern. Dans ces expériences de diffusion inélastique de lumière, l'écart en fréquence des photons rétrodiffusés par l'échantillon est mesuré à l'aide d'un interféromètre Fabry-Perot. Cette différence de fréquence est causée par la création ou destruction des magnons, et elle correspond à leur fréquence d'excitation. Le vecteur d'onde de ces magnons

[2]Nous avons vérifié que cette approche prédit correctement la période des rubans dans la multicouche de [Co/Ni] (50nm), même si elle développe des rubans forts.

est donné par la relation $k = \frac{4\pi}{\lambda_{laser}}\sin(\theta_i)$, où θ_i est l'angle d'incidence du laser et $\lambda_{laser} = 532$nm. Donc, en variant cet angle, différentes valeurs de k sont sondées. Ainsi, la relation de dispersion des ondes de spin est obtenue. La Fig. 7.5(a) montre schématiquement la configuration expérimentale utilisée. Les résultats de ces mesures à deux champs magnétiques différents sont montrés dans les Figs. 7.5(b) et 7.5(c). Les données expérimentales coïncident avec les simulations, et pour $\mu_0 H = 14$ mT, on observe que la branche de basse fréquence devient molle. Donc, ces mesures vérifient d'origine dynamique de la nucléation des rubans magnétiques dans l'échantillon de $Co_{40}Fe_{40}B_{20}$.

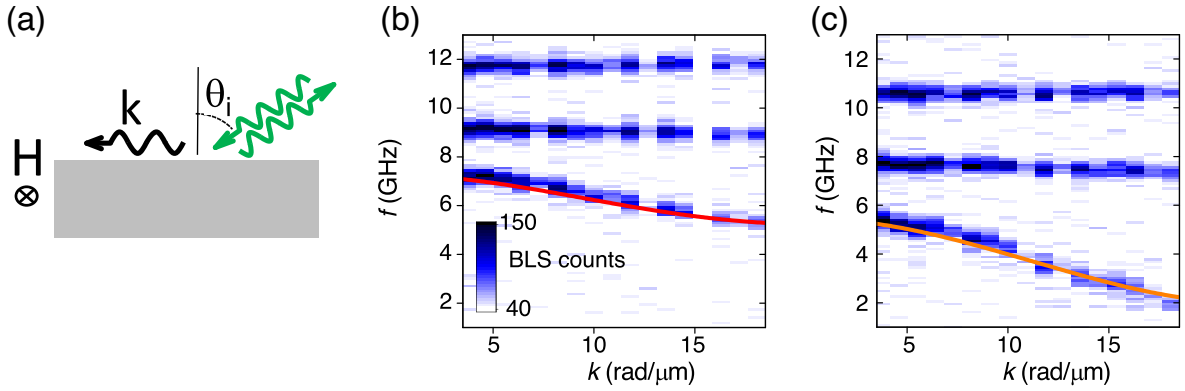

Figure 7.5: Expériences de diffusion de Brillouin. (a) Configuration dans laquelle les mesures ont été réalisées. Les relations de dispersion des ondes de spin de $Co_{40}Fe_{40}B_{20}$(180nm) à $\mu_0 H = 30$mT (b) et $\mu_0 H = 14$mT (c) ont été mesurées par BLS. Les données de simulations SWIIM sont aussi montrées (lignes solides). Il est possible d'extrapoler l'existence du mode mou qui est à l'origine de la nucléation des rubans.

Modes de rubans magnétiques

La nucléation des rubans est une transition de deuxième ordre qui est accompagnée par une brisure spontanée de la symétrie quand leur phase prend une valeur bien définie. Cette phase ϕ peut être représentée comme un movement rigide des rubans dans la direction du vecteur d'onde. La texture magnétique est totalement définie par la combinaison de cette phase et son amplitude A. C'est-à-dire, elle est décrite par un paramètre d'ordre scalaire et complexe $\psi = A\, e^{i\phi}$ associé au groupe de symétrie U(1). Dans cet espace paramétrique, la densité d'énergie vient donnée par un potentiel du type "chapeau mexicain". Cette énergie ne dépend pas de la phase, et en conséquence, les oscillations de phase sont un mode de Goldstone. Les oscillations de l'amplitude auront une fréquence non-nulle et peuvent être interprétées comme le mode d'Higgs correspondant. Cette interprétation nous permet de réinterpréter plusieurs travaux sur la dynamique de rubans magnétiques [128–134].

Pour mettre en évidence ces modes nous avons réalisé des mesures BLS résolues en vecteur d'onde. Comme est montre dans les Figs. 7.6(a,b), nous avons pu trouver deux

branches une fois les rubans sont nucléés. Pour confirmer la nature de ces modes, nous avons comparé ces mesures aux simulations mumax3 réalisées par D. Stoeffler (voir Fig. 7.6(c)). Il est possible d'observer que la branche de plus basse fréquence correspond au mode de Goldstone tandis que la deuxième branche, correspond au mode d'amplitude (Higgs, ne pas montré dans le résumé).

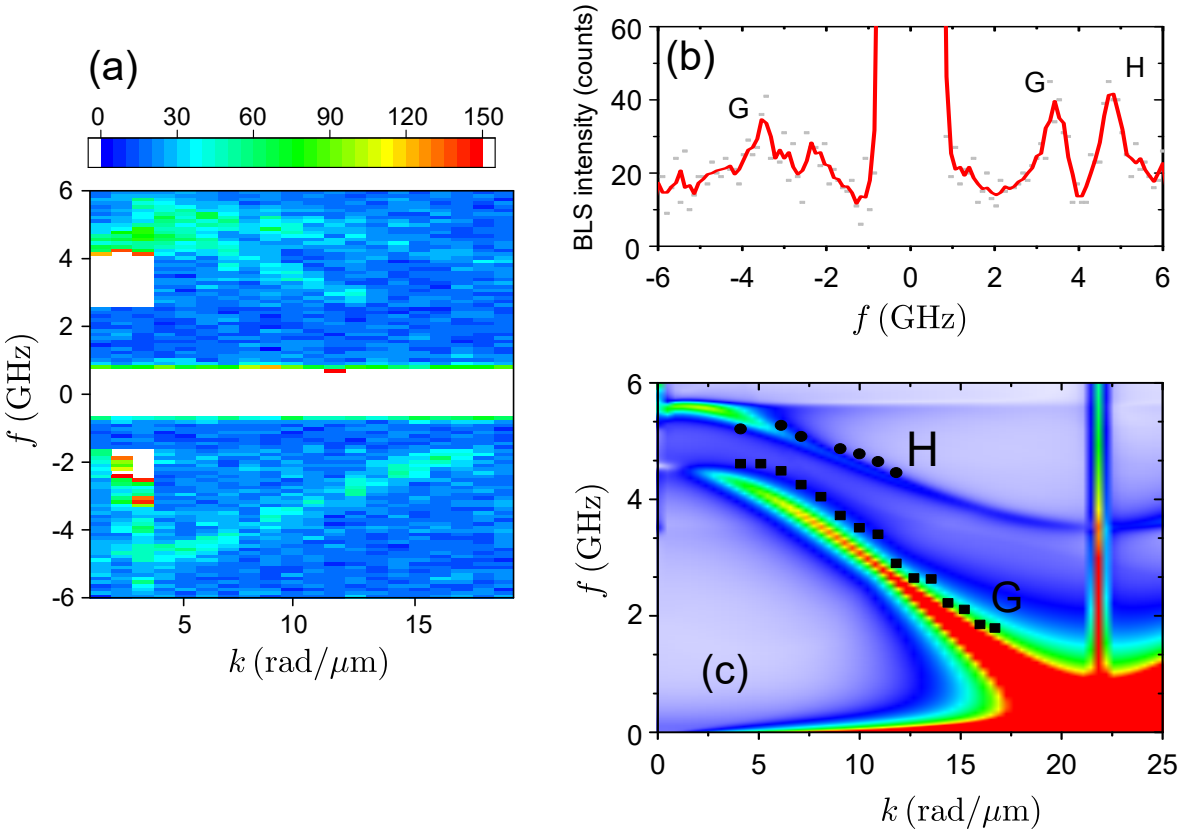

Figure 7.6: Mesures BLS et simulations mumax3 du système de rubans du CoFeB. (a) mesures BLS qui montrent la relation de dispersion à 7 mT après avoir saturé l'échantillon à 30 mT. (b) Intensité de mesures BLS correspondant à $k = 9$ rad/μm. Les modes de Goldstone et Higgs sont étiquetés avec les lettres G et H, respectivement. Les données crues (points grises) ont été moyennées chaque trois points. (c) Simulation mumax3 de la relation de dispersion à 7 mT. Les points noirs montrent les données expérimentales de (a).

Conclusion générales

Le but de ce travail était de comprendre comment les distributions inhomogènes de l'aimantation affectent les modes des ondes de spin. Pour cela, nous avons étudié deux systèmes : les rubans magnétiques, où la distribution non uniforme de la magnetisation apparaisse de façon spontanée ; et la bicouche, où le contraste d'aimantation de saturation est imposée par fabrication.

Les deux systèmes ont été étudiés dans la configuration Damon-Eshbach, qui présent la particularité de définir la précession anisotropique ($\boldsymbol{m}$) dans le plan délimité par la direction de propagation (k) et la droite normale au film. Ceci conduit à des profils

d'aimantation dynamiques complexes. En outre, l'interaction dipolaire joue un rôle fondamental dans la physique des deux structures. Dans la bicouche, elle est responsable de l'hybridation non réciproque des modes de basse fréquence. Dans les rubans faibles, la minimisation de l'énergie dipolaire impose structures de fermeture de flux, qui détermine, en dernière instance, le profil d'aimantation statique et la dynamique associée.

Dans les deux cas, la rupture de symétrie joue un rôle fondamental. D'une part, dans le cas d'une bicouche, la symétrie verticale brisée se traduit par une non-réciprocité gauche-droite due à l'interaction dipolaire, qui mélange les composantes dans le plan et hors du plan. D'autre part, la nucléation en bandes impose une rupture de symétrie spontanée, qui peut être décrite par un paramètre d'ordre complexe scalaire, lié à une symétrie U(1). L'identification de cette symétrie permet de distinguer des oscillations de phase, à identifier avec un mode de Golstone, des oscillations d'amplitude, qui correspondent à un mode d'Higgs.

Les deux études rapportées contribuent à l'objectif scientifique à long terme d'un meilleur contrôle de la propagation des ondes de spin. La bicouche a été conçue pour fonctionner comme une diode magnonique, qui pourrait être utilisée dans les circuits entièrement magnétiques pour éviter les réflexions indésirables. Pour les domaines en rubans, leur configuration dépend de l'histoire du champ et peut être modifiée par des courants électriques [139]. Ceci permet leur implémentation en tant que cristaux magnoniques reprogrammables [8]. En outre, ce travail représente un pas en avant dans l'étude des modes d'onde de spin dans les textures magnétiques. En revisitant la texture statique du domaine des bandes comme un cas particulier de mode d'onde de spin, la complexité du problème est réduite. En d'autres termes, nous avons prouvé que l'approche dynamique de la nucléation des textures est un outil utile pour comprendre la dynamique des textures une fois nucléées.

Appendix A

Stripe-energy integration

This Appendix presents the explicit calculation of the energy density averaged over one period of magnetic stripes. The total stripe energy normalized by the dipolar energy is given by

$$\frac{2}{\mu_0 M_S^2}\langle E_T\rangle = -Q\left\langle m_z^2\right\rangle + \Lambda^2\left\langle(\vec{\nabla}\vec{m})^2\right\rangle - 2\,h\left\langle\sqrt{1-m_x^2-m_z^2}\right\rangle, \tag{A.1}$$

where Q is the first order PMA, Λ is the exchange length, $h = H/M_S$ and $m_i = M_i/M_S$ are given by Eq. 1.22.

A.0.1 Second-order calculation

To resolve these integrals we will use the identity $\frac{1}{\lambda}\int_0^\lambda \cos^2(k\,x) = \frac{1}{2}$. The PMA and the exchange terms can be calculated as

$$\begin{aligned}\left\langle m_z^2\right\rangle &= \frac{1}{t\,\lambda}\int_0^t\int_0^\lambda\left[\left(A\,\frac{k}{\kappa}\,\cos(k\,x)\cos\left(\kappa\,z\right)\right)^2\right]\mathrm{d}x\mathrm{d}z \\ &= \left(A\,\frac{k}{\kappa}\right)^2\frac{1}{2}\frac{1}{2} = \left(A\,\frac{k}{2\,\kappa}\right)^2;\end{aligned} \tag{A.2}$$

$$\begin{aligned}\left\langle(\vec{\nabla}\vec{m})^2\right\rangle &= \frac{1}{t\,\lambda}\int_0^t\int_0^\lambda\left(\frac{\partial m_x}{\partial x}\right)^2+\left(\frac{\partial m_x}{\partial z}\right)^2+\left(\frac{\partial m_z}{\partial x}\right)^2+\left(\frac{\partial m_z}{\partial z}\right)^2\mathrm{d}x\mathrm{d}z \\ &= \frac{A^2}{4}\left[k^2+\kappa^2+\left(\frac{k}{\kappa}\right)^2k^2+\left(\frac{k}{\kappa}\right)^2\kappa^2\right] \\ &= \frac{A^2}{4}\left[2\,k^2+\kappa^2+\left(\frac{k^2}{\kappa}\right)^2\right];\end{aligned} \tag{A.3}$$

At second order the Zeeman energy can be approximated as $\sqrt{1-m_x^2-m_z^2} = 1-\frac{1}{2}(m_x^2+m_z^2)$. Therefore, the one period averaged is given by

$$\begin{aligned}
&\left\langle \sqrt{1-m_x^2-m_z^2} \right\rangle \approx 1 - \left\langle \frac{m_x^2}{2} + \frac{m_z^2}{2} \right\rangle = \\
&= 1 - \frac{1}{t\,\lambda}\int_0^t\int_0^\lambda \left[\frac{1}{2}\left(A\,\sin(k\,x)\sin\left(\kappa\,z\right)\right)^2 + \frac{1}{2}\left(A\,\frac{k}{\kappa}\,\cos(k\,x)\cos\left(\kappa\,z\right)\right)^2\right] \mathrm{d}x\mathrm{d}z \\
&= 1 - \frac{A^2}{2}\frac{1}{4}\left[1+\left(\frac{k}{\kappa}\right)^2\right].
\end{aligned} \tag{A.4}$$

A.0.2 Fourth-order calculation

The energy also presents terms depending on higher powers of the amplitude. In particular, fourth-order terms (m_i^4) can be calculated from Eq. 5.3 as

$$b(h,\,k^2)A^4 = \Lambda^2\left\langle(\vec{\nabla}m_y)^2\right\rangle + 2\,\frac{h}{8}\left\langle m_x^4 + 2\,m_x^2\,m_z^2 + m_z^4\right\rangle - Q_2\left\langle m_z^4\right\rangle, \tag{A.5}$$

where $Q_2 = \dfrac{2K_2}{\mu_0 M_S^2}$ and K_2 is the second-order anisotropy constant. Developing $m_y = \frac{m_x^2+m_z^2}{2}$, we calculate

$$\begin{aligned}
\left\langle(\vec{\nabla}m_y)^2\right\rangle &= \frac{1}{t\,\lambda}\int_0^t\int_0^\lambda\left[\left(\frac{\partial m_y}{\partial x}\right)^2 + \left(\frac{\partial m_y}{\partial z}\right)^2\right]\mathrm{d}x\mathrm{d}z \\
&= \frac{1}{4\,t\,\lambda}\int_0^t\int_0^\lambda\left[\left(\frac{\partial m_x^2}{\partial x}+\frac{\partial m_z^2}{\partial x}\right)^2 + \left(\frac{\partial m_x^2}{\partial z}+\frac{\partial m_z^2}{\partial z}\right)^2\right]\mathrm{d}x\mathrm{d}z \\
&= \frac{1}{4\,t\,\lambda}\int_0^t\int_0^\lambda\left[\left(2\,m_x\,\frac{\partial m_x}{\partial x}+2\,m_z\,\frac{\partial m_z}{\partial x}\right)^2 + \left(2\,m_x\,\frac{\partial m_x}{\partial z}+2\,m_z\,\frac{\partial m_z}{\partial z}\right)^2\right]\mathrm{d}x\mathrm{d}z \\
&= \frac{A^4}{t\,\lambda}\int_0^t\int_0^\lambda\left\{\left[k\sin(k\,x)\cos(k\,x)\sin^2\left(\kappa\,z\right) - \frac{k^3}{\kappa^2}\sin(k\,x)\,\cos(k\,x)\cos^2\left(\kappa\,z\right)\right]^2\right. \\
&\left. + \left[\kappa\sin^2(k\,x)\sin\left(\kappa\,z\right)\,\cos\left(\kappa\,z\right) - \frac{k^2}{\kappa}\,\cos^2(k\,x)\cos\left(\kappa\,z\right)\,\sin\left(\kappa\,z\right)\right]^2\right\}\mathrm{d}x\mathrm{d}z
\end{aligned} \tag{A.6}$$

This expression can be integrated using the following identities

$$\begin{aligned}
&\frac{1}{2\pi}\int_0^{2\pi}\cos^4(x)\,dx = 3/8,\\
&\frac{1}{2\pi}\int_0^{2\pi}\cos^2(x)\sin^2(x)\,dx = 1/8.
\end{aligned} \tag{A.7}$$

Applying them, we finally obtain

$$\begin{aligned}
&\left\langle(\vec{\nabla}m_y)^2\right\rangle = \\
&= A^4\left[\left(k^2\,\frac{3}{8}\,\frac{1}{8} - \frac{2k^4}{\kappa^2}\,\frac{1}{8}\,\frac{1}{8} + \frac{k^6}{\kappa^4}\,\frac{3}{8}\,\frac{1}{8}\right) + \left(\kappa^2\,\frac{3}{8}\,\frac{1}{8} - 2\,k^2\,\frac{1}{8}\,\frac{1}{8} + \frac{k^4}{\kappa^2}\,\frac{3}{8}\,\frac{1}{8}\right)\right] \\
&= \frac{A^4}{64}\left(k^2 + \frac{k^4}{\kappa^2} + 3\,\frac{k^6}{\kappa^4} + 3\,\kappa^2\right).
\end{aligned} \tag{A.8}$$

It can be noticed that this term is positive for all real values of k and κ. The fourth order terms of the Zeeman and second-order anisotropy interaction are

$$\begin{aligned}
\left\langle m_x^4 + 2\,m_x^2\,m_z^2 + m_z^4\right\rangle = \frac{A^4}{t\,\lambda}\int_0^t\int_0^\lambda \{&[\sin(k\,x)\sin(\kappa\,z)]^4 + \\
&+ 2\left[\frac{k}{\kappa}\sin(k\,x)\sin(\kappa\,z)\;\cos(k\,x)\cos(\kappa\,z)\right]^2 + \\
&+ \left[\frac{k}{\kappa}\cos(k\,x)\cos(\kappa\,z)\right]^4\}\,\mathrm{d}x\mathrm{d}z = \\
&= A^4\left[\frac{3}{8}\,\frac{3}{8}\left(1+\frac{k^4}{\kappa^4}\right) + 2\,\frac{1}{8}\,\frac{1}{8}\,\frac{k^2}{\kappa^2}\right] = \\
&= A^4\frac{1}{64}\left[9\left(1+\frac{k^4}{\kappa^4}\right) + \frac{2\,k^2}{\kappa^2}\right]
\end{aligned} \tag{A.9}$$

$$\left\langle m_z^4\right\rangle = \frac{A^4}{t\,\lambda}\int_0^t\int_0^\lambda\left[\frac{k}{\kappa}\cos(k\,x)\cos(\kappa\,z)\right]^4 = \frac{9}{64}\,\frac{k^4}{\kappa^4}A^4. \tag{A.10}$$

Appendix B

Extra Kerr measurements

Kerr hysteresis loop CoFeB 150nm

Kerr microscopy measurements were performed on CoFeB 150nm. As this thickness is closer to the critical thickness (t_c = 127 nm) than the CoFeB 180nm sample, the nucleation field is lower.

We have observed that the hysteresis loops of this sample present a much more complicated inner structure, meaning that the anisotropies that affect M_{sur} are more important. This fact is also visible in the polar plot in Fig. B.1. This increase of the IP anisotropy was also shown in Ref. [40].

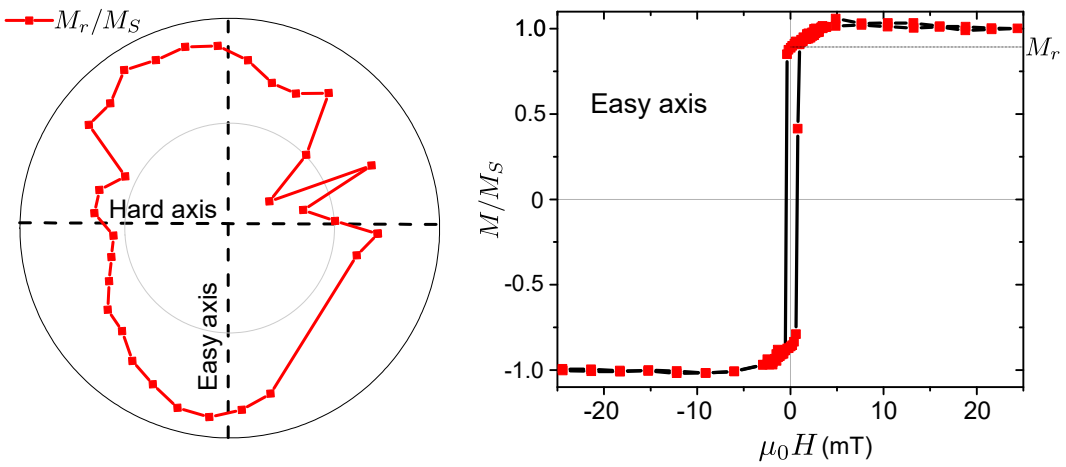

Figure B.1: Tranversal-Kerr integrated-intensity as function of the IP applied magnetic field. Sample thickness: $t = 150$ nm. The variation of M_r/M_S with the applied field angle is shown in the polar plot.

Kerr microscopy CoFeB 150nm

In the same sample Kerr images were acquired at remanence after applying a magnetic field in a certain direction. If this direction coincides with the IP easy axis,

then a unique domain wall which is well-aligned with this axis is found (Fig. B.2(a)). However, if the magnetic field is applied in the perpendicular direction a much more complicated magnetic structure appears (Fig. B.2(c)). This shows that in the studied sample (CoFeB 150nm) the IP plane anisotropy affects the magnetic textures at low field.

Figure B.2(b) shows the magentic configuration if the field was applied in the direction perpendicular to the easy axis, but the sensitivity is parallel to it. In this case a modulated structure appears. We suppose that this is a signature of a modulation of the magnetic stripe domains, which are too small to be resolved by the microscope.

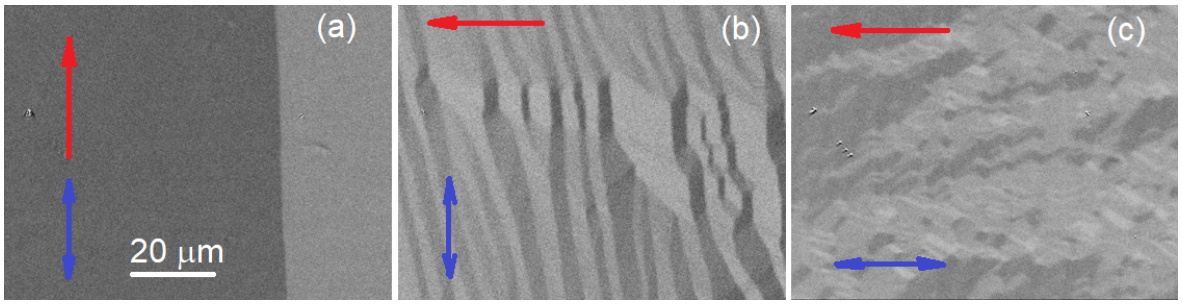

Figure B.2: Kerr microscope images at $H = 0$ after saturation at 30 mT in the direction indicated by the red arrow. The blue arrow indicates the sensitivity axis. The easy axis is along the vertical direction. The scale is the same for the three images.

Appendix C

Exchange determination from OOP-FMR

To calculate the exchange and the surface anisotropy in thin films, a variant of the method suggested Talagala et al. [62] was used. For that, the field shifts between the PSSW modes measured with the OOP FMR were extracted. Figure 5.4 shows an example of the peaks that can be identified. Each of these peaks corresponds to a different OOP wave vector κ_n, which can be found using Equation 2.33, that depends on the surface anisotropy K_s and the exchange constant A. These two parameters are, *a priori*, unknown parameters.

However, we can measure the field shift between each of these peaks and the one corresponding to κ_0. In our case, this is the peak with the biggest amplitude. If $K_s = 0$, the field shift should follow

$$\mu_0(H_n - H_0) = \frac{2A}{M_S}\left(\frac{n\,\pi}{t}\right)^2. \tag{C.1}$$

However, this is not our case. Thus, we conclude that $K_s \neq 0$. If we consider $\kappa_0 << \kappa_{n\neq 0}$, we can approximate $\kappa_0 = 0$. In this case, the field shift is given by Equation C.1. By introducing it into 2.33, the shift $\Delta H_n = (H_n - H_0)$ can be calculated from

$$\mathrm{tg}\left(t\sqrt{\frac{\Delta H_n M_S}{2\,A}}\right) = \frac{2\,K_s\,\sqrt{2\,\Delta H_n M_S A}}{\Delta H_n M_S A - 2\,K_s^2}. \tag{C.2}$$

This non-linear equation can fit the measured ΔH_n graphically. For that, both terms of this expression are plotted as functions of ΔH. By adjusting the two unknown parameters A and K_s, it is possible to obtain that the crossing of the two curves happens at the measured ΔH_n. The graphical solution using the ΔH_n from Fig. 5.4 is presented in Fig. C.1. The difference between the two terms of Eq. C.2 at the measured ΔH_n can be minimized numerically.

With this first approximation, A and K_s are calculated. Using these parameters, the

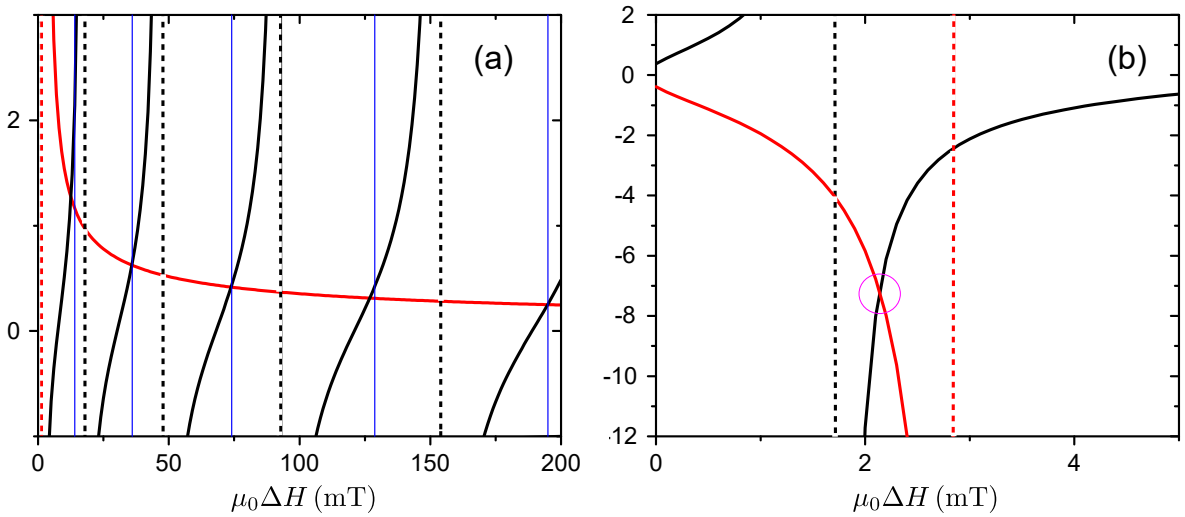

Figure C.1: Graphic solution to find A and K_s. (a) Right (red) and left (black) terms of equation C.2 are plotted. The values of $A = 16.5$ pJ/m and $K_s = 0.18$ mJ/m^2 have been chosen to make the intersection of these two curves coincide with the experimental ΔH_n, indicated in blue. (b) Detail of the first cross, which corresponds to κ_0.

value of κ_0 can be estimated. For CoFeB this value shifts up the resonance frequency of the first mode by $\Delta H_0 = 2.1$ mT. By adding this field to ΔH_n the true shifts from the mode with $K_s = 0$ are found. Then the minimization process performed previously is repeated for the values of $\Delta H_n + \Delta H_0$. This procedure results in a more precise value of A and K_s.

This calculation can be iterated several times to converge to the correct values of A and K_s. For small values of $Q_s = \dfrac{2\,K_s}{t\,\mu_0\,M_s^2}$, two iterations are enough to obtain reliable parameters.

If $K_s > 0$, then the surface uniaxial anisotropy is OOP. In the opposite case, the surface anisotropy defines an easy plane.

Appendix D

Kalinikos-Slavin stray-free calculations

The basis used in the Kalinikos-Slavin (KS) approach has to be chosen in agreement with the symmetries of the studied system. For the case of thin films with PMA that present stripe domains, we already know that there is one static modulated solution to the LL equation at H_c. If $Q \to 0$, the profile of the mode is given by the stray-field free ansatz of Expression 1.22. To find the complete branch of the dispersion relation from which this static mode belongs, the basis has to include this ansatz. Therefore, we can propose the decomposition of the dynamic magnetization in the following orthonormal basis

$$\{S(z)\hat{x},\, S(z)\hat{x},\, C(z)\hat{z},\, C(z)\hat{x}\}, \tag{D.1}$$

with $S(z) = \sqrt{\frac{2}{t}}\sin(\kappa\, z)$ and $C(z) = \sqrt{\frac{2}{t}}\cos(\kappa|, z)$. In this basis, one of the components is fully pinned, while the other its totally unpinned. The first and the last element of the basis can be combined to obtain the stray-field free ansatz.

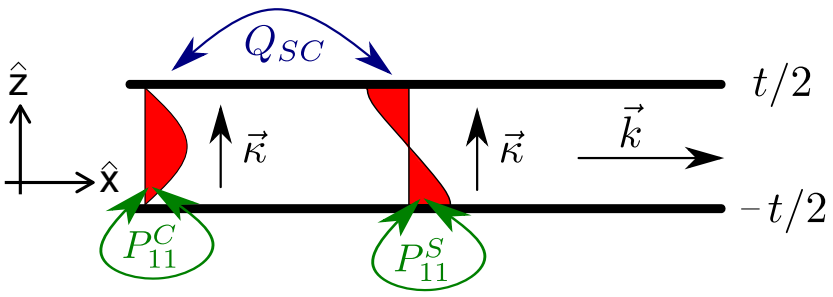

Figure D.1: Sine-cosine basis. The self- and mutual-interaction are depicted by the green and blue arrows, respectively.

As this basis is different from the fully unpinned basis used in Chapters 2 and 4, the dynamic matrix elements may change. The exchange interaction field does not change, since the four profiles contribute with the same effective field proportional to

$\Lambda^2 \left(\frac{\pi}{t}\right)^2$.

On the other hand, the dipolar interaction between the dynamical components of the magnetization is affected by this change of basis. One relevant fact is that the dipolar self-interaction is different for cosine and sine profiles. They can be obtained from the Appendix in Ref. [140]. For each profile, they read

$$P_{11}^C(k) = \frac{(kt)^2}{\pi^2 + (kt)^2}\left[1 + \frac{2\pi^2}{\pi^2 + (kt)^2}\frac{1 + e^{-|k|t}}{|k|t}\right] \tag{D.2}$$

$$P_{11}^S(k) = \frac{(kt)^2}{\pi^2 + (kt)^2}\left[1 - \frac{2(kt)^2}{\pi^2 + (kt)^2}\frac{1 + e^{-|k|t}}{|k|t}\right]. \tag{D.3}$$

Here P_{11}^C and P_{11}^S are the k-dependent self-demagnetizing factors corresponding to the totally pinned and unpinned profiles, respectively. The mutual-demagnetizing factor is also different from the previously calculated one. It can be extracted from the convolution of both profiles with the magnetostatic Green's function $G_Q(z, z') = \frac{k}{2}e^{-|k(z-z')|}\mathrm{sg}(z - z')$ as

$$Q_{SC}(k) = \frac{2}{t}\frac{k}{2}\int_{-t/2}^{t/2} dz \int_{-t/2}^{t/2} dz' e^{-|k(z-z')|}\ \mathrm{sg}(z - z')\ \sin\left(\frac{\kappa z}{2}\right)\ \cos\left(\frac{\kappa z'}{2}\right), \tag{D.4}$$

where $\mathrm{sg}(x)$ is the sign function defined as $x/|x|$. This integral can be solved by using the following identity

$$\begin{aligned}\int_{-t/2}^{t/2} dz \int_{-t/2}^{t/2} dz' \mathrm{sg}(z - z') f\left[|(z - z')|\right] = \int_{-t/2}^{t/2} dz \int_{-t/2}^{z} dz' f\left[(z - z')\right]\ - \\ \int_{-t/2}^{t/2} dz \int_{z}^{t/2} dz' f\left[-(z - z')\right],\end{aligned} \tag{D.5}$$

which leads to

$$Q_{SC}(k) = \pi kt\ \frac{\pi^2 + kt\ (-2 - 2e^{-kt} + kt)}{2(\pi^2 + (kt)^2)^2}. \tag{D.6}$$

The others terms in the dynamic matrix are the same that for the fully unpinned basis. Hence, it reads

$$\bar{C}' = \begin{pmatrix} 0 & \Omega_{x0} & -i2Q_{SC} & 0 \\ -\Omega_{z0} & 0 & 0 & i2Q_{SC} \\ -i2Q_{SC} & 0 & 0 & \Omega_{x1} \\ 0 & i2Q_{SC} & -\Omega_{z1} & 0 \end{pmatrix} \tag{D.7}$$

where

$$\begin{aligned}
\Omega_{x,C} =& P_{11}^{C} + h + \Lambda^2 k^2 + \frac{\Lambda^2 \pi^2}{t^2}, \\
\Omega_{z,C} =& 1 - \mathrm{Q} - P_{11}^{C} + h + \Lambda^2 k^2 + \frac{\Lambda^2 \pi^2}{t^2}, \\
\Omega_{x,S} =& P_{11}^{S} + h + \Lambda^2 k^2 + \frac{\Lambda^2 \pi^2}{t^2}, \\
\Omega_{z,S} =& 1 - \mathrm{Q} - P_{11}^{S} + h + \Lambda^2 k^2 + \frac{\Lambda^2 \pi^2}{t^2},
\end{aligned} \tag{D.8}$$

$\mathrm{Q}=\frac{2K_1}{\mu_0 M_S^2}$, $h = H_0/M_S$ and $\Lambda = \sqrt{\frac{2A_{\mathrm{ex}}}{\mu_0 M_s^2}}$ is the exchange length. We note that the factor $(1-Q)$ is the effective demagnetization field produced by the surfaces of the thin film and reduced by the PMA.

By solving the equation $\det(|\bar{C}' - \mathbb{I}\Omega|) = 0$, the normal mode frequencies $\omega = \omega_M \Omega$ can be calculated. The results are shown in Fig. D.2, and they match quite well the SWIIM frequencies for the lower mode.

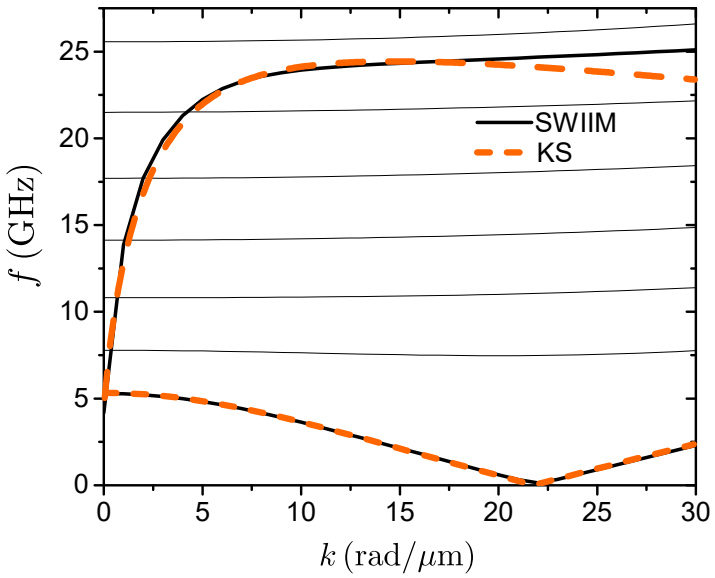

Figure D.2: In orange dashed lines, the two dispersion relations obtained by the KS approach using the sine-cosine basis at the nucleation field $\mu_0 H_c = 11.77$ mT. In black, the first modes calculated with SWIIM for $\mu_0 H = 12.43$ mT. The two SWIIM modes that can be described with a sine and a cosine are highlighted with a wider line.

We observe that this toy model captures the fundamental physics behind the nucleation process, and it can be used to give a better understanding of the softening mechanism.

The eigenvectors obtained as solutions to the eigenvalue problem have the following structure

$$\boldsymbol{\eta}_k = \begin{pmatrix} \eta_{x,C} \\ \eta_{z,C} \\ \eta_{x,S} \\ \eta_{z,S} \end{pmatrix}. \tag{D.9}$$

The results show that the two pinned component are in quadrature with respect to each other (same for the two unpinned components), that means that the coefficients $\eta_{z,C}$ and $\eta_{z,S}$ are purely imaginary, while $\eta_{x,C}$ and $\eta_{x,S}$ are purely real. At nucleation, ($k = k_c = 22$ rad/μm and $\mu_0 H = \mu_0 H_c = 11.8$ mT), both $\eta_{z,C}$ and $\eta_{x,S}$ become null.

In addition to the KS-approach, any other method to calculate the dispersion relation is valid to find the nucleation field. In particular, SWIIM would give a better approximation, because their thickness profiles are not constrained to be an exact sine and cosine. Figure D.3 shows the softening of the minima calculated with KS and SWIIM. For the used parameters, while KS gives $\mu_0 H = 11.77$ mT, SWIIM minimum frequency vanishes at $\mu_0 H = 12.45$ mT. This figure also shows the behavior of $\sqrt{K_A^0}$ (see Section 5.3.2), calculated by the energy minimization. Stripe nucleation is expected when K_A^0 changes of sign and $\sqrt{K_A^0}$ becomes imaginary. Using the same parameters as in the dynamic approaches, we obtain $\mu_0 H = 11.25$ mT. This last value must coincide with the one calculated from 1.31 and it should be less precise than the other two, as the used ansatz does not fulfill the LL equation.

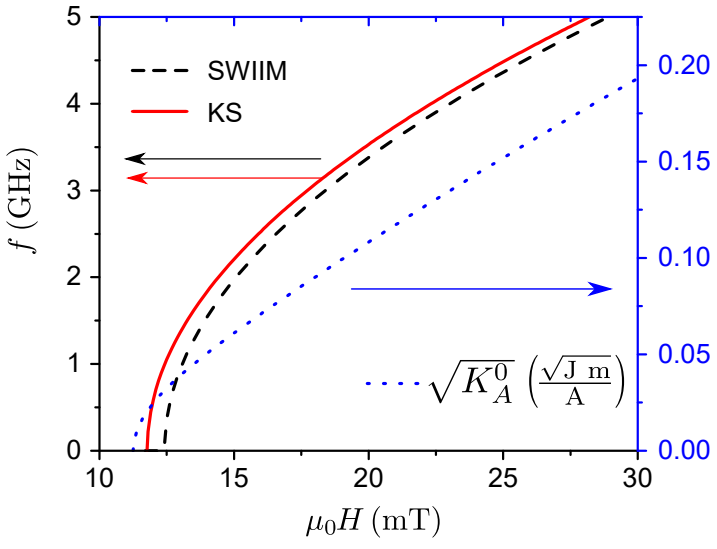

Figure D.3: Softening of the DE0 minimum. On the left axis, frequency of the DE0 mode at $k = 21.9$ rad/μm calculated using SWIIM and KS analytical approach. On the right axis, the value of $\sqrt{K_A^0}$ for the same magnetic parameters. We observe that the nucleation field is slightly different for the three methods. Same magnetic parameters that Fig. 5.6. For SWIIM, surface anisotropy $K_s = 0$.

Bibliography

[1] Sander, D., Valenzuela, S. O., Makarov, D., Marrows, C., Fullerton, E., Fischer, P., *et al.* The 2017 magnetism roadmap. *Journal of Physics D: Applied Physics*, **50** (36), 363001, 2017. x, 98

[2] Mahmoud, A., Ciubotaru, F., Vanderveken, F., Chumak, A. V., Hamdioui, S., Adelmann, C., *et al.* Introduction to spin wave computing. *Journal of Applied Physics*, **128** (16), 161101, 2020. x, 98

[3] Grundler, D. Reconfigurable magnonics heats up. *Nature Physics*, **11** (6), 438–441, 2015. x, 95, 98

[4] The International Technology Roadmap for Semiconductors 2.0, Semiconductor Industry Association (2015). https://www.semiconductors.org/resources/2015-international-technology-roadmap-for-semiconductors-itrs. x, 98

[5] Elachi, C. Waves in active and passive periodic structures: A review. *Proceedings of the IEEE*, **64** (12), 1666–1698, 1976. x, 98

[6] Chumak, A., Serga, A., Hillebrands, B. Magnonic crystals for data processing. *Journal of Physics D: Applied Physics*, **50** (24), 244001, 2017. x, 98

[7] Wagner, K., Kákay, A., Schultheiß, K., Henschke, A., Sebastian, T., Schultheiß, H. Magnetic domain walls as reconfigurable spin-wave nanochannels. *Nature nanotechnology*, **11** (5), 432–436, 2016. x, xi

[8] Yu, H., Xiao, J., Schultheiss, H. Magnetic texture based magnonics. *Physics Reports*, 2021. URL https://www.sciencedirect.com/science/article/pii/S0370157320304270. x, 9, 51, 96, 98, 107

[9] Yan, P., Wang, X. S., Wang, X. R. All-magnonic spin-transfer torque and domain wall propagation. *Phys. Rev. Lett.*, **107**, 177207, 2011. URL https://link.aps.org/doi/10.1103/PhysRevLett.107.177207. x, 98

[10] Chumak, A. V. In: Spintronics Handbook - Spin-Transport and Magnetism. E. Y. Tsymbal and I. Žutić (CRC Press Boca Raton 2019) Vol 1, Chap. 6, pp. xxx-yyy, 2019. x, 99

[11] Chumak, A. V., Serga, A. A., Hillebrands, B. Magnon transistor for all-magnon data processing. *Nature communications*, **5** (1), 1–8, 2014. x, 69, 99

[12] Sushruth, M., Grassi, M., Ait-Oukaci, K., Stoeffler, D., Henry, Y., Lacour, D., *et al.* Electrical spectroscopy of forward volume spin waves in perpendicularly magnetized materials. *Phys. Rev. Research*, **2**, 043203, 2020. URL https://link.aps.org/doi/10.1103/PhysRevResearch.2.043203. xi, 36, 42

[13] Ait Oukaci, K., Lacour, D., Stoeffler, D., Sarpi, B., Montaigne, F., Belkhou, R., *et al.* Weak stripe angle determination by quantitative x-ray magnetic microscopy. *Phys. Rev. Applied*, **14**, 024083, 2020. URL https://link.aps.org/doi/10.1103/PhysRevApplied.14.024083. xii, 17, 76

[14] Ait Oukaci, K., Stoeffler, D., Grassi, M., Sarpi, B., Bailleul, M., Henry, Y., *et al.* Staggered Néel caps originating from intrinsic undulation of a weak stripe magnetic texture, 2021 (in preparation). xii, 71

[15] Henry, Y., Gladii, O., Bailleul, M. Propagating spin-wave normal modes: A dynamic matrix approach using plane-wave demagnetizating tensors, arXiv1611.06153, 2016. xii, 33, 67, 102

[16] Stancil, D. D., Prabhakar, A. Spin waves, tomo 5. Springer, 2009. 1, 36

[17] Jackson, J. D. Classical electrodynamics. John Wiley & Sons, 1999. 3, 23, 24

[18] Eyrich, C. Exchange stiffness in thin-film cobalt alloys (Simon Fraser University thesis), 2010. 4

[19] Abo, G. S., Hong, Y., Park, J., Lee, J., Lee, W., Choi, B. Definition of magnetic exchange length. *IEEE Transactions on Magnetics*, **49** (8), 4937–4939, 2013. 4, 5

[20] Grünberg, P., Mayr, C., Vach, W., Grimsditch, M. Determination of magnetic parameters by means of brillouinscattering. Examples: Fe, Ni, $Ni_{0.8}Fe_{0.2}$. *Journal of Magnetism and Magnetic Materials*, **28** (3), 319–325, 1982. 4

[21] Schlömann, E. A sum rule concerning the inhomogeneous demagnetizing field in nonellipsoidal samples. *Journal of Applied Physics*, **33** (9), 2825–2826, 1962. URL https://doi.org/10.1063/1.1702557. 6, 7

[22] Osborn, J. Demagnetizing factors of the general ellipsoid. *Physical review*, **67** (11-12), 351, 1945. 6

[23] Moskowitz, R., Della Torre, E. Theoretical aspects of demagnetization tensors. *IEEE Transactions on Magnetics*, **2** (4), 739–744, 1966. 6, 7

[24] Hubert, A., Schäfer, R. Magnetic domains: the analysis of magnetic microstructures. Springer Science & Business Media, 2008. 9, 10, 11, 15, 48, 102

[25] Seul, M., Andelman, D. Domain shapes and patterns: the phenomenology of modulated phases. *Science*, **267** (5197), 476–483, 1995. 9

[26] Nahas, Y., Prokhorenko, S., Fischer, J., Xu, B., Carretero, C., Prosandeev, S., *et al.* Inverse transition of labyrinthine domain patterns in ferroelectric thin films. *Nature*, **577** (7788), 47–51, 2020. 9

[27] Kivelson, S. A., Bindloss, I. P., Fradkin, E., Oganesyan, V., Tranquada, J. M., Kapitulnik, A., *et al.* How to detect fluctuating stripes in the high-temperature superconductors. *Rev. Mod. Phys.*, **75**, 1201–1241, 2003. URL https://link.aps.org/doi/10.1103/RevModPhys.75.1201. 9

[28] Heckl, W. M., Möhwald, H. A narrow window for observation of spiral lipid crystals. *Berichte der Bunsengesellschaft für physikalische Chemie*, **90** (12), 1159–1163, 1986. URL https://onlinelibrary.wiley.com/doi/abs/10.1002/bbpc.19860901208. 9

[29] Rosensweig, R. E., Zahn, M., Shumovich, R. Labyrinthine instability in magnetic and dielectric fluids. *Journal of Magnetism and Magnetic Materials*, **39** (1-2), 127–132, 1983. 9

[30] Muller, M. W. Distribution of the magnetization in a ferromagnet. *Phys. Rev.*, **122**, 1485–1489, 1961. URL https://link.aps.org/doi/10.1103/PhysRev.122.1485. 10

[31] Brown, W. F. Rigorous calculation of the nucleation field in a ferromagnetic film or plate. *Phys. Rev.*, **124**, 1348–1353, 1961. URL https://link.aps.org/doi/10.1103/PhysRev.124.1348. 10

[32] Huber, E. E., Smith, D. O. Properties of permalloy films having a magnetoelastic easy axis normal to the film. *Journal of Applied Physics*, **30** (4), S267–S269, 1959. URL https://doi.org/10.1063/1.2185923. 11

[33] Lommel, J. M., Graham, C. D. Rotatable anisotropy in composite films. *Journal of Applied Physics*, **33** (3), 1160–1161, 1962. URL https://doi.org/10.1063/1.1728641.

[34] Lehrer, S. S. Rotatable anisotropy in negative magnetostriction ni–fe films. *Journal of Applied Physics*, **34** (4), 1207–1208, 1963. URL https://doi.org/10.1063/1.1729437. 11

[35] Spain, R. J. Dense-banded domain structure in“rotatable anisotropy”permalloy films. *Applied Physics Letters*, **3** (11), 208–209, 1963. 11

[36] Saito, N., Fujiwara, H., Sugita, Y. A new type of magnetic domain in thin Ni-Fe films. *Journal of the Physical Society of Japan*, **19** (3), 421–422, 1964. URL https://doi.org/10.1143/JPSJ.19.421. 11

[37] Murayama, Y. Micromagnetics on stripe domain films. i. critical cases. *Journal of the Physical Society of Japan*, **21** (11), 2253–2266, 1966. URL https://doi.org/10.1143/JPSJ.21.2253. 11

[38] Landau, L. D., Lifshitz, E. Statistical physics, part 1: Volume 5, 1980. 13

[39] Lemerle, S., Ferré, J., Chappert, C., Mathet, V., Giamarchi, T., Le Doussal, P. Domain wall creep in an ising ultrathin magnetic film. *Phys. Rev. Lett.*, **80**, 849–852, 1998. URL https://link.aps.org/doi/10.1103/PhysRevLett.80.849. 14

[40] Ait Oukaci, K. Domaines magnétiques périodiques pour la propagation guidée d'ondes de spin, (thesis in French), 2021. 14, 71, 72, 78, 102, 111

[41] Hubert, A. Stray-field-free magnetization configurations. *physica status solidi (b)*, **32** (2), 519–534, 1969. 15

[42] Holz, A., Kronmüller, H. The nucleation of stripe domains in thin ferromagnetic films. *physica status solidi (b)*, **31** (2), 787–798, 1969. URL https://onlinelibrary.wiley.com/doi/abs/10.1002/pssb.19690310238. 15

[43] Asti, G., Ghidini, M., Mulazzi, M., Pellicelli, R., Solzi, M., Chesnel, K., *et al.* Nucleation of weak stripe domains: Determination of exchange and anisotropy thermal variation. *Phys. Rev. B*, **76**, 094414, 2007. URL https://link.aps.org/doi/10.1103/PhysRevB.76.094414. 15, 17

[44] Landau, L. D. and Lifshitz, E. On the theory of the dispersion of magnetic permeability in ferromagnetic bodies (english). In: Collected Papers of L.D. Landau, pages. 101 – 114. Pergamon, 1965. 18

[45] Landau, L., Lifshitz, E. On the theory of the dispersion of magnetic permeability in ferromagnetic bodies. *Phys. Z. Sowjet.*, **8** (153), 1935. 18, 102

[46] Lakshmanan, M. The fascinating world of the Landau-Lifshitz-Gilbert equation: an overview. *Phil. Trans. R. Soc. A*, **369** (1939), 1280–1300, 2011. URL https://royalsocietypublishing.org/doi/abs/10.1098/rsta.2010.0319. 18

[47] Hillebrands, B., Ounadjela, K. Spin dynamics in confined magnetic structures I. Springer Science & Business Media, 2003. 18

[48] Guslienko, K. Y., Slavin, A. N. Magnetostatic Green's functions for the description of spin waves in finite rectangular magnetic dots and stripes. *Journal of Magnetism and Magnetic Materials*, **323** (18), 2418 – 2424, 2011. URL http://www.sciencedirect.com/science/article/pii/S0304885311002897. 23, 24, 25

[49] Bailleul, M. Propagation et confinement d'ondes de spin dans les microstructures magnétiques. Thesis, Ecole Polytechnique X, 2002. URL https://pastel.archives-ouvertes.fr/tel-00001976. 23

[50] Guslienko, K. Y., Demokritov, S. O., Hillebrands, B., Slavin, A. N. Effective dipolar boundary conditions for dynamic magnetization in thin magnetic stripes. *Phys. Rev. B*, **66**, 132402, 2002. URL https://link.aps.org/doi/10.1103/PhysRevB.66.132402. 24

[51] Guslienko, K. Y., Slavin, A. N. Spin-waves in cylindrical magnetic dot arrays with in-plane magnetization. *Journal of Applied Physics*, **87** (9), 6337–6339, 2000. URL https://doi.org/10.1063/1.372698. 24

[52] Guslienko, K. Y., Pishko, V., Novosad, V., Buchanan, K., Bader, S. D. Quantized spin excitation modes in patterned ferromagnetic stripe arrays. *Journal of Applied Physics*, **97** (10), 10A709, 2005. URL https://doi.org/10.1063/1.1850364. 24

[53] Bayer, C., Jorzick, J., Demokritov, S. O., Slavin, A. N., Guslienko, K. Y., Berkov, D. V., *et al.* Spin-Wave Excitations in Finite Rectangular Elements, pages. 57–103. Berlin, Heidelberg: Springer Berlin Heidelberg, 2006. URL https://doi.org/10.1007/10938171_2. 24

[54] Bayer, C., Jorzick, J., Hillebrands, B., Demokritov, S. O., Kouba, R., Bozinoski, R., *et al.* Spin-wave excitations in finite rectangular elements of $Ni_{80}Fe_{20}$. *Phys. Rev. B*, **72**, 064427, 2005. URL https://link.aps.org/doi/10.1103/PhysRevB.72.064427. 24

[55] Arias, R. E. Spin-wave modes of ferromagnetic films. *Phys. Rev. B*, **94**, 134408, 2016. URL https://link.aps.org/doi/10.1103/PhysRevB.94.134408. 24

[56] Bailleul, M. Spectroscopie d'ondes de spin pour l'électronique de spin (HDR in French), 2011. 24

[57] Kalinikos, B. A., Slavin, A. N. Theory of dipole-exchange spin wave spectrum for ferromagnetic films with mixed exchange boundary conditions. *Journal of Physics C: Solid State Physics*, **19** (35), 7013–7033, 1986. URL https://doi.org/10.1088/F0022-3719/F19/F35/F014. 26, 28, 30, 55

[58] Eshbach, J. R., Damon, R. W. Surface magnetostatic modes and surface spin waves. *Phys. Rev.*, **118**, 1208–1210, 1960. URL https://link.aps.org/doi/10.1103/PhysRev.118.1208. 28, 42, 54

[59] Schilz, W. Experimental evidence for coupling between dipole and exchange dominated spin waves in epitaxial YIG. *Solid State Communications*, **11** (5), 615 – 616, 1972. URL http://www.sciencedirect.com/science/article/pii/0038109872904735. 28

[60] Adam, J. D., O'Keeffe, T. W., Patterson, R. W. Magnetostatic wave to exchange resonance coupling. *Journal of Applied Physics*, **50** (B3), 2446–2448, 1979. URL https://doi.org/10.1063/1.326980. 28

[61] Rado, G., Weertman, J. Spin-wave resonance in a ferromagnetic metal. *Journal of Physics and Chemistry of Solids*, **11** (3), 315 – 333, 1959. URL http://www.sciencedirect.com/science/article/pii/0022369759902331. 29

[62] Talagala, P., Fodor, P. S., Haddad, D., Naik, R., Wenger, L. E., Vaishnava, P. P., *et al.* Determination of magnetic exchange stiffness and surface anisotropy constants in epitaxial $Ni_{1-x}Co_x(001)$ films. *Phys. Rev. B*, **66**, 144426, 2002. URL https://link.aps.org/doi/10.1103/PhysRevB.66.144426. 30, 113

[63] Kalinikos, B. A., Kostylev, M. P., Kozhus, N. V., Slavin, A. N. The dipole-exchange spin wave spectrum for anisotropic ferromagnetic films with mixed exchange boundary conditions. *Journal of Physics: Condensed Matter*, **2** (49), 9861–9877, 1990. URL https://doi.org/10.1088/0953-8984/2/49/012. 30

[64] Smith, N., Markham, D., LaTourette, D. Magnetoresistive measurement of the exchange constant in varied-thickness permalloy films. *Journal of Applied Physics*, **65** (11), 4362–4365, 1989. URL https://doi.org/10.1063/1.343273. 33

[65] Gurevich, A., Anisimov, A. Intrinsic spin wave relaxation processes in yttrium iron garnets. *Zh. Eksp. Teor. Fiz*, **68**, 677–688, 1975. 34

[66] Suhl, H. Theory of the magnetic damping constant. *IEEE Transactions on Magnetics*, **34** (4), 1834–1838, 1998. 34

[67] Gilbert, T. L. A phenomenological theory of damping in ferromagnetic materials. *IEEE Transactions on Magnetics*, **40** (6), 3443–3449, 2004. 35

[68] Kostylev, M. P., Serga, A. A., Schneider, T., Neumann, T., Leven, B., Hillebrands, B., *et al.* Resonant and nonresonant scattering of dipole-dominated spin waves from a region of inhomogeneous magnetic field in a ferromagnetic film. *Phys. Rev. B*, **76**, 184419, 2007. URL https://link.aps.org/doi/10.1103/PhysRevB.76.184419. 36

[69] Shtykov, V. V., Smolskiy, S. M. Introduction to Quantum Electronics and Nonlinear Optics. Springer, 2020. 38

[70] Bilzer, C., Devolder, T., Crozat, P., Chappert, C., Cardoso, S., Freitas, P. P. Vector network analyzer ferromagnetic resonance of thin films on coplanar waveguides: Comparison of different evaluation methods. *Journal of Applied Physics*, **101** (7), 074505, 2007. URL https://doi.org/10.1063/1.2716995. 39

[71] Bilzer, C. Microwave susceptibility of thin ferromagnetic films: metrology and insight into magnetization dynamics. Tesis Doctoral, Université Paris Sud-Paris XI, 2007. 40

[72] Solano Córdova, J. N. Broadband ferromagnetic resonance characterization for CoFeB, Py, YIG thin films and Py/YIG bilayer system. B.S. thesis, Quito, 2017. 39

[73] Bailleul, M. Shielding of the electromagnetic field of a coplanar waveguide by a metal film: Implications for broadband ferromagnetic resonance measurements. *Applied Physics Letters*, **103** (19), 192405, 2013. URL https://doi.org/10.1063/1.4829367. 39, 40

[74] Ghodgaonkar, D., Varadan, V., Varadan, V. Free-space measurement of complex permittivity and complex permeability of magnetic materials at microwave frequencies. *IEEE Transactions on instrumentation and measurement*, **39** (2), 387–394, 1990. 40

[75] Olson, F. A., Kirchner, E. K., Mehta, K. B., Peternell, F. J., Morley, B. C. Propagation of magnetostatic surface waves in yig rods. *Journal of Applied Physics*, **38** (3), 1218–1220, 1967. URL https://doi.org/10.1063/1.1709546. 41

[76] Brundle, L. K., Freedman, N. J. Magnetostatic surface waves on a y.i.g. slab. *Electronics Letters*, **4** (7), 132–134, 1968. 41

[77] Serga, A. A., Chumak, A. V., Hillebrands, B. YIG magnonics. *Journal of Physics D: Applied Physics*, **43** (26), 264002, 2010. 42

[78] Bailleul, M., Olligs, D., Fermon, C., Demokritov, S. O. Spin waves propagation and confinement in conducting films at the micrometer scale. *Europhysics Letters (EPL)*, **56** (5), 741–747, 2001. 42

[79] Vlaminck, V., Bailleul, M. Spin-wave transduction at the submicrometer scale: Experiment and modeling. *Phys. Rev B*, **81**, 014425, 2010. 42

[80] Ciubotaru, F., Devolder, T., Manfrini, M., Adelmann, C., Radu, I. P. All electrical propagating spin wave spectroscopy with broadband wavevector capability. *Applied Physics Letters*, **109** (1), 012403, 2016. URL https://doi.org/10.1063/1.4955030. 42

[81] Vlaminck, V., Bailleul, M. Current-induced spin-wave Doppler shift. *Science*, **322**, 410, 2008. 42

[82] Gladii, O., Haidar, M., Henry, Y., Kostylev, M., Bailleul, M. Frequency nonreciprocity of surface spin wave in permalloy thin films. *Phys. Rev B*, **93**, 054430, 2016. 42

[83] Lucassen, J., Schippers, C. F., Rutten, L., Duine, R. A., Swagten, H. J., Koopmans, B., *et al.* Optimizing propagating spin wave spectroscopy. *Applied Physics Letters*, **115** (1), 012403, 2019. 42

[84] Faraday, M. I. experimental researches in electricity.—nineteenth series. *Philosophical Transactions of the Royal Society of London*, (136), 1–20, 1846. 47

[85] LL.D., J. K. Xliii. on rotation of the plane of polarization by reflection from the pole of a magnet. *The London, Edinburgh, and Dublin Philosophical Magazine and Journal of Science*, **3** (19), 321–343, 1877. URL https://doi.org/10.1080/14786447708639245. 48

[86] McCord, J., Erkartal, B., von Hofe, T., Kienle, L., Quandt, E., Roshchupkina, O., *et al.* Revisiting magnetic stripe domains — anisotropy gradient and stripe asymmetry. *Journal of Applied Physics*, **113** (7), 073903, 2013. URL https://doi.org/10.1063/1.4792517. 48

[87] McCord, J. Progress in magnetic domain observation by advanced magneto-optical microscopy. *Journal of Physics D: Applied Physics*, **48** (33), 333001, 2015. 48

[88] Bennett, B., Maradudin, A., Swanson, L. A theory of the brillouin scattering of light by acoustic phonons in a metal. *Annals of Physics*, **71** (2), 357 – 394, 1972. URL http://www.sciencedirect.com/science/article/pii/0003491672901224. 49

[89] Demokritov, S., Tsymbal, E. Light scattering from spin waves in thin films and layered systems. *Journal of Physics: Condensed Matter*, **6** (36), 7145–7188, 1994. URL https://doi.org/10.1088/F0953-8984/F6/F3/F002. 49

[90] Sandercock, J., Wettling, W. Light scattering from thermal acoustic magnons in yttrium iron garnet. *Solid State Communications*, **13** (10), 1729 – 1732, 1973. URL http://www.sciencedirect.com/science/article/pii/0038109873902767. 49

[91] Stashkevich, A. A., Djemia, P., Fetisov, Y. K., Bizière, N., Fermon, C. High-intensity brillouin light scattering by spin waves in a permalloy film under microwave resonance pumping. *Journal of Applied Physics*, **102** (10), 103905, 2007. URL https://doi.org/10.1063/1.2815673. 50

[92] Borovik-Romanov, A. S., Kreines, N. M., Zhotikov, V. G., Laiho, R., Levola, T. Optical detection of ferromagnetic resonance in k2cuf4. *Journal of Physics C: Solid State Physics*, **13** (5), 879–885, 1980. URL https://doi.org/10.1088/0022-3719/13/5/018. 50

[93] Grassi, M., Geilen, M., Louis, D., Mohseni, M., Brächer, T., Hehn, M., *et al.* Slow-wave-based nanomagnonic diode. *Phys. Rev. Applied*, **14**, 024047, 2020. URL https://link.aps.org/doi/10.1103/PhysRevApplied.14.024047. 51, 55, 56, 57, 99

[94] Jalas, D., Petrov, A., Eich, M., Freude, W., Fan, S., Yu, Z., *et al.* What is and what is not an optical isolator. *Nature Photon*, **7**, 579, 2013. 52

[95] Lan, J., Yu, W., Wu, R., Xiao, J. Spin-wave diode. *Phys. Rev X*, **5**, 041049, 2015. 52

[96] Brächer, T., Boulle, O., Gaudin, G., Pirro, P. Creation of unidirectional spin-wave emitters by utilizing interfacial dzyaloshinskii-moriya interaction. *Phys. Rev B*, **95**, 064429, 2017. 52

[97] Chen, J., Yu, T., Liu, C., Liu, T., Madami, M., Shen, K., *et al.* Excitation of unidirectional exchange spin waves by a nanoscale magnetic grating. *Phys. Rev B*, **100**, 104427, 2019. 52

[98] Caloz, C., Alù, A., Tretyakov, S., Sounas, D., Achouri, K., Deck-Léger, Z.-L. Electromagnetic nonreciprocity. *Phys. Rev. Applied*, **10**, 047001, 2018. URL https://link.aps.org/doi/10.1103/PhysRevApplied.10.047001. 52

[99] Seshadri, S. R. Surface magnetostatic modes on a ferrite slab. In: Proc. IEEE **58**. 506, 1970. 53

[100] Shichi, S., Kanazawa, N., Matsuda, K., Okajima, S., Hasegawa, T., Okada, T., *et al.* Spin wave isolator based on frequency displacement nonreciprocity in ferromagnetic bilayer. *J. Appl. Phys*, **117**, 17D125, 2015. 53

[101] Sebastian, T., Schultheiß, K., Obry, B., Hillebrands, B., Schultheiß, H. Micro-focused brillouin light scattering: imaging spin waves at the nanoscale. *Front. Phys*, **3**, 35, 2015. 64

[102] Haidar, M., Bailleul, M., Kostylev, M. P., Lao, Y. Nonreciprocal Oersted field contribution to the current-induced frequency shift of magnetostatic surface waves. *Phys. Rev. B*, **89**, 094426, 2014. 64

[103] Camley, R. Nonreciprocal surface waves. *Surf. Sci. Rep.*, **7**, 103, 1987. 64, 99

[104] Kostylev, M. Non-reciprocity of dipole-exchange spin waves in thin ferromagnetic films. *J. Appl. Phys*, **113**, 053907, 2013. 67

[105] Stancil, D. D., Henty, B. E., Cepni, A. G., Van't Hof, J. P. Observation of an inverse Doppler shift from left-handed dipolar spin waves. *Phys. Rev. B*, **74**, 060404, 2006. URL https://link.aps.org/doi/10.1103/PhysRevB.74.060404. 68

[106] O'Handley, R. C. Magnetostriction of transition-metal-metalloid glasses: Temperature dependence. *Phys. Rev. B*, **18**, 930–938, 1978. URL https://link.aps.org/doi/10.1103/PhysRevB.18.930. 71

[107] Díaz, J., Quirós, C., Alvarez-Prado, L. M., Aroca, C., Ranchal, R., Ruffoni, M., *et al.* Determination of the magnetostrictive atomic environments in FeCoB alloys. *Phys. Rev. B*, **85**, 134437, 2012. URL https://link.aps.org/doi/10.1103/PhysRevB.85.134437. 71

[108] Hehn, M., Padovani, S., Ounadjela, K., Bucher, J. P. Nanoscale magnetic domain structures in epitaxial cobalt films. *Phys. Rev. B*, **54**, 3428–3433, 1996. URL https://link.aps.org/doi/10.1103/PhysRevB.54.3428. 71

[109] Suran, G., Naili, M., Niedoba, H., Machizaud, F., Acher, O., Pain, D. Magnetic and structural properties of Co-rich CoFeZr amorphous thin films. *Journal of Magnetism and Magnetic Materials*, **192** (3), 443 – 457, 1999. URL http://www.sciencedirect.com/science/article/pii/S0304885398004296. 71, 73

[110] Yu, J., Chang, C., Karns, D., Ju, G., Kubota, Y., Eppler, W., *et al.* Thermal annealing effect on FeCoB soft underlayer for perpendicular magnetic recording. *Journal of applied physics*, **91** (10), 8357–8359, 2002. 73

[111] Leaf, G., Kaper, H., Yan, M., Novosad, V., Vavassori, P., Camley, R. E., *et al.* Dynamic origin of stripe domains. *Phys. Rev. Lett.*, **96**, 017201, 2006. URL https://link.aps.org/doi/10.1103/PhysRevLett.96.017201. 81, 102

[112] Bailleul, M., Olligs, D., Fermon, C. Micromagnetic phase transitions and spin wave excitations in a ferromagnetic stripe. *Phys. Rev. Lett.*, **91**, 137204, 2003. URL https://link.aps.org/doi/10.1103/PhysRevLett.91.137204. 81

[113] Zeng, X., Yang, G., Yan, M. A theoretical study on critical phenomena of magnetic soft modes. *Physica B: Condensed Matter*, **506**, 168–172, 2017. URL https://www.sciencedirect.com/science/article/pii/S0921452616305427. 81, 102

[114] Anderson, P. W. Plasmons, gauge invariance, and mass. *Phys. Rev.*, **130**, 439–442, 1963. URL https://link.aps.org/doi/10.1103/PhysRev.130.439. 82

[115] Goldstone, J., Salam, A., Weinberg, S. Broken symmetries. *Phys. Rev.*, **127**, 965–970, 1962. URL https://link.aps.org/doi/10.1103/PhysRev.127.965. 82

[116] Higgs, P. W. Broken symmetries and the masses of gauge bosons. *Phys. Rev. Lett.*, **13**, 508–509, 1964. URL https://link.aps.org/doi/10.1103/PhysRevLett.13.508. 82

[117] Pekker, D., Varma, C. Amplitude/Higgs modes in condensed matter physics. *Annu. Rev. Condens. Matter Phys.*, **6** (1), 269–297, 2015. 83

[118] Shimano, R., Tsuji, N. Higgs mode in superconductors. *Annual Review of Condensed Matter Physics*, **11** (1), 103–124, 2020. URL https://doi.org/10.1146/annurev-conmatphys-031119-050813. 83

[119] Léonard, J., Morales, A., Zupancic, P., Donner, T., Esslinger, T. Monitoring and manipulating higgs and goldstone modes in a supersolid quantum gas. *Science*, **358** (6369), 1415–1418, 2017. URL https://science.sciencemag.org/content/358/6369/1415. 83

[120] Meier, Q. N., Stucky, A., Teyssier, J., Griffin, S. M., van der Marel, D., Spaldin, N. A. Manifestation of structural higgs and goldstone modes in the hexagonal manganites. *Phys. Rev. B*, **102**, 014102, 2020. URL https://link.aps.org/doi/10.1103/PhysRevB.102.014102. 83

[121] Rüegg, C., Normand, B., Matsumoto, M., Furrer, A., McMorrow, D. F., Krämer, K. W., *et al.* Quantum magnets under pressure: controlling elementary excitations in tlcucl 3. *Physical review letters*, **100** (20), 205701, 2008. 83

[122] Zavjalov, V., Autti, S., Eltsov, V., Heikkinen, P., Volovik, G. Light higgs channel of the resonant decay of magnon condensate in superfluid 3 he-b. *Nature communications*, **7** (1), 1–6, 2016. 83

[123] Banerjee, C., Gruszecki, P., Klos, J. W., Hellwig, O., Krawczyk, M., Barman, A. Magnonic band structure in a Co/Pd stripe domain system investigated by Brillouin light scattering and micromagnetic simulations. *Phys. Rev. B*, **96**, 024421, 2017. URL https://link.aps.org/doi/10.1103/PhysRevB.96.024421. 90

[124] Gruszecki, P., Banerjee, C., Mruczkiewicz, M., Hellwig, O., Barman, A., Krawczyk, M. Chapter two - the influence of the internal domain wall structure on spin wave band structure in periodic magnetic stripe domain patterns. In: R. L. Stamps, H. Schultheiß (eds.) Recent Advances in Topological Ferroics and their Dynamics, tomo 70 de *Solid State Physics*, pages. 79–132. Academic Press, 2019. URL https://www.sciencedirect.com/science/article/pii/S0081194719300037. 90

[125] Buijnsters, F. J., Fasolino, A., Katsnelson, M. I. Zero modes in magnetic systems: General theory and an efficient computational scheme. *Phys. Rev. B*, **89**, 174433, 2014. URL https://link.aps.org/doi/10.1103/PhysRevB.89.174433. 91

[126] Brächer, T., Pirro, P., Hillebrands, B. Parallel pumping for magnon spintronics: Amplification and manipulation of magnon spin currents on the micron-scale. *Physics Reports*, **699**, 1 – 34, 2017. URL http://www.sciencedirect.com/science/article/pii/S0370157317302004. 92, 95, 97

[127] Bauer, H. G., Majchrak, P., Kachel, T., Back, C. H., Woltersdorf, G. Nonlinear spin-wave excitations at low magnetic bias fields. *Nature communications*, **6** (1), 1–7, 2015. 92, 95

[128] Camara, I. S., Tacchi, S., Garnier, L.-C., Eddrief, M., Fortuna, F., Carlotti, G., *et al.* Magnetization dynamics of weak stripe domains in Fe–N thin films: a multitechnique complementary approach. *Journal of Physics: Condensed Matter*, **29** (46), 465803, 2017. URL https://doi.org/10.1088/1361-648X/aa8f36. 92, 105

[129] Ben Youssef, J., Vukadinovic, N., Billet, D., Labrune, M. Thickness-dependent magnetic excitations in permalloy films with nonuniform magnetization. *Phys. Rev. B*, **69**, 174402, 2004. URL https://link.aps.org/doi/10.1103/PhysRevB.69.174402.

[130] Vukadinovic, N., Vacus, ., Labrune, M., Acher, ., Pain, D. Magnetic excitations in a weak-stripe-domain structure: A 2D dynamic micromagnetic approach. *Phys.*

Rev. Lett., **85**, 2817–2820, 2000. URL https://link.aps.org/doi/10.1103/PhysRevLett.85.2817. 92

[131] Vukadinovic, N., Labrune, M., Youssef, J. B., Marty, A., Toussaint, J. C., Le Gall, H. Ferromagnetic resonance spectra in a weak stripe domain structure. *Phys. Rev. B*, **65**, 054403, 2001. URL https://link.aps.org/doi/10.1103/PhysRevB.65.054403. 92

[132] Ebels, U., Wigen, P., Ounadjela, K. Domain FMR in epitaxial Co(0 0 0 1) films with stripe domains. *Journal of Magnetism and Magnetic Materials*, **177-181**, 1239 – 1240, 1998. URL http://www.sciencedirect.com/science/article/pii/S0304885397003090, international Conference on Magnetism (Part II).

[133] Ebels, U., Buda, L., Ounadjela, K., Wigen, P. E. Ferromagnetic resonance excitation of two-dimensional wall structures in magnetic stripe domains. *Phys. Rev. B*, **63**, 174437, 2001. URL https://link.aps.org/doi/10.1103/PhysRevB.63.174437. 92

[134] Ebels, U., Buda, L. D., Ounadjela, K., Wigen, P. E. Small amplitude dynamics of nonhomogeneous magnetization distributions: The excitation spectrum of stripe domains. In: B. Hillebrands, K. Ounadjela (eds.) Spin Dynamics in Confined Magnetic Structures I, pages. 167–217. Berlin, Heidelberg: Springer Berlin Heidelberg, 2002. URL https://doi.org/10.1007/3-540-40907-6_6. 92, 105

[135] Lührmann, B., Dötsch, H., Sure, S. High-frequency excitations of stripe-domain lattices in magnetic garnet films. *Applied Physics A*, **57** (6), 553–559, 1993. 92

[136] Ramesh, M., Wigen, P. Ferromagnetodynamics of parallel stripe domains-domain walls system. *Journal of magnetism and magnetic materials*, **74** (2), 123–133, 1988. 92

[137] Krawczyk, M., Grundler, D. Review and prospects of magnonic crystals and devices with reprogrammable band structure. *Journal of Physics: Condensed Matter*, **26** (12), 123202, 2014. URL https://doi.org/10.1088/0953-8984/26/12/123202. 95

[138] Tacchi, S., Gruszecki, P., Madami, M., Carlotti, G., Kłos, J. W., Krawczyk, M., *et al.* Universal dependence of the spin wave band structure on the geometrical characteristics of two-dimensional magnonic crystals. *Scientific Reports*, **5** (1), 1–9, 2015. 95

[139] Liu, C., Wu, S., Zhang, J., Chen, J., Ding, J., Ma, J., *et al.* Current-controlled propagation of spin waves in antiparallel, coupled domains. *Nature nanotechnology*, **14** (7), 691–697, 2019. 96, 107

[140] Kalinikos, B. A., Slavin, A. N. Theory of dipole-exchange spin wave spectrum for ferromagnetic films with mixed exchange boundary conditions. *J. Phys C*, **19**, 7013, 1986. 116

Université de Strasbourg

Matías Pablo GRASSI

Ondes de spin dans des distributions de l'aimantation inhomogènes

PROJET FINANCÉ PAR L'ANR - PROJECT FUNDED BY THE ANR

Résumé

Des distributions inhomogènes de l'aimantation existent lorsque le matériau n'est pas uniforme, ou lorsqu'une texture magnétique se forme dans un matériau homogène. Dans les deux cas, les symétries brisées modifient l'excitation et la propagation des ondes de spin et donnent lieu à des phénomènes surprenants.

Dans ce contexte, nous avons étudié la propagation des ondes de spin dans une bicouche avec un contraste de l'aimantation de saturation dans la configuration Damon-Eshbach. Nous avons trouvé, à l'aide de simulations et expériences (spectroscopie d'ondes de spin propagatives et diffusion de Brouillon), que le système montre une très forte non-réciprocité en fréquence qui peut être utilisée pour réaliser une diode magnonique.

Par ailleurs, nous avons étudié la dynamique des ondes de spin dans des couches minces qui présentent des domaines magnétiques en rubans faibles. Nous avons montré que ces ondes de spin peuvent être interprétées comme une extension des modes de Damon-Eshbach dans l'état saturé, qui s'adaptent à la brisure de symétrie. Nous avons également montré que les deux modes d'ondes de spin de plus basse fréquence correspondent aux modes de Goldstone et Higgs de la texture en rubans. Ces résultats ont été confirmés par des mesures de diffusion Brillouin et de résonance ferromagnétique.

Mot clés : ondes de spin, dynamique de spins, non-réciprocité, domaines en rubans, modes de Higgs et Goldstone.

Abstract

Inhomogeneous magnetization distributions may exist because the magnetic parameters are distributed, or because magnetic textures nucleate in homogenous materials. In both cases, the broken symmetries affect the spin-wave excitation and propagation, leading to a number of intriguing phenomena.

In this context, we have studied the propagation of spin waves in a bilayer with a saturation magnetization contrast for the Damon-Eshbach configuration. We have found, by means of simulations and experiments (Propagating Spin Wave Spectroscopy and Brillouin Light Scattering), that this system shows a strong frequency non-reciprocity which can be used for the realization of a spin-wave diode.

We have also studied the spin-wave dynamics in thin films which exhibit weak magnetic stripe domains. We have shown how these modes can be interpreted as an extension of the Damon-Eshbach spectrum of the saturated state, which adapts to the symmetry breaking. Furthermore, we have identified the two lowest frequency modes to the Goldstone- and Higgs- modes of the stripe texture. These results were confirmed by Brillouin Light Scattering and Ferromagnetic Resonance experiments.

Keywords: spin waves, spin dynamics, non-reciprocity, stripe domains, Higgs and Goldstone modes.